# Continental crust production during the early Earth: Constraints from geodynamic models

Dissertation
zur Erlangung des Grades
Doktor der Naturwissenschaften
im Promotionsfach Mineralogie
am Fachbereich Chemie, Pharmazie, Geographie und Geowissenschaften der
Johannes Gutenberg-Universität Mainz

von
Andrea Piccolo
geboren in Este(PD), Italy

JOHANNES GUTENBERG UNIVERSITÄT MAINZ

Mainz, 2019

Gutachter:

Tag der mündlichen Prüfung:
28.05.2019

# CONTENTS

# LIST OF FIGURES

# LIST OF TABLES

# ABSTRACT

Most of the continental crust was produced by the end of Archean. Although the earliest continental crust is pivotal for understanding the Earth habitability, the geodynamic processes that assisted its production during the Archean are still not well understood. Geological data are too scarce to have a coherent picture of Archean geodynamics, thus, to conceive physically and chemically consistent scenarios, indirect methods such as geodynamic and petrological modelling are needed.

In this thesis, I combine geodynamical and petrological modelling to identify the main geodynamical processes that assisted the production of the earliest felsic crust. I performed both 2D-3D systematic numerical experiments, employing several pre-computed phase diagrams for both mantle and mafic crust that store the density and melt fraction as a function of P-T conditions. Earliest felsic crust is mainly composed of Tonalite-Trondhjemite-Granodiorite suites (TTGs), which are the product of partial melting of hydrous mafic meta-basalts. Mafic crustal phase diagrams had been produced in a such way that it is possible to track the chemical evolution of the hydrated crust.

The first part of the thesis is devoted to exploring the effects of having a variable but high upper mantle potential temperature ($T_P = 1450 - 1600^{\circ}$C) and mantle radiogenic heat production values of the Archean mantle (Chapter 2), using a 2D finite element code. Due to the high mantle potential temperature and high radiogenic heating, the asthenosphere partially melts producing mafic melts that are converted into new hydrated mafic crust and dry mafic intrusions, which heat the prescribed mafic crust that partially melt producing felsic melts. The extraction of felsic melts leaves behind a dense complementary mafic residuum that drips into the mantle, causing a feedback between mantle melting, felsic crust production and gravitational instabilities. These processes are fast and promote the compositional evolution of both the mantle and the crust. The

production of felsic crust and complementary mafic dense residuum facilitates these processes at lower mantle potential temperature ($T_P$ = 1450°C) suggesting that $T_P$ cannot spontaneously grow to high values and the recorded high $T_P$ might be associated with mantle upwelling. These results were used to provide physical relationship that can be integrated into 1D parametrized cooling history in the perspective of constraining the effect of such transient processes on the overall cooling of the planet Earth (Chapter 4).

The second part of the thesis is devoted to exploring the effect of mantle plume on felsic crust production (Chapter 3). A 3D finite difference numerical code was further developed to perform both 2D and 3D simulations, by integrating melt extraction to simulate crustal forming processes. The thickness of the lithosphere, the initially prescribed mantle potential temperature and the radiogenic heat production has been varied to study the effect of a short lived and hot plume ($T^{Pl}$ = 1600°C). The results suggest that high mantle potential temperatures ($T_P \geq$ 1500°C) promote the total removal of the lithosphere in less than 10 Myrs due to the continuous asthenospheric melting. At low $T_P$ ($\geq$ 1450°C), on the other hand, the fate of the lithosphere depends on the prescribed vigour of convection, lithospheric thickness and radiogenic heating of the mantle. Moreover, at low potential temperature, the produced felsic crust tends to accumulate at the rim of the plume-impact structures generating proto-continental terrains mimicking features of modern plate-boundaries. The main differences between 2D and 3D experiments concerns the stability of the oceanic plateau. In 2D experiments, thickened crust is more stable allowing the generation of felsic melts at higher pressure than in the 3D cases that are less prone to generate felsic melts at high pressure ($> 1GPa$).

This work is a first attempt to connect geodynamic processes to the chemical evolution of both mantle and crust. It shows the importance of considering petrology in geodynamic modelling and gives important insights in the effects of continental crust production during the Archean.

# KURZFASSUNG

Der größte Teil der kontinentalen Kruste wurde Ende des Archaikums gebildet. Die geodynamischen Prozesse die zu dessen Entstehung führten sind noch immer nicht vollständig verstanden, obwohl diese frühe kontinentale Kruste ausschlaggebend ist, um die Bewohnbarkeit der Erde zu verstehen. Geologische Daten sind zu spärlich um ein stimmiges Bild über die Dynamik des Archaikums zu erhalten. Daher, um physikalisch und chemisch konsistente Szenarien zu entwickeln, sind indirekte Methoden wie geodynamische und petrologische Modellierungen erforderlich.

In dieser Arbeit kombiniere ich geodynamische und petrologische Modellierung, um die primären geodynamischen Prozesse zu identifizieren, die die Produktion der frühesten felsischen Kruste förderten. Hierzu habe ich systematische numerische Experimente sowohl in 2D als auch in 3D durchgeführt, unter der Verwendung von zuvor berechneten Phasendiagrammen. Die Phasendiagramme geben die Dichte und den Schmelzanteil als Funktion von Druck (P) und Temperatur (T) für jeweils den Mantel und der mafischen Kruste an. Die früheste felsische Kruste besteht hauptsächlich aus Tonalit-Trondhjemit-Granodiorit-Folgen (TTGs), die das Ergebnis von partieller Schmelzung von wasserhaltigen mafischen Meta-Basalten sind. Die mafischen Krustenphasendiagramme wurden so erstellt, dass die chemische Entwicklung der hydrierten Kruste verfolgt werden kann.

Der erste Teil der Dissertation widmet sich den Auswirkungen einer variablen, aber hohen potentiellen Temperatur des oberen Mantels ($T_P$ = 1450-1600 °C) und der radiogenen Wärmeproduktion des archaischen Mantels (Kapitel 2), unter der Verwendung eines 2D Finite-Elemente-Codes. Aufgrund der hohen potentiellen Manteltemperatur und der hohen radiogenen Erwärmung, kommt es zur partiellen Aufschmelzung der Asthenosphäre. Die hieraus entstehenden mafischen Schmelzen werden in eine neue hydratisierte mafische Kruste sowie in trockene mafische

Intrusionen umgewandelt. Dies erwärmt die mafische Kruste, die teilweise schmilzt und felsische Schmelzen erzeugt. Die Extraktion der felsischen Schmelze hinterlässt ein dichtes mafisches Residuum, welches in den Mantel sinkt und eine Rückkopplung zwischen Mantelschmelzung, felsische Krustenproduktion und Gravitationsinstabilitäten verursacht. Diese Prozesse sind schnell und fördern die Zusammensetzungsentwicklung von sowohl dem Mantel als auch der Kruste. Die Produktion der felsischen Kruste und dem assoziierten mafischen dichten Residuum ermöglichen diese Prozesse bei einer niedrigeren potentiellen Manteltemperatur (TP = 1450 °C). Dies deutet darauf hin, dass TP spontan nicht auf hohe Werte anwachsen kann und dass die verzeichnete hohe TP möglicherweise mit Mantelauftrieb assoziiert ist. Diese Ergebnisse wurden verwendet, um eine physikalische Beziehung bereitzustellen, die integrieret werden kann in eine 1D parametrisierte Abkühlungsgeschichte zur Einschränkung der Wirkung solcher vorübergehenden Prozesse auf die gesamte Abkühlung der Erde (Kapitel 4).

Der zweite Teil der Dissertation widmet sich der Untersuchung von dem Einfluss eines Mantelplumes auf die felsische Krustenproduktion (Kapitel 3). Ein 3D numerischer Finite-Differenzen-Code wurde weiterentwickelt, um sowohl 2D als auch 3D Simulationen durchzuführen, indem Schmelzextraktion zur Simulation von Krustenbildungsprozessen integriert wurde. Die Mächtigkeit der Lithosphäre, die anfängliche potentielle Manteltemperatur und die radiogene Wärmeproduktion wurden verändert, um den Einfluss von einem kurzlebigen und heißen Plume ($T^{Pl}$ = 1600 °C) zu studieren. Die Ergebnisse suggerieren, dass eine hohe potentielle Manteltemperatur ($T_P \geq 1500$ °C) die gesamte Entfernung der Lithosphäre in weniger als 10 Millionen Jahren fördert aufgrund der fortlaufenden asthenosphärischen Aufschmelzung. Bei niedriger $T_P$ (≥ 1450° C) hingegen hängt das Schicksal der Lithosphäre von der vorgeschriebenen Konvektionskraft, der Lithospährenmächtigkeit sowie der radiogenen Erwärmung des Mantels ab. Weiterhin tendiert die produzierte felsische Kruste dazu sich am Rand der Plumewirkungsstrukturen zu akkumulieren bei geringer potentieller Temperatur, was zur Generierung proto-kontinentaler Terrains führt, die Merkmale moderner Plattengrenzen nachahmen. Die Hauptunterschiede zwischen 2D und 3D Experimenten betreffen die Stabilität des ozeanischen Plateaus. In 2D Experimenten ist die verdickte Kruste stabiler, was die Erzeugung von felsischen Schmelzen bei höherem Druck ermöglicht, als in den 3D Fällen, die weniger dazu neigen, felsische Schmelzen bei hohem Druck (> 1 GPa) zu bilden.

Diese Arbeit ist ein erster Versuch geodynamische Prozesse mit der chemischen Entwicklung von Mantel und Kruste zu verbinden. Es zeigt, wie wichtig es ist, die Petrologie in geodynamischer Modellierung zu berücksichtigen und gibt uns wichtige Einblicke in die Auswirkungen von kontinentaler Krustenproduktion während des Archaikums.

CHAPTER 1

# INTRODUCTION

*The story so far: In the beginning the Universe was created. This has made a lot of people very angry and been widely regarded as a bad move.*

Douglas Adams, The Restaurant at the End of the Universe

One of the most remarkable features of Earth is the bimodal composition of its outermost layer, which is made of two distinct geological units: oceanic and continental lithosphere. Oceanic lithosphere is composed of a relatively depleted mantle and a thin mafic crust capped by deep basin sedimentary sequences (~ 6-7 km). By contrast, continental lithosphere is compositionally heterogeneous, with a depleted and thick lithospheric mantle, overlaid with a thick felsic crust (~ 40 km). Its average composition is high in silica and low in magnesium, which ultimately results in low density rocks with respect to its oceanic counterpart (Rudnick and Gao, 2003).

This contrasting chemical composition is reflected both in their longevity and surface elevation relative to the sea. Oceanic crust is young (≤200 Myrs), while continental crust is old and records the geological history of Earth from the beginning of the Archean[1] to the recent past. Continental lithosphere is intrinsically buoyant while the oceanic lithosphere becomes denser with time, which makes it more prone to be subducted at convergent margins. During its long geological history, continental crust has been eroded, producing clastic to fine grained sediments, or underwent to partial melting, altering the original composition. Nevertheless, part of continental crust has survived throughout the geological time, providing a glimpse in the complex evolution of the surface and innermost planet during its initial stage. Most biological activity is focused both in the continents and continental shelves, as their average elevation with

[1] The Hadean-Archean boundary is defined by the lack of preserved rocks (Kamber, 2015; Sleep, 2018)

respect to the sea level guarantee direct contact with oxygen and sunlight (Zahnle et al., 2007; Sleep, 2018). Therefore, the habitability of the planet and the sustainability of the biosphere as it is known is linked to the evolution of the landmasses and continental crust. Consequently, given the importance of continental crust for reconstructing the geological and biological history, there is a growing scientific interest on its evolution and generation.

But how and when did Earth develop its bimodal composition? Most continental crust was produced by the end of the Archean Dhuime et al. (2012); Taylor (1967), when it also reached its actual surface extent (Cawood and Hawkesworth, 2018). The end of Archean is associated with major changes in the geodynamic processes, that are reflected in the composition of newly generated mafic and felsic crust (Ganne and Feng, 2017; Palin and Dyck, 2018; Brown and Johnson, 2018; Johnson et al., 2019; Herzberg et al., 2010). Therefore, it is clear that in order to understand how the Earth has developed the suitable conditions to develop coherent continental masses as well as for its habitability, it is necessary to focus on the generation of the earliest continental crust. The necessary condition to produce such high volume of continental crust is having liquid water at the surface (Campbell and Taylor, 1983), even though it is not a sufficient condition (Höning et al., 2019). As a consequence, understanding the geodynamic processes acting during the early Earth has become a pivotal topic to understand the generation of the earliest continental crust production. However, the dearth of the geological data cannot provide a definitive answer and many questions remain still unsolved.

My current work aims to understand the generation of the building block of the earliest continental crust. But, before moving to the current experimental work, it is necessary to review the continental crust and its average composition which gives important insights in the processes that were behind its generation. Then, it is necessary to ask what are the presently site of production and destruction of continental crust and how much the modern-age continental crust differs from the earliest one.

## 1.1 Continental Crust

### Continental crust composition and crustal recycling

Continental crust occupies 40 % of the Earth's surface, and even though its mass is 0.3-0.57% of the total silicate Earth, it contains most of the incompatible elements (20-70%) (Rudnick and Gao, 2003). Its thickness is variable but on average 40 km. It can be subdivided in at least three layers: upper, middle and lower crust (Rudnick and Gao, 2003; Hawkesworth and Kemp, 2006). The compositional distribution of the continental crust is unimodal, and its average composition

is andesitic[2] (Kamber, 2015; Rudnick and Gao, 2003). It is internally differentiated, with most of the felsic components of the crust is stored in the upper crust, while the lower crust is mainly composed by residual metamorphic rocks (Rudnick and Gao, 2003; Hawkesworth and Kemp, 2006).

Andesitic compositions cannot be a direct product of mantle partial melting, which, instead, produce mafic to ultramafic melts (Kay and Kay, 1993). Therefore, continental crust must have been generated through a multistage process, that must have involved at least two steps: production of mafic melts and their refinement into more felsic ones (Hawkesworth and Kemp, 2006; Rudnick and Gao, 2003). The two possible mechanisms that generate high silica rocks are fractional crystallization and partial melting of pre-existing mafic rocks (i.e. basalts) (Hawkesworth and Kemp, 2006). Both processes requires that melts or protolith is hydrated, since water shift the temperature of the solidus allowing higher production and compositional range of felsic melts (Campbell and Taylor, 1983). These two mechanisms are not mutually exclusive, as they might occurs within the same setting (Annen, 2009).

Both mechanisms do not come for free, and the production of felsic crust implies the generation of 3-4 times of residual mafic rocks (Kemp and Hawkesworth, 2003). However, this complementary residuum is not represented in the geological records, creating a chemical mass balance problem (Lee et al., 2006; Kay and Kay, 1988, 1993). Residuum must have a mafic-ultramafic composition, and as a function of the P-T conditions at which is formed, its composition can result in dense mineralogical composition (Kay and Kay, 1988, 1993; Jagoutz and Kelemen, 2015; Rapp et al., 2003). If the residuum is sufficiently dense, it could founder into underlying mantle and be readily recycled. From the chemical perspective it is clear that the continental crust generation cannot be explored without accounting for the disposal of the complementary residuum. Therefore, the issues that must be addressed is related to finding a geodynamic setting able to encompass both production of felsic crust and disposal of its complementary residuum.

## Present-day continental crust production and destruction, and crustal growth with time

Presently, felsic crust is mainly produced in continental/oceanic arcs (Hawkesworth and Kemp, 2006; Jagoutz, 2014; Arndt, 2013). In oceanic/continental arcs, slab dehydration promotes mantle melting, generating hydrous mafic melts. These melts are collected at the bottom of the growing arc, and they can cool and then re-melt, or starting a slow differentiation processes (Jagoutz,

[2] ~60 wt% of $SiO_2$ and ~5 wt% of MgO.

2014; Kay and Kay, 1993; Annen, 2009). The resulting mafic residuum is denser then underlying mantle and is recycled through Rayleigh-Taylor instabilities (Behn et al., 2007; Jagoutz, 2014; Kay and Kay, 1988). In oceanic/continental arcs the production of felsic crust is occurring because of slab dehydration, and the disposal of the complementary residuum is occurring via gravitational instabilities. Felsic crust might be produced in intraplate settings (i.e., plume-related) as well as these settings are not fully understood. The most accessible ones are related to continental flood basalt provinces (such as Paranà-Etekenda), which are associated with felsic volcanic activity (Coffin and Eldholm, 1994). On other hand oceanic plateaus (such as Ontaga Plateau) are less accessible and there is still no evidence of active felsic melts production. In such scenarios the production of felsic crust is mediated both by internal differentiation of mafic melts and melting of older and hydrated basalts. Presently, such settings are not producing the most juvenile felsic crust, and most of felsic crust is produced in subduction related setting (Jagoutz and Kelemen, 2015).

Subduction is not only assisting the generation of new continental crust, but it is also a site in which continental crust is destroyed. Oceanic crust is capped by sedimentary layers (which is reworked continental crust), and part of them are subducted together with the oceanic lithosphere (Scholl and von Huene, 2007). During continental collisions, especially during the incipient stage, continental crust might be subducted and lost from the surface environment (Replumaz et al., 2010; Ingalls et al., 2016). It has been estimated that subduction related net addition of new felsic crust is close to zero (Scholl and von Huene, 2007). Which leads to the following issues: how did the continental crust increase in volume, and which of the forming processes evolved with time or was different in the past?

Crustal growth curves are computed following several assumptions, the most important being that the total volume of the continental crust never exceeded the present-day value (Dhuime et al., 2018) see Fig. 1.1. Some of them are predicting that most continental crust was produced by the end Archean (Dhuime et al., 2012; Taylor, 1967); while many others speculate that most continental crust was generated during the Phanerozoic (Goodwin, 1996) or that the crust has been growing monotonically during the whole Earth's history (Hurley and Rand, 1969). A recently published continental crust growth curve infers that at least 65% of total felsic crust was generated by the end of the Archean (Dhuime et al., 2018, 2012). It is not clear what kind of processes were operating during the Archean, and how it was possible to produce such amount of continental crust. Therefore, it is necessary to focus the attention on what happened during the Hadean-Archean, starting from the geological record.

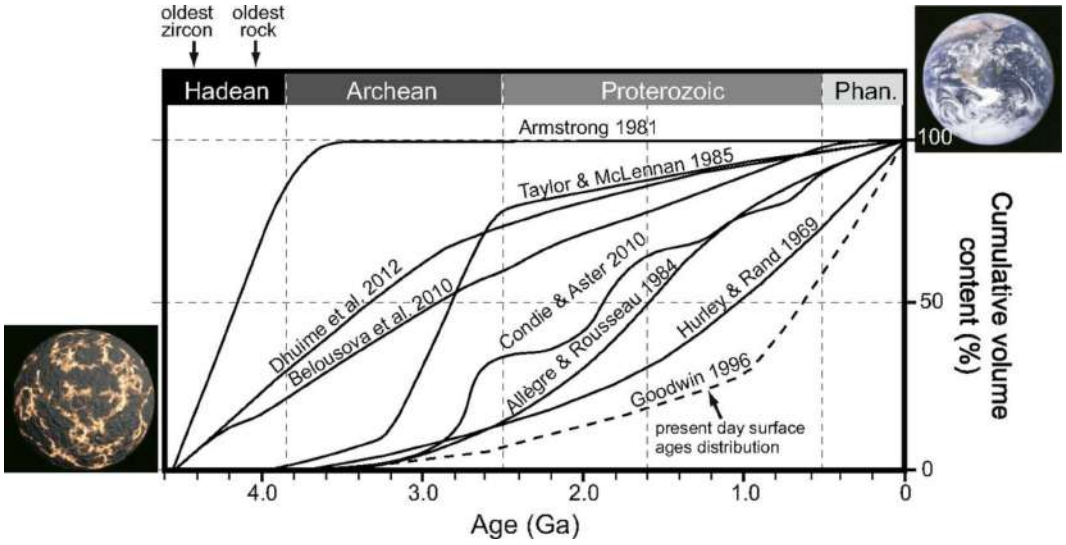


Figure 1.1: This picture are taken from (Cawood et al., 2013), and depicts several crustal growth curves. The *x-axis* is the time, while the *y-axis* is cumulative volume of continental crust.

## 1.2 Archean continental crust

### Tonalite-Trondhiemite-Granodiorite suites

Archean crust constitutes approximately less than 10% of the actual preserved continental crust (Cawood et al., 2013). Archean crust's average composition is like the present-day continental crust (i.e. andesitic), but its composition is bimodal with a minimum on its average composition (Kamber, 2015). Intermediate compositions are not represented in Archean records, while the crust is mainly composed by mafic igneous product and high silica rocks (i.e. granitoids).

Granitoids represents 60-65% of the total felsic components and are divided into two main categories: potassic granitoids and mixture types; sodic granitoids (Moyen, 2011; Moyen and Martin, 2012). The major component of the Archean continental crust are sodic granitoids (~ 50 % of the total felsic components), which are mainly composed of Tonalite-Trondhjemite-Granodiorite suites lithotype (TTGs) (Jahn et al., 1981; Moyen, 2011; Palin et al., 2016). Most of the discussions concerning the origin of the primordial continental crust has been focused on the production of TTGs especially from geodynamical perspectives (Sizova et al., 2015; Moyen, 2011; Martin et al., 2014; Palin et al., 2016). It is widely accepted that TTGs are the product of partial melting of hydrated meta-basalts (Moyen, 2011; Moyen and Stevens, 2006; Palin et al., 2016; Rapp et al., 2003). Natural TTG examples feature a particular trace element signature that requires at least two conditions:

- The mafic protolith had to be enriched in LILE-LREE; this requirement suggest that the

mantle source of basalt could have been either enriched and undepleted (plume-related) (Martin et al., 2014; Guitreau et al., 2012) or contaminated by fluids (as for example the one released by subducting slabs) (Arndt, 2013). Regardless of the mantle source it is widely accepted that the most likely TTGs' mafic source is the typical enriched Archean tholeiite (EAT), which is one of the most abundant basalts in Archean terrains (Condie, 1981; Bédard et al., 2003).

- The mafic residuum had to be composed of variable amounts of garnet, amphibole, rutile and plagioclase (Palin et al., 2016; Moyen, 2011; Moyen and Stevens, 2006) [3]. That requires that the partial melting of the hydrated meta-basalts must have occurred at variable but high depth and high temperature (Moyen, 2011; Moyen and Martin, 2012; Palin et al., 2016).

Most of the scientific debate concerning TTG generation has focused on the geodynamic settings, in which these requirement are met. The models that have been proposed spans from the more uniformitarian ones (such as subduction-related models) (Arndt, 2013; Martin et al., 2014; Moyen and Van Hunen, 2012) to the one that invoke other processes (such as, plume-related settings assisted by gravitational instabilities) (Bédard, 2006; Bédard et al., 2013). However, as a consequence of the dearth of unambiguous geological data, it has been not possible to discriminate the most likely processes during the Hadean-Archean.

Most of the geodynamic processes depend on the mantle potential temparature (Sizova et al., 2014; Fischer and Gerya, 2016b; van Hunen and van den Berg, 2008). Early Earth's mantle was hotter than contemporary one due to the high radiogenic heat production and primordial heat (Herzberg et al., 2010; Korenaga, 2008; Sleep, 2000). Therefore, Earth might not have behaved as nowadays, and its convection mode could have been radically different. In order to solve the issues concerning why Earth has continents, and why most of the continental crust had been produced by the end of Archean, the attention must be unavoidably focused on the geodynamic processes that occurred during Archean.

## Early Earth's geodynamic and TTGs generation

Most of the discussions on TTGs are focused on if they are generated in subduction-related settings or not. Some Archean terrains feature structure that can be reconciled with those that are observed in oceanic/continental arcs. One example is the North Atlantic Craton in which

[3] TTGs can broadly be divided in three categories: (1) high $Al_2O_3$, $Na_2O$, $Sr$, $La/Yb$, and low $Y$ and $Nb/Ta$; (2) low $Al_2O_3$, $Na_2O$, $Sr$,$La/Yb$, and high $Y$ and $Nb/Ta$; (3) Transitional compositions between 1-2. (Moyen, 2011; Palin et al., 2016)

terrains featuring different ages are juxtaposed separated by shear zones (Van Kranendonk, 2010; Nutman et al., 2013). But many other Archean terrains (e.g., East Pilbara Terrains) feature dome-and-keel structures in which TTGs domes are rising towards shallower crustal level, while mafic crust is sinking towards lower ones (Van Kranendonk et al., 2007; Collins et al., 1998; Bouhallier et al., 1995). Such geometries are recording partial convective overturn (Collins et al., 1998; Bodorkos et al., 2006) which are induced by the inverted density gradient due to the relative position of dense mafic and felsic rock units (François et al., 2014; Bodorkos et al., 2006; Chardon et al., 1998). In these terrains, TTGs are autochthonous and their metamorphism, generation and mobilization are associated to thermal events, which are correlated with the emplacement of mafic effusive crust (Chardon et al., 1996; Choukroune et al., 1995; Van Kranendonk et al., 2015). These terrains are believed to be dominated by Rayleigh-Taylor gravitational instabilities, that are ultimately resulting from the density differences between different crustal units and between mantle and crust (Bédard, 2006; Bédard et al., 2013; Zegers and van Keken, 2001; Johnson et al., 2013).

Subduction has a central role in the discussion concerning early Earth's geodynamics as slab pull forces are presently driving plate-tectonics (Conrad and Lithgow-Bertelloni, 2002). Therefore, assessing if subduction was operational or not, automatically implies to answer if plate-tectonics was active throughout the Earth history. The feasibility of subduction seems to be extremely dependent on the mantle potential temperature ($T_P$), as it controls the rheology of plates and the thickness of oceanic crust (Sizova et al., 2014, 2010; Van Kranendonk et al., 2007). Archean $T_P$ was higher than present-day one (~ 1280-1350 °C) and its estimation spans from 1400 to 1600 $^{\circ}C$ (Herzberg et al., 2010; Ganne and Feng, 2017; Aulbach and Arndt, 2019). Mantle $T_P$ has been constantly decreasing as a consequence of the secular cooling and radiogenic heating decay. Higher mantle $T_P$ implies more vigorous convection and more production of mafic melts. The combination of these two effects has the effect of producing thicker oceanic crust that is rheologically weakened by percolating melt (Sizova et al., 2010). These two factors inhibit the operation of subduction, making it discontinuous or preventing it to occur (van Hunen and van den Berg, 2008; Sizova et al., 2010). In such scenario the evolution of the lithosphere is fully mediated by magmatic and gravitational processes (Sizova et al., 2015; Fischer and Gerya, 2016a; Bédard, 2006; Zegers and van Keken, 2001; Johnson et al., 2013). By contrast if the mantle potential temperature were lower, magmatic processes might have been coexisted with discontinous subduction (Fischer and Gerya, 2016b; Sizova et al., 2015).

Plate tectonics and subduction might have become the dominant geodynamic processes at the end of the Archean with a transition period that started at 3.0 Ga and finished at 2.5-7 Ga (Ganne and Feng, 2017; Dhuime et al., 2012; Brown and Johnson, 2018; Johnson et al., 2019).

This transition period is reflected in both the petrological cooling history and in the secular changes of both mafic and continental crust (Ganne and Feng, 2017; Johnson et al., 2019). As a consequence, before the onset of plate tectonics, Earth might have been a stagnant-lid planet, in which the surface tectono-compositional evolution might have been ruled by punctuated and intensive magmatic activity (Bédard, 2018; O'Neill and Debaille, 2014; Condie et al., 2018).

Before the onset of plate tectonics the production of continental crust (TTGs) might have been triggered by intense magmatic activity. The refinement of the mafic crust might have occurred by the thermal maturation caused by the emplacement of mafic intrusions (Van Kranendonk et al., 2015; Choukroune et al., 1995; Smithies et al., 2009). Such processes generate high amounts of residuum that promoted the occurrence of gravitational instabilities, which enhanced the generation of the proto-continental crust (Bédard, 2006; Zegers and van Keken, 2001). Ultimately, the generation of large scale continents is a consequence of the intense magmatic activity and is further promoted by crustal recycling. Presently, these dynamics are not occurring anymore and there is no modern analogue that can help to have a coherent physical framework to understand the earliest continental crust production. As a consequence, to understand how the earliest continent's building block were produced, it is necessary to use indirect means, such as numerical modeling.

## 1.3 Thesis goal

As I briefly outlined in the previous sections, understanding how the continents have been generated is pivotal to understand why the planet is habitable. Most continental crust was produced by the end of the Archean. However, there is still a harsh and open debate on what the geodynamic processes were that were assisting its generation during the infancy of the planet. Early Earth is a daunting topic, with many unsolved questions and with highly controversial answers. Geological data are scarce and perhaps not representative of the whole dynamics of the planet at that time. More importantly, there is no modern analogue that allows us to make any comparisons.

As a consequence, I believe that it is natural to understand the potential early Earth geodynamic using indirect means, like numerical modeling. In my contributions, I use both 2D and 3D numerical experiments to understand the dynamic processes that assisted the generation of the earliest proto-continents. My analysis will be focused mainly on the effect that such processes has in the upper mantle and lithosphere. Aiming at exploring these dynamic without neglecting the petrological aspects, I coupled the numerical simulation with representative phase diagrams. The usage of real density and melt production, gives further insights on

continental crust generation and reproduces the feedback between mafic residuum disposal and continental crust generation. The current approach is novel, and is a first attempt to couple the effect of magmatic processes on the compositional evolution of the crust, using petrological constraints.

## 1.4 Thesis outline

**Chapter 2:** *Generation of Earth's early continents from a relatively cool Archean mantle*[4]: Earth's mantle temperature has a strong effect on the stability of the lithosphere. More importantly, it affects the feasibility of many geodynamic processes that are believed to have occurred during the Archean. However, mantle potential temperature is still unconstrained, with estimations spanning from 1500 °C to 1600 °C. Such differences are important to understand the potential geodynamic mechanisms that were assisting the generation of continental crust, therefore, in this chapter I performed systematic 2D numerical experiments to constrain the lithospheric behavior with respect to the initial mantle potential temperature, lithospheric geotherm, rheology and efficiency of magmatic processes. As function of these parameters, several transient behaviours emerge, but all of them ultimately result in mantle cooling, strong mantle depletion and contamination with recycled compositional mafic crust. All these results suggest that high mantle potential temperature might be unsustainable over geological timescales, therefore, they prompt the idea that the recorded high mantle potential temperature is potentially related with lower mantle upwellings (like thermal or mantle plume). Furthermore, the result demonstrate that TTGs melts might be generated at even lower $T_P$ as previously thought, and that stagnant lid with strong intraplate deformation might be the suitable place to generate high amounts of compositionally proper TTGs.

**Chapter 3:** *Plume-Lid Interaction during Archean and implication for the generation of early continental crust.* Following the previous chapter, I explore the evolution of a lithosphere interacting with a small and transient plume. The first question that I address is related to the temperature at which mafic crust is produced, and whether a plume-related setting is able to replicate the variability of mafic crust observed in Archean rocks. Then, following the conclusion of the previous chapter, I study the effect of variable mantle potential temperature on the dynamics of the system, and their relative effect on continental crust generation. The results suggest that a pure plume-setting cannot reproduce the full gamut of pressure conditions recorded by natural TTGs, although it reproduces a first order pattern. A plume is associated with lithospheric thinning, that decreases the pressure of generation of felsic melts. This suggests

[4]This chapter has been published in Geochemistry, Geophysics, Geosystems, (Piccolo et al., 2019)

that some degree of intraplate compression or a long-lasting mantle plume are necessary to build up a oceanic plate able to persist long enough to produce felsic melts with proper compositions.

**Chapter 4:** *The instability of the earliest lithosphere, and its thermal effects.* Most of the effect herein observed are ruled by gravitational instabilities. The produced mafic intrusions heat the pre-existent crust, which partially melt and evolves producing dense residuum. Crust becomes increasingly unstable until it drips off, generating a catastrophic removal of both intrusions and mafic residuum.

**Chapter 5:** Outlook and future perspectives. In this chapter I briefly describe the main finding, and suggest how the work must be improved to give more reliable answer.

# REFERENCES


Annen, C., 2009. From plutons to magma chambers: Thermal constraints on the accumulation of eruptible silicic magma in the upper crust. Earth and Planetary Science Letters 284, 409–416.

Arndt, N.T., 2013. The formation and evolution of the continental crust. Geochemical Perspectives 2, 405.

Aulbach, S., Arndt, N.T., 2019. Eclogites as palaeodynamic archives: Evidence for warm (not hot) and depleted (but heterogeneous) archaean ambient mantle. Earth and Planetary Science Letters 505, 162–172.

Bédard, J.H., 2006. A catalytic delamination-driven model for coupled genesis of Archaean crust and sub-continental lithospheric mantle. Geochimica et Cosmochimica Acta 70, 1188–1214.

Bédard, J.H., 2018. Stagnant lids and mantle overturns: implications for archaean tectonics, magmagenesis, crustal growth, mantle evolution, and the start of plate tectonics. Geoscience Frontiers 9, 19–49.

Bédard, J.H., Brouillette, P., Madore, L., Berclaz, A., 2003. Archaean cratonization and deformation in the northern superior province, canada: an evaluation of plate tectonic versus vertical tectonic models. Precambrian Research 127, 61–87.

Bédard, J.H., Harris, L.B., Thurston, P.C., 2013. The hunting of the snArc. Precambrian Research 229, 20–48. URL: http://dx.doi.org/10.1016/j.precamres.2012.04.001, doi:10.1016/j.precamres.2012.04.001.

Behn, M.D., Hirth, G., Kelemen, P.B., 2007. Trench-parallel anisotropy produced by foundering of arc lower crust. Science 317, 108–111.

Bodorkos, S., Sandiford, M., Benn, K., Mareschal, J., Condie, K., 2006. Thermal and mechanical controls on the evolution of archean crustal deformation: examples from western australia. GEOPHYSICAL MONOGRAPH-AMERICAN GEOPHYSICAL UNION 164, 131.

Bouhallier, H., Chardon, D., Choukroune, P., 1995. Strain patterns in Archaean dome-and-basin structures: The Dharwar craton (Karnataka, South India). Earth and Planetary Science Letters 135, 57–75. doi:https://doi.org/10.1016/0012-821X(95)00144-2.

Brown, M., Johnson, T., 2018. Secular change in metamorphism and the onset of global plate tectonics. American Mineralogist 103, 181–196.

Campbell, I., Taylor, S., 1983. No water, no granites-no oceans, no continents. Geophysical Research Letters 10, 1061–1064.

Cawood, P.A., Hawkesworth, C., Dhuime, B., 2013. The continental record and the generation of continental crust. Bulletin 125, 14–32.

Cawood, P.A., Hawkesworth, C.J., 2018. Continental crustal volume, thickness and area, and their geodynamic implications. Gondwana Research .

Chardon, D., Choukroune, P., Jayananda, M., 1996. Strain patterns, décollement and incipient sagducted greenstone terrains in the archaean dharwar craton (south india). Journal of Structural Geology 18, 991–1004.

Chardon, D., Choukroune, P., Jayananda, M., 1998. Sinking of the dharwar basin (south india): implications for archaean tectonics. Precambrian Research 91, 15–39.

Choukroune, P., Bouhallier, H., Arndt, N., 1995. Soft lithosphere during periods of archaean crustal growth or crustal reworking. Geological Society, London, Special Publications 95, 67–86.

Coffin, M.F., Eldholm, O., 1994. Large igneous provinces: crustal structure, dimensions, and external consequences. Reviews of Geophysics 32, 1–36.

Collins, W., Kranendonk, V., MJ, Teyssier, C., 1998. Partial convective overturn of archaean crust in the east pilbara craton, western australia: driving mechanisms and tectonic implications. Journal of Structural Geology 20, 1405–1424.

Condie, K.C., 1981. Archean greenstone belts. volume 3. Elsevier.

Condie, K.C., Puetz, S.J., Davaille, A., 2018. Episodic crustal production before 2.7 ga. Precambrian Research 312, 16–22.

Conrad, C.P., Lithgow-Bertelloni, C., 2002. How mantle slabs drive plate tectonics. Science 298, 207–209.

Dhuime, B., Hawkesworth, C.J., Cawood, P.A., Storey, C.D., 2012. A change in the geodynamics of continental growth 3 billion years ago. Science 335, 1334–1336.

Dhuime, B., Hawkesworth, C.J., Delavault, H., Cawood, P.A., 2018. Rates of generation and destruction of the continental crust: implications for continental growth. Philosophical Transactions of the Royal Society A: Mathematical, Physical and Engineering Sciences 376, 20170403.

Fischer, R., Gerya, T., 2016a. Early earth plume-lid tectonics: A high-resolution 3d numerical modelling approach. Journal of Geodynamics 100, 198–214.

Fischer, R., Gerya, T., 2016b. Regimes of subduction and lithospheric dynamics in the precambrian: 3d thermomechanical modelling. Gondwana Research 37, 53–70.

François, C., Philippot, P., Rey, P., Rubatto, D., 2014. Burial and exhumation during archean sagduction in the east pilbara granite-greenstone terrane. Earth and Planetary Science Letters 396, 235–251.

Ganne, J., Feng, X., 2017. Primary magmas and mantle temperatures through time. Geochemistry, Geophysics, Geosystems 18, 872–888. URL: https://doi.org/10.1002/2016GC006787, doi:10.1002/2016GC006787.

Goodwin, A.M., 1996. Principles of Precambrian geology. Elsevier.

Guitreau, M., Blichert-Toft, J., Martin, H., Mojzsis, S.J., Albarède, F., 2012. Hafnium isotope evidence from archean granitic rocks for deep-mantle origin of continental crust. Earth and Planetary Science Letters 337, 211–223.

Hawkesworth, C.J., Kemp, A., 2006. Evolution of the continental crust. Nature 443, 811.

Herzberg, C.T., Condie, K.C., Korenaga, J., 2010. Thermal history of the Earth and its petrological expression. Earth and Planetary Science Letters 292, 79–88. URL: http://dx.doi.org/10.1016/j.epsl.2010.01.022, doi:10.1016/j.epsl.2010.01.022.

Höning, D., Tosi, N., Hansen-Goos, H., Spohn, T., 2019. Bifurcation in the growth of continental crust. Physics of the Earth and Planetary Interiors 287, 37–50.

van Hunen, J., van den Berg, A.P., 2008. Plate tectonics on the early earth: limitations imposed by strength and buoyancy of subducted lithosphere. Lithos 103, 217–235.

Hurley, P.M., Rand, J.R., 1969. Pre-drift continental nuclei. Science 164, 1229–1242.

Ingalls, M., Rowley, D.B., Currie, B., Colman, A.S., 2016. Large-scale subduction of continental crust implied by india–asia mass-balance calculation. Nature Geoscience 9, 848.

Jagoutz, O., 2014. Arc crustal differentiation mechanisms. Earth and Planetary Science Letters 396, 267–277.

Jagoutz, O., Kelemen, P.B., 2015. Role of arc processes in the formation of continental crust. Annual Review of Earth and Planetary Sciences 43, 363–404.

Jahn, B.M., Glikson, A.Y., Peucat, J.J., Hickman, A.H., 1981. Ree geochemistry and isotopic data of archean silicic volcanics and granitoids from the pilbara block, western australia: implications for the early crustal evolution. Geochimica et Cosmochimica Acta 45, 1633–1652.

Johnson, T., Kirkland, C., Gardiner, N., Brown, M., Smithies, R., Santosh, M., 2019. Secular change in ttg compositions: Implications for the evolution of archaean geodynamics. Earth and Planetary Science Letters 505, 65–75.

Johnson, T.E., Brown, M., Kaus, B.J.P., VanTongeren, J.A., 2013. Delamination and recycling of Archaean crust caused by gravitational instabilities. Nature Geoscience 7, 47–52. URL: http://www.nature.com/doifinder/10.1038/ngeo2019, doi:10.1038/ngeo2019.

Kamber, B.S., 2015. The evolving nature of terrestrial crust from the hadean, through the archaean, into the proterozoic. Precambrian Research 258, 48–82.

Kay, R., Kay, S.M., 1988. Crustal recycling and the aleutian arc. Geochimica et Cosmochimica Acta 52, 1351–1359.

Kay, R.W., Kay, S.M., 1993. Delamination and delamination magmatism. Tectonophysics 219, 177–189.

Kemp, A., Hawkesworth, C.J., 2003. Granitic perspectives on the generation and secular evolution of thecontinental crust. The crust, Treaties on Geochemistry , 3–349.

Korenaga, J., 2008. Urey ratio and the structure and evolution of Earth's mantle. Reviews of Geophysics 46. URL: https://doi.org/10.1029/2007RG000241, doi:10.1029/2007RG000241.

Lee, C.T.A., Cheng, X., Horodyskyj, U., 2006. The development and refinement of continental arcs by primary basaltic magmatism, garnet pyroxenite accumulation, basaltic recharge and delamination: insights from the sierra nevada, california. Contributions to Mineralogy and Petrology 151, 222–242.

Martin, H., Moyen, J.F., Guitreau, M., Blichert-Toft, J., Le Pennec, J. L, 2014. Why Archaean TTG cannot be generated by MORB melting in subduction zones. Lithos 198-199, 1–13. URL: http://dx.doi.org/10.1016/j.lithos.2014.02.017, doi:10.1016/j.lithos.2014.02.017.

Moyen, J.F., 2011. The composite Archaean grey gneisses: Petrological significance, and evidence for a non-unique tectonic setting for Archaean crustal growth. Lithos 123, 21–36. doi:https://doi.org/10.1016/j.lithos.2010.09.015.

Moyen, J.F., Martin, H., 2012. Forty years of TTG research. Lithos 148, 312–336.

Moyen, J.F., Stevens, G., 2006. Experimental constraints on TTG petrogenesis: implications for Archean geodynamics. Archean geodynamics and environments , 149–175.

Moyen, J.F., Van Hunen, J., 2012. Short-term episodicity of Archaean plate tectonics. Geology 40, 451–454.

Nutman, A.P., Bennett, V.C., Friend, C.R., Hidaka, H., Yi, K., Lee, S.R., Kamiichi, T., 2013. The itsaq gneiss complex of greenland: Episodic 3900 to 3660 ma juvenile crust formation and recycling in the 3660 to 3600 ma isukasian orogeny. American Journal of Science 313, 877–911.

O'Neill, C., Debaille, V., 2014. The evolution of Hadean–Eoarchaean geodynamics. Earth and Planetary Science Letters 406, 49–58.

Palin, R.M., Dyck, B., 2018. Metamorphic consequences of secular changes in oceanic crust composition and implications for uniformitarianism in the geological record. Geoscience Frontiers 9, 1009–1019.

Palin, R.M., White, R.W., Green, E.C., 2016. Partial melting of metabasic rocks and the generation of tonalitic–trondhjemitic–granodioritic (ttg) crust in the archaean: Constraints from phase equilibrium modelling. Precambrian Research 287, 73–90.

Piccolo, A., Palin, R.M., Kaus, B.J., White, R.W., 2019. Generation of earth's early continents from a relatively cool archean mantle. Geochemistry, Geophysics, Geosystems 0.

Rapp, R.P., Shimizu, N., Norman, M.D., 2003. Growth of early continental crust by partial melting of eclogite. Nature 425, 605–609. URL: http://dx.doi.org/10.1038/nature02031http://10.0.4.14/nature02031.

Replumaz, A., Negredo, A.M., Guillot, S., Van Der Beek, P., Villaseñor, A., 2010. Crustal mass budget and recycling during the india/asia collision. Tectonophysics 492, 99–107.

Rudnick, R.L., Gao, S., 2003. Composition of the continental crust. Treatise on geochemistry 3, 659.

Scholl, D.W., von Huene, R., 2007. Crustal recycling at modern subduction zones applied to the past—issues of growth and preservation of continental basement crust, mantle geochemistry, and supercontinent reconstruction. Geological Society of America Memoirs 200, 9–32.

Sizova, E., Gerya, T., Brown, M., 2014. Contrasting styles of phanerozoic and precambrian continental collision. Gondwana Research 25, 522–545.

Sizova, E., Gerya, T.V., Brown, M., Perchuk, L.L., 2010. Subduction styles in the Precambrian: Insight from numerical experiments. Lithos 116, 209–229. URL: http://dx.doi.org/10.1016/j.lithos.2009.05.028, doi:10.1016/j.lithos.2009.05.028.

Sizova, E., Gerya, T.V., Stüwe, K., Brown, M., 2015. Generation of felsic crust in the Archean: A geodynamic modeling perspective. Precambrian Research 271, 198–224. URL: http://dx.doi.org/10.1016/j.precamres.2015.10.005, doi:10.1016/j.precamres.2015.10.005.

Sleep, N.H., 2000. Evolution of the mode of convection within terrestrial planets. Journal of Geophysical Research: Planets 105, 17563–17578.

Sleep, N.H., 2018. Geological and geochemical constraints on the origin and evolution of life. Astrobiology 18, 1199–1219.

Smithies, R.H., Champion, D.C., Van Kranendonk, M.J., 2009. Formation of Paleoarchean continental crust through infracrustal melting of enriched basalt. Earth and Planetary Science Letters 281, 298–306.

Taylor, S.R., 1967. The origin and growth of continents. Tectonophysics 4, 17–34.

Van Kranendonk, M.J., 2010. Two types of Archean continental crust: Plume and plate tectonics on early Earth. American Journal of Science 310, 1187–1209.

Van Kranendonk, M.J., Hugh Smithies, R., Hickman, A.H., Champion, D., 2007. secular tectonic evolution of archean continental crust: interplay between horizontal and vertical processes in the formation of the pilbara craton, australia. Terra Nova 19, 1–38.

Van Kranendonk, M.J., Smithies, R.H., Griffin, W.L., Huston, D.L., Hickman, A.H., Champion, D.C., Anhaeusser, C.R., Pirajno, F., 2015. Making it thick: a volcanic plateau origin of palaeoarchean continental lithosphere of the pilbara and kaapvaal cratons. Geological Society, London, Special Publications 389, 83–111.

Zahnle, K., Arndt, N., Cockell, C., Halliday, A., Nisbet, E., Selsis, F., Sleep, N.H., 2007. Emergence of a habitable planet. Space Science Reviews 129, 35–78.

Zegers, T.E., van Keken, P.E., 2001. Middle Archean continent formation by crustal delamination. Geology 29, 1083–1086.

CHAPTER 2

# GENERATION OF EARTH'S EARLY CONTINENTS FROM A RELATIVELY COOL ARCHEAN MANTLE


## Abstract

Several lines of evidence suggest that the Archean (4.0–2.5 Ga) mantle was hotter than today's potential temperature ($T_P$) of 1350 °C. However, the magnitude of such difference is poorly constrained, with $T_P$ estimation spanning from 1500 °C to 1600 °C during the Meso-Archean (3.2-2.8 Ga). Such differences have major implications for the interpreted mechanisms of continental crust generation on the early Earth, as their efficacy is highly sensitive to the $T_P$. Here, we integrate petrological modeling with thermo-mechanical simulations to understand the dynamics of crust formation during Archean. Our results predict that partial melting of primitive oceanic crust produces felsic melts with geochemical signatures matching those observed in Archean cratons from a mantle $T_P$ as low as 1450 °C thanks to lithospheric-scale Rayleigh–Taylor-type instabilities. These simulations also infer the occurrence of intraplate deformation events that allow an efficient transport of crustal material into the mantle, hydrating it.


## 2.1 Introduction

The Earth's earliest-formed continental crust is characterized by tonalite, trondhjemite and granodiorite (TTG) (Jahn et al., 1981) that are widely accepted to have been produced via high-temperature partial melting of hydrous meta-basalts (Moyen and Martin, 2012). While the geodynamic processes that formed these cratonic nuclei continue to be debated, there is a general lack of evidence for oceanic-arc/subduction-driven systems akin to those characterising

the modern Earth (Rapp et al., 2003) having dominantly operated prior to the Neo-Archean (c. 2.8–2.5 Ga (Condie et al., 2016; Brown and Johnson, 2018)) or, as many authors suggested, even during the whole Archean (Bédard, 2018; Hamilton, 2007). It should be noted that Archean craton records variable processes, some of which produced features similar to Phanerozoic terrains. The geological data testify the occurrence of plate-boundary-like sequences and linear tectonic features (Van Kranendonk, 2010; Kranendonk et al., 2002). However, due to the paucity of continuum-reliable data, it is not possible to provide a definitive answer regarding the global geodynamic processes that were acting (Bédard, 2018; Van Kranendonk, 2010; Bédard and Harris, 2014; Cutts et al., 2014; Van Kranendonk et al., 2007). Archean continental crust has a dome and keel structure in which TTG batholiths intrude through overlying mafic lavas, which records a vertical reorganization of rocks as consequence of the inverse density profile (Collins et al., 1998; Bédard et al., 2003; Chardon et al., 1996). The morphology and spatial distribution of dome and keel structures in Archean terranes is inconsistent with them having formed via subduction(Collins et al., 1998; Bédard et al., 2003; Chardon et al., 1996; Bouhallier et al., 1995; Van Kranendonk, 2010). The metamorphic history of these terrain witness periods of quiescence alternating with thermal events correlating with eruption of high quantities of mafic lavas, during which the whole lithosphere was likely significantly weakened (Bédard et al., 2003; Chardon et al., 1996; Choukroune et al., 1995). Such events correlate with the remobilization of older continental crust, which undergoes partial melting to produce felsic material, alongside potential removal of lithospheric mantle (Bédard, 2006; Zegers and van Keken, 2001; Choukroune et al., 1995). Together, these observations are consistent with a tectonic setting mainly dominated by vertical tectonics, periodically fuelled by magmas derived from anomalously hot mantle sources, such as plumes (Van Kranendonk, 2010; Fischer and Gerya, 2016a). In such a scenario, continental crust would be produced via intra-crustal melting and differentiation and dense mafic residua would be continuously removed via Rayleigh–Taylor instabilities (RTIs) (Wiemer et al., 2018). Owing to the higher $T_P$, the RTIs would induce decompression melting of the asthenosphere, which would add heat to further assist continued TTG magma generation (Bédard, 2006).

The majority of Archean TTGs feature a distinctive trace element signature (e.g. high La/Yb and low Nb/Ta ratios) that requires their separation from a garnet-, hornblende-, plagioclase-, and rutile-bearing source rock (Moyen and Martin, 2012), such as garnet amphibolite or garnet granulite. These lithologies stabilize in metamorphosed mafic rock types along geothermal gradients of 900–1000 °C/GPa (Palin et al., 2016a; Johnson et al., 2017). Partial melting of mafic crust must therefore have occurred at high-pressure conditions and would produce high amounts of dense residuum, which is not preserved in the Archean record. Thus, a successful

geodynamic model aimed at explaining the continental crust production, must be able to predict how the mafic residuum is recycled (Bédard, 2006; Zegers and van Keken, 2001; Jagoutz and Kelemen, 2015). The geochemical signature featured by some Archean rocks resembles an arc signature, prompting the idea that the only means to transport hydrated basalts into the mantle is a subducting plate (Van Hunen and Moyen, 2012; Arndt, 2013; Wyman, 2013). Subduction models could explain how hydrous basalts are transported to great depths, providing a consistent framework to understand continental crust production. On the other hand, geological field data are more consistent with models characterized purely by vertical tectonics (Hamilton, 2007; Bédard et al., 2003; Chardon et al., 1998), which cannot replicate subduction-like geochemical features (Arndt, 2013; Wyman, 2013; Moyen and Van Hunen, 2012).

While the early Earth is known to have been hotter than today, estimates for the absolute mantle $T_P$ during the Palaeo- to Meso-Archean (4.0–3.2 Ga) vary from 1500 °C (Ganne and Feng, 2017) to over 1600 °C (Herzberg et al., 2010). This range is significant, as the bulk of all of the continental crust is thought to have formed during this period of time (Dhuime et al., 2012), and even small differences in mantle $T_P$ have significant effects on the efficacy of different crust-forming processes (Johnson et al., 2013; Sizova et al., 2010, 2014; van Hunen and van den Berg, 2008; Gerya, 2014). Previous geodynamic modeling with a hot (1550-1600 °C) mantle $T_P$ (Johnson et al., 2013) suggested that the eclogitized roots of overthickened mafic crust could have delaminated into the mantle, although they did not consider TTG generation in the same environment. Other numerical studies addressing crust-forming processes did not explore the effect of variable $T_P$ and have not examined changes in composition and density of the mafic crust during partial melting and melt extraction (Rozel et al., 2017; Fischer and Gerya, 2016a; Sizova et al., 2015). Although such studies have predicted the unstable nature of the lithosphere at high mantle $T_P$, they did not explore the effect that magmatism has on thermal weakening the lithosphere, but instead considered a lithosphere prone to be delaminated and gravitationally unstable (e.g. Fischer and Gerya (2016a) and Sizova et al. (2015) employed a high initial crustal Moho temperature, that implies a weak lithosphere).

Here, we employ a new generation of integrated petrological and thermo-mechanical models to examine the effect of variable mantle $T_P$ on the mineral assemblages produced during heating and thickening of Archean mafic crust, the geochemistry of derivative partial melts, and the removal of crustal melt-depleted residua (see Fig. 2.1). This modeling replicates a magmatic-dominated geodynamic environment, which is thought to have characterized the pre-plate tectonic Earth (Fischer and Gerya, 2016a; Cawood et al., 2013), and likely involved repeated internal restructuring via cyclical RTI events (Fischer and Gerya, 2016a; Johnson et al., 2013; Sizova et al., 2015; Collins et al., 1998).

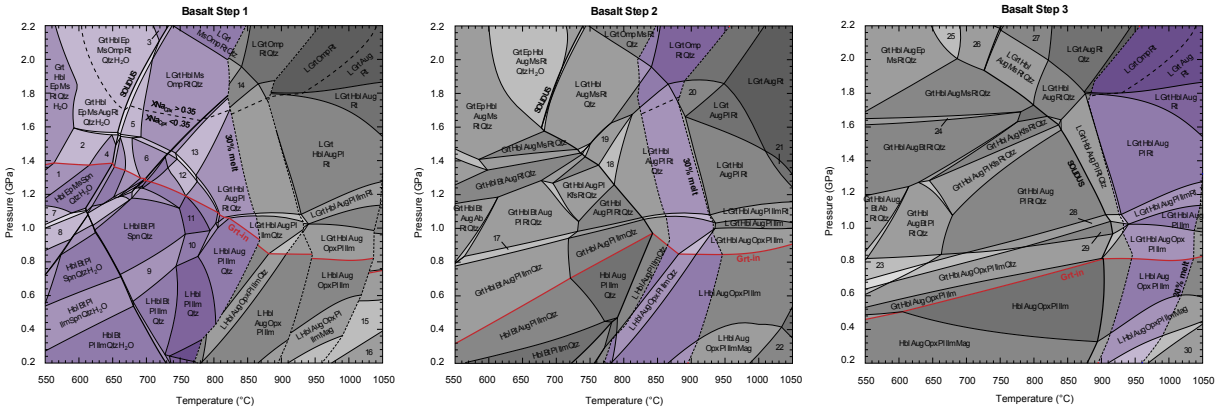


Figure 2.1: The purple area in each phase diagram represents the phase relation that can be seen by a rock during a prograde metamorphic between the solidus and the 15% melt modal amount. The red line represents the garnet-in boundary. The leftmost picture represents the first Basalt Step (BS1), the most fertile and hydrated rock. The middle one represents the second basalt step (BS2), while the rightmost is the last Basalt Step (BS3), which is used also for anhydrous intrusions

## 2.2 Methods

### 2.2.1 Geodynamic simulations

The geodynamic simulations used a Lagrangian thermo-mechanical finite-element code MVEP2 (Johnson et al., 2013; Thielmann and Kaus, 2012), which solves the 2D fundamental continuum mechanics equations using a extended Boussinesq approximation. The advection of material properties within the numerical domain is handled by a marker-in-cell technique. The fundamental equations are:

$$\frac{\partial v_i}{\partial x_i} = 0 \tag{2.1}$$

where $v$ is the velocity vector,

$$\frac{\partial \tau_{ij}}{\partial x_j} - \frac{\partial P}{\partial x_i} = -\rho g_z \tag{2.2}$$

where, $P$ is pressure, $\tau_{ij}$ is the deviatoric stress component along the considered direction, $\rho$ is density, and $g_z$ is the gravity vector component ($g_z = 9.81\ ms^{-2}$).

$$\rho C_p \left( \frac{\partial T}{\partial t} + v_i \frac{\partial T}{\partial x_i} \right) = \frac{\partial}{\partial x_i} \left( K \frac{\partial T}{\partial x_i} \right) + H_a + H_s + H_r + H_l \tag{2.3}$$

$$H_s = \tau_{ij} \left( \dot{\epsilon}_{ij} - \dot{\epsilon}_{ij}^{el} \right) \tag{2.4}$$

$$H_a = T\alpha v_z g \tag{2.5}$$

$C_p$ is the heat capacity, $T$ is the temperature, and $K$ is the heat conductivity, which is a function of temperature, pressure, and composition (Sizova et al., 2015). $H_r$, $H_s$, $H_l$ and $H_a$ are radiogenic heat production, shear heating (eq. (2.4)), latent heat, and adiabatic heating (eq. (2.5)) respectively. Latent heat is considered for the melt reactions and is handled by changing the heat capacity and thermal expansivity as function of the melt production (e.g. (Sizova et al., 2015)):

$$\alpha_{eff} = \alpha + \frac{\rho Q_l}{T}\left(\frac{\partial M}{\partial P}\right) \tag{2.6}$$

$$C_{peff} = C_p + Q_l\left(\frac{\partial M}{\partial T}\right) \tag{2.7}$$

Where $\alpha_{eff}$ and $C_{peff}$ are the effective thermal expansivity and heat capacity of the partially melted rock, respectively. $Q_l$ is the latent heat. While heat conductivity changes accordingly to an empirical law (Clauser and Huenges, 1995):

$$K(X, P, T) = \left(k_1 + \frac{k_2}{T + 0.77}\right)\exp\left(Pk_3\right) \tag{2.8}$$

where $k_1$, $k_2$ and $k_3$ are empirical parameters that describe how the conductivity changes as function of pressure and temperature (see Table A1).

#### 2.2.1.1 Rheological Model

MVEP2 is a visco-elasto-plastic code. As a consequence, the deviatoric stress tensor is computed using three constitutive equations that connect it with the strain rate tensor;

$$\dot{\epsilon}_{ij} = \dot{\epsilon}_{ij}^{vis} + \dot{\epsilon}_{ij}^{el} + \dot{\epsilon}_{ij}^{pl} = \frac{\tau_{ij}}{2\eta_{eff}} + \frac{\diamond\tau_{ij}}{2G} + \dot{\gamma}\frac{\partial Q}{\partial \tau_{ij}} \tag{2.9}$$

where $\dot{\epsilon}_{ij}$ is the total strain rate tensor, the superscript *el,vis,pl* indicate respectively the elastic, viscous and plastic strain rate. $\diamond\tau_{ij}$ is the Jaumann objective stress rate, G is the shear modulus. $\eta_{eff}$ is the effective viscosity. $\dot{\gamma}$ is the plastic multiplier, Q is the plastic flow potential, which is equal to the second invariant of the deviatoric stress tensor, in a dilatation-free media (Kaus, 2010). We briefly describe the method and numerical implementation, which is explained in more detail in Kaus (2010).

The creep viscosity was computed using the following equations (from Hirth and Kohlstedt (2004)):

$$\eta_{diff} = A_{diff}^{-1} d^{p} exp\left(\frac{E_{act} + PV_{act}}{RT}\right) exp\,(AM) \tag{2.10}$$

$$\eta_{disl} = A_{disl}^{-\frac{1}{n}} \dot{\epsilon}_{II}^{\frac{1}{n}-1} exp\left(\frac{E_{act} + PV_{act}}{nRT}\right) exp\left(\frac{AM}{n}\right) \tag{2.11}$$

$A_{diff}$ and $A_{disl}$ are the pre-exponential factors for diffusion and dislocation respectively (see Table A1), $d$ and $p$ are the grain size and the grain size exponent, respectively, and n is the stress exponent. $E_{act}$ and $V_{act}$ are the activation energy and activation volume. $A$ is an empirical parameter that describes the porosity weakening associated with melt production and $M$ is the actual volumetric degree of melt after the melt extraction, $\dot{\epsilon}_{II}$ is the second invariant of the strain rate tensor (all parameters used are listed in Table A1). The effective viscosity ($\eta_{eff}$) is computed with a quasi-harmonic average between diffusion and dislocation creep viscosity. Brittle rheology was modeled using a Drucker–Prager yield criteria:

$$F(\tau_{II}) = \tau_{II} - C\cos\left(\phi_{dry}\right) - P\sin\left(\phi_{dry}\right)\lambda_{melt} \tag{2.12}$$

$$\lambda_{melt} = 1 - \frac{P_f}{P_l} \tag{2.13}$$

$F$ is the yield function, $C$ the cohesion of the material, $\phi$ is the dry friction angle. $\lambda_{melt}$ is the weakening factor induced by the melt phase percolating within the rocks during the melt extraction.

At the beginning of the timestep, $F$ is assumed $\leq 0$, which implies that the plastic deformation mode is not active:

$$\dot{\lambda} \geq 0, F \leq 0, \dot{\lambda}F = 0 \tag{2.14}$$

The numerical code computes trial stresses using a viscoelastic rheology, after which the resultant stresses are used to compute $F(\tau_{II})$:

$$\tau_{ij} = 2\eta_{ve}(\dot{\epsilon}_{ij}) + \chi\tau_{ij}^{old} \tag{2.15}$$

with

$$\chi = \left(1 + \frac{G\Delta t}{\eta_{eff}}\right)^{-1} \tag{2.16}$$

$$\eta_{ve} = \left[\frac{1}{\eta_{eff}} + \frac{1}{\Delta tG}\right]^{-1} \tag{2.17}$$

where $\tau_{ij}^{old}$ is the deviatoric stress of the previous timestep and $\Delta t$ is the current time increment.

If $F(\tau_{ij})$ is > 0, the code computes a plastic strain rate as such the trial stresses become equal to the stresses predicted by the yield criteria:

$$\tau_{ij} = 2\eta_{ve}(\dot{\epsilon}_{ij} - \dot{\epsilon}_{ij}^{pl}) + \chi\tau_{II}^{old} \tag{2.18}$$

Eq. 2.18 can be rearranged:

$$\tau_Y = 2\eta_{vep}\dot{\epsilon}_{II} + \chi\tau_{II}^{old} \tag{2.19}$$

yielding an effective viscosity:

$$\eta_{vep} = \left(\frac{\tau_Y - \chi\tau_{II}^{old}}{2\dot{\epsilon}_{II}}\right) \tag{2.20}$$

where $\dot{\epsilon}_{ij}^{pl}$ is the plastic strain rate, $\tau_Y$ is the yield stress and $\eta_{vep}$ represents an effective viscosity resulting from all the three deformation mechanisms. If the rock is not yielding, the effective viscosity is given by eq. 2.17, otherwiseis given by eq. 2.20.

The effective viscosity can vary between a lower and upper threshold values of $10^{18}$ and $10^{24}$ Pas respectively. If the effective viscosity yielded by eq. (2.16) is outside this range, it is automatically set equal to the lower or upper bound. This strategy, which is common for all geodynamic software packages, is imposed for numerical stability as roundoff errors can affect the performance and accuracy of the direct solvers.

## 2.2.2 Petrological modeling and melt extraction

### 2.2.2.1 Melt extraction

The extraction of melt from each source rock and its emplacement are assumed to be instantaneous over the timescales considered in the geodynamic model, although these processes operate at different rates in the natural environment. While the rate of crystallization for intrusive rocks was modeled according to pluton size, the crystallization of volcanic rocks was considered instantaneous ( cf. Sizova et al. (2015) ). At each timestep, the melt quantity is interpolated from the phase diagrams ($M^E$). The interpolated value, however, does not incorporate the extraction event that occurred between two depletion steps. To avoid any melt overproduction, we correct the value using the previously melt extracted, yielding an effective melt quantity ($M*$):

$$M* = M^E - \sum_{i=1}^{ts-1} M_{ext}(i) \tag{2.21}$$

$M_{ext}$ is the volume of melt that has migrated from the source during each extraction event,

and $ts$ is the total number of extraction events.

After the computation of $M*$,the code tests whether if this value is higher than $M1$, which represents the minimum melt fraction above which melt can escape from the source. This value is the numerical expression of the critical amount of melt in high-pressure metabasic rocks (Rushmer, 1995). Since the critical amount of melt depends on the deformation, geometric configuration of the minerals and reaction rates, we use a constant value that is varied within the simulations. As a consequence, we neglect some real-world complexities. There are two cases: $M^* < M1$ or $M^* \geqslant M1$. In the first case, $M$, the effective amount of melt used in the eq. 2.11, 2.10 and in the density computation (see below), is $M = M^*$ and $M_{ext} = 0$, in the latter $M = M2$ and $M_{ext} = M^* - M2$. $M2$ is the minimum amount of melt that remains in the source, which controls melt-driven viscous weakening and the buoyancy of the media after melt extraction. As with $M1$, $M2$ depends on many factors that cannot be easily parameterized, and for simplicity we set it as a variable input parameter. After each extraction event, all particles are vertically compacted, reproducing the mass and volume change of the source rocks. After the current melt extracted is computed for each node, we sum the contribution along $z$ direction, yielding an effective thickness of extracted material. This effective thickness is used to apply a compaction to the particles, which creates space for newly generated crust.

The volume of extracted melt is converted into extrusive or intrusive crust, whose proportion is defined by the parameter $I_R$ ($= V_{intrusion}/V_{Totmelt}$) which is an non-dimensional quantity that ranges from 0 to 1 (0% to 100 %). The intrusion is emplaced where the maximum ratio between the fluid over-pressure and effective viscosity is achieved:

$$div(Crust) = \frac{P_{liquid} - P_{solid}}{\eta_{eff}} \tag{2.22}$$

$div(Crust)$ is the ratio between fluid over-pressure and effective viscosity, $P_{liquid}$ is the hydrostatic liquid pressure computed accordingly to the melt density, while $P_{solid}$ is the lithospheric pressure. The depth of emplacement depends on the density of the melt and on the rheology of the crust and it changes according to the dynamics of the system.

#### 2.2.2.2 Petrological modeling

Petrological modeling of metamorphism and partial melting in Archean crust was performed in the $Na_2O$–CaO–$K_2O$–FeO–MgO–$Al_2O_3$–$SiO_2$–$H_2O$–$TiO_2$–$O_2$ system using *THERMOCALC* version 3.45i (Powell and Holland, 1988), internally consistent thermodynamic dataset ds62 of Holland and Powell (2011), and the following $a$–$x$ relations: epidote, olivine (Holland and Powell, 2011), silicate melt, augite, hornblende (Green et al., 2016), garnet, orthopyroxene, biotite,

chlorite (White et al., 2014), magnetite–spinel (White et al., 2002), ilmenite–hematite (White et al., 2000), Cbar-1 plagioclase, K-feldspar (Holland and Powell, 2003), and muscovite–paragonite (White et al., 2014). All calculations utilized the initial bulk-rock composition for an average LILE-enriched Archean tholeiite (EAT, ref. Condie (2003)), which has been suggested on major- and trace-element geochemical grounds to be the most suitable source rock for Archaean TTGs (Moyen and Martin, 2012; Martin et al., 2014).

The bulk chemical composition of a rock imparts a primary control on the phases that stabilize as a function of P–T conditions, solidus topology, and ultimately on their rheology, density and radiogenic heat productivity. All together these effects have first-order controls on the dynamics of the target system. To encompass such complex feedback, we parameterized the chemical evolution of the rocks by discretizing it, and assuming that it compositionally evolves only as function of melt loss. We averaged the chemical composition of the residuum along the same melt-fraction isoline to produce new phase diagrams. Such chemical evolution is matched to individual particles that carry all petrophysical information and are advected within the numerical domain.

All particles have their own identification number and rock type. Rock type connects the particles with the petro-thermo-chemical properties of the modeled lithotype, and with phase diagrams. To enforce the chemical composition evolution, the rock type of a particles can change if the total melt extracted exceeds a threshold value, *M3* (see below and Supplementary Material Fig. A12). We do not explicitly deal with reaction lines; the residual composition and associated phase diagram is computed beforehand (see below for further details). Albeit more sophisticated and correct methods exist and have been already applied (Rummel et al., 2018; Riel et al., 2018), they require more computational cost and resources, that make them currently unsuitable for obtaining statistically significant results for the Archean dynamics. Radiogenic heat productivity is assumed to diminish at each depletion step and it discretely varies within an interval whose extremes are the inferred Archean and the modern-day values for the respective lithologies (e.g. Mantle radiogenic heat production interval spans from 0.022 to 0.066 $\mu W m^{-3}$ and each evolutionary stage entails a decrease of 0.022 $\mu W m^{-3}$).

Petrophysical properties of metamorphic rock types, such as whole-rock density, individual melt and residuum density, volumetric melt fraction ($M^E$) and constituent mineral compositions and proportions, were calculated using *THERMOCALC* and used as input data for geodynamic modeling. Given that melt-loss is an open-system process, $M^E$ was adjusted during each extraction event; consequently, this value differs from $M$ (effective volumetric degree of melt). A unique phase diagram was thus calculated for each rock type (e.g. Basalt Step 4 and Mafic Intrusion). All petrophysical properties of unmelted protolith, extracted melt, and depleted

residuum (e.g. density) were calculated for each node as a function of pressure, temperature, composition ($X$) and $M$:

$$\rho_{eff}(X, P, T, M) = M\rho_{melt}(X, P, T) + (1 - M)\rho_{solid}(X, P, T) \tag{2.23}$$

where $\rho_{melt}(X, P, T)$ is the density of the melt, $\rho_{solid}(X, P, T)$ is the density of the solid fraction. Since we do not consider continental crust reworking, we do not use phase diagrams for the felsic crustal rocks, and its density is computed by using a simple parameterization:

$$\rho_{felsic}(P, T) = \rho_0 \left[1 - \alpha(T - T_0)\right] \left[1 + \beta(P - P_0)\right] \tag{2.24}$$

where $\rho_0$ is the reference density (2650 kg $m^{-3}$), $T_0$ and $P_0$ are respectively the reference temperature and pressure.

The initial mafic crust was assumed to be LILE-enriched Archaean tholeiite (EAT) derived from a primitive un-differentiated dry mantle (Condie, 2005). Phase diagrams were calculated for specific bulk-rock compositions depending on the number of times that melt had been extracted, as follows:

1. Mantle rocks: phase equilibria for the asthenospheric mantle source rock were calculated using the fertile peridotite (MFP) composition presented by Johnson et al. (2013) –the $a$–$x$ relations and thermodynamic datasets are outlined therein –, and a total melt extraction threshold of 25% (i.e. M3 = 25%) was applied. Following melt loss, the complementary effective bulk composition for lithospheric mantle (also taken from Johnson et al. (2013)) was termed mantle depletion step 1 (MDS1). During our systematic analysis, the rheological flow law of MFP was changed to simulate stiffening of the mantle as consequence of melt extraction. The stiffening of the mantle is modeled by increasing the pre-exponential factor of diffusion and dislocation creep by one order of magnitude (see Table A2 for further information). MDS1 was allowed to melt, and if the incremental melt extraction exceed 45 % of total melt extracted the rock type and phase diagram was changed for the last time; MDS2 was not allowed to melt again, meaning that no further chemical evolution of the mantle took place in our model.

2. Crustal rocks: phase equilibria for mafic crustal units were computed using *THERMOCALC* 3.45 (Powell and Holland, 1988), using the Holland and Powell (2011) dataset (ds62) and the $a$–$x$ relations of Green et al. (2016) as outlined above (see Figure 2.1). A phase diagram for undepleted EAT (BS1) was utilised as a baseline reference system from which subsequent pseudosections were derived. A melt-extraction threshold (M3) of 15%

was applied for these crustal lithologies (following Rushmer (1995)) , with sequential melt loss producing increasingly depleted source rocks and melts termed basalt step 2 (BS2), basalt step 3 (BS3), and basalt step 4 (BS4) (Palin et al., 2016a), the last of which has an anhydrous residue and thus no longer produces significant quantities of melt. Bulk compositions for melt-depleted lithologies were calculated using the read-bulk-info matrix function, which was adjusted to account for 15% relative melt loss at the P–T conditions of melt extraction calculated on the 15% melt proportion contour from the source lithology. This threshold was chosen owing to it representing the upper limit of favorable conditions for efficient melt segregation and escape from partially melted mafic rocks, as determined experimentally for garnet amphibolites by Rushmer (1995). While such a value is affected by several factors (i.e. strain, temperature, grain size, and shape), it represents a defensible cut-off for the lithologies and general P–T conditions of melting observed in this simulation, which match those used during the experiments of Rushmer (1995).

Phase diagrams for residual lithotypes used these critical melt fractions, within the perspective of minimizing the number of phase diagrams to be discretized while being able to capture the first order effect of the chemical composition evolution. We use a lower melt threshold (*M1*) to incorporate all kinds of magmatic processes that may occur during the extraction. All melts generated are termed "felsic" and either erupt as lavas or stall as intrusions in the middle to lower crust. These felsic melts can be derived from BS1, BS2, BS3 or BT2. The bulk compositions used for modeling are given in Tab. 2.1. The effusive basalt associated with the mantle phase MDS1 has a different composition but it is modeled using the same phase diagrams of the BS1 as most metabasalts have similar melting evolution (Palin et al., 2016b). We differentiate it from the other kind of basalts (Basalt Type 2, BT2) to track the amount of basalt coming from a depleted mantle source. It produces small amount of felsic melt, and then is converted into a dense residue without following the path assigned to the EAT basalts. In any case the amount of BT2 is negligible respect to the EAT protoliths, as it does not contribute significantly to overall felsic magma production.

In each timestep both intrusive and effusive crust produced by the mantle derived melts. Intrusive mafic systems are complex and feature internal differentiation, producing composite suites of rock dominated by dry gabbro and ultramafic cumulates (Cox, 1980). Such complexity cannot be handled by the current melt extraction parameterization. Therefore, we choose to simplify it introducing an effective dense unfertile material that is emplaced as intrusive body within the lower crust or as underplated mafic materials. We assume that these composite intrusions feature a high magnesium number and to model these dense bodies we employ the

Table 2.1: Composition of basalts used in geodynamic models from which TTG magmas were derived All the compositions are listed as mole % oxide. (*) Basalt Step 4 has the same phase diagram of Basalt Step 3, but, after the extraction, the predicted composition is the one listed

| Rock Types | $H_2O$ | $SiO_2$ | $Al_2O_3$ | CaO | MgO | $FeO^{Tot}$ | $K_2O$ | $Na_2O$ | $TiO_2$ | O |
|---|---|---|---|---|---|---|---|---|---|---|
| BS1/BT2 | 6.830 | 49.693 | 8.992 | 9.214 | 10.205 | 9.814 | 0.442 | 2.628 | 1.125 | 1.058 |
| BS2 | 4.443 | 47.975 | 9.118 | 10.330 | 11.775 | 11.238 | 0.227 | 2.373 | 1.304 | 1.226 |
| BS3 | 2.329 | 45.712 | 9.198 | 11.557 | 13.489 | 12.738 | 0.102 | 1.947 | 1.509 | 1.419 |
| BS4(*) | 1.163 | 43.856 | 9.173 | 12.879 | 14.824 | 13.380 | 0.044 | 1.284 | 1.751 | 1.647 |

same phase diagram of the Basalt Step 3, without melting, of which composition resembles Archean picrites. Intrusion as possible source of the felsic crust was not considered to avoid over-estimation of felsic material and preferring to investigate the effects of the evolution of the hydrous mafic crust. In previous work (Sizova et al., 2015) the dry underplated basalt have been considered as available source of felsic crust as well. However, the bulk of continental crust produced in their simulation were originated by dry intrusions, and it has been interpreted as intermediate material (i.e. andesite). However intermediate rocks are rare in the Archean terrains (Anhaeusser, 2014), and we choose to focusing only in the mafic protolith that could really bear TTGs. However, the density of these intrusion is higher than a normal dry basalt, so in order to check if the prediction of such approach is correct we performed a test using the anhydrous basalt employed in Johnson et al. (2013), yielding a similar results.

Our approach has an important limitation related to the dehydration reactions. Our modeling approach cannot handle the dehydratation reaction and the magmatic processes. All the mafic crust phase diagrams have computed assuming that the BS1 is always minimally saturated in water at the solidus. This approach guarantees that the rocks were always saturated during the prograde metamorphism and it implicitly assumes that the rocks are always fully hydrated. In any case, with the exception of perfectly anhydrous, metabasalt all partially or fully hydrated metabasalts will produce the majority of their melt at similar conditions across the amphibolite-to-granulite boundary (Palin et al., 2016a). So, our numerical experiments represent the most favourable conditions to produce continental crust in a vertical setting.

In summary, the compositional evolution starts with a fertile peridotite (MFP) that melts as consequence of the increase of $T_P$ due to mantle radiogenic heat production and decompression. After 25% of melt extracted the mantle fertile peridotite evolves toward the Mantle Depletion Step 1 which could produce new basalts with different composition (Basalt Type 2). If the MDS1 and the initial Lithospheric Mantle experience 20% melt extraction it is converted into Mantle Depletion Step 2 and is considered fully depleted. The product of MFP is dense mafic intrusion (Intrusion) and tholeiitic basalts (Basalt Step 1). The hydrated basalt is buried and heated from below, and if it melts, it generates high silica melt, that is extracted generating

Felsic Crust. Basalt Step 1 evolves towards the Basalt Step 2 (after 15% melt extraction), which eventually melts again producing new felsic crust, and evolving towards the Basaltic step 3 and then to Basaltic step 4. If total melt extracted is higher than the respective threshold (15, 30, 45% respectively) the phase diagram and rock type are changed.

### 2.2.3 Results

**Initial Setup** Our baseline scenario (Reference model) is represented by a two-dimensional numerical model comprising numerous layers (see Supplementary Material (Gerya and Meilick, 2011; Kaus et al., 2010; Gerya et al., 2008; Ranalli, 1995), Figure A1). With increasing depth, this comprised an 80 km thick lithosphere with a 24 km thick crust, of which the uppermost portion is composed of 16 km of hydrated (fertile) basalts (Basalt Step 1, BS1) overlying 8 km of anhydrous (unfertile) basalt/gabbro (Intrusion). The underlying lithospheric mantle is considered partially depleted, consistent with the predicted Archean residual mantle composition (Johnson et al., 2013; Herzberg et al., 2010). The asthenospheric mantle is composed of anhydrous fertile peridotite (MFP). The mineral assemblages (with or without melt) that would be stable at each P–T conditions through this profile were calculated using thermodynamic phase equilibrium modeling (see Methods), alongside bulk-rock physical properties (e.g. density). These phase assemblages dynamically evolved with simulation time and were re-calculated at each node as P, T, and bulk composition constraints changed.

The lithosphere featured an initially segmented geotherm: a crustal segment, with a Moho temperature ($T_{Moho}$) of 800 °C, which produced an apparent geotherm of 1000 °C/GPa, and a lithospheric mantle segment, with a $T_P$ at the base of the lithosphere of 1550 °C. This reference model assumes effective melt weakening ($\lambda_{melt}$ = 0.01), which reduces the brittle strength of the lithosphere during melt-loss events (Sizova et al., 2015). As the hydrated basalts (BS1) are buried, they partially melt, with phase equilibrium modeling used to calculate the compositions of generated magmas. Such melts are high-silica magmas that can be extracted to form felsic crust (see Methods). Once the calculated volume of melt generated reaches a critical threshold, accumulated melt is extracted from the system. As this changes the bulk composition of the system, a new phase diagram was calculated to determine the stable mineral assemblage following melt loss (see Fig. 1). Such stepwise melt-loss and depletion was permitted to occur up to three times, such that melt was extracted from each basalt when its cumulative total reached 15%, after which the rock is considered fully melt-depleted (Basalt Step 1 to Basalt Step 4, BS1-4). Likewise, the asthenospheric mantle was allowed to change phase diagrams two times when the total melt extracted reached the two thresholds values (25% and 45%). These stages are denoted MFP to Mantle depletion step 1-2, MDS1-2. Extracted melt is either converted into

hydrated basalt (BS1) if extruded, consistent with an Archean subaqueous environment (Kump and Barley, 2007), or as anhydrous basalt/gabbro if intruded.

MDS1 produces small amounts of melt that generate a distinct basalt (BT2) to highlight the difference between the basalt that is produced from a more fertile source with respect to those produced by a partially depleted one. BT2 undergoes a single stage before being converted in unfertile residue (see Methods). Initially, 50% of the mafic melt produced was assumed to stall during ascent through the crust and form intrusions. While this is lower than the average noted for the present-day Earth (80–90% intrusion)(Crisp, 1984), this ratio is highly variable between geological environments; for example, plume-related magmatism is typically characterised by 66% of magmas forming intrusions (Crisp, 1984; White et al., 2006), and this ratio can evolve with time depending on the rheological structure of the crust changing during cooling (Rubin, 1993). In our modeling, extrusion is assumed to occur via dike formation, with the diking efficiency controlled by the rheological structure of the crust (Rubin, 1993). In most simulations, we employ a conservative scenario in which the eruptive efficiency remains constant throughout the simulation, which mimics stiffening of the crust due to eruption of high amounts of mafic lavas (Rubin, 1993). This ratio produces a strong crust, which promotes diking and efficient effusive volcanism, consistent with the thick volcano-sedimentary sequences in Paleo-Archaean terrains (e.g. the East Pilbara craton (Hickman and Van Kranendonk, 2012)).

**Reference Model:** The reference model exhibited three main stages: an incubation stage, a drip stage, which features strong intraplate deformation, and a steady-state stage (Fig. 2.2). During the *incubation stage* (0–14 Myrs), the asthenosphere undergoes partial melting as a consequence of the high $T_P$. Melt is extracted from the uppermost partially-melted area, and the mantle depleted residue sinks, generating small convective cells within the partially molten area of the asthenosphere (see Fig. 2.2a) . These convection cells locally induce decompression melting that generates further mafic intrusive and eruptive material. Heat is mainly provided to the crust by the emplacement of stalled magmas and generates warm geotherms, consistent with those recorded in Meso-Archean terranes (Brown, 2007). By contrast the radiogenic heat production has a smaller effect at this stage due to the paucity of relatively radiogenic felsic crust, which has been shown to play a major role for the generation of significant amount of continental crust (Bodorkos et al., 2006). Burial of hydrated lavas following continued eruptions stabilizes amphibolite, garnet amphibolite, and garnet granulite with depth (Figs. 2.1 and 2.3), which form at approximately 16 km, 30 km, and 36 km depth in the crust, respectively. Representative densities of each lithology along these geotherms comprise 3050–3150 kg $m^{-3}$, 3250–3300 kg $m^{-3}$, and 3450–3550 kg $m^{-3}$, respectively. Both garnet amphibolite and garnet

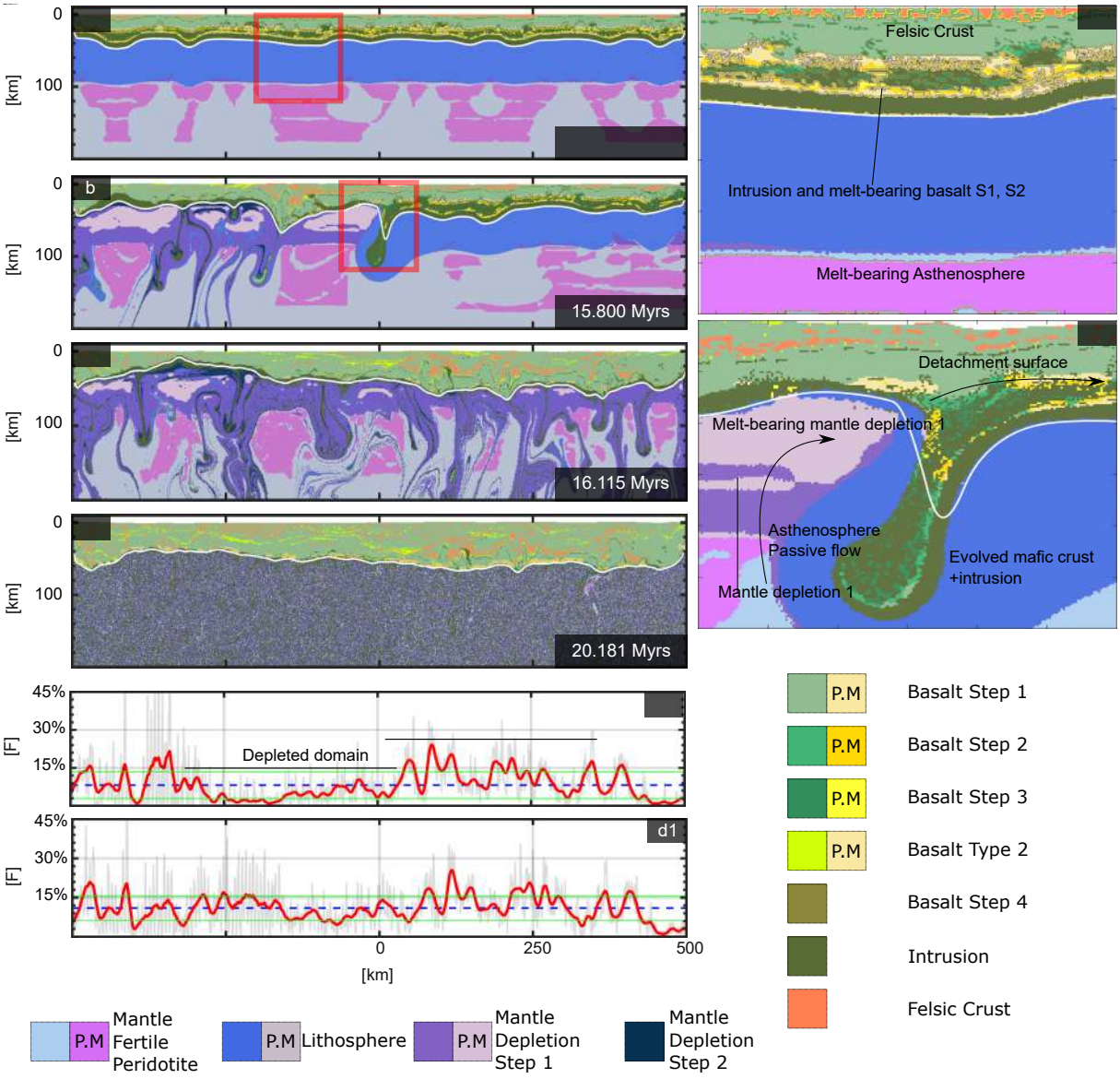


Figure 2.2: **Temporal evolution of the reference simulation ($T_P$ = 1550 °C, $T_{Moho}$ = 800 °C, $\lambda_{melt}$=0.01,$\phi_{dry}$=30° and an intrusive/extrusive ratio = 50%.** Three characteristic evolutionary stages are shown: **a):** incubation, **b-c):** dripping and intraplate deformation sub-stage and **d):** steady state stage. **a1** and **b1** are related respectively to **a** and **b** and are enlargement of the area surrounded by the thick rectangular boxes. **c1** and **d1** are the monodimensional profile, in which $F$, the relative amount of felsic crust, is plotted against the horizontal direction. The red line is the moving average of the raw data - grey lines in the same plot- with a window of 20 km, the blue line represent the global average and the two green lines represent 1 STD of the data.

granulite melt to produce TTG-like magmas with major and trace element signatures matching Archaean examples. The burial is mainly controlled by the distribution of the magmatic activity, that is focused beneath small convection cells in the asthenosphere. The mafic intrusions heat up the crust, driving the production and extraction of felsic magmas from amphibolite/garnet-

amphibolite (hydrated metabasalt), and leaving a complementary mafic residuum. This process allows RTIs to develop (Fig. 2.3b).

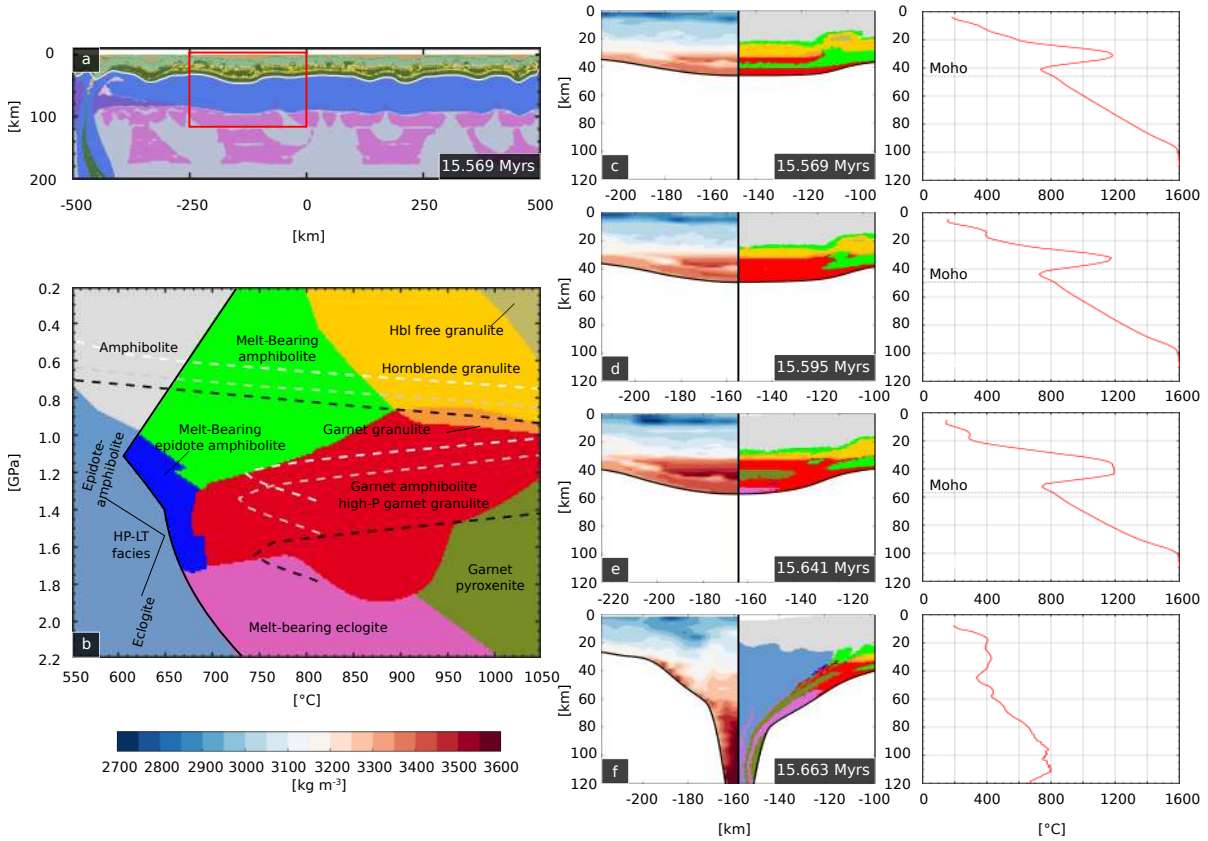


Figure 2.3: **Petrophysical architecture of a drip**. **a):** The reference scenario in the embryonic stage of drip formation; **b):** Petrological diagram showing rock types stable at different pressure–temperature conditions within the drip, taken from Palin et al. (2016a). Colour coding for rock type is used for subsequent plots. The dashed lines represents the geotherm along the axis of the drip (white, grey and black refer respectively to **c**,**d** and **e** sub-panels); **c):** Embryonic pre-drip stage when intrusion of magma begins to heat the lower crust. Rock types at this depth are dominantly amphibolite and garnet amphibolite and have densities of around 3200–3400 $\mathrm{kg}m^{-3}$ ; **d):** Densification of lower crustal units occurs soon after initial drip embryo development. The density of the lower crust is increased with respect to the mantle, due to mafic residue left over from extraction of felsic crust; **e):** Minor eclogite-facies rocks form at the base of the crust as a result of thickening and drip development; **f):** Dripping eventually occurs owing to gravitational instability.

Partial melting of amphibolite/garnet-amphibolite followed by melt extraction generates large volumes of negatively buoyant mafic/ultramafic residue (Fig. 3), which forms drips in thickened crust (Fig. 2.3b). Increased pressure in these regions acts to further stabilize garnet and destabilize feldspar, causing their sagging bases to transform to eclogite upon reaching pressures of ~1.8 GPa, (Fig. 2.3c-d). Further melting of these relatively dry eclogitic residual rocks is limited, consistent with observations that TTGs derived from eclogite-facies precursors represent minor (<10%) components of all Archean terrains (Moyen, 2011). During the incubation stage, the

crust is weakened due to two factors: continuous emplacement of mafic intrusions that heats the lithosphere, and the production of mafic (high-density) residuum which destabilizes the entire lower-middle crust (see Fig. 2.3, Fig. 2.4b, where it is shown the density and viscosity field respectively).

The *dripping stage* (~14-22 Myrs) starts as soon as the first drip nucleates, as shown in our simulations at the left-hand side of the numerical domain (Fig.2.4). The relatively high viscosity of the lithosphere enables the transmission of the gravitational pull force to the whole crust, which yields plastically due to weakening by magma percolation. The formation of drips allows asthenospheric mantle upwelling, which produces mafic melt that intrudes into and further weakens the crust. The crust is rafted apart by the asthenosphere and its horizontal displacement facilitates the nucleation of adjacent RTIs, enhancing the local compression associated with their development (Elkins-Tanton, 2007; Beall et al., 2017) (see Fig. 2.4). Local vertical stretching further increases the density of residual rocks (see Fig.2.3). The rapid evolution of the drips drags in the lower–middle crustal rocks from the adjacent area, whose migration locally induces intraplate extension near the drips (see Fig. 2.4). The viscosity of the crust is sufficiently high to couple the buoyant mafic crust and the dense residual rocks. Brittle deformation controls the amount of material that can be dragged by the drips; since during the incubation-dripping stage the friction angle is decreased by the percolating mafic magmas, large amounts of composite material founders into the mantle (felsic and hydrous components). The dripped composite crust sinks and stalls at the bottom of the model, generating thermal/compositional anomalies.

The prolonged stretching of the crust generates narrow 2D rift-like structures in which asthenosphere penetrates the crust. These processes result in a lateral variation in crustal structure coincident with felsic composition anomalies, which strongly resemble observed Archean dome and keel tectonic architecture (Fig. 2.2) (Hamilton, 2007; Collins et al., 1998; Bouhallier et al., 1995). The drip stage lasts 8 Myr, during which the proportion of felsic components increases to an average volume of 12%, and up to 25% in the stretched region (with a production rate of 696 $km^3 km^{-1} Myrs^{-1}$). Since significant amounts of cold volcanic crust are erupted at the surface, the resulting geotherm has a cold upper crust and hot lower crust, whilst the mantle $T_P$ cools significantly by around 120 °C, producing a new ambient temperature of 1430 °C (see Supplementary Material, Fig. A2). Importantly, the asthenospheric mantle becomes well mixed with residual and intrusive crustal components, which could allow partial hydration of the mantle that could trigger further melting (Bédard, 2006; Bédard et al., 2013); however, this processes is not considered here. Intraplate deformation associated with the dripping stage is analogous to that proposed for the disaggregation of the Superior Craton, with our model providing a mechanism through which Archean lithosphere is weakened and rafted apart by

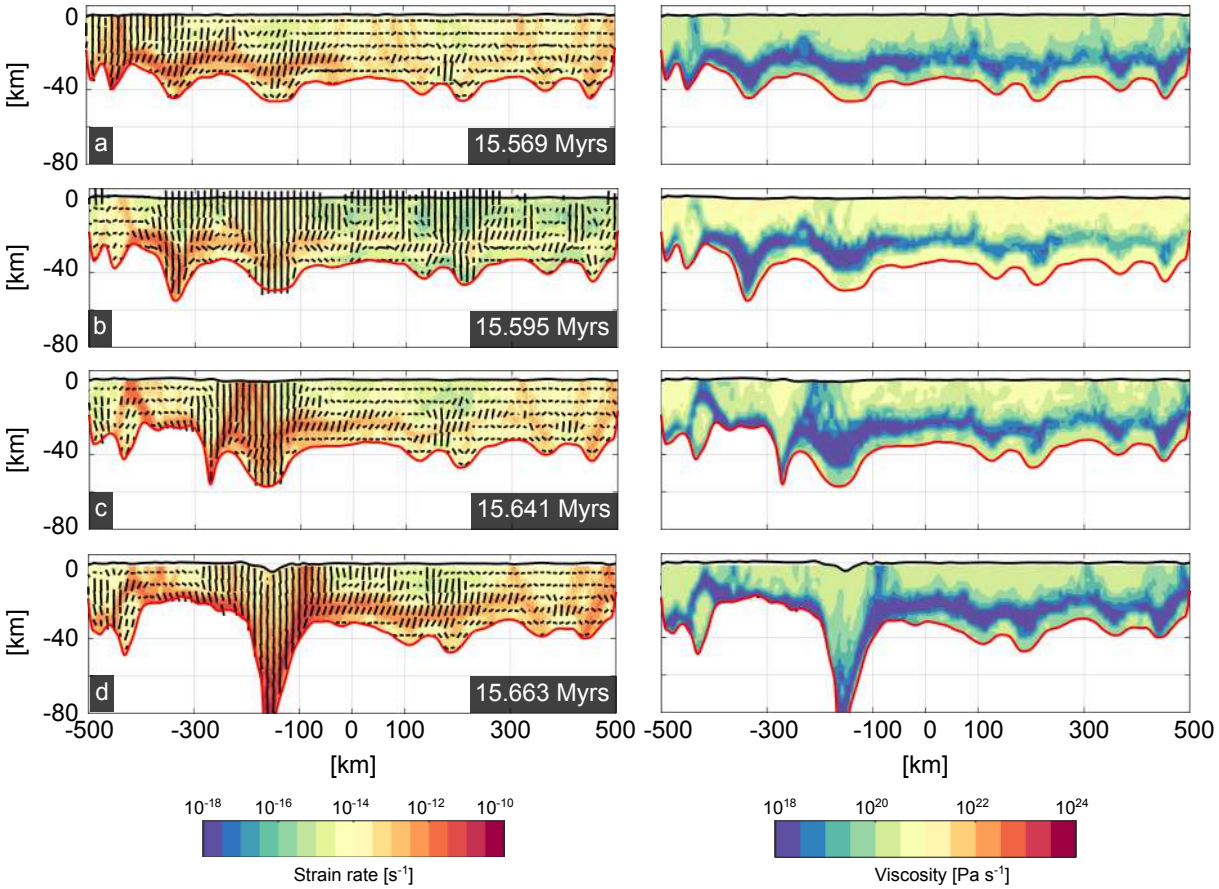


Figure 2.4: **Strain rate and viscosity field** The left and right column represent strain rate and viscosity field, respectively, of the crust. The thick black and red lines are the topography and the Moho respectively. At the top of the strain rate field the minimum axis of the stress tensor ($\sigma_3$) is shown. **a):** After the first drip, the stress is propagated through the entire section of the crust, which concurrently helps to develop the adjacent drip and generates short lived crustal scale shear zones in the right part of the box; **b):** The second drip starts enucleating, dragging the adjacent material. The stress field rotates generating extension in the left area and dragging dense material from the middle crust of the adjacent area; **c):** After the delamination of the second drips, the asthenosphere upwells to fill the empty space left, generating melting that further weakens the crust, triggering a symmetric extension that facilitates the development of the third instabilities (whose density and metamorphic evolution is shown in Figs 2.2,2.3); **d):** The extension propagates, assisted by drag force exerted by the asthenosphere and by the complete development of the third drips.

mantle processes (Bédard and Harris, 2014; Bédard, 2018).

As a consequence of the dripping stage, the mantle cools, reducing its fertility, and its viscosity increases, making convection less efficient. While the crustal geotherm is cold as a consequence of the intense and fast magmatic thickening, resulting in a stiff crust (akin to the heat-pipe model (Moore and Webb, 2013)). These conditions inhibit dripping, which is confined to the lowermost crust. These lower crustal drips are small compared to the initial one and have only minor geodynamic effects. The compositional evolution of the crust reaches a *steady-*

*state stage*, in which the felsic crust proportion steadily increases, concurrent with slow minor dripping of the mafic residuum. During the steady state stage, the mantle magmatic activity is no longer continuous and magma production is associated with small mantle upwellings triggered by the old dripped material that has become buoyant as consequence of its thermal equilibration. The original lithospheric mantle has been completely eroded, which makes the new crust virtually unsubductable (Bédard, 2018).

**Sensitivity to the initial rheological structure and intrusive/effusive ratio:** The initial rheological structure of the lithosphere affects the evolution of the numerical experiments. Increasing $T_{Moho}$ weakens the crust and lithosphere because the respective geothermal gradient increases, and the viscosity decreases as a result. If the viscosity is low, the dense material in the lower-middle crust is fully decoupled from the buoyant supracrustal units. As a consequence the gravitational pull exerted by the RTIs is not effective, and the intraplate deformation observed in the reference experiment is suppressed, resulting in a lateral thickened and compositionally homogeneous crust (see Supplementary Material Fig. A3 and Fig. A4). Low brittle strength values ($\lambda_{melt}$ < 0.1, $\phi_{dry}$< 15 °) for the lithosphere favour intraplate deformation, drip formation, significant mantle cooling, and recycling of large amounts of variably-hydrated mafic and felsic material into the mantle (Fig. 2.5 and Supplementary Material, Fig. A6). A strong lithosphere, on the other hand, has the opposite effect and results in a coherent lithosphere dominated by magmatic processes (see Supplementary Material, Fig. A5).

The variation in the ratio between plutonism and volcanism does not significantly affect the four-stage evolution observed in the reference scenario unless more than 80% of mantle-derived magmas stall during ascent, in which case the total crustal recycling process is completed within 2 Myr. Retaining higher volumes of partial melt in the mantle (2% rather than 0.2%) decreases the timescales of the incubation stage (see Supplementary Material, Fig. A7 and Fig A8 which show the crustal thickness evolution).

**Effect of $T_P$:** The duration of the incubation stage is inversely proportional to $T_P$. For example, at $T_P$ = 1450 °C, the initial incubation stage lasts over four times longer than the reference scenario (65 Myrs compared to 14 Myrs). All dense lithologies (i.e. dry intrusion and mafic dense residuum, BS2-4) act in tandem to generate gravitational instabilities. The production of residuum facilitates the process by increasing the effective thickness of negatively buoyant material and favouring gravitational instabilities under a wide range of thermal conditions, especially at lower $T_P$. Before the onset of the drip instabilities, the ratio between new hot mantle-derived intrusions and mafic residuum is approximately 1:1, with the former being rheologically weaker and denser than mafic lower crust. This ratio grows in favour of the dense

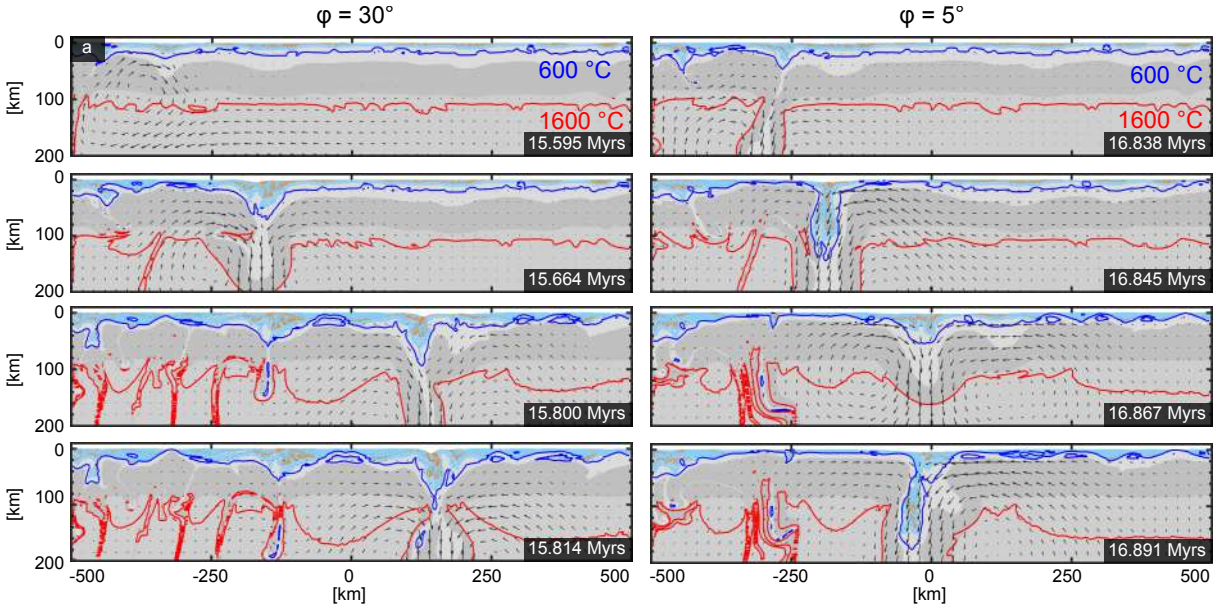


Figure 2.5: **Effect of the strength of the crust on bringing hydrated material in the mantle.** In these simulations, blue colours represent newly hydrated crust, orange newly formed TTG, and grey the lower crust, mantle lithosphere and asthenosphere. The red and blue lines represent respectively the 600 and 1600 $^{\circ}C$ isotherms. Simulations are performed for a friction angle that is **a)** similar to that of dry, intact crust, **b)** represents that of a hydrated and damaged crust. Other parameters are the same as in the reference test (i.e. $T_{Moho}$=800 $^{\circ}$C, $\lambda_{melt}$=0.01). Decreasing the friction angle results in a thinner crust and promotes periods of horizontal tectonics during which significant volumes of hydrated crust are transported into the mantle.

residuum as function of the $T_{Moho}$, the initial thickness and inversely respect with $T_P$. The amount of dense residuum required to trigger the drip instabilities in the reference scenario is 4 km (effective thickness, 12% of total crust thickness) with roughly the same amount of new dense intrusions. If the $T_P$ (1450 $^{\circ}$C) is lower, the amount of residuum is 8 km, meanwhile the amount of intruded material is halved compared to the reference scenario. The average volume of hydrous basalt that has depleted before the onset of the dripping stage thus gives a measure of the compositional evolution of the crust (see Supplementary Material and Fig. A2), as its maximum value represents how much of the hydrated crust has been converted while the crust was stable.

The average amount of metabasalt that must be converted into dense mafic residuum to trigger dripping instabilities monotonically increases with decreasing $T_P$ (from 20% at 1550 $^{\circ}$C to 72% at 1450 $^{\circ}$C). Drips induced by such processes buffer the upper mantle $T_P$, such that localized mantle "cool spots" may have been present during the Archean associated with sites of TTG-like magma generation that immediately precede the drip (Fig. 2.6). Higher initial mantle $T_P$ (>1550 $^{\circ}$C) promotes drip tectonics and total recycling of the crust without requiring large amounts of mafic dense residuum. The amount of intraplate deformation depends on the

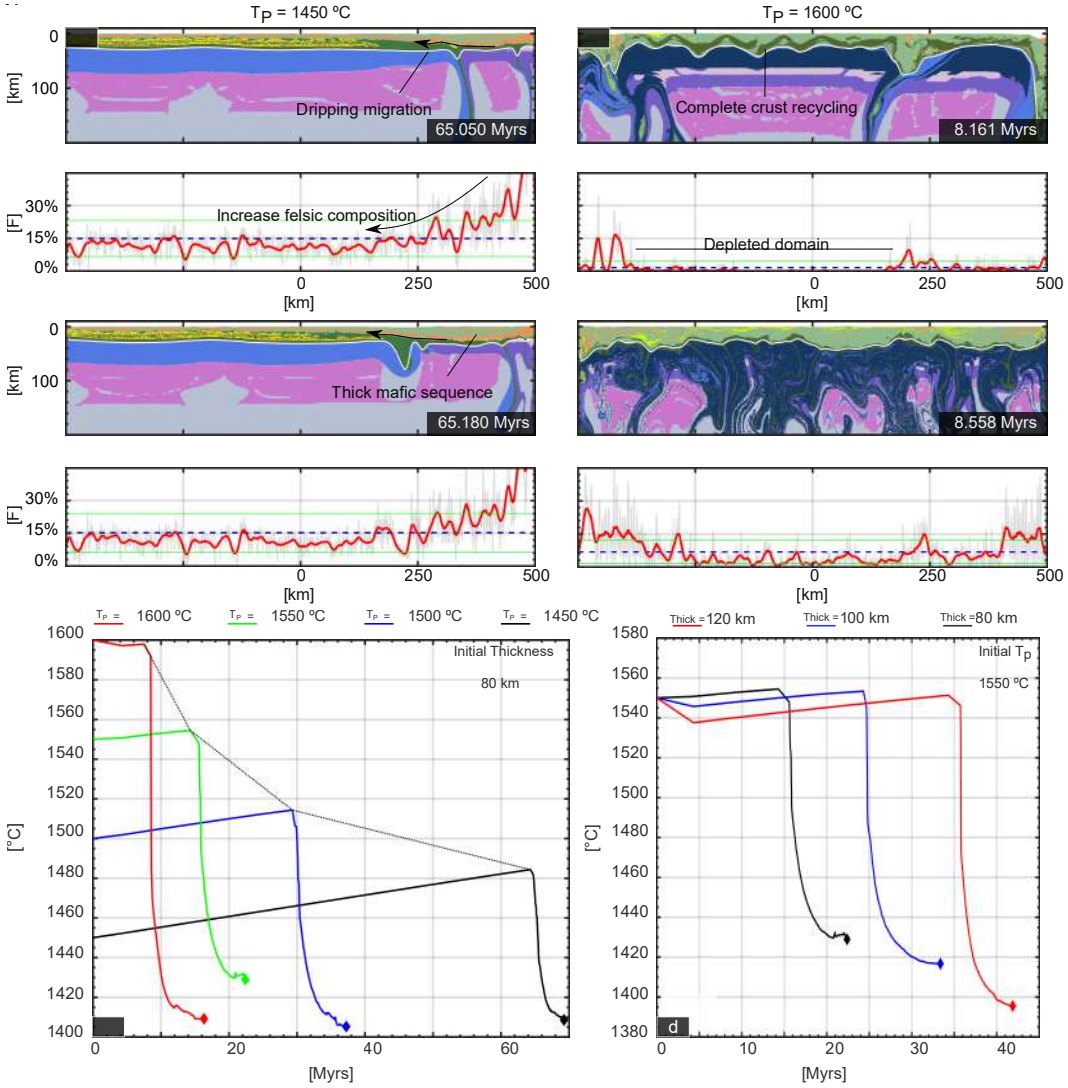


Figure 2.6: **Effect of dripping instabilities on underlying mantle potential temperature ($T_P$).** All the compositional plot use the same legend as in Fig. 2.2. **a):** Evolution of the dripping stage for an initial $T_P$ of 1450 ˚C. A relatively low initial $T_P$ prolongs the incubation stage, promoting the generation of significant volumes of felsic crust and associated dense, mafic residuum. Dripping is triggered by negative buoyancy and rheological weakening induced by the intrusion of hot mafic magmas; **b):** As in (a), but with an initial $T_P$ of 1600 ˚C. Here, enhanced dripping causes the primitive crust to be completely recycled, regardless of the amount of felsic crust generated at any location. Multiple rifts develop simultaneously and enhance destruction of the primary mafic crust and derived felsic crust produced during the incubation stage; **c):** Temporal evolution of average $T_P$ for experiments with different initial $T_P$ values (red, green, blue and black lines represents experiment with an initial $T_P$ of 1600, 1550, 1500 and 1450 ˚C respectively); **d):** Temporal evolution of experiments featuring the same $T_P$ of 1550 ˚C, but with different lithospheric thickness (black is 80 km, blue is 100 km and red is 120 km). In all cases, the asthenospheric mantle $T_P$ decreases rapidly as a result of addition of colder lithospheric material via dripping instabilities.

amount of extracted mafic melts, and effectively ceases for mantle $T_P$ values less than 1500˚C.

**Crustal production rates and melting conditions:** The average amount of continental crust produced in these simulations during the incubation stage is 350± 280 $km^3km^{-1}Myrs^{-1}$ while during the dripping stage the average production rate is 728± 254 $km^3km^{-1}Myrs^{-1}$ (see Supplementary Material, Fig. A9). The continental crust production rate during the dripping stage does not correlate with the initial $T_P$, which only controls its rate of production during the incubation stage. The processes that control dripping-assisted continental crust production is mainly ruled by the feedback between asthenosphere decompression melting and the RTIs . The production of mafic melt is limited by the mantle depletion, thus the independence from the $T_P$ is related to the decreases of mantle fertility and by the extreme mantle cooling rate.

The P–T conditions at which hydrated mafic crust experienced melting varied substantially during each experiment. In general, during the incubation stage TTG melt production is confined to low pressures, with a temperature gradient mainly controlled by the temperature of the intrusions. During the dripping stage, the thickness of the proto-mafic crust rapidly increases, shifting the melting conditions of the mafic protolith to higher pressures and temperatures, crossing the P–T conditions necessary for producing TTG magmas with Archean major and trace element compositions shown by Palin et al. (2016a). Our reference scenario features high-pressure melting conditions at the end of the dripping stage. However, the variability of the melt conditions and their median values depends strongly on the initial conditions (e.g. high $T_{Moho}$ produce a horizontal homogenous thickened crust, which limits high pressure TTGs). The ratio between mafic intrusion/extrusion exerts a strong control and increasing it would result in a thinner crust that is completely outside the optimum field of TTGs generation. However, a slight increase (e.g. 65%) produces a perfect fit to the TTGs' optimum field with respect to the reference scenario (see Supplementary Material, Fig. A10-A11, A13). TTGs have been classified in three categories: low pressure (LP, $0 < P < 1.0$ GPa ), middle pressure (MP, $1.0 < P < 2.0$ GPa) and high pressure (HP, P>2.0 GPa) (Moyen, 2011; Fischer and Gerya, 2016a). The classification is based on a global dataset of TTGs, and on the extensive experimental studies on TTGs generation (Moyen and Stevens, 2006). The three categories represents three different P-T conditions in which TTGs might have been generated, in which the most important parameter is the pressure of generation. Such classification has been used to infer three different geodynamic settings to account TTGs production. The most abundant category is represented by the MP TTGs, 60% of all TTGs analyzed, while the other two represents respectively 20% of the total TTGs analyzed (Moyen, 2011). The relative amount of these three type of TTGs have been widely used in geodynamical modeling to assess the proper condition of the TTGs generation (Rozel et al., 2017; Fischer and Gerya, 2016a). Yet, the validity of this classification has been recently questioned using thermodynamic modeling (Palin et al., 2016a), which demonstrate that the three types

can be generated by prograde metamorphic paths over a much narrower pressure window. Our numerical experiments agree with Palin et al. (2016a), however, if they are compared with the Moyen (2011)'s classification, our model mostly are unable to replicate the distribution of the three categories. However, the model that most closely fits Moyen (2011)'s classification is the one featuring the lowest $I_R$ (i.e. 20% see Figure S13). If $I_R$ evolves during the whole experiments and accordingly the rheology of the crust, it is possible to cover the full gamut of conditions predicted by Palin et al. (2016a) and Moyen (2011).

## 2.3 Discussion

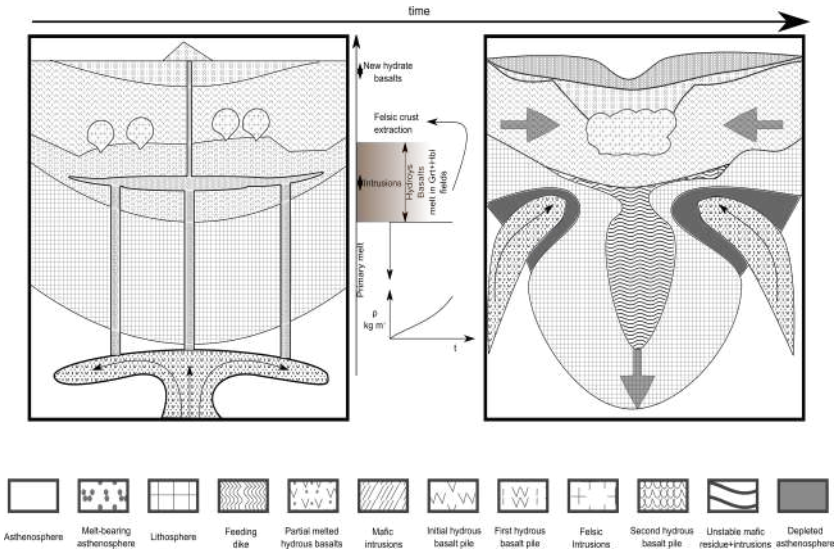


Figure 2.7: **Simplified cartoon model** : Melt coming from the astenosphere percolates through the lithosphere, heating and both plastically and thermally weakening it. Part of the mafic melts are emplaced in the lower crust, while the remnants are erupted. The thickness of the crust increases, while the thermal energy provided by the intrusions starts heating the previously generated hydrous crust which melts producing large amounts of garnet enriched residuum. As soon as a critical amount of residuum is reached, RTIs are triggered, and asthenosphere fills the space left by the delaminated lithosphere. This results in a feedback between mantle melting and new crust production that enhances convection yielding a colder and depleted mantle.

The thermal–tectonic effects of partial melting of an Archean mafic crust have been incorporated into two-dimensional numerical simulations of early-Earth geodynamics, and show that drip tectonics can occur at even lower $T_P$ than previously thought, owing to the concurrent emplacement of intrusions and production of garnet-rich mafic residuum via melting and melt loss. In our experimental framework, the mantle magmatic processes mostly control the rheological and density structure of the crust by heating it and producing felsic melts and complementary mafic dense residuum. Therefore, $T_P$ control is indirectly exerted through

the production of mafic magmas that fuel the process of continental crust production leading ultimately to RTIs. A colder $T_P$ (<1550°C) reduces the magmatic flux coming from the mantle, increasing the timescales of the incubation stage and increasing the importance of the mafic residuum on the dynamics of the experiment (see Fig. 2.7 for a brief summary). Without the production of mafic dense residuum, the RTIs would not spontaneously form at this reduced $T_P$ (Johnson et al., 2013) .

The large-scale geodynamic processes observed in our numerical experiments involving melting and foundering of the residue can be compared in some respects to those proposed for oceanic-arcs (Jagoutz and Kelemen, 2015; Jagoutz, 2014), where the production of felsic crust via crystal fractionation of hydrated mafic parental magmas produces dense mafic cumulates. Both processes have similar consequences: the ultramafic cumulates and the residuum of the fractional crystallization founder back into the mantle leaving a crust enriched in felsic material (Behn et al., 2007). The operation of RTIs at present-day $T_P$ highlights how they are an inevitable consequence of continental crust production and mantle magmatic processes. In the modern Earth, the mantle is partially molten in spatially restricted domains. Oceanic arcs are magmatically active as the subducting slab release fluids into the mantle triggering massive melting and reducing its viscosity (Schmidt and Poli, 1998; Behn et al., 2007), which jointly with the differentiation of mafic melts favours RTIs. However, this process would not trigger the feedback that induce a high felsic crust production and is different from drip-vertical tectonics (Fischer and Gerya, 2016a; Zegers and van Keken, 2001; Bédard, 2006). Our results predict that RTIs could have driven the generation of continental crust for the whole Archean, providing further support to the suggestion that has been made in previous numerical studies (Fischer and Gerya, 2016b; Sizova et al., 2015), and that dripping is associated with a rapid decrease of $T_P$. Lourenço et al. (2018) observed the same behavior in global scale geodynamical models, and emphasized the role radiogenic heating has on the thermal history of rocky planets. Our results show that high mantle potential temperature could not last for long geological timescales, and that the radiogenic heat affects the long term stability of the lithosphere regardless of the initial $T_P$.

## 2.4 Conclusions

Whilst a widely used estimate of Meso-Archaean mantle $T_P$ of ~ 1600°C has been proposed based on calculated primary magma solutions for a small number of non-arc basalts (Herzberg et al., 2010), a more recent analysis of a significantly larger dataset ( 22,000 samples) suggests that the Archean mantle may have had a lower $T_P$ value of ~ 1500°C (Ganne and Feng, 2017).

Our models show that large volumes of TTGs can be produced via crustal melting without requiring exceptionally high $T_P$, and thus provide further support to the lowermost $T_P$ estimates. Several studies argue that the average upper-mantle $T_P$ could have been lower than the current estimation and invoke local temperature anomalies being responsible for rocks recording apparent high $T_P$ (Ganne and Feng, 2017; Arndt, 2013; Kamber, 2015). However, metamorphic activity during the Archean seems to have been frequently punctuated by magmatic events, correlating with enhanced amounts of continental crust production, suggesting even fluctuations as function of the time (Bédard, 2018; Moyen and Van Hunen, 2012; O'Neill et al., 2015). These findings prompt the idea that regardless of the inherent variation of $T_P$ , the thermal history of the Earth has not been monotonic (O'Neill et al., 2015; Sleep, 2000; Davies, 1995; Condie et al., 2018). It has been argued that such peak corresponds to plate tectonic activity to justify the production of continental crust (Moyen and Van Hunen, 2012; O'Neill et al., 2015), while our simulations demonstrate that dripping assisted continental crust production could be a viable alternative, consistent with the geological record. Therefore, variation of $T_P$ either in space and time can potentially trigger this process while creating large amounts of felsic crust. The only requirement is that the whole upper mantle is sufficiently hot to produce mafic melts or that the crust bears sufficient amount of dense mafic residuum and intrusions (e.g. $T_P \geqslant 1450–1500$ $^{\circ}$C). The Archean upper mantle could therefore not have featured a consistent $T_P$ everywhere, supporting suggestions made from various independent lines of evidence for intermittent thermal histories on the early Earth in which fluctuations of $T_P$ were associated explicitly with periodic mantle overturn (Davies, 1995; Condie et al., 2018) and with local variation of $T_P$ associated with long lasting plumes in a stagnant lid planet (Bédard, 2018).

# REFERENCES


Anhaeusser, C.R., 2014. Archaean greenstone belts and associated granitic rocks–a review. Journal of African Earth Sciences 100, 684–732.

Arndt, N.T., 2013. The formation and evolution of the continental crust. Geochemical Perspectives 2, 405.

Beall, A.P., Moresi, L., Stern, T., 2017. Dripping or delamination? a range of mechanisms for removing the lower crust or lithosphere. Geophysical Journal International 210, 671–692.

Bédard, J.H., 2006. A catalytic delamination-driven model for coupled genesis of Archaean crust and sub-continental lithospheric mantle. Geochimica et Cosmochimica Acta 70, 1188–1214.

Bédard, J.H., 2018. Stagnant lids and mantle overturns: implications for archaean tectonics, magmagenesis, crustal growth, mantle evolution, and the start of plate tectonics. Geoscience Frontiers 9, 19–49.

Bédard, J.H., Brouillette, P., Madore, L., Berclaz, A., 2003. Archaean cratonization and deformation in the northern superior province, canada: an evaluation of plate tectonic versus vertical tectonic models. Precambrian Research 127, 61–87.

Bédard, J.H., Harris, L.B., 2014. Neoarchean disaggregation and reassembly of the superior craton. Geology 42, 951–954.

Bédard, J.H., Harris, L.B., Thurston, P.C., 2013. The hunting of the snArc. Precambrian Research 229, 20–48. URL: http://dx.doi.org/10.1016/j.precamres.2012.04.001, doi:10.1016/j.precamres.2012.04.001.

Behn, M.D., Hirth, G., Kelemen, P.B., 2007. Trench-parallel anisotropy produced by foundering of arc lower crust. Science 317, 108–111.

Bodorkos, S., Sandiford, M., Benn, K., Mareschal, J., Condie, K., 2006. Thermal and mechanical controls on the evolution of archean crustal deformation: examples from western australia. GEOPHYSICAL MONOGRAPH-AMERICAN GEOPHYSICAL UNION 164, 131.

Bouhallier, H., Chardon, D., Choukroune, P., 1995. Strain patterns in Archaean dome-and-basin structures: The Dharwar craton (Karnataka, South India). Earth and Planetary Science Letters 135, 57–75. doi:https://doi.org/10.1016/0012-821X(95)00144-2.

Brown, M., 2007. Metamorphic Conditions in Orogenic Belts: A Record of Secular Change. International Geology Review 49, 193–234. URL: https://doi.org/10.2747/0020-6814.49.3.193, doi:10.2747/0020-6814.49.3.193.

Brown, M., Johnson, T., 2018. Secular change in metamorphism and the onset of global plate tectonics. American Mineralogist 103, 181–196.

Cawood, P.A., Hawkesworth, C., Dhuime, B., 2013. The continental record and the generation of continental crust. Bulletin 125, 14–32.

Chardon, D., Choukroune, P., Jayananda, M., 1996. Strain patterns, décollement and incipient sagducted greenstone terrains in the archaean dharwar craton (south india). Journal of Structural Geology 18, 991–1004.

Chardon, D., Choukroune, P., Jayananda, M., 1998. Sinking of the dharwar basin (south india): implications for archaean tectonics. Precambrian Research 91, 15–39.

Choukroune, P., Bouhallier, H., Arndt, N., 1995. Soft lithosphere during periods of archaean crustal growth or crustal reworking. Geological Society, London, Special Publications 95, 67–86.

Clauser, C., Huenges, E., 1995. Thermal conductivity of rocks and minerals. Rock physics & phase relations 3, 105–126.

Collins, W., Kranendonk, V., MJ, Teyssier, C., 1998. Partial convective overturn of archaean crust in the east pilbara craton, western australia: driving mechanisms and tectonic implications. Journal of Structural Geology 20, 1405–1424.

Condie, K.C., 2003. Incompatible element ratios in oceanic basalts and komatiites: tracking deep mantle sources and continental growth rates with time. Geochemistry, Geophysics, Geosystems 4, 1–28.

Condie, K.C., 2005. High field strength element ratios in archean basalts: a window to evolving sources of mantle plumes? Lithos 79, 491–504.

Condie, K.C., Aster, R.C., van Hunen, J., 2016. A great thermal divergence in the mantle beginning 2.5 ga: geochemical constraints from greenstone basalts and komatiites. Geoscience Frontiers 7, 543–553.

Condie, K.C., Puetz, S.J., Davaille, A., 2018. Episodic crustal production before 2.7 ga. Precambrian Research 312, 16–22.

Cox, K.G., 1980. A Model for Flood Basalt Vulcanism. Journal of Petrology 21, 629–650. URL: http://dx.doi.org/10.1093/petrology/21.4.629.

Crisp, J.A., 1984. Rates of magma emplacement and volcanic output. Journal of Volcanology and Geothermal Research 20, 177–211.

Cutts, K.A., Stevens, G., Hoffmann, J.E., Buick, I.S., Frei, D., Münker, C., 2014. Paleo-to mesoarchean polymetamorphism in the barberton granite-greenstone belt, south africa: Constraints from u-pb monazite and lu-hf garnet geochronology on the tectonic processes that shaped the belt. Bulletin 126, 251–270.

Davies, G.F., 1995. Punctuated tectonic evolution of the Earth. Earth and Planetary Science Letters 136, 363–379.

Dhuime, B., Hawkesworth, C.J., Cawood, P.A., Storey, C.D., 2012. A change in the geodynamics of continental growth 3 billion years ago. Science 335, 1334–1336.

Elkins-Tanton, L.T., 2007. Continental magmatism, volatile recycling, and a heterogeneous mantle caused by lithospheric gravitational instabilities. Journal of Geophysical Research: Solid Earth 112.

Fischer, R., Gerya, T., 2016a. Early earth plume-lid tectonics: A high-resolution 3d numerical modelling approach. Journal of Geodynamics 100, 198–214.

Fischer, R., Gerya, T., 2016b. Regimes of subduction and lithospheric dynamics in the precambrian: 3d thermomechanical modelling. Gondwana Research 37, 53–70.

Ganne, J., Feng, X., 2017. Primary magmas and mantle temperatures through time. Geochemistry, Geophysics, Geosystems 18, 872–888. URL: https://doi.org/10.1002/2016GC006787, doi:10.1002/2016GC006787.

Gerya, T., Perchuk, L., Burg, J.P., 2008. Transient hot channels: perpetrating and regurgitating ultrahigh-pressure, high-temperature crust–mantle associations in collision belts. Lithos 103, 236–256.

Gerya, T.V., 2014. Precambrian geodynamics: concepts and models. Gondwana Research 25, 442–463.

Gerya, T.V., Meilick, F.I., 2011. Geodynamic regimes of subduction under an active margin: effects of rheological weakening by fluids and melts. Journal of Metamorphic Geology 29, 7–31. URL: http://doi.wiley.com/10.1111/j.1525-1314.2010.00904.x, doi:10.1111/j.1525-1314.2010.00904.x.

Green, E.C.R., White, R.W., Diener, J.F.A., Powell, R., Holland, T.J.B., Palin, R.M., 2016. Activity–composition relations for the calculation of partial melting equilibria in metabasic rocks. Journal of Metamorphic Geology 34, 845–869.

Hamilton, W.B., 2007. Earth's first two billion years—the era of internally mobile crust. Geological Society of America Memoirs 200, 233–296.

Herzberg, C.T., Condie, K.C., Korenaga, J., 2010. Thermal history of the Earth and its petrological expression. Earth and Planetary Science Letters 292, 79–88. URL: http://dx.doi.org/10.1016/j.epsl.2010.01.022, doi:10.1016/j.epsl.2010.01.022.

Hickman, A.H., Van Kranendonk, M.J., 2012. Early Earth evolution: evidence from the 3.5-1.8 Ga geological history of the Pilbara region of Western Australia. Episodes 35, 283–297.

Hirth, G., Kohlstedt, D., 2004. Rheology of the upper mantle and the mantle wedge: A view from the experimentalists. Inside the subduction Factory 138, 83–105.

Holland, T.J.B., Powell, R., 2003. Activity–composition relations for phases in petrological calculations: an asymmetric multicomponent formulation. Contributions to Mineralogy and Petrology 145, 492–501.

Holland, T.J.B., Powell, R., 2011. An improved and extended internally consistent thermodynamic dataset for phases of petrological interest, involving a new equation of state for solids. Journal of Metamorphic Geology 29, 333–383.

van Hunen, J., van den Berg, A.P., 2008. Plate tectonics on the early earth: limitations imposed by strength and buoyancy of subducted lithosphere. Lithos 103, 217–235.

Jagoutz, O., 2014. Arc crustal differentiation mechanisms. Earth and Planetary Science Letters 396, 267–277.

Jagoutz, O., Kelemen, P.B., 2015. Role of arc processes in the formation of continental crust. Annual Review of Earth and Planetary Sciences 43, 363–404.

Jahn, B.M., Glikson, A.Y., Peucat, J.J., Hickman, A.H., 1981. Ree geochemistry and isotopic data of archean silicic volcanics and granitoids from the pilbara block, western australia: implications for the early crustal evolution. Geochimica et Cosmochimica Acta 45, 1633–1652.

Johnson, T.E., Brown, M., Gardiner, N.J., Kirkland, C.L., Smithies, R.H., 2017. Earth's first stable continents did not form by subduction. Nature 543, 239–242.

Johnson, T.E., Brown, M., Kaus, B.J.P., VanTongeren, J.A., 2013. Delamination and recycling of Archaean crust caused by gravitational instabilities. Nature Geoscience 7, 47–52. URL: http://www.nature.com/doifinder/10.1038/ngeo2019, doi:10.1038/ngeo2019.

Kamber, B.S., 2015. The evolving nature of terrestrial crust from the hadean, through the archaean, into the proterozoic. Precambrian Research 258, 48–82.

Kaus, B.J., 2010. Factors that control the angle of shear bands in geodynamic numerical models of brittle deformation. Tectonophysics 484, 36–47.

Kaus, B.J.P., Mühlhaus, H., May, D.A., 2010. A stabilization algorithm for geodynamic numerical simulations with a free surface. Physics of the Earth and Planetary Interiors 181, 12–20. URL: http://linkinghub.elsevier.com/retrieve/pii/S0031920110000877, doi:10.1016/j.pepi.2010.04.007.

Kranendonk, M.J.V., Hickman, A.H., Smithies, R.H., Nelson, D.R., Pike, G., 2002. Geology and tectonic evolution of the archean north pilbara terrain, pilbara craton, western australia. Economic Geology 97, 695–732.

Kump, L.R., Barley, M.E., 2007. Increased subaerial volcanism and the rise of atmospheric oxygen 2.5 billion years ago. Nature 448, 1033–1036. URL: http://dx.doi.org/10.1038/nature06058http://www.nature.com/nature/journal/v448/n7157/suppinfo/nature06058{_}S1.html.

Lourenço, D.L., Rozel, A.B., Gerya, T., Tackley, P.J., 2018. Efficient cooling of rocky planets by intrusive magmatism. Nature Geoscience 11, 322.

Martin, H., Moyen, J.F., Guitreau, M., Blichert-Toft, J., Le Pennec, J. L, 2014. Why Archaean TTG cannot be generated by MORB melting in subduction zones. Lithos 198-199, 1–13. URL: http://dx.doi.org/10.1016/j.lithos.2014.02.017, doi:10.1016/j.lithos.2014.02.017.

Moore, W.B., Webb, A.A.G., 2013. Heat-pipe earth. Nature 501, 501–505.

Moyen, J.F., 2011. The composite Archaean grey gneisses: Petrological significance, and evidence for a non-unique tectonic setting for Archaean crustal growth. Lithos 123, 21–36. doi:https://doi.org/10.1016/j.lithos.2010.09.015.

Moyen, J.F., Martin, H., 2012. Forty years of TTG research. Lithos 148, 312–336.

Moyen, J.F., Stevens, G., 2006. Experimental constraints on TTG petrogenesis: implications for Archean geodynamics. Archean geodynamics and environments , 149–175.

Moyen, J.F., Van Hunen, J., 2012. Short-term episodicity of Archaean plate tectonics. Geology 40, 451–454.

O'Neill, C., Lenardic, A., Condie, K.C., 2015. Earth's punctuated tectonic evolution: cause and effect. Geological Society, London, Special Publications 389, 17–40.

Palin, R.M., White, R.W., Green, E.C., 2016a. Partial melting of metabasic rocks and the generation of tonalitic–trondhjemitic–granodioritic (ttg) crust in the archaean: Constraints from phase equilibrium modelling. Precambrian Research 287, 73–90.

Palin, R.M., White, R.W., Green, E.C., Diener, J.F., Powell, R., Holland, T.J., 2016b. High-grade metamorphism and partial melting of basic and intermediate rocks. Journal of Metamorphic Geology 34, 871–892.

Powell, R., Holland, T., 1988. An internally consistent dataset with uncertainties and correlations: 3. applications to geobarometry, worked examples and a computer program. Journal of metamorphic Geology 6, 173–204.

Ranalli, G., 1995. Rheology of the earth, 413 pp.

Rapp, R.P., Shimizu, N., Norman, M.D., 2003. Growth of early continental crust by partial melting of eclogite. Nature 425, 605–609. URL: http://dx.doi.org/10.1038/nature02031http://10.0.4.14/nature02031.

Riel, N., Bouilhol, P., van Hunen, J., Cornet, J., Magni, V., Grigorova, V., Velic, M., 2018. Interaction between mantle-derived magma and lower arc crust: quantitative reactive melt flow modelling using styx. Geological Society, London, Special Publications 478, SP478–6.

Rozel, A.B., Golabek, G.J., Jain, C., Tackley, P.J., Gerya, T.V., 2017. Continental crust formation on early Earth controlled by intrusive magmatism. Nature 545, 47–52.

Rubin, A.M., 1993. Dikes vs. diapirs in viscoelastic rock. Earth and Planetary Science Letters 119, 641–659.

Rummel, L., Kaus, B.J., White, R.W., Mertz, D.F., Yang, J., Baumann, T.S., 2018. Coupled petrological-geodynamical modeling of a compositionally heterogeneous mantle plume. Tectonophysics 723, 242–260.

Rushmer, T., 1995. An experimental deformation study of partially molten amphibolite: Application to low-melt fraction segregation. Journal of Geophysical Research: Solid Earth 100, 15681–15695.

Schmidt, M.W., Poli, S., 1998. Experimentally based water budgets for dehydrating slabs and consequences for arc magma generation. Earth and Planetary Science Letters 163, 361–379.

Sizova, E., Gerya, T., Brown, M., 2014. Contrasting styles of phanerozoic and precambrian continental collision. Gondwana Research 25, 522–545.

Sizova, E., Gerya, T.V., Brown, M., Perchuk, L.L., 2010. Subduction styles in the Precambrian: Insight from numerical experiments. Lithos 116, 209–229. URL: http://dx.doi.org/10.1016/j.lithos.2009.05.028, doi:10.1016/j.lithos.2009.05.028.

Sizova, E., Gerya, T.V., Stüwe, K., Brown, M., 2015. Generation of felsic crust in the Archean: A geodynamic modeling perspective. Precambrian Research 271, 198–224. URL: http://dx.doi.org/10.1016/j.precamres.2015.10.005, doi:10.1016/j.precamres.2015.10.005.

Sleep, N.H., 2000. Evolution of the mode of convection within terrestrial planets. Journal of Geophysical Research: Planets 105, 17563–17578.

Thielmann, M., Kaus, B.J., 2012. Shear heating induced lithospheric-scale localization: Does it result in subduction? Earth and Planetary Science Letters 359, 1–13.

Van Hunen, J., Moyen, J.F., 2012. Archean subduction: fact or fiction? Annual Review of Earth and Planetary Sciences 40, 195–219.

Van Kranendonk, M.J., 2010. Two types of Archean continental crust: Plume and plate tectonics on early Earth. American Journal of Science 310, 1187–1209.

Van Kranendonk, M.J., Hugh Smithies, R., Hickman, A.H., Champion, D., 2007. secular tectonic evolution of archean continental crust: interplay between horizontal and vertical processes in the formation of the pilbara craton, australia. Terra Nova 19, 1–38.

White, R., Powell, R., Clarke, G.L., 2002. The interpretation of reaction textures in Fe-rich metapelitic granulites of the Musgrave Block, central Australia: constraints from mineral equilibria calculations in the system $K_2O$-FeO-MgO-$Al_2O_3$-$SiO_2$-$H_2O$-$TiO_2$-$Fe_2O_3$. Journal of metamorphic Geology 20, 41–55.

White, R.W., Powell, R., Holland, T.J.B., Johnson, T.E., Green, E.C.R., 2014. New mineral activity–composition relations for thermodynamic calculations in metapelitic systems. Journal of Metamorphic Geology 32, 261–286.

White, R.W., Powell, R., Holland, T.J.B., Worley, B.A., 2000. The effect of $TiO_2$ and $Fe_2O_3$ on metapelitic assemblages at greenschist and amphibolite facies conditions: mineral equilibria calculations in the system $K_2O$-FeO-MgO-$Al_2O_3$-$SiO_2$-$H_2O$-$TiO_2$-$Fe_2O_3$. Journal of Metamorphic Geology 18, 497–512.

White, S.M., Crisp, J.A., Spera, F.J., 2006. Long-term volumetric eruption rates and magma budgets. Geochemistry, Geophysics, Geosystems 7.

Wiemer, D., Schrank, C.E., Murphy, D.T., Wenham, L., Allen, C.M., 2018. Earth's oldest stable crust in the pilbara craton formed by cyclic gravitational overturns. Nature Geoscience 11, 357.

Wyman, D., 2013. A critical assessment of neoarchean "plume only" geodynamics: evidence from the superior province. Precambrian Research 229, 3–19.

Zegers, T.E., van Keken, P.E., 2001. Middle Archean continent formation by crustal delamination. Geology 29, 1083–1086.

CHAPTER 3

# PLUME–LID INTERACTIONS DURING THE ARCHEAN AND IMPLICATIONS FOR THE GENERATION OF EARLY CONTINENTAL CRUST

## 3.1 Introduction

Continental crust has a lower density compared to its oceanic counterpart, which has enabled it to avoid recycling back into the mantle over geological timescales. Over 60% of continental material present on Earth today was produced during the Archean (Hawkesworth et al., 2010; Dhuime et al., 2012), although its production is thought to have varied over time. Many episodes of continental crust growth are associated with major outpourings of mantle-derived magmas, that suggests a planetary-scale thermal reorganization (Condie et al., 2018; O'Neill et al., 2015). Earth's mantle potential temperature ($T_P$) is known to have been hotter during the Archean compared to the present-day value of ~ 1350 °C although its absolute value is debated with estimates spanning from 1400 °C to 1600 °C (Ganne and Feng, 2017; Herzberg et al., 2010; Aulbach and Arndt, 2019). The end of the Archean is characterized by a transitional regime, in which mantle start to cool faster than the Eo-Meso Archean and in which the chemical composition of the newly produced mafic and continental crust becomes more similar to the Phanerozoic ones (Ganne and Feng, 2017; Condie et al., 2016; Johnson et al., 2019; Palin and Dyck, 2018). These major changes may reflect the evolution of planet's convection mode, and is associated with a progressively decaying of crustal growth rate (Hawkesworth et al., 2010; Dhuime et al., 2012) as well as constant decrease in ambient $T_P$. Several independent lines of research suggest that even though the Earth had more bulk heat, the astenosphere could have had a lower temperature, thus associating the high $T_P$ recorded in mantle plumes or hotter upwellings coming from the

lower mantle (Kamber, 2010, 2015; Bédard, 2018). As a consequence, it is believed that hot plumes played an important role in shaping Earth's evolution during its infancy, potentially promoting short-lived tectonic events throughout the Archean and sporadic continental crust production (Moyen and Van Hunen, 2012; Van Hunen and Moyen, 2012; Fischer and Gerya, 2016b).

The earliest preserved continental crust is primarily composed of tonalite-trondhjemite-granodiorite suites (*TTGs*), and it is widely accepted that they originated from partial melting of hydrous meta-basalts (Palin et al., 2016; Moyen, 2011; Moyen and Stevens, 2006). *TTGs* feature a distinct trace element compositions indicating that mafic source must have melted at pressure and temperature conditions equivalent to the base of oceanic plateaus or shallowly subducted slabs (Kamber, 2015; Palin et al., 2016; Moyen, 2011) and it must have been enriched in LILE and LREE (Jahn et al., 1981; Moyen and Stevens, 2006; Martin et al., 2014; Condie, 1981; Johnson et al., 2017). As such, enriched Archean tholeiite (*EAT*) has been considered to be the most likely source rock for the TTG production (Bédard, 2006; Martin et al., 2014; Moyen and Stevens, 2006; Condie, 1981). LILE-enriched tholeiites occur today in oceanic plateaus (Moyen and Stevens, 2006; Martin et al., 2014), implying a genetic relationship between continental crust production and plumes. Mantle plumes were more abundant during the Archean, with potentially 20% of the planet's surface occupied by oceanic plateau —approximately six-times the present-day value —(Kamber, 2015, 2010; Bédard, 2018), and LILE-enriched basalts were more common at the time than nowadays, therefore there were enough material to refine into felsic crust.

Most Archean terranes have experienced several thermal events since their initial formation, correlated with high mantle's magmatic input, general remobilization of the crust, and generation of new felsic crust (Choukroune et al., 1995; Van Kranendonk, 2010). In some cases, these terranes records tectono-magmatic events consistent with the operation of plate tectonics (Van Kranendonk, 2010; Sizova et al., 2015). Archean *TTGs* commonly form granite greenstone belts characterized by pluton of TTGs surrounded by greenstones exhibiting a foliation that parallels the rims of the plutons (Chardon et al., 1996, 1998; Bouhallier et al., 1995), indicative of partial convective overturn (Collins et al., 1998; Van Kranendonk, 2010). It has been widely recognized that the Archean structures can not be easily reconciled with formation in subduction zone environments dominated by horizontal tectonics (Hamilton, 2007; Bédard et al., 2003; Bédard, 2018; Van Kranendonk, 2010). The strong correlation between juvenile continental crust production, mafic magmatic activity and contemporaneous generation of the cratonic lithospheric mantle, and associated high-temperature metamorphism have been considered a clear indicator of the influence of mantle plumes (Smithies et al., 2009; Bédard et al., 2003; Van Kranendonk, 2010; Kamber, 2015). Many conceptual models developed to reconcile

these observations predict that Rayleigh-Taylor Instabilities (*RTIs*) or in general gravitational instabilities, generated by dense rocks at the base of thickened oceanic plateau, drove most of the tectono-magmatic evolution (Bédard, 2006; Bédard et al., 2013; Zegers and van Keken, 2001; Rapp et al., 2003; Johnson et al., 2013; Fischer and Gerya, 2016a; Sizova et al., 2015). The gravitational instabilities are a consequence of the production of felsic magmas, as its extraction leaves behind rocks featuring dense mineralogies (i.e. garnet, rutile) and of their eclogitization due to the increased thickness of the oceanic plateau. *RTIs* efficiently remove dense residuum and old lithosphere, enhance mantle melting and promote a progressive change in mantle composition and production of new crust (Bédard, 2006; Johnson et al., 2013; Van Thienen et al., 2004; Fischer and Gerya, 2016a; Sizova et al., 2015), explaining rapid continental growth and the generation of extremely residual mantle.

These geological-geochemical data clearly demonstrate the importance plume-lid interactions in shaping the chemical evolution of lithosphere. However, the evolving thermal conditions that favored felsic crust production in plume settings remain poorly understood. Furthermore, there are very few modern analogues to test these hypothesis in a fully integrated way (e.g. Iceland Reimink et al. (2014)), meaning that indirect methods, such as geodynamic simulations, must be used to understand the controlling parameters of plume-lid interaction with respect to continental crust production. Many numerical experiments have already been performed to describe the Archean geodynamic processes. These numerical studies provide useful insights to understand the Archean tectonic evolution, and they replicate many processes that are predicted to have occurred during the generation of the primordial continental crust. However, they are limited by simplified melting model, which are unable to fully capture the petrological evolution of the mafic crust (Sizova et al., 2015; Fischer and Gerya, 2016a; Johnson et al., 2013; Rozel et al., 2017), by the 2D numerical box employed (Sizova et al., 2015; Rozel et al., 2017; Johnson et al., 2013; François et al., 2014; Piccolo et al., 2019). Here, we explore the effect of a short lived hot plume, aiming to understand its effect on felsic crust production and on the overall dynamics. Furthermore, we investigate the condition at which the mafic melts are produced to verify if plume related geodynamic settings can give insights on the mantle thermal state. We carried out systematic numerical experiments in 2D and 3D, coupled with the state-of-the-art of petrological phase diagrams, and we simulate for the first time a self-consistent felsic crust generation in 3D.

## 3.2 Methods

### 3.2.1 Numerical Modeling

The geodynamic simulations are performed using *LaMEM* a marker in cell, finite difference 3D petro-thermo-mechanical code (Reuber et al., 2018), which solves the fundamental continuum mechanics conservation equations for mass, momentum and energy. Advection of the material properties is carried out by markers, that transport the historical information (e.g temperature, total strain) and rock type. We slightly modified the continuity equation to incorporate the effect of the melt extraction:

$$\frac{\partial v_i}{\partial x_i} - \dot{S} + \bar{S} = 0 \tag{3.1}$$

$v_i$ is the velocity vector component along the $x_i$ direction (i.e *x,y,z*) and $\dot{S}$ and $\bar{S}$ are respectively the negative and positive source term induced by extraction or injection of melt (see Tab. B1 and below for further explanations). While the conservation of momentum equations are not affected by the compaction and retains its canonical form:

$$\frac{\partial \tau_{ij}}{\partial x_j} - \frac{\partial P}{\partial x_i} + \rho g_i = 0 \tag{3.2}$$

$\tau_{ij}$ is the deviatoric stress tensor, $P$ is the pressure, $\rho$ is the density and $g_i$ is the gravity vector component along the $i$ direction.

*LaMEM* employs a viscous-elasto-plastic rheological constitutive equations that connects the deviatoric stress tensor components ($\tau_{ij}$) to the total strain rate tensor components ($\dot{\epsilon}_{ij}$) as follows:

$$\dot{\epsilon}_{ij} = \dot{\epsilon}_{ij}^{vis} + \dot{\epsilon}_{ij}^{el} + \dot{\epsilon}_{ij}^{pl} = \frac{\tau_{ij}}{2\eta_{eff}} + \frac{\diamond \tau_{ij}}{2G} + \dot{\gamma}\frac{\partial Q}{\partial \tau_{ij}} \tag{3.3}$$

$$\diamond\ \tau_{ij} = \frac{\partial \tau_{ij}}{\partial t} + \tau_{ik}\omega_{kj} - \omega_{ki}\tau_{kj} \tag{3.4}$$

$$\omega_{ij} = \frac{1}{2}\left(\frac{\partial v_i}{\partial x_j} - \frac{\partial v_j}{\partial x_i}\right) \tag{3.5}$$

Where $\dot{\epsilon}_{ij}$ is the total strain rate tensor, the superscript *el,vis,pl* indicate the elastic (*el*), viscous (*vis*) and plastic (*pl*) strain rate. $\diamond\tau_{ij}$ is the Jaumann objective stress rate, $G$ is the shear modulus. $\omega$ is the spin tensor, $\dot{\gamma}$ is the plastic multiplier, $Q$ is the plastic flow potential, which is equal to the second invariant of the deviatoric stress tensor ($\tau_{II}$), according to a dilatation-free

non associative Prandtl-Reuss flow rule. $\eta_{eff}$ is the viscosity which is computed using the following equation:

$$\eta_{eff} = \frac{1}{2} B_n^{-\frac{1}{n}} \dot{\epsilon}_{II}^{\frac{1}{n}-1} exp\left(\frac{E_a + PV_a}{nRT}\right) \tag{3.6}$$

$B_n$ is the pre-exponential factor, $n$ is the stress exponent, $\dot{\epsilon}_{II}$ is the second invariant of the strain rate tensor, $R$ is the gas constant, $E_a$ and $V_a$ are respectively the activation energy and volume.

The plastic rheology is enforced by the application of the Drucker-Prager failure criterion (Drucker and Prager, 1952):

$$F = \tau_{II} - \sin(\phi)P - Ccos(\phi) \leq 0 \tag{3.7}$$

$F$ is the yield function, $\phi$ is the friction angle and $C$ is the rock's cohesion. During plastic deformation $C$ and $\phi$ can linearly decrease from the initial values ($C_0$, $\phi_0$) to a final values ($C_1$, $\phi_1$) simulating the progressive damage of a rock. The plastic weakening starts when materials accumulate at least 0.1 of total plastic deformation and it stops when the material reaches a plastic strain of 1.0.

Conservation of energy is computed according to:

$$\rho C_p \frac{DT}{Dt} = \frac{\partial}{\partial x_i}\left(k\frac{\partial T}{\partial x_i}\right) + H_a + H_s + H_r \tag{3.8}$$

$$H_a = T\alpha\left(\frac{\partial P}{\partial x_i} v_i\right) \tag{3.9}$$

$$H_s = \chi\left(\dot{\epsilon}_{ij} - \dot{\epsilon}_{ij}^{el}\right)\tau_{ij} \tag{3.10}$$

where $C_p$ is the heat capacity, $DT/dt$ is the objective temperature time derivative, $k$ is the heat conductivity, $H_r$ is the radiogenic heat productivity ($H_r = \rho A$, where $A$ is the amount of heat produced per unit of mass). $H_a$ is the adiabatic heating and is computed according the eq. 3.9 (in which $\alpha$ is the thermal expansivity) while $H_s$ is the dissipative heating, $\chi$ is the shear heating efficiency, and in all the experiments $\chi = 1$.

The material properties used to resolve the equation are computed on the fly, using the relative amount of each rock type in each control volume:

$$X(V) = \sum_{i=1}^{nPhases} Ph_{Rat} X(i) \tag{3.11}$$

Where *X(V)* is a generic property (e.g. density) evaluated, $Ph_{Rat}$ is the phase proportion of the rock type *i* in a control volume, and *X(i)* is the property related to a particular rock type.

### 3.2.2 Melt extraction and petrological modelling

#### 3.2.2.1 Melt Extraction

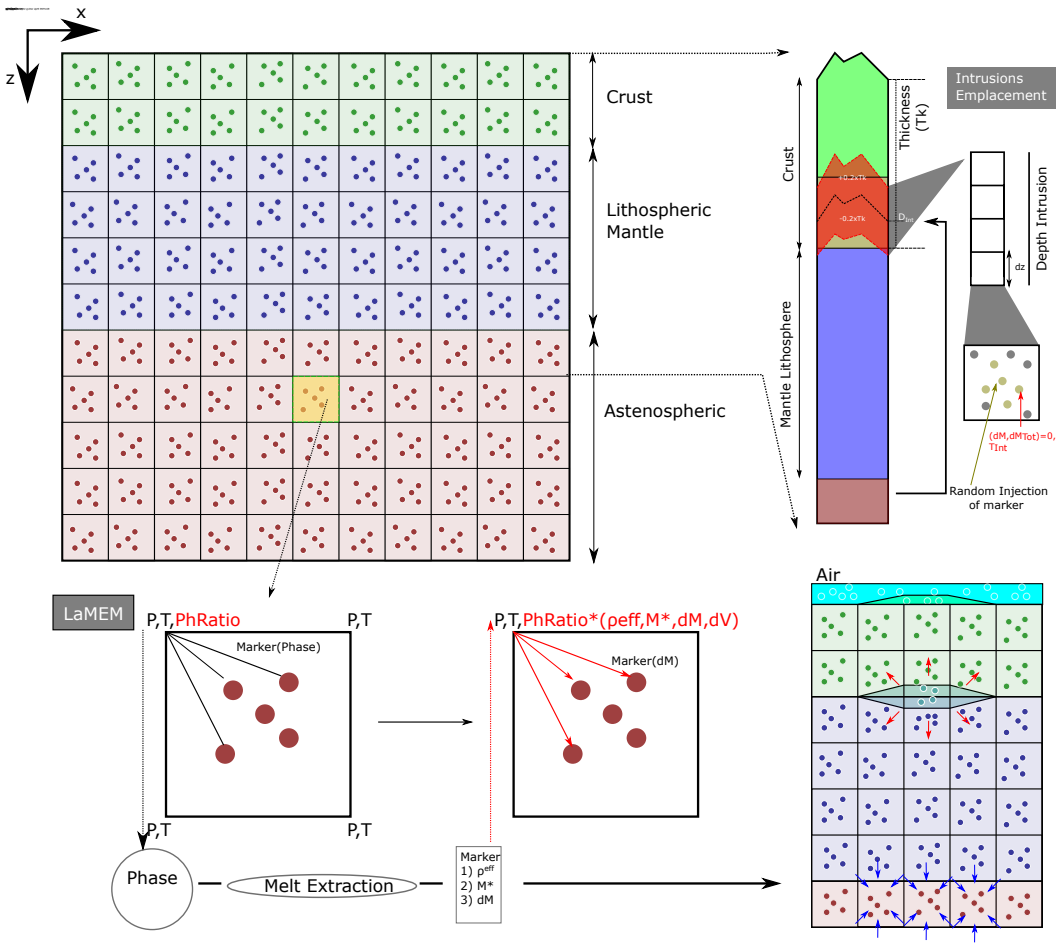


Figure 3.1: Schematic representation of melt-extraction algorithm. For each timestep all the rock-type properties are interpolated into the main grid. Then from pressure and temperature, the density and melt quantity are interpolated from the phase diagrams and scaled accordingly to the $Ph_{Rat}$. After the computation of the total melt extracted, the negative and positive source term are applied to the grid. The intrusion emplacement depth interval is chosen according to the relative depth to the Moho, and the injected volume is evenly distributed along this depth interval

In the simulations, melt extraction and emplacement are considered to occur instantaneously. Each timestep the amount of melt produced by a rock type (*Ph*) is interpolated from the phase diagrams (see Fig.3.1) and corrected accordingly the previously extracted melt ($M^{ext}$), yielding

the corrected value, $M^*$. After the correction it is evaluated whether the volumetric melt fraction is enough to trigger melt extraction. If $M^*$ is higher than a critical melt fraction quantity, $M_{trs}$, a fixed quantity of melt can escape from the source, and its volume ($V_{ext}$, extracted volume) is computed according to:

$$V_{ext}(i,j,k,Ph) = \begin{cases} Ph_{Rat}(i,j,k)dM\Delta x(i)\Delta y(j)\Delta z(k), & \text{if } M^* - dM \geq M_{trs} \\ Ph_{Rat}(M^* - M_{trs})\Delta x(i)\Delta y(j)\Delta z(k), & \text{if } M^* - dM < M_{trs} \end{cases} \tag{3.12}$$

Where $\Delta x(i)$, $\Delta y(j)$, $\Delta z(k)$ are the size of the current control volume corner, and $dM$ is the amount of melt that can escape ($i,j,k$ are the node indexes). If the difference between M$^*$ and $M_{trs}$ is less than $dM$, the quantity of melt extracted is equal to it, and thus $M_{trs}$ represents the minimal amount of melt that can be retained in a rock.

The total amount of melt extracted from the rock $Ph$ is computed by integrating each volumetric contribution along the $z$ direction and correcting it for the different volume of the melt and rock (as in Wallner and Schmeling (2016)):

$$V_{ext}^{Tot}(i,j,Ph) = Vol_{cor} \sum_{k=0}^{n^{end}} V_{ext}(i,j,k) \tag{3.13}$$

$V_{ext}^{Tot}$ is the total amount of melt extracted from the current rock type, $Vol_{cor}$ is the volumetric correction, $n^{end}$ is the last node of the numerical domain.

The total amount of melt extracted is variably converted into extrusions and intrusions:

$$\begin{cases} Vol_{eff}(i,j,Ph) = (1 - I_R)V_{ext}^{Tot}(i,j) \\ Vol_{int}(i,j,Ph) = (I_R)V_{ext}^{Tot}(i,j) \end{cases} \tag{3.14}$$

Where $I_R$ is the relative proportion of intrusions, $Vol_{eff}$ and $Vol_{Int}$ is the extruded and intruded volume respectively. The extrusive volcanic rocks are converted into an effective thickness (dividing the $Vol_{extr}(i,j,Ph)$ by $\Delta x(i) * \Delta y(j)$), which is used to shift the internal free surface.

The intrusions are emplaced in a specific area of the crust (see Fig.3.1) (Wallner and Schmeling (2016)), whose extension and location depends on the current crustal thickness:

$$\begin{cases} v_{int}(i,j,k) = \left( \frac{V_{Int}}{D_{Min}(i,j) - D_{Max}(i,j)} \right) \Delta z(k) \\ D_{Min/Max}(i,j) = Z_{Moho}(i,j) + (D \pm D_{int})Tk(i,j) \end{cases} \tag{3.15}$$

Where $D_{Min}$ and $D_{Max}$ are the extreme of the intrusion interval, $D$ is the depth of intrusion and $D_{int}$ is the relative dimension of half of the intrusion interval (which is an input parameter),

*Tk* is the thickness of the crust at *i,j* point. The control volumes within the interval of intrusion receive a volume quantity equal to $v_{int}$. Then a number of particles proportional to $v_{int}$ are randomly injected simulating local sill intrusion. This strategy implies that the generation of plutonic bodies is incremental in good agreement with previous work (Annen, 2009; Cashman et al., 2017). The volumetric source term used in the eq. 3.1 are computed by assembling a melt contribution to each rock type (see eq. 3.11):

$$\begin{cases} \dot{S} = \frac{1}{dt}\left(1 - \frac{\Delta x(i)\Delta y(j)\Delta z(k)}{1-V_{ext}(i,j,k)}\right) \\ \bar{S} = \frac{1}{dt}\left(1 - \frac{\Delta x(i)\Delta y(j)\Delta z(k)}{1+v_{int}(i,j,k)}\right) \end{cases} \tag{3.16}$$

The source term is computed assuming that that extraction and injection locally shrink or expand the control volume during the current timestep.

The volumetric source term is associated with local over and under pressure. In order to prevent that local pressure fluctuations slowing down the convergence of the non–linear iterations, we use lithostatic pressure both for the rheological consitituve laws and for the interpolation the melt quantity during the melt extraction.

#### 3.2.2.2 Petrological Modeling

Each marker is associated with a rock-type which links it to calculated phase diagrams and the associated thermo-mechanical properties. Markers may change the rock type as a function of the total melt extracted. During the non-linear iterations (*NLI*) pressure and temperature are computed; the density and relative amount of melt are linearly interpolated from phase diagrams using the solutions of the current *NLI*. Melt extraction is applied only to adjust the density during the iterations. However, the source term is computed before the *NLI* and is based on the previous time-step, while the injection of the new rocks is based on the final solution.

The phase diagrams store the melt quantity and the density of the solid fraction while the density of the melt is assumed constant (2700 and 2400 $kgm^{-3}$ for mantle and mafic phase diagrams respectively). Felsic crust formed as a consequence of crystallized TTGs magmas is modeled as a passive phase with a constant density (2700 $kgm^{-3}$), and it is not associated with any phase diagram.

The rock-types are divided into two sets: 1) Mantle (*Ml*); 2) Mafic Crust (*MC*) (as in (Piccolo et al., 2019)):

1. Mantle phase diagrams represent six different steps of mantle depletion (*MD0%, MD10%, MD20%, MD30%, MD40% and MD50%*) and were computed using *Perple_X* (Connolly,

Table 3.1: Composition of mantle phases diagram. All the compositions are listed as mole % oxide.

| Rock Types | $SiO_2$ | $Al_2O_3$ | $Cr_2O_3$ | FeO | MgO | CaO | $Na_2O$ |
|---|---|---|---|---|---|---|---|
| MD0% | 48.809 | 8.195 | 1.066 | 10.438 | 27.501 | 3.590 | 0.401 |
| MD10% | 49.235 | 7.047 | 1.126 | 10.241 | 29.232 | 2.843 | 0.276 |
| MD20% | 49.782 | 5.463 | 1.156 | 10.161 | 31.385 | 1.924 | 0.128 |
| MD30% | 50.328 | 3.815 | 1.163 | 10.023 | 33.930 | 0.723 | 0.018 |
| MD40% | 50.202 | 3.327 | 1.070 | 9.517 | 35.782 | 0.102 | 0.000 |
| MD50% | 49.309 | 3.608 | 0.994 | 8.812 | 37.276 | 0.001 | 0.000 |

2009). We used the activity-composition model of Jennings and Holland (2015), and all calculations assume a buffered oxygen fugacity (all the compositions are listed in Tab.3.1, and all phase diagrams are shown in Fig. B1). The first step of depletion (Mantle Step 0%) is modeled using the pyrolite composition from McDonough and Sun (1995). As calculating the new composition on the fly is computationally too demanding, the chemical evolution is assumed to be only a function of the amount of extracted melt. We compute the depleted phase diagrams using the average composition of the residuum along the 10% melt isoline in every phase diagram (e.g. MD10% is computed using the residuum of the *MD0%*, *MD20%* is computed using the residuum composition of *MD10%*, etc.).

2. Mafic phase diagram represents four depletion steps (*BS0%*, *BS15%*, *BS30%* and *BS45%*). All phase diagrams were computed using THERMOCALC 3.45 (Powell and Holland, 1988), using the Holland and Powell (2011) dataset (ds62). The starting phase diagram has the composition of a typical enriched Archean basalt (EAT). All solution model used to produce these phase diagram: *a-x* relations were used: epidote, olivine (Holland and Powell, 2011), silicate melt, augite, hornblende (Green et al., 2016), garnet, orthopyroxene, biotite, chlorite (White et al., 2014), magnetite–spinel (White et al., 2002), ilmenite–hematite (White et al., 2000), Cbar-1 plagioclase, K-feldspar (Holland and Powell, 2003), and muscovite–paragonite (White et al., 2014)

Table 3.2: Composition of basalts. All the compositions are listed as mole % oxide. (*) Basalt Step 45% has the same phase diagram of Basalt Step 30 %, but, after the extraction, the predicted composition is the one listed. Basalt Step 45% is used to describe the density of the dry Intrusions.

| Rock Types | $H_2O$ | $SiO_2$ | $Al_2O_3$ | CaO | MgO | $FeO^{Tot}$ | $K_2O$ | $Na_2O$ | $TiO_2$ | O |
|---|---|---|---|---|---|---|---|---|---|---|
| BS0% | 6.830 | 49.693 | 8.992 | 9.214 | 10.205 | 9.814 | 0.442 | 2.628 | 1.125 | 1.058 |
| BS15% | 4.443 | 47.975 | 9.118 | 10.330 | 11.775 | 11.238 | 0.227 | 2.373 | 1.304 | 1.226 |
| BS30% | 2.329 | 45.712 | 9.198 | 11.557 | 13.489 | 12.738 | 0.102 | 1.947 | 1.509 | 1.419 |
| BS45%(*) | 1.163 | 43.856 | 9.173 | 12.879 | 14.824 | 13.380 | 0.044 | 1.284 | 1.751 | 1.647 |

For the mantle phase diagrams, progressive melting and melt loss from *MD*0% to *MD*50%

results in the progressive decrease in *FeO* content, melt fertility and density (Griffin et al., 2003) (see Fig. B1). During the Archean mantle melting was widespread, and the extraction of the resulting mafic melts generated large volumes of harzburgite-dunite, which are the major component of cratonic lithosphere (Herzberg and Rudnick, 2012; Griffin et al., 2003). We use this simplified depletion scheme to capture at least the first-order effect of depletion, despite not systematically studying craton generation herein. There are several processes that might have been responsible for craton generation, most of which are related to physical-chemical processes that are not specifically modeled here, such as collision or dehydration of the foundered mafic crust (Bédard, 2006; Gray and Pysklywec, 2010). Nevertheless it is important to take mantle depletion into account, as it may have helped to stabilize proto-lithosphere. Melt extracted from the mantle is converted into anhydrous intrusions and extruded hydrated EAT (BS0%). We assume that effusive rocks are always hydrated, consistent with the inferred Archean sub-marine environment (Kump and Barley, 2007).

Mafic phases are represented by five rock-types: *BS0%, BS15%, BS30%, BS45%* and their anhydrous intrusive equivalents, where BS0% is the protolithic metabasalt composition. BS0% is assumed to be fully hydrated, and that the molar volume of water is sufficient to minimally saturate the solidus at 1.0 GPa (Palin et al., 2016), taken to be the base of the crust. $H_2O$ is stored in hydrous minerals (like amphibole), partitions into the melt phase during hydrated mineral consumption. After 15% of melting and melt extraction, the rock type is changed to the following basaltic step. BS45% is most depleted lithotype and has the same composition of BS30% but is no longer able to produce melts. The mafic intrusions are assumed to be anhydrous, and unable to produce any melt, and are modeled as if they had the same composition of BS45% (as in (Piccolo et al., 2019)). For simplicity, we choose to not model them as productive lithotype to avoid overproduction of felsic magma, even if in reality they may contain a small amount of $H_2O$ and undergo low degrees of melting. They represent the composite underplated bodies expected to be found at the base of an evolving oceanic plateau (Van Kranendonk, 2010; Palin and Dyck, 2018; Cox, 1980).

## 3.3 Results

### 3.3.1 Initial Setup

We performed systematic experiments in 2D and 3D. The 2D numerical setups are boxes whose $y$ axis is 2 km (3 grid nodes) compared with 100's of km for the $x$ and $z$ directions. The 2D tests are performed to test the melt extraction parameters (i.e. $M^{trs}$ and $dM$) and to investigate the relative differences with 3D setups. We performed numerical experiments to test the effect

of the initial $T_P$, convective vigor (varying the temperature of the lower bottom boundary), radiogenic heating, and the initial thickness on model behavior.

All numerical experiments shares the same boundary conditions being:

- Mechanical: free slip on all boundaries except for the top boundary, which features an internal free surface with a stress free open top boundary;
- Thermal: the top and bottom faces are isothermal (Top=20 °C, while the bottom boundary temperatures are set to be 1700 ° C in most of the experiments), while the lateral boundaries have no flux boundary conditions;

The 2D numerical domain size is 1000×2×520 km with 257×3×257 nodes (along $x$, $y$ and $z$ directions respectively), while the 3D numerical setups is 800×800×520 km in size with a 257×257×257 nodes. The air layer is 20 km thick in all cases.

The initial compositional field features an initial 100 km thick lithosphere, divided into 30 km of mafic crust and 70 km of depleted harzburgite (*MD30%*). The ratio between crust and lithospheric mantle is constant in all the numerical experiments. The upper crust is composed of hydrous basalts (*BS0%*), whose thickness is 15 km while the lower crust is made up of dry and infertile mafic intrusions. The asthenosphere is composed of pyrolytic and fertile mantle McDonough and Sun (1995) (MD0%). The plume is purely thermal, and it has the same composition as the upper mantle. The plume is placed at the centre of the model and has a radius that is varied from 150 to 200 km. Mantle lithologies are modelled with a dry olivine rheology flow law (Hirth and Kohlstedt, 2004). The hydrous mafic crust and the felsic crust are modelled with wet quartzite flow law, while the residual mafic composition (BS45%) and dry intrusions have a mafic granulite rheology (Ranalli, 1995). All geological units have the same initial friction angle (30°) and cohesions (10 MPa). New intrusive bodies (felsic or mafic) could affect the plastic properties of the surrounding rocks and may damage them. To simulate the weakening associated with the opening of dikes filled with melts, previous works employed an effective friction angle (Gerya et al., 2015; Sizova et al., 2014, 2015). However, this strategy generates a sudden jump of the rocks plastic properties, which could affect the ability of the system equations to converge. To incorporate such processes without affecting the performance of the numerical experiment, rocks are allowed to be plastically weakened. The cohesion and friction angle varies linearly as function of the accumulated plastic deformation until they reach 30% of their original values.

All references scenarios assume that mantle $I_R$ is equal to 0.6 (consistently with plume geodynamic estimates (Crisp, 1984; White et al., 2006)), and the interval of intrusions is between the Moho depth and 0.6 of the total thickness of the crust, while mafic crust $I_R$ is 1, with an

interval of intrusion spanning from 0.5 to 0.9 of the total crustal thickness.

The $T_P$ temperature of the experiments ranged from 1350°C to 1550 °C , while the temperature of the plume is kept constant at 1600 °C. The initial geothermal gradient of the lithosphere is a linear double stage geotherm, featuring a $T_{Moho}$ of 800 °C and a temperature at the base of the lithosphere that depends on the $T_P$.

### 3.3.2 Plume-Lid Interaction in 2D

Melt fraction ($M^*$) affects the buoyancy of the media and consequently the velocity of the rising plume. If the amount of melt produced within the plume is not effectively compensated by the melt extraction, the plume accelerates with time, affecting the stability of the lithosphere. Each timestep a fixed amount of melt is extracted from a partially molten source, and as a result, a compaction term introduced. In order to test the relative importance of each parameter, nine experiments were performed varying the mantle melt extraction efficiency ($dM$) and melt extraction threshold ($M^{trs}$) from 0.001 to 0.05. The bulk of the numerical experiment performed suggest that the most important parameter is $dM$, while $M^{trs}$ only affects the final productivity of mafic crust and enhances the ability of the residual crust to delaminate/drip. By contrast, varying the depth of intrusions affects the amount of felsic crust produced, and promotes melting of mafic crust at higher pressures (see Fig. B2), while the other dynamics are similar to the references experiments. Simulations feature two main stages: 1) a *Tectonically active stage*, in which the arrival of the plume triggers lithospheric instabilities that plastically deforms the crust 2) *Steady state stage* featured by a steady-state condition in which a new proto-lithospheric mantle gradually forms.

At the end of every numerical experiment performed, the new felsic crust is concentrated near the Moho, while the upper crust is composed of mafic hydrous crust punctuated by felsic crust domes.

In the following paragraphs we describe two representative examples:

#### 3.3.2.1 Melt Extraction

**Low efficiency melt extraction (dM=0.001), plume radius = 200 km.** During ascent, the plume is cylindrical (see Fig. 3.2) and laterally spreads as soon as melting begins. Owing to the low melt extraction efficiency, the plume's ascent and spreading velocity increases with time, enhancing the production of melt and consequently its density contrast with lithospheric mantle. This enhanced density contrast triggers RTIs of the lithosphere and a penecontemporaneous erosion of its base. The initial lithospheric RTIs instabilities split the plume head in two branches.

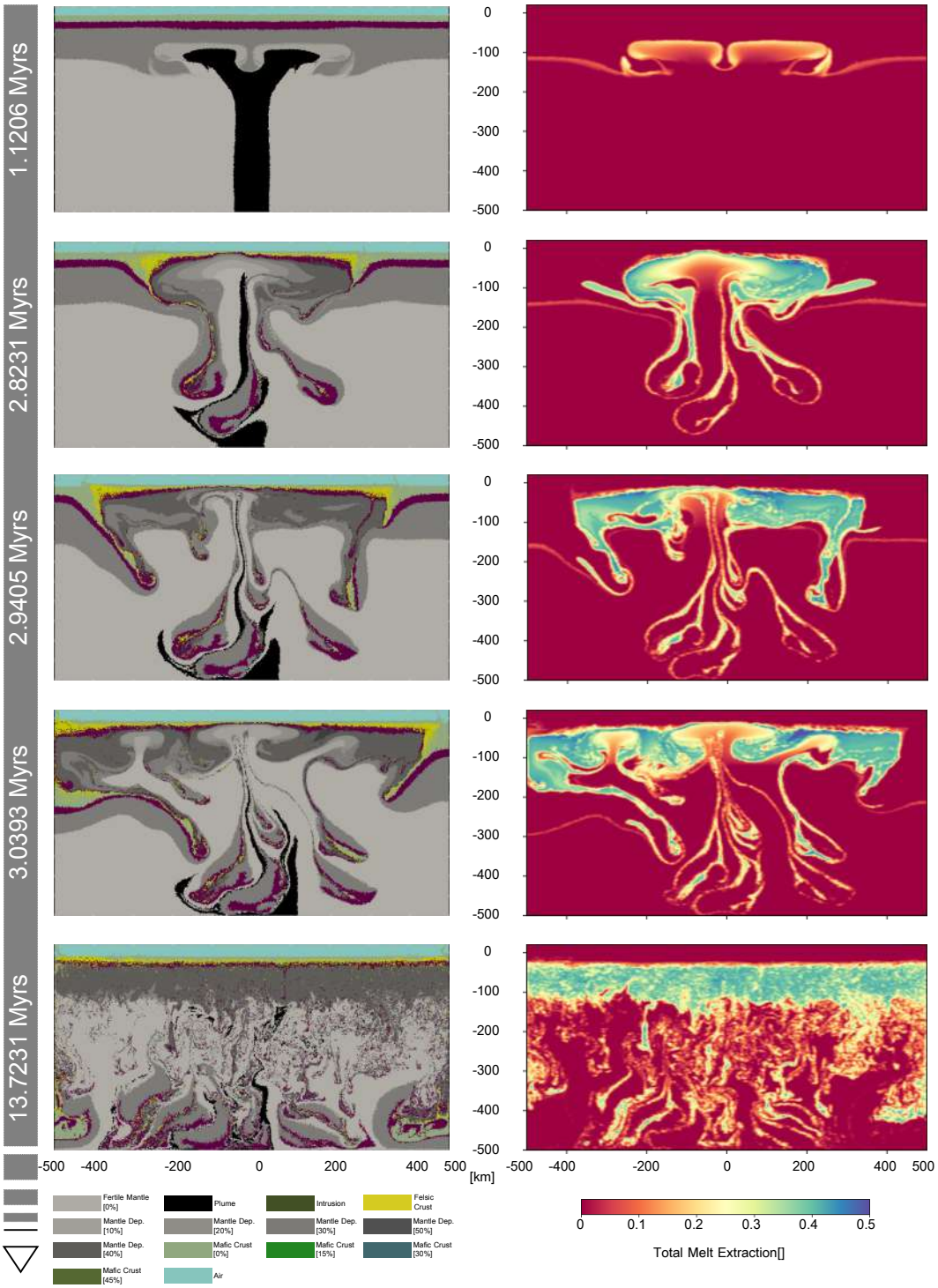


Figure 3.2: **Test low melt extraction efficiency, $T_P$=1500 °C, dM=0.001, $M^{trs}$=0.001**: **a):** Compositional field; **b):** Total melt extracted during the simulation

Meanwhile new mafic intrusions are emplaced in the lower-middle crust, but due to their limited

extent, the heat transferred from the mantle is insufficient to trigger felsic crust production. The amount of extracted melt triggers major compositional changes and the original plume material changes to simulate the evolution from a peridotitic composition to a more residual one (the plume changes its phase into MS10-20%, see Fig. 3.2).

The continuous addition of new dry intrusions and the production of residual composition triggers a substantial peeling off and delamination of the lower crust and RTIs that locally destroy the lithosphere and blocks the plume's buoyancy flux (Fig. 3.2, 2.8231 Myrs). Asthenospheric mantle flows in the created space, melting and enhancing the disruption of the lithosphere. The newly partially molten asthenosphere spreads beneath the crust, thinning it in the center and thickening it at the rim of the plume-impact structure. Since the amount of extracted melt is limited, the newly generated mafic melts are unable to compensate for the stretching of the crust. The amount of felsic crust produced significantly increases in the thickened portion of the mafic crust. The spreading of the partially molten mantle exert a traction on the newly composite crust, which laterally expands. The lateral propagating impact structure force the old mafic crust to partially subduct at the rim, but since it is not enough dense, the processes is inefficient, and provokes a continuous migration of the compression towards the outer portion of the domain, not yet affected by the plume. The resulting thickened areas are associated with felsic crust anomalies, while the central area initially affected by the plume has considerably less amount of felsic crust.

After all mantle lithosphere has delaminated, the production of new mafic and felsic crust slowly decreases with time. The mantle becomes sufficiently cold to no longer allow continuous melting and the generated residual mantle starts to collect at the bottom of the crust in a compositionally distinct layer. This proto-lithospheric mantle convects, and its temperature decreases with time. The produced felsic crust is located at the bottom of the newly composite crust.

**Moderate melt extraction efficiency (dM=0.01), Plume radius 200 km.** The amount of melt extracted from the plume is higher than in the previous experiment. This prevent initial mantle lithosphere drips from developing. The thickening of the mafic crust is significantly higher, and the dynamics of the system is mainly controlled by the crustal evolution (see Fig. 3.3).

After 1.5 Myrs of localized thickening, the crust becomes unstable. While the first crustal scale RTIs develops, small amounts of felsic crust is generated resulting in dense residue. The unstable crust drips, blocking the buoyancy flux of the mantle plume. The lithospheric mantle is locally destroyed, allowing the asthenosphere to come in direct contact with the crust. The

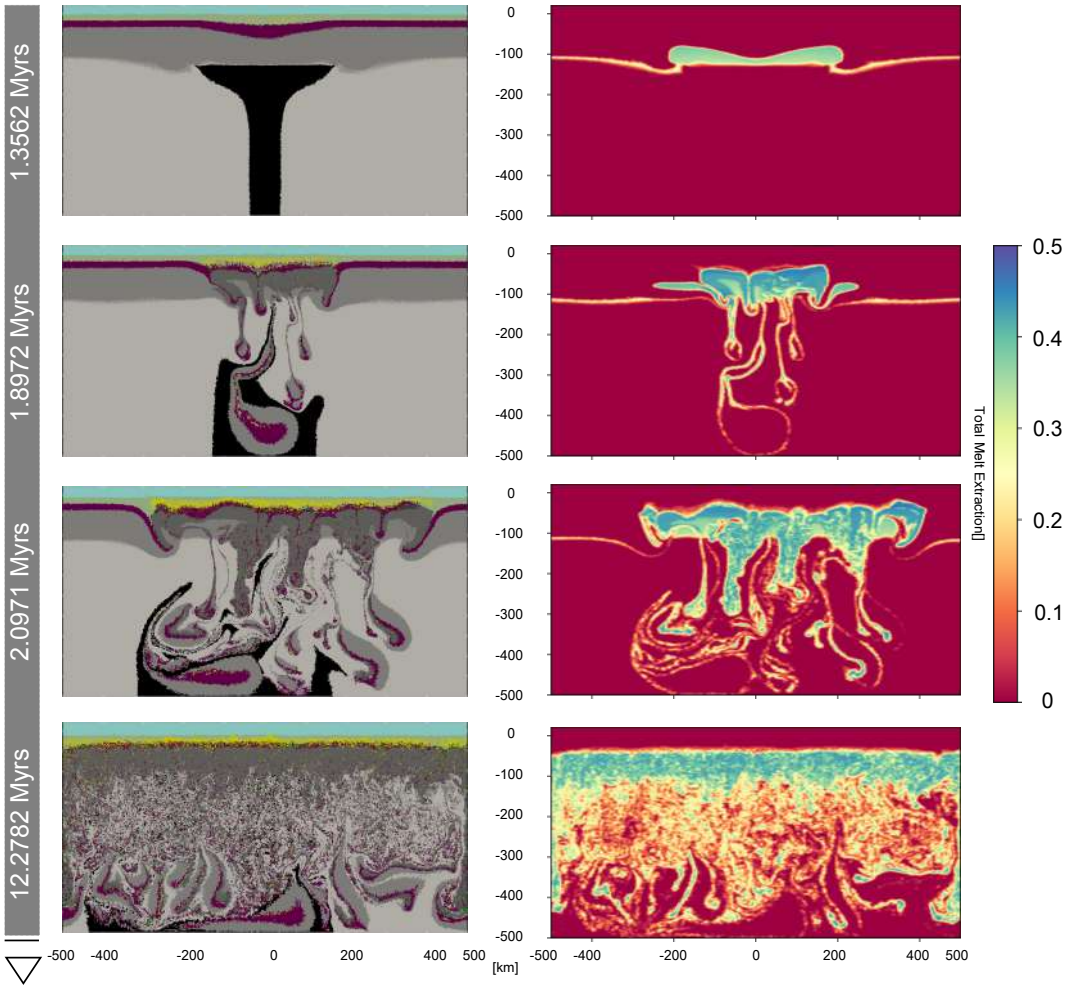


Figure 3.3: **Moderate melt extraction efficiency $T_P$=1550 °C, dM=0.01,$M^{trs}$=0.001**: **a):** Compositional field; **b):** Total melt extracted during the simulation.

amount of melt increases, generating an evolving oceanic plateau, which starts to spread laterally.

The adjacent lower crust starts to delaminate, removing the lithosphere and enhancing the production of both new mafic and felsic crust. After all the lower crust is removed, most of the original mafic crust has been recycled. The numerical simulation enters its final stage, in which the production of new mafic crust is inhibited, while the felsic crust is still being produced. During this stage, a new proto-lithospheric mantle forms, and as for the previous numerical experiments, the lower crust is mainly composed of felsic crust.

**Effect of $T_P$ and the initial lithospheric thickness** Most of the numerical experiments features the same dynamics. The plume generates a lithospheric-scale instability that propagates

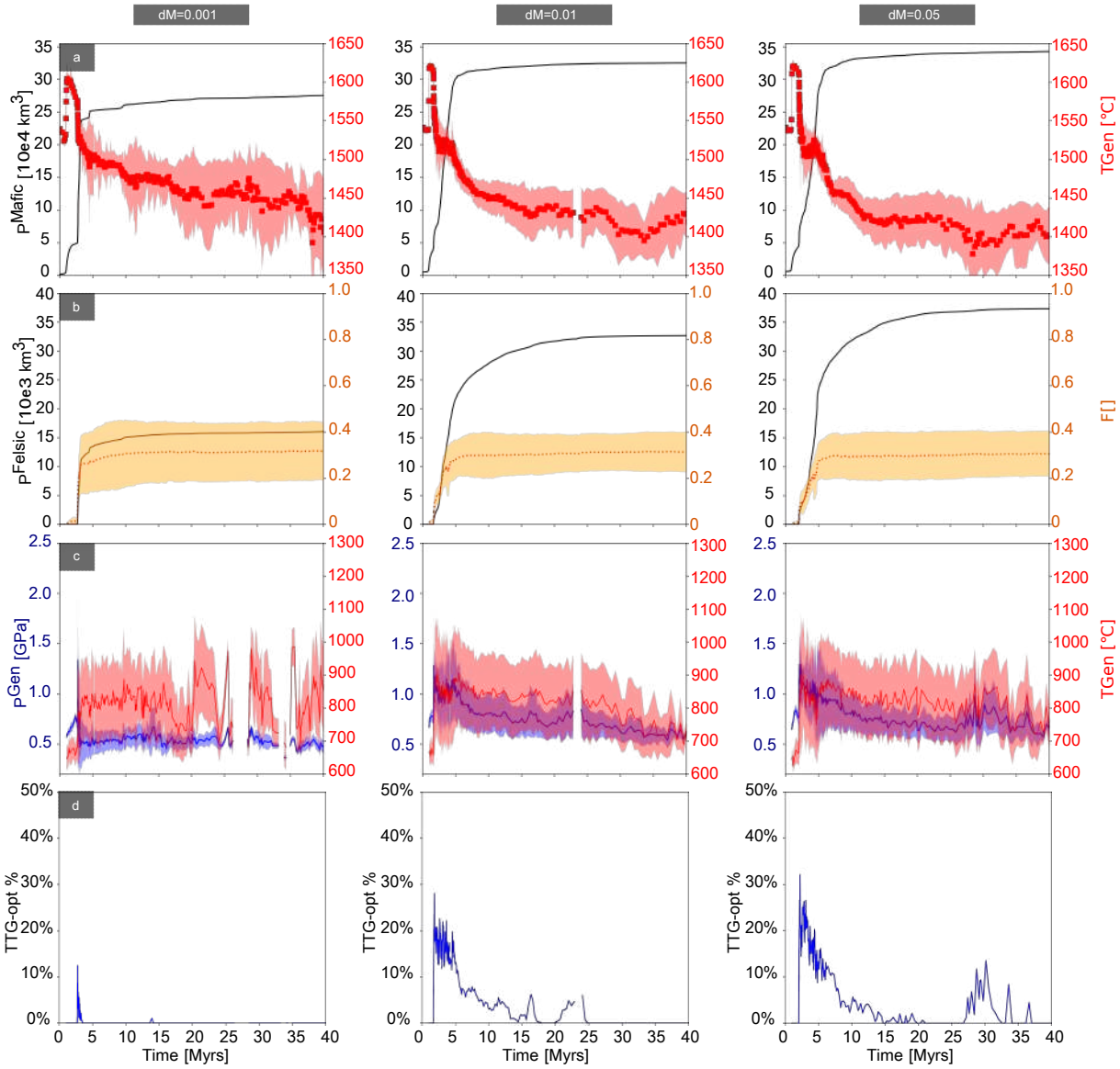


Figure 3.4: **a)**: Mafic crust production($P^{Mafic}$) (black line). The red shaded area represents the mafic melt generation temperatures (squares average generation temperature, red shaded area and lines standard deviations); **b)**: Temporal evolution felsic crust production ($P^{Felsic}$). The orange dashed line represents the average amount of felsic crustal components, *F*, while the orange shaded area represents one standard deviation envelope (see Supplementary material for further explanations and eq. B2) ; **c)**: The red shaded area and the correlated red dashed line represents the standard deviation of the melt extraction temperature condition and the average melt extraction condition, while the blue shaded area and dashed line represents the standard deviation and the average pressure conditions; **d):** TTG-opt with time, see main text, for further explanation.

throughout the domain. The initial $T_P$ controls the timescales of the processes while the relative amount of mafic crust produced appears to be not strongly by the initial $T_P$ (see Fig. B3). However, the behavior of the system is highly sensitive to the initial lithospheric thickness, mantle radiogenic heating, and convective vigor of the mantle (which is controlled by the lower

thermal boundary condition).

Most of the experiments features an initial lithospheric thickness (*Tkl*) of 100 km, which promotes the propagation of gravitational instabilities. The *Tkl* assumed for the reference tests described above, represents the minimum thickness at which the mantle underlying the lithosphere is not melting at $T_P$ of 1500 °C. Lowering the *Tkl* at high $T_P$ ($\geqslant$ 1450 °C) does not affect the timescale of the processes but it slightly affects the production of both felsic and mafic crust. A thinner lithosphere inhibits the propagation of gravitational instabilities at lower $T_P$ ($\leqslant$ 1400 °C) as function of the lower thermal boundary condition and mantle radiogenic heat production(see Fig. B4b-c). The experiment shown in Fig. B4b features a two stage evolution: an initial stage in which mafic and felsic crustal growth is a consequence of the plume activity (0-2 Myrs) and then, after 20 Myrs of slow evolution (see Fig. B3g), a new crustal growth stage begins, in which both mafic and felsic crust grows until they reach similar values to those of an experiment with the same $T_P$ but higher *Tkl* (see Fig. B3c and g). The second crustal growth event is triggered by mantle radiogenic heating and by small upwellings coming from the lower part of the upper mantle. By contrast, if the convective vigor (bottom temperature equal to 1600°C) and radiogenic heating are lowered ($A = 0.3310^{-5}\ \mu W kg^{-1}$), the second growth phase is suppressed, and the propagation of gravitational instabilities is slow (see Fig. B4c). Both mafic and felsic crust total production is significantly lower than in the references scenario (Figs. B4a-b, and B3c-g).

The ratio between crust and lithospheric mantle thickness (0.3 of the total *Tkl* is made of crustal units) and the initial Moho temperature are the same in all experiments. As a consequence, experiments featuring the same initial *Tkl* have the same crustal density profile. Higher lithospheric thickness promotes unstable lower crust, favoring the propagation of gravitational instabilities. Mafic crust production is associated with peeling/dripping-off of the lower crust and promotes lateral propagation of the gravitational instabilities. If the crustal thickness is low (i.e. ≤ 30 km), the required amount of new crust to propagates gravitational instabilities increases. As a consequence, $T_P$ plays a first order role on the evolution of the experiments, because it controls the viscosity contrast between crust and mantle, and because it controls the rate of new crust addition. If the mantle is not sufficient hot to generate large volumes of new mafic melts, the lithosphere is stable, and the evolution of the system depends on long-term processes (such as mantle radiogenic heating). If the lower thermal boundary features higher $T_P$ and the radiogenic heat production is high (which depends on the amount of residual mantle produced and on the recycled amount of crust), small upwellings produce instabilities, triggering a later stage of crustal growth.

**Crust production and melting conditions** Both of the simulations described above encompass most of the features that can be observed in all simulations. Specifically, these include an initial stage of mafic crust forming event, followed by a stagnation stage in which the mantle is unable to produce large amount of new mafic melts.

The two experiments show different crustal growth behavior. A low $dM$ value (= 0.001) enhances the velocity of the processes and ultimately leads to a minor production of new mafic and felsic crust. The initial tectonically active stage featured a quasi-vertical slope in the productivity of mafic crust ($P^{Mafic}$) and felsic crust ($P^{Felsic}$) (see Figure 3.4). The average temperature of mafic melt production has an initial spike associated with plume interaction with the lithosphere, after which it exponentially decays towards a temperature that is lower than the initial $T_P$ ($\Delta T^{\circ}C$=100$^{\circ}C$). The P-T conditions at which felsic crust is produced features low-pressure and high-temperature conditions, with an initial high-pressure anomaly associated with the short-lived pseudo-subduction events ($P \geq$ 1GPa). The plume related mafic crust represents at least half of the total mafic crust produced, while the high-pressure felsic crust represents 2/3 of the total felsic crust produced.

Experiments with a higher value of $dM$ ($\geq$ 0.01), show a different melting behavior. The plume signature is confined to the initial stage, then, after the initial drips, most of the mafic crust is produced from normal asthenosphere. The volume of mafic crust produced is higher, and it is generated by portion of mantle featuring variable temperatures. The slope between ($P^{Mafic}$) and time is lower than the lower efficiency ones. After the main phases of mafic crust production is over, new felsic crust is produced as a consequence of the heat transmitted by the asthenosphere and by the slowly cooling intrusions. These observation suggest that the felsic crust production is closely related with mantle magmatic activity.

TTGs features a wide range of compositions, and their trace element signature is variable, which indicate different pressure-temperature conditions of generation. It has been shown that EATs produce TTGs melts with a composition that best fits the average one of the Archean TTGs in a narrow P-T window (1.0-1.8 GPa, 800-950 $^{\circ}$ C), (Palin et al., 2016). In order to measure the amount of TTGs that most likely feature a similar composition of the natural examples, we sum all the extracted felsic melts within the optimum TTGs window and divided it by the total felsic melt extracted (TTG-opt) (see Fig. 3.4). The value of TTG-opt depends on the ability to build an oceanic plateau and, as a consequence, $dM$ has a primary controls on the relative amount of TTG-opt generated. If $dM$ is extremely low (= 0.001), the new crust produced is unable to compensate for recycling, yielding an extremely thin and hot crust, and thus only 10% of TTGs melt is produced in the optimal P-T window. Increasing $dM$, on the other hand, results in a thicker plateau promoting high pressure melting and thus larger amount of TTG-like melts

(TTG-opt=30%). Changing the relative depth and interval of the mafic intrusions promotes high pressure melting and increases TTG-opt respect the previously described scenarios (Fig.B2). In all the previously described scenarios TTG-opt rapidly grow during the initial stage of the experiments and then it exponentially decays with time. At lower $T_P$ (=1400 °C) the amount of TTGs produced within the optimal window is higher and more continuous with time. The experiment with low *Tkl* (75 km), but high mantle radiogenic heating features two main pulses of magmatic activity, correlated with a significative production of new TTGs produced at optimal P-T conditions. By contrast if the convective vigor and $H_r$ are reduced, TTG-opt is higher, but associated with a small addition of new felsic crust (Fig. B5).

### 3.3.3 Plume-Lid Interaction in 3D

The 3D numerical experiments follow the 2D models to test the predictive power provided by the latter. The first parameters that have been investigated are related to the melt extraction efficacy and the effect of a smaller radius, then the effect of the background mantle potential temperature is tested against the initial lithospheric thickness and the radius of the plume. We keep the temperature of the plume constant, implying that the dynamics vary according to the background temperature. We choose to not explore the effect of high $T_P$ of the plume to not overlap the P-T condition of komatiitic magma production (1700-1800°C (Condie, 2001; Schmeling and Arndt, 2017)). The velocity of the plume is highest at low $T_P$ and lowest at 1550 °C. The initial stage of each experiment features the same evolution: the hemispheric plume changes shape into a more cigar-like shape, and spreads beneath the initially prescribed lithosphere, generating melts and locally increasing the thickness of the crust. This stage has a variable duration that depends on the radius of the plume and the relative thermal differences, between the mantle and plume.

#### 3.3.3.1 Effect of Melt Extraction parameters

We consider two end-member scenarios: low ($dM = 0.001$) and high ($dM = 0.05$) melt extraction efficiency. The $M^{trs}$ is constant and assumed to be close to zero. The initial radius of the plume is smaller than the 2D experiments, while the $T_P$ and plume temperature are kept constant. The radius was lowered to minimize the plume mechanical effect, which is stronger in 3D, and to focus only on the effect of melt extraction parameter.

**Inefficient melt extraction (dM=0.001)** (see Fig. 3.5 and Fig B6): The plume rises to the base of the lithosphere, interacting with it, generating sub-lithospheric convection cells. The partially molten rocks of the plume generate strong density contrasts that triggers the first

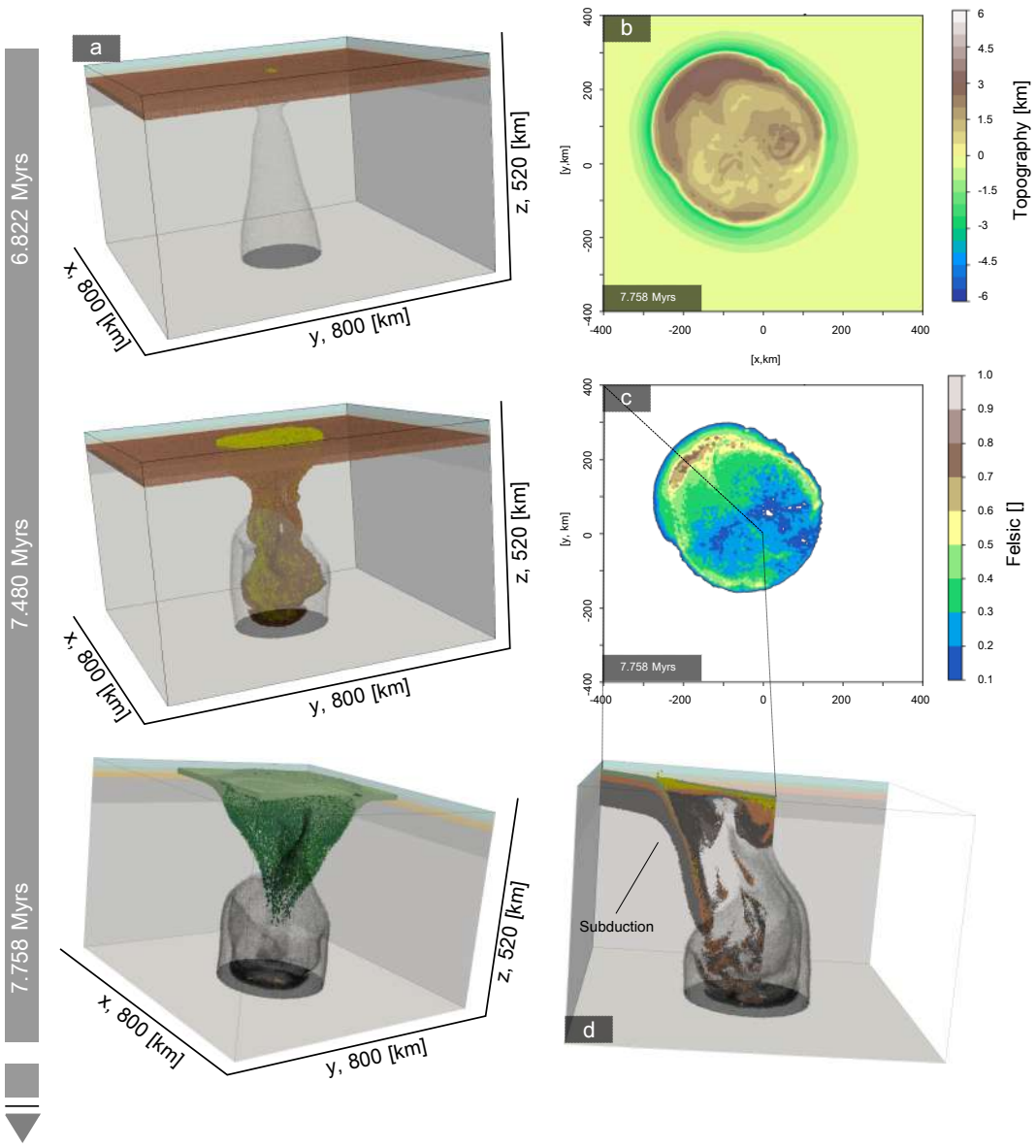


Figure 3.5: **Plume radius = 150 km, dM = 0.001, $T_P$=1500 °C, $T^{Pl}$=1600 °C: a):** Evolution of the numerical experiment from the initial stage to the subduction stage. The picture depict the lower crust (orange color with transparency), the plume (black color with transparency) and felsic crust (yellow). The bottom left picture represents the subduction slab (green); **b):** Topography contour map taken at 7.758 Myrs. Topography is measured respect the average depth of the free surface.; **c)** Normalized amount of felsic crust component along z direction taken at 7.758; **d):** Profile along the direction drawn in c).

drips and peel off the lower crust. The production of felsic crust is limited, and focused near the center of the plume impact structure (see Fig. 3.5a ).

After ≤ 1 Myrs, the crust drips and delaminates. The lower crust founders rapidly into the mantle and blocks the buoyancy flux of the plume. This destroys the coherency of the plume and forces it to laterally expand and mix with normal asthenosphere, favoring the thermal

equilibration with the surrounding mantle.

After the initial drips and delamination events, the lithosphere is locally destroyed, and descending of drips induce asthenospheric return flow, producing more melt and smaller secondary drips. The partially molten asthenosphere rapidly depletes, becoming residual mantle, and it expands in all directions. The expansion of the newly generated residual mantle promotes the delamination of the lower crust that puts in direct contact the hydrated mafic crust with mantle lithologies. The residual mantle exchanges heat with the hydrated mafic crust, which starts melting producing felsic melts, and cools (see Fig.3.5a, 7.48 Myrs). The injection of new mafic intrusions enhances the production of new felsic crust by heating the pre-existent mafic crust. After the mafic intrusions becomes cold and negatively buoyant they founders into the mantle, inducing an asthenospheric return flow resulting in more mafic and felsic crust production.

After this initial stage, the propagation of the gravitational instabilities becomes anisotropic. The asthenospheric flow stretches the newly formed mafic crust, extending it in all directions. At the rim of the impact structure, the old-prescribed initial mafic crust is compressed. The compression fronts migrates outwardly respect the plume axis, and since most of the crust is too strong to be subducted, it thickens. However, the pushing forces generated by the asthenosphere is not equal in all directions, and in some portion of the domain, the old-prescribed crust is effectively subducted (Fig. 3.5a(7.758 Myrs),and d). However this forced subduction is not continuous and does not efficiently transport material into the mantle (see B6) and it is not similar to the one observed during the Phanerozoic. It differs from delamination events for a more localized deformation and for crustal-scale shear zone that are similar to the one observed in subduction zones. This "proto-subduction zones" are a site of accumulation of felsic crust, that has been passively transported from the inner part of the plume impact structure. These processes results in a high felsic compositional anomalies (80% of the crust is composed by felsic crust, see Fig. 3.5c) generating small continental crust terrains.

The topography and amount of felsic crust generated are highest nearby the proto-subduction zone (see Fig. 3.5b-c). The topographic anomalies and the relative amount of felsic crust increase from the original plume impact structures towards the rims and toward the subduction zone. After reaching the limit of the numerical box, the proto-subduction zone breaks off, as such it is difficult to estimate how far this zone could propagate and whether it could evolve into a large, more Phanerozoic style subduction zone. After the disruption of the proto-subduction zone, the experiment features the same dynamics, however, no new proto-subduction zones are observed. These processes falter once all the original lithospheric mantle is eroded, delaminated and dripped off, leaving the crust in direct contact with the mantle. The dynamic of the processes

is governed by the evolution of the new lithosphere and punctuated by local asthenospheric upwellings.

The proto-subduction initiation observed in our experiment is similar to those reported by Gerya et al. (2015) and other works (Baes et al., 2016; Ueda et al., 2008; Burov and Cloetingh, 2010), however there are also several key differences. In these earlier studies, plumes actively induce the subduction by penetrating and bending lithosphere. In our numerical experiment, the plume indirectly triggers the subduction. Most of the processes are controlled by the asthenospheric return flow induced by the first drip. Asthenospheric flow, in conjunction with the production of mafic melts and their low extraction efficiency, generates high forces that push the surrounding old lithosphere forcing the subduction. The physical process is the same, but the main driver is different in our numerical experiments.

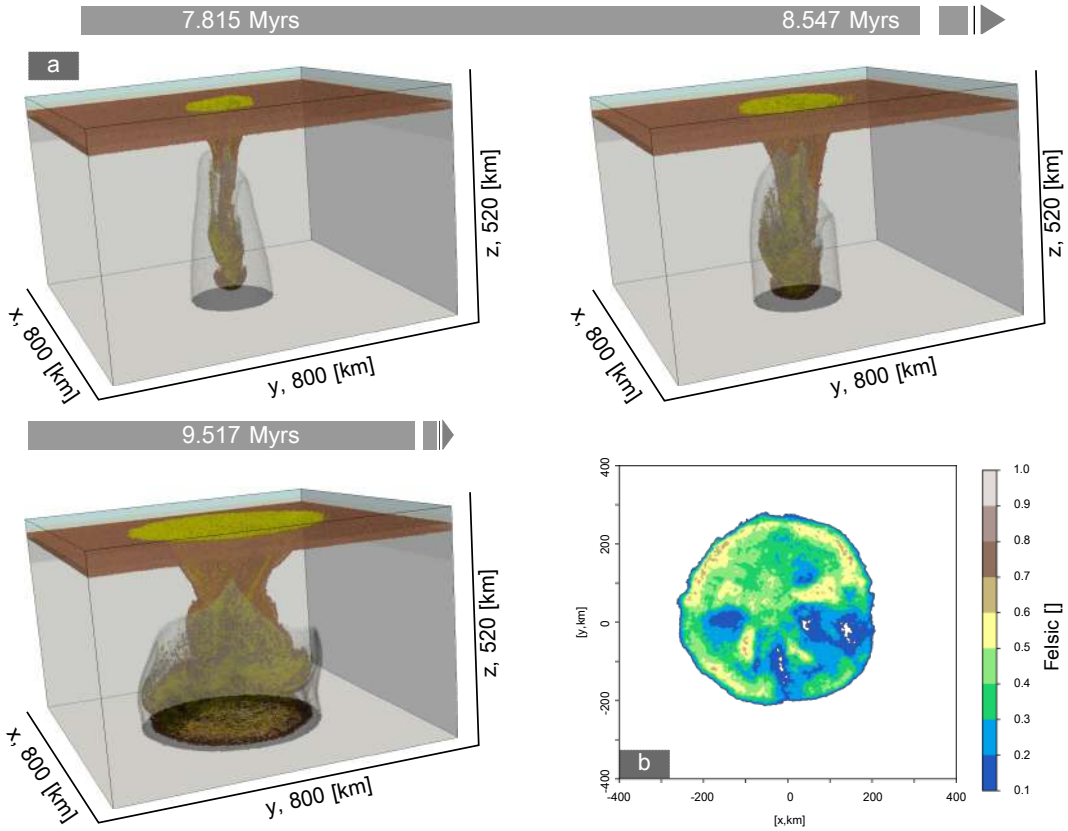


Figure 3.6: **Efficient melt extraction, plume radius:150 km, dM=0.05 a):** Evolution of the experiments during the first drip and development of the basaltic plateau; **b):** Relative amount of felsic crust along z direction.

**Efficient melt extraction (dM=0.05)** (see Fig 3.6): High melt extraction efficiency leads to localized production of new crust. The number of mafic intrusions is greater than for the low efficiency experiments, which leads to an efficient thermal maturation of the lower-middle crust.

Felsic crust production is high, and the shapes of these anomalies match that of the plume impact structure. Due to its radius, the plume is unable to trigger a catastrophic delamination/peeling off the lower crust, but the first drip events can reduce the buoyancy flux of the plume and promote its mixing with the colder asthenosphere.

Asthenospheric return flow enhances the production of mafic and felsic crust. Once residual mantle forms, the dynamics are controlled by gravitational instabilities occurring between the colder and residual mantle and the fertile asthenosphere. The asthenosphere upwelling starts spreading and triggers peeling off the lower crust of the adjacent area, enhancing the production of new crust (felsic and mafic).

The experiments feature a constant expansion of the original plume impact structure, and its dynamics is not controlled by the plume, but rather by the normal asthenosphere.

**Effect of the plume radius(r=200 km, dM=0.05)** : A larger plume radius enhances all the dynamic effects previously described, and promotes the generation of large-scale delamination events, which stretch and deform the newly formed crust (see Fig. 3.7a and Fig. B7a(1.789-2.489 Myrs)). Initially the propagation of the instabilities and the related production of new felsic crust expands radially and, the system has a tendency to generate coherent delamination along the lower-upper crust interface. The delamination generates local positive topographic anomalies with arcuate shapes, which collapse after the detachment of dense crust from mature and more felsic new crust. After the complete removal of the lithospheric mantle, new mafic crust production slowly shuts down, and high residual mantle start convecting beneath the crust. The production of new crust is associated with local upwelling of asthenosphere that penetrate the proto-lithosphere.

The final state features a complex topography, recording multiple tectonic events of the terrains (see 3.7b), with topographic anomalies associated with the delamination event whereas the felsic anomalies have a random pattern.

### 3.3.4 Effects of $T_P$ and initial lithospheric Thickness

$T_P$ controls the timescales of the processes, and the amount of generated mafic crust produced. Increasing $T_P$ (=1550 °C) decreases the ascent velocity of the plume, as its density contrast with asthenospheric mantle is reduced ($T_P$ of the plume is always 1600 °C). Once it reaches the lithosphere, it produces large volumes of new mafic crust, which drips off resulting in lithospheric recycling in less than 1 Myrs. The mantle becomes totally depleted and perfectly mixed with all recycled mafic and felsic crust (see Fig. 3.8b). Initially, the lithospheric instabilities propagate radially from the center of the numerical domain, then during the catastrophic removal

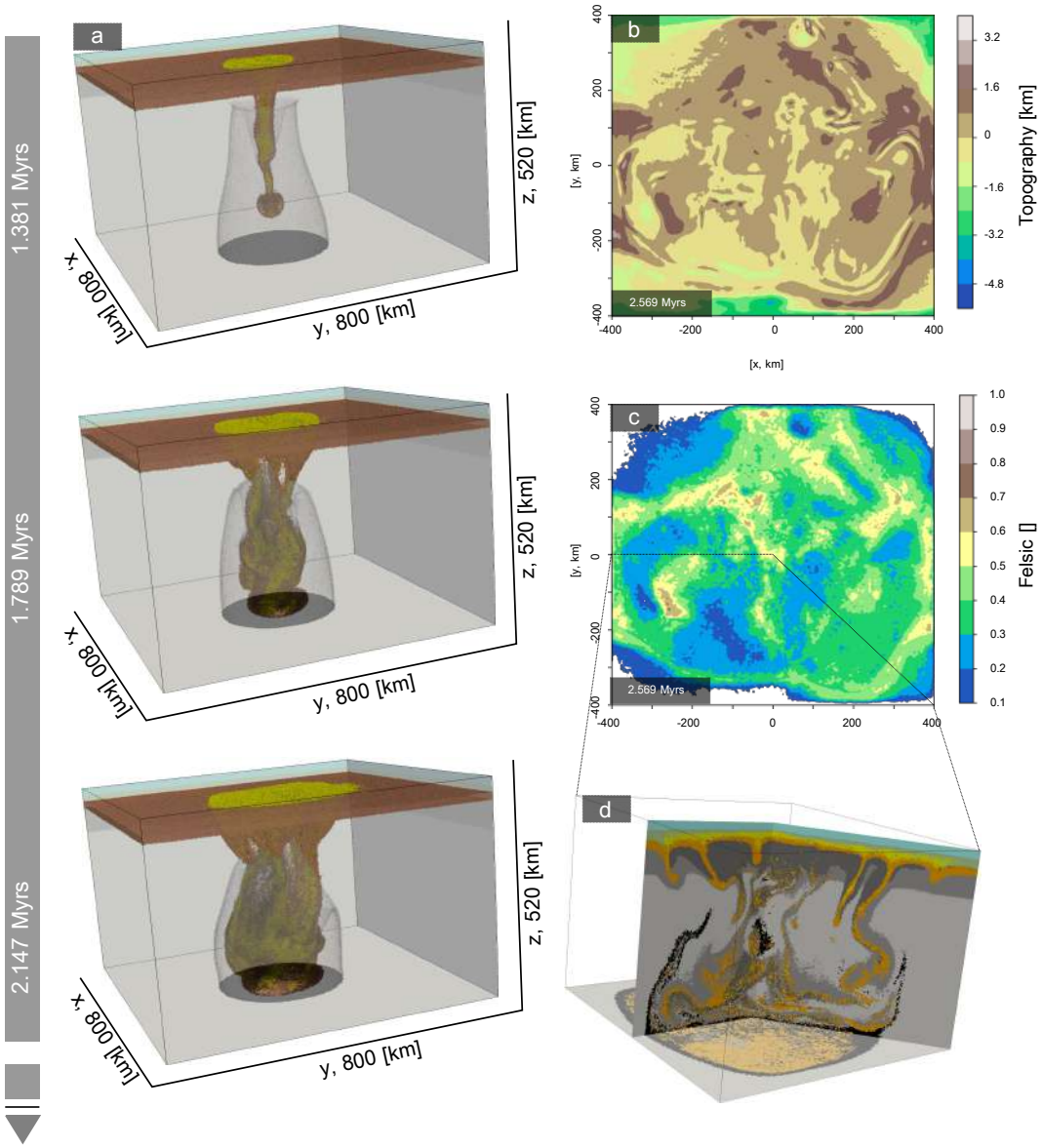


Figure 3.7: **Effect of large plume radius, plume radius = 200 km, dM = 0.05, $T_P$=1500 °C, $T^{Pl}$=1600 °C a)**: Compositional field evolution (from top to bottom); **b):** Contour of topography at 2.569 Myrs; **c):** Normalized amount of Felsic crust along $z$ direction; **d):** Section along the profile drawn in c).

of the lithospheric mantle and lower crust, the propagation follows intermittently different directions. During the catastrophic removal of the lithospheric mantle the initially produced felsic crust rifts, and is transported away from the original production site.

At low $T_P$ ($T_P$=1350-1400 °C) the propagation of the impact structure of the plume, mafic crust recycling and felsic melt generation are occurring thanks to small-scale peeling-off events (e.g. at $T^{Pl}$ 1400 °C see Fig. 3.8a and Fig. B8). The surface velocities are low compared to the experiments with higher $T_P$. Due to lower mafic melt production per unit of time, the amount of

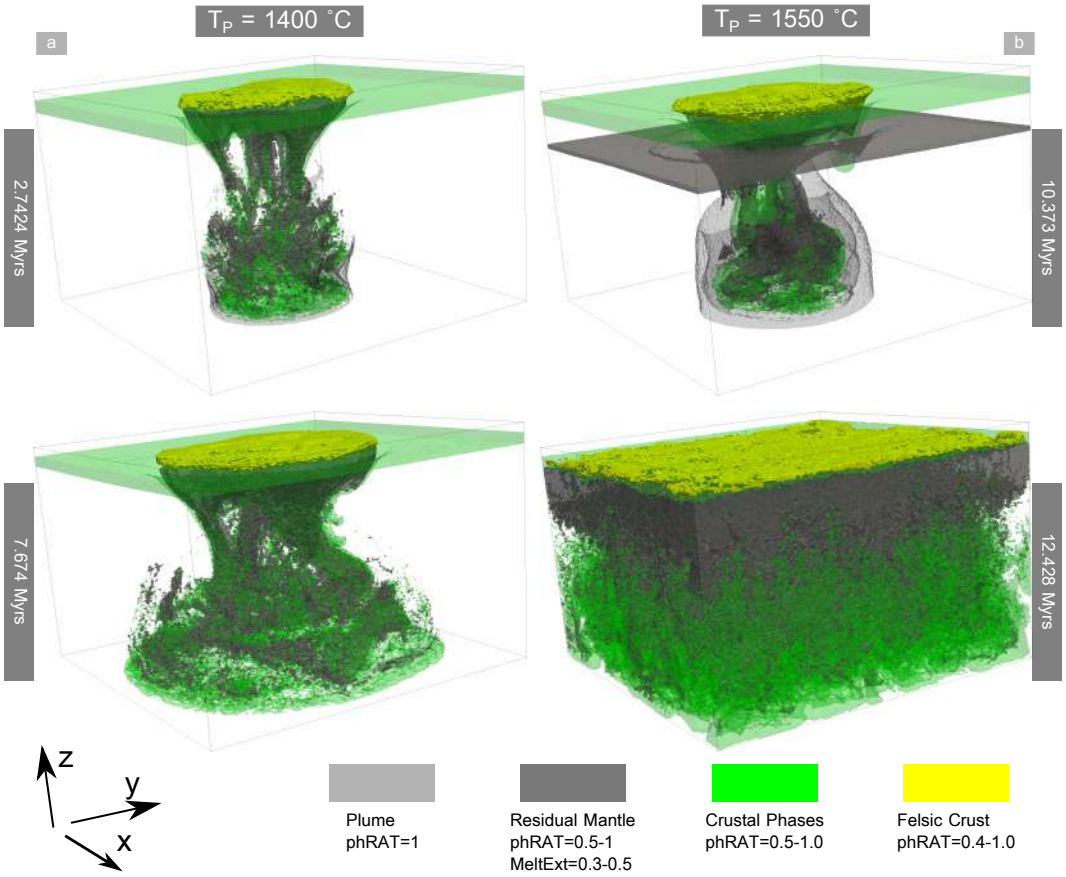


Figure 3.8: **Plume radius = 200 km, dM = 0.05, $T^{Pl}$=1600 °C**. This figure represents two experiments featuring the same conditions of the one showed in 3.7 but with different upper mantle $T_P$. The left column represents the lowest $T_P$ tested (1400 °C), while the right column represents the highest $T_P$ tested (1550 °C). The phase field is simplified to visualize only the crustal phases (green with transparency), residual mantle (dark gray), the actual felsic crust stored in the crust (yellow) and the initially prescribed plume (black color with transparency). Crustal phases represents all mafic and felsic crust phases, without being necessarily stored in the crust, while the felsic crust plotted represents the TTGs effectively stored in the actual crust (i.e. the portion of the domain between the Moho and the topography). The plot is constructed using the interval of *PhRAT* values between a minimum value and 1, except for the residual mantle phases, that must have at least 30% total melt extracted to be considered residual.

felsic crust, F, is higher than in the reference scenarios. The plume impact structure propagates radially, and the highest crustal thickness and topography are located in its rim; in its innermost part crust recycling and production develop as consequence of *RTIs* (see Fig B8). This dichotomy is reflected in the strain rate: in the innermost part of the plume structure, the strain rate distribution is spatially variable, following the occurrence of both the small asthenospheric upwelling that penetrates the proto-lithospheric mantle and drips; while in the outermost part of the impact structure, the strain rate is homogeneously distributed and associated with the decoupling surface between upper and lower crust (see Fig. B8 and Fig. B9). Decreasing the

initial lithospheric thickness has the same effect as in 2D cases. However, the 3D effects of the plume results in a more efficient propagation of the plume-impact structure. We performed low *Tkl* experiments using initial $T_P$ spanning from 1350 to 1400 °C but we find no difference between with the experiment featuring the same $T_P$ but higher initial *Tkl*.

All experiments featuring lower $T_P$ have a common feature: the accumulation of felsic crust in the outermost part of the plume-impact structure. Most of the felsic crust produced is transported toward the rim, generating a narrow circular belt with extremely felsic enriched crust (F≥ 70 %). These felsic anomalies have higher topography respect to the inner part of the impact structure. Furthermore, the area affected by the peeling-off of the lower crust forms a small basin that propagates outwards.

### 3.3.5 Felsic Crust production and P-T conditions

The pressure and temperature at which felsic crust is produced in these 3D simulations are different from those in the 2D experiments. We carried out several experiments spanning from the melt extraction properties of mafic crust to the distribution of intrusions within the crust. The results show that the felsic crust production pressures are generally low to intermediate (circa 0.4-1.0 GPa). The oceanic plateau generated during the 3D experiments has a short life-time, and is unable to sustain the amount of dense mafic crust added to the crust. This greatly limits the thickness of the plateau which is the main factor that controls the pressure of felsic melts generation (see Fig. B10). The volume of TTGs-like melts is low, and associated with plume-related magmatism. Furthermore, at high $T_P$ (1550 °C) the small quantity of TTGs-like crust produced are readily recycled into the mantle; the relative amount of felsic crust, F, increases and then decreases during the plume related magmatism (see Fig. 3.9). At lower $T_P$ the amount of felsic crust recycling is limited and the total felsic crust produced remains in the crust.

The style of magma production resembles that observed in the 2D experiments. High $T_P$ is associated with a more efficient removal of the lithosphere, which promotes mafic and felsic melts production (see Fig. 3.9). At lower $T_P$, on the other hand, the magma production rate is lower, and the amount of felsic crust produced is less than $5 \times 10^6$ km$^3$ respect the high $T_P$ cases in which the total amount of felsic crust is 2-3 times higher (see Fig. 3.9). Importantly the initially prescribed plume is a transient feature of the model and its role is to destabilize the lithosphere. In both 2D and 3D experiments the majority of newly generated felsic and mafic crust forms from normal asthenosphere mantle. The low-pressure condition of melt generation is due to efficient transmission of heat from the intrusions and removal of the dense root of the plateau. The striking difference between 2D and 3D experiments is related to the survival of

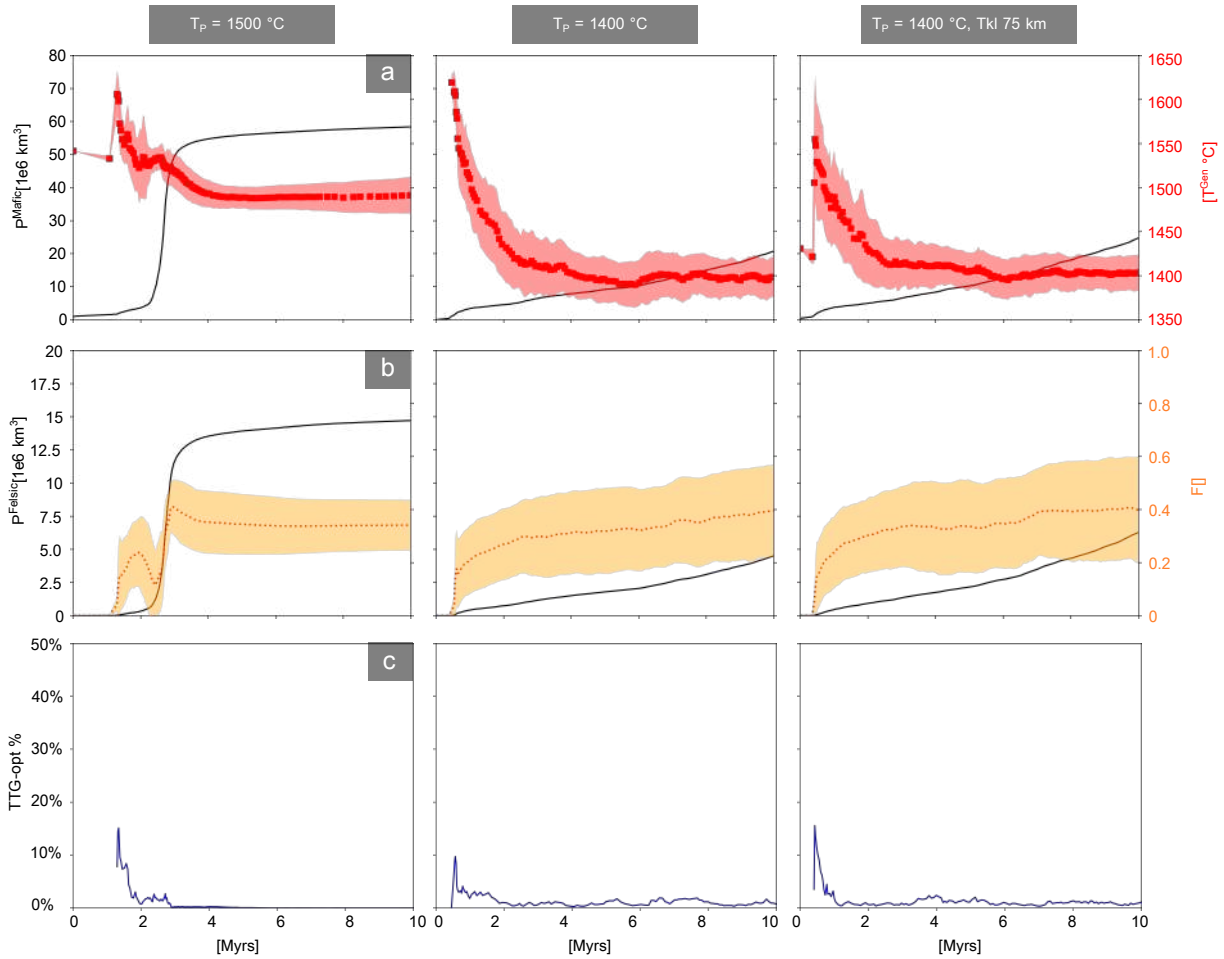


Figure 3.9: **Plume radius = 200 km, dM = 0.05, $T^{Pl}$=1600 °C**. all the experiments features the same initial input parameter except for the initial $T_P$ or the initial lithospheric thickness. **a)**: Cumulative mafic melt production (black thick line) and average mafic melt temperature ( the colored area represents the standard deviation of the condition, while the square marker represents the average temperature of extraction) against time; **b)**: Cumulative felsic crust production (black thick line) and relative Felsic amount, F (the shaded orange area represents the maximum and minimum F, while the dashed orange line represents the average F) against time; **c):** TTGs percentages against time

the oceanic plateau. In 2D, the oceanic plateau lasts long enough to allow the production of high pressure felsic crust ($P \geq 1$GPa), while in the 3D experiments it is a transient feature that last as long as the plume buoyancy flux.

## 3.4 Discussion

**Structural evolution** The structural evolution of all numerical experiments is governed by gravitational instabilities, such as delamination and RTIs. After the first drip, the initial

plume impact structure starts expanding via delamination of the lower crust. At the rim, the delamination of the lower crust generates a homogeneous deformed area. In the inner part, however, deformation is chaotic and associated with newly generated mafic crust, *RTI* instabilities or by incipient partial convective overturn, producing dome and keel geometries, a typical feature of many Archean cratons (Collins et al., 1998; Van Kranendonk, 2010; Bédard et al., 2003; Bouhallier et al., 1995). Felsic crust tends to accumulate near the rim of plume-related structures, but at high $T_P$ (≥ 1500°C) they are easily rafted apart, yielding homogeneous felsic component distribution throughout the domain. At low $T_P$ (≥ 1400°C) plateau expansion is slow (0-4 cm/yrs) and occurs radially from the plume's axis, producing strong felsic crust anomalies at the rim generating a small continuous continental crust terrain that extends for 100 km, with high topographies and bounded by retro and fore basins. These features resemble plate-like boundary sequences that are sometimes observed in Archean terrains (Nutman et al., 2013; Cutts et al., 2014; Van Kranendonk, 2010). At higher $T_P$ the generation of coherent felsic domains is more difficult due to the high velocities of the processes. The final stage of the numerical experiments features a layered crust in which most of the newly generated felsic crust is stored at high depth, while the upper crust consist of newly mafic crust, consistent with Archean upper crust compositions (Condie, 1993; Kamber, 2010, 2015; Nicoli and Dyck, 2018).

**Mafic crust production** Our reference scenarios consider a hemispheric plume at the bottom of the numerical domain with $T_P$ of 1600 $^{\circ}C$. The maximum amount of new crust generated from the plume is 40-50% of the total initially prescribed plume's volume (~ 6-8 $10^6$ $km^3$), however, most of experiments produces 2-10 times more mafic crust than this via additional sources. Moreover, the plume is destroyed by the gravitational instabilities that promote its mixing with the normal asthenosphere. Such behavior is reflected in the temperature at which the mafic melts are generated, which exponentially decay with time from the plume-related temperature towards 1400 °C. As a consequence, the plume is associated with a more vigorous recycling of the old lithosphere (lithospheric mantle and initially prescribed mafic crust), and is associated with a local-scale cooling, which would reflect on the chemical composition of the mafic products. At high $T_P$ the production of new mafic crust is fast and the growth phase lasts for less than 1 Myrs, while at lower $T_P$ (i.e. <1400 °C) the process takes longer and in two distinct pulses, one associated with plume-related magmatism and one related to peeling off events. Our 3D numerical experiments are too memory-intensive to dynamically predict the chemical composition of the basalts generated at different pressure-temperature conditions, although general ranges in these values gives some insights in the variability of their chemical composition. Most of the new mafic melts stem from heterogeneous mantle and

they over-represent the initial asthenosphere $T_P$.

Our numerical experiments predict the generation of several distinct units of mafic crust featuring different $T^{Gen}$, which could be translated into different rocks compositions. Archean mafic crust is composed of several volcanic cycles, in which mafic crust has a different chemical composition (Van Kranendonk et al., 2015; Anhaeusser, 2014; Condie, 1981), despite having formed in similar geodynamic settings (i.e. intraplate vs. arc). Our numerical experiments partially reproduce this variability, assuming that the temperature of extraction is the primary control on the effusive products chemical composition, and furthermore, predicts that most of the newly generated mafic crust is representative of the actual asthenospheric $T_P$, while plume-related products are less common. Secular cooling of the Earth's mantle is believed to be reflected by the changing chemical composition of basalts preserved in continental terranes worldwide (Herzberg et al., 2010; Ganne and Feng, 2017). However to have a glimpse on the chemical variation, it is necessary to analyze mafic crust that is produced in geodynamic setting that samples primitive melts (Palin and Dyck, 2018; Herzberg et al., 2010). Since no complete ophiolite sequences of Archean age have been proven (Palin and Dyck, 2018; Bickle et al., 1994; Hamilton, 2007; Kamber, 2015) it is necessary to understand if given rocks in a typical greenstone belt are related to plume volcanism or could potentially store information of the background asthenospheric mantle temperature. Our numerical experiments shows that plume-related enviroments as a consequence of the gravitational instabilities could potentially feature high mafic crust compositional variability and that most of the newly generated crust represents the thermal condition of the mantle.

**Felsic crust production** In our simulations, felsic crust is produced contemporaneously with the new mafic crust. The production rates are similar, and in general the amount of newly felsic material is ~0.1-0.25 of the total mafic crust produced. Portions of the generated felsic crust are recycled into the mantle as a function of the initial $T_P$. Our results confirm that intrusion and thus juvenile mafic crust production is associated with felsic crust production and that the heating effect of intrusions is fundamental for the formation of felsic crust (Jain, 2018; Rozel et al., 2017; Sizova et al., 2015; Piccolo et al., 2019).

The 2D and 3D experiments shown here record remarkable differences in the P-T conditions at which felsic TTG-like melts are produced. Such differences are consequence of the 3D effects on the stability of the oceanic plateau. Most of experiments (both 2D-3D) have a general tendency to produce low-pressure ($\leq$ 1 GPa) felsic crust. 2D experiments yields maximum 30-40% of common TTGs generated (using the optimum P-T reported by Palin et al. (2016)), with a decrease in the relative amount of TTGs produced with time (with a remarkable exception

of low $T_P$ experiments). 3D experiments, on the other hand, feature an initial spike of relative high-pressure (> 1 GPa) felsic crust followed by a constant decreases of the pressure at which the new felsic crust is produced, which is reflected in the average crustal thickness with time (~ 50 – 25 km). These estimates and distribution of extraction pressure are affected by the extraction parameters (such as the depth of intrusions, the relative intrusion thickness layer). However, it seems that the TTGs produced are not extracted in the optimum field predicted by thermodynamical model (Palin et al., 2016), which means that might have a different composition respect the average natural TTGs one. Nonetheless, our P-T conditions are variably featuring both low-high pressures, although the high-pressure ones are under-represented, which is consistent with Moyen (2011)' s observations that predict Archean felsic melts were produced at variable depth. Plume-related geodynamic settings are associated with a thinning of the lithosphere, and with a general cooling of the mantle, which is reflected in the formation temperature of the mafic crust and in the crustal equilibrium thickness. The bulk of the geological data suggests an autochtonous growth of the felsic crust, and a close association with plume-related geodynamic setting (Bédard et al., 2003; Bédard, 2018; Kamber, 2015; Van Kranendonk et al., 2015; Smithies et al., 2009). However, according to our results, the processes yield a more granitic crust (cf. Palin et al. (2016)). Previous geodynamical modeling addressing similar issues were carried out in 2D (Piccolo et al., 2019; Sizova et al., 2015; Rozel et al., 2017; Johnson et al., 2013) or in 3D without extracting the felsic crust Fischer and Gerya (2016a). Previous 2D experiments produced similar TTGs proportions than natural examples (Piccolo et al., 2019; Rozel et al., 2017; Sizova et al., 2015),whereas in contrast 3D experiments shows a more complex scenario. Fischer and Gerya (2016a) estimated the amount of felsic melts produced in their model and they noted that during the initial stage of the simulations most of the felsic melts produced occurs at low pressures (P<1 GPa). However, they showed that after the first removal events, the melt were produced at progressively higher depth, as a consequence of a slow growth phases (Fischer, 2016; Fischer and Gerya, 2016a). In our baseline scenario, the mantle plume ascends through the asthenosphere at a high velocity, and induces a peak in mafic crust growth. Hot intrusions start penetrating most of the lower-middle crust, producing dense and extremely low viscous rocks. These conditions promote the *RTIs* and therefore limits the mechanical stability of the crust promoting efficient removal and thinning of the crust. In order to understand the suitability of the plume-related setting for the TTGs production, it is necessary to estimate the amount of hot material coming from the lower mantle and compare it with the timescales at which RTIs instabilities are developing. Alternatively, the most suitable settings to produce TTG like melts require more strong intraplate deformation, as has been shown in Piccolo et al. (2019) and Sizova et al. (2015). Another solution to this problem is to

consider the mantle is weakly hydrated, and allowing the intrusions to be a source of TTGs like melts, as it has been suggested in Van Kranendonk (2010); Van Kranendonk et al. (2015); Macpherson et al. (2006).

**Limitations** Our numerical experiments featured complex behavior as a function of the initial background $T_P$, plume radius, and the initial lithospheric thickness, yet they are nevertheless limited. The first limitation is related to the plume itself: initially the plume is modeled as a hemisphere situated at the bottom of the domain, and represents a solitary temporary thermal anomaly (or thermals following the nomenclature given in Jellinek et al. (2002)). Its initial radius and temperature control the plume ascent velocity. Its volume is correlated to the potential duration of plume-lid interactions. Thus, the effect of long-lasting upwellings that are believed to have been frequent during Archean (Van Kranendonk, 2010; Bédard, 2018) are not considered. Moreover, we also disregard the production of komatiitic lava, as they require a higher potential temperature (Schmeling and Arndt, 2017; Herzberg et al., 2010) compared to the ones that we prescribed.

An additional limitation concerns the petrological model that does not incorporate all potentially important metamorphic processes (i.e. dehydration reactions, fluid migration (Arndt, 2013)), which are important for the long-term compositional evolution of the Archean crust. The numerical experiment represents the most favorable scenario to produce felsic crust. We assume that felsic crust is represented by a single type, neglecting the chemical differences that could emerge from P-T melting conditions. We do not consider latent heat of melting reactions, which modulates both the production of melt and the source cooling rate. In particular, this effect could increase the differences between experiments featuring different $T_P$. In spite of these limitations, our numerical experiments are consistent with previous attempts to model Archean geodynamics (Fischer and Gerya, 2016a; Sizova et al., 2015; Gerya et al., 2015; Piccolo et al., 2019), but there are several limits on the ability of building a thickened mafic crust. In any case, felsic crust extraction produces dynamics that were not observed in previous 3D experiments and allowed to model scenarios that were not explored before.

## 3.5 Conclusion

Our 2D-3D numerical experiments predict several fundamental differences of the plume-lid interaction as a function of the initial thickness and initial $T_P$. At high $T_P$ most of the deformation and production of new mafic crust is mediated by the asthenospheric mantle flow resulting from gravitational instabilities ($T_P \geq 1500^{\circ}$C). At low $T_P$ ($T_P \leq 1450^{\circ}$C) most of the newly generated

crust is closely related to plume activity. This variability of temperature at which basalt is generated indicates that even plume-related environments can store important information regarding the mantle potential temperature. Our numerical experiments predicts that significant amount of new felsic crust are produced in such environments, even tough, the P-T conditions do not match the most suitable ones to produce high amounts of TTGs-like melts, and further investigation are required. Our results, thus, provide key insights on the production of felsic crust on the early Earth.

# REFERENCES


Anhaeusser, C.R., 2014. Archaean greenstone belts and associated granitic rocks–a review. Journal of African Earth Sciences 100, 684–732.

Annen, C., 2009. From plutons to magma chambers: Thermal constraints on the accumulation of eruptible silicic magma in the upper crust. Earth and Planetary Science Letters 284, 409–416.

Arndt, N.T., 2013. The formation and evolution of the continental crust. Geochemical Perspectives 2, 405.

Aulbach, S., Arndt, N.T., 2019. Eclogites as palaeodynamic archives: Evidence for warm (not hot) and depleted (but heterogeneous) archaean ambient mantle. Earth and Planetary Science Letters 505, 162–172.

Baes, M., Gerya, T., Sobolev, S.V., 2016. 3-d thermo-mechanical modeling of plume-induced subduction initiation. Earth and Planetary Science Letters 453, 193–203.

Bédard, J.H., 2006. A catalytic delamination-driven model for coupled genesis of Archaean crust and sub-continental lithospheric mantle. Geochimica et Cosmochimica Acta 70, 1188–1214.

Bédard, J.H., 2018. Stagnant lids and mantle overturns: implications for archaean tectonics, magmagenesis, crustal growth, mantle evolution, and the start of plate tectonics. Geoscience Frontiers 9, 19–49.

Bédard, J.H., Brouillette, P., Madore, L., Berclaz, A., 2003. Archaean cratonization and deformation in the northern superior province, canada: an evaluation of plate tectonic versus vertical tectonic models. Precambrian Research 127, 61–87.

Bédard, J.H., Harris, L.B., Thurston, P.C., 2013. The hunting of the snArc. Precambrian Research 229, 20–48. URL: http://dx.doi.org/10.1016/j.precamres.2012.04.001, doi:10.1016/j.precamres.2012.04.001.

Bickle, M.J., Nisbet, E.G., Martin, A., 1994. Archean greenstone belts are not oceanic crust. The Journal of Geology 102, 121–137.

Bouhallier, H., Chardon, D., Choukroune, P., 1995. Strain patterns in Archaean dome-and-basin structures: The Dharwar craton (Karnataka, South India). Earth and Planetary Science Letters 135, 57–75. doi:https://doi.org/10.1016/0012-821X(95)00144-2.

Burov, E., Cloetingh, S., 2010. Plume-like upper mantle instabilities drive subduction initiation. Geophysical research letters 37.

Cashman, K.V., Sparks, R.S.J., Blundy, J.D., 2017. Vertically extensive and unstable magmatic systems: a unified view of igneous processes. Science 355, eaag3055.

Chardon, D., Choukroune, P., Jayananda, M., 1996. Strain patterns, décollement and incipient sagducted greenstone terrains in the archaean dharwar craton (south india). Journal of Structural Geology 18, 991–1004.

Chardon, D., Choukroune, P., Jayananda, M., 1998. Sinking of the dharwar basin (south india): implications for archaean tectonics. Precambrian Research 91, 15–39.

Choukroune, P., Bouhallier, H., Arndt, N., 1995. Soft lithosphere during periods of archaean crustal growth or crustal reworking. Geological Society, London, Special Publications 95, 67–86.

Collins, W., Kranendonk, V., MJ, Teyssier, C., 1998. Partial convective overturn of archaean crust in the east pilbara craton, western australia: driving mechanisms and tectonic implications. Journal of Structural Geology 20, 1405–1424.

Condie, K.C., 1981. Archean greenstone belts. volume 3. Elsevier.

Condie, K.C., 1993. Chemical composition and evolution of the upper continental crust: contrasting results from surface samples and shales. Chemical geology 104, 1–37.

Condie, K.C., 2001. Mantle plumes and their record in Earth history. Cambridge University Press.

Condie, K.C., Aster, R.C., van Hunen, J., 2016. A great thermal divergence in the mantle beginning 2.5 ga: geochemical constraints from greenstone basalts and komatiites. Geoscience Frontiers 7, 543–553.

Condie, K.C., Puetz, S.J., Davaille, A., 2018. Episodic crustal production before 2.7 ga. Precambrian Research 312, 16–22.

Connolly, J., 2009. The geodynamic equation of state: what and how. Geochemistry, Geophysics, Geosystems 10.

Cox, K.G., 1980. A Model for Flood Basalt Vulcanism. Journal of Petrology 21, 629–650. URL: http://dx.doi.org/10.1093/petrology/21.4.629.

Crisp, J.A., 1984. Rates of magma emplacement and volcanic output. Journal of Volcanology and Geothermal Research 20, 177–211.

Cutts, K.A., Stevens, G., Hoffmann, J.E., Buick, I.S., Frei, D., Münker, C., 2014. Paleo-to mesoarchean polymetamorphism in the barberton granite-greenstone belt, south africa: Constraints from u-pb monazite and lu-hf garnet geochronology on the tectonic processes that shaped the belt. Bulletin 126, 251–270.

Dhuime, B., Hawkesworth, C.J., Cawood, P.A., Storey, C.D., 2012. A change in the geodynamics of continental growth 3 billion years ago. Science 335, 1334–1336.

Drucker, D.C., Prager, W., 1952. Soil mechanics and plastic analysis or limit design. Quarterly of applied mathematics 10, 157–165.

Fischer, R., 2016. From early Earth plume-lid tectonics to present-day plate tectonics: A high-resolution 3D numerical modelling approach. Ph.D. thesis. ETH Zurich.

Fischer, R., Gerya, T., 2016a. Early earth plume-lid tectonics: A high-resolution 3d numerical modelling approach. Journal of Geodynamics 100, 198–214.

Fischer, R., Gerya, T., 2016b. Regimes of subduction and lithospheric dynamics in the precambrian: 3d thermomechanical modelling. Gondwana Research 37, 53–70.

François, C., Philippot, P., Rey, P., Rubatto, D., 2014. Burial and exhumation during archean sagduction in the east pilbara granite-greenstone terrane. Earth and Planetary Science Letters 396, 235–251.

Ganne, J., Feng, X., 2017. Primary magmas and mantle temperatures through time. Geochemistry, Geophysics, Geosystems 18, 872–888. URL: https://doi.org/10.1002/2016GC006787, doi:10.1002/2016GC006787.

Gerya, T.V., Stern, R.J., Baes, M., Sobolev, S.V., Whattam, S.A., 2015. Plate tectonics on the Earth triggered by plume-induced subduction initiation. Nature 527, 221–225.

Gray, R., Pysklywec, R.N., 2010. Geodynamic models of Archean continental collision and the formation of mantle lithosphere keels. Geophysical Research Letters 37, 2–6. doi:10.1029/2010GL043965.

Green, E.C.R., White, R.W., Diener, J.F.A., Powell, R., Holland, T.J.B., Palin, R.M., 2016. Activity–composition relations for the calculation of partial melting equilibria in metabasic rocks. Journal of Metamorphic Geology 34, 845–869.

Griffin, W., O'Reilly, S., Abe, N., Aulbach, S., Davies, R., Pearson, N., Doyle, B., Kivi, K., 2003. The origin and evolution of archean lithospheric mantle. Precambrian Research 127, 19–41.

Hamilton, W.B., 2007. Earth's first two billion years—the era of internally mobile crust. Geological Society of America Memoirs 200, 233–296.

Hawkesworth, C.J., Dhuime, B., Pietranik, A.B., Cawood, P.A., Kemp, A.I.S., Storey, C.D., 2010. The generation and evolution of the continental crust. Journal of the Geological Society 167, 229–248.

Herzberg, C.T., Condie, K.C., Korenaga, J., 2010. Thermal history of the Earth and its petrological expression. Earth and Planetary Science Letters 292, 79–88. URL: http://dx.doi.org/10.1016/j.epsl.2010.01.022, doi:10.1016/j.epsl.2010.01.022.

Herzberg, C.T., Rudnick, R.L., 2012. Formation of cratonic lithosphere: an integrated thermal and petrological model. Lithos 149, 4–15.

Hirth, G., Kohlstedt, D., 2004. Rheology of the upper mantle and the mantle wedge: A view from the experimentalists. Inside the subduction Factory 138, 83–105.

Holland, T.J.B., Powell, R., 2003. Activity–composition relations for phases in petrological calculations: an asymmetric multicomponent formulation. Contributions to Mineralogy and Petrology 145, 492–501.

Holland, T.J.B., Powell, R., 2011. An improved and extended internally consistent thermodynamic dataset for phases of petrological interest, involving a new equation of state for solids. Journal of Metamorphic Geology 29, 333–383.

Jahn, B.M., Glikson, A.Y., Peucat, J.J., Hickman, A.H., 1981. Ree geochemistry and isotopic data of archean silicic volcanics and granitoids from the pilbara block, western australia: implications for the early crustal evolution. Geochimica et Cosmochimica Acta 45, 1633–1652.

Jain, C., 2018. Self-consistent generation of continents and their influence on global mantle dynamics. Ph.D. thesis. ETH Zurich.

Jellinek, A.M., Lenardic, A., Manga, M., 2002. The influence of interior mantle temperature on the structure of plumes: Heads for venus, tails for the earth. Geophysical research letters 29, 27–1.

Jennings, E.S., Holland, T.J., 2015. A simple thermodynamic model for melting of peridotite in the system ncfmasocr. Journal of Petrology 56, 869–892.

Johnson, T., Kirkland, C., Gardiner, N., Brown, M., Smithies, R., Santosh, M., 2019. Secular change in ttg compositions: Implications for the evolution of archaean geodynamics. Earth and Planetary Science Letters 505, 65–75.

Johnson, T.E., Brown, M., Gardiner, N.J., Kirkland, C.L., Smithies, R.H., 2017. Earth's first stable continents did not form by subduction. Nature 543, 239–242.

Johnson, T.E., Brown, M., Kaus, B.J.P., VanTongeren, J.A., 2013. Delamination and recycling of Archaean crust caused by gravitational instabilities. Nature Geoscience 7, 47–52. URL: http://www.nature.com/doifinder/10.1038/ngeo2019, doi:10.1038/ngeo2019.

Kamber, B.S., 2010. Archean mafic–ultramafic volcanic landmasses and their effect on ocean–atmosphere chemistry. Chemical Geology 274, 19–28.

Kamber, B.S., 2015. The evolving nature of terrestrial crust from the hadean, through the archaean, into the proterozoic. Precambrian Research 258, 48–82.

Kump, L.R., Barley, M.E., 2007. Increased subaerial volcanism and the rise of atmospheric oxygen 2.5 billion years ago. Nature 448, 1033–1036. URL: http://dx.doi.org/10.1038/nature06058http://www.nature.com/nature/journal/v448/n7157/suppinfo/nature06058{_}S1.html.

Macpherson, C.G., Dreher, S.T., Thirlwall, M.F., 2006. Adakites without slab melting: high pressure differentiation of island arc magma, mindanao, the philippines. Earth and Planetary Science Letters 243, 581–593.

Martin, H., Moyen, J.F., Guitreau, M., Blichert-Toft, J., Le Pennec, J. L, 2014. Why Archaean TTG cannot be generated by MORB melting in subduction zones. Lithos 198-199, 1–13. URL: http://dx.doi.org/10.1016/j.lithos.2014.02.017, doi:10.1016/j.lithos.2014.02.017.

McDonough, W.F., Sun, S.S., 1995. The composition of the earth. Chemical geology 120, 223–253.

Moyen, J.F., 2011. The composite Archaean grey gneisses: Petrological significance, and evidence for a non-unique tectonic setting for Archaean crustal growth. Lithos 123, 21–36. doi:https://doi.org/10.1016/j.lithos.2010.09.015.

Moyen, J.F., Stevens, G., 2006. Experimental constraints on TTG petrogenesis: implications for Archean geodynamics. Archean geodynamics and environments , 149–175.

Moyen, J.F., Van Hunen, J., 2012. Short-term episodicity of Archaean plate tectonics. Geology 40, 451–454.

Nicoli, G., Dyck, B., 2018. Exploring the metamorphic consequences of secular change in the siliciclastic compositions of continental margins. Geoscience Frontiers .

Nutman, A.P., Bennett, V.C., Friend, C.R., Hidaka, H., Yi, K., Lee, S.R., Kamiichi, T., 2013. The itsaq gneiss complex of greenland: Episodic 3900 to 3660 ma juvenile crust formation and recycling in the 3660 to 3600 ma isukasian orogeny. American Journal of Science 313, 877–911.

O'Neill, C., Lenardic, A., Condie, K.C., 2015. Earth's punctuated tectonic evolution: cause and effect. Geological Society, London, Special Publications 389, 17–40.

Palin, R.M., Dyck, B., 2018. Metamorphic consequences of secular changes in oceanic crust composition and implications for uniformitarianism in the geological record. Geoscience Frontiers 9, 1009–1019.

Palin, R.M., White, R.W., Green, E.C., 2016. Partial melting of metabasic rocks and the generation of tonalitic–trondhjemitic–granodioritic (ttg) crust in the archaean: Constraints from phase equilibrium modelling. Precambrian Research 287, 73–90.

Piccolo, A., Palin, R.M., Kaus, B.J., White, R.W., 2019. Generation of earth's early continents from a relatively cool archean mantle. Geochemistry, Geophysics, Geosystems 0.

Powell, R., Holland, T., 1988. An internally consistent dataset with uncertainties and correlations: 3. applications to geobarometry, worked examples and a computer program. Journal of metamorphic Geology 6, 173–204.

Ranalli, G., 1995. Rheology of the earth, 413 pp.

Rapp, R.P., Shimizu, N., Norman, M.D., 2003. Growth of early continental crust by partial melting of eclogite. Nature 425, 605–609. URL: http://dx.doi.org/10.1038/nature02031http://10.0.4.14/nature02031.

Reimink, J.R., Chacko, T., Stern, R.A., Heaman, L.M., 2014. Earth's earliest evolved crust generated in an iceland-like setting. Nature Geoscience 7, 529.

Reuber, G.S., Kaus, B.J.P., Popov, A.A., Baumann, T.S., 2018. Unraveling the physics of the yellowstone magmatic system using geodynamic simulations. Frontiers in Earth Science 6, 117.

Rozel, A.B., Golabek, G.J., Jain, C., Tackley, P.J., Gerya, T.V., 2017. Continental crust formation on early Earth controlled by intrusive magmatism. Nature 545, 47–52.

Schmeling, H., Arndt, N., 2017. Modelling komatiitic melt accumulation and segregation in the transition zone. Earth and Planetary Science Letters 472, 95–106.

Sizova, E., Gerya, T., Brown, M., 2014. Contrasting styles of phanerozoic and precambrian continental collision. Gondwana Research 25, 522–545.

Sizova, E., Gerya, T.V., Stüwe, K., Brown, M., 2015. Generation of felsic crust in the Archean: A geodynamic modeling perspective. Precambrian Research 271, 198–224. URL: http://dx.doi.org/10.1016/j.precamres.2015.10.005, doi:10.1016/j.precamres.2015.10.005.

Smithies, R.H., Champion, D.C., Van Kranendonk, M.J., 2009. Formation of Paleoarchean continental crust through infracrustal melting of enriched basalt. Earth and Planetary Science Letters 281, 298–306.

Ueda, K., Gerya, T., Sobolev, S.V., 2008. Subduction initiation by thermal–chemical plumes: numerical studies. Physics of the Earth and Planetary Interiors 171, 296–312.

Van Hunen, J., Moyen, J.F., 2012. Archean subduction: fact or fiction? Annual Review of Earth and Planetary Sciences 40, 195–219.

Van Kranendonk, M.J., 2010. Two types of Archean continental crust: Plume and plate tectonics on early Earth. American Journal of Science 310, 1187–1209.

Van Kranendonk, M.J., Smithies, R.H., Griffin, W.L., Huston, D.L., Hickman, A.H., Champion, D.C., Anhaeusser, C.R., Pirajno, F., 2015. Making it thick: a volcanic plateau origin of palaeoarchean continental lithosphere of the pilbara and kaapvaal cratons. Geological Society, London, Special Publications 389, 83–111.

Van Thienen, P., Van den Berg, A.P., Vlaar, N.J., 2004. Production and recycling of oceanic crust in the early Earth. Tectonophysics 386, 41–65.

Wallner, H., Schmeling, H., 2016. Numerical models of mantle lithosphere weakening, erosion and delamination induced by melt extraction and emplacement. International Journal of Earth Sciences 105, 1741–1760.

White, R., Powell, R., Clarke, G.L., 2002. The interpretation of reaction textures in Fe-rich metapelitic granulites of the Musgrave Block, central Australia: constraints from mineral equilibria calculations in the system $K_2O$-FeO-MgO-$Al_2O_3$-$SiO_2$-$H_2O$-$TiO_2$-$Fe_2O_3$. Journal of metamorphic Geology 20, 41–55.

White, R.W., Powell, R., Holland, T.J.B., Johnson, T.E., Green, E.C.R., 2014. New mineral activity–composition relations for thermodynamic calculations in metapelitic systems. Journal of Metamorphic Geology 32, 261–286.

White, R.W., Powell, R., Holland, T.J.B., Worley, B.A., 2000. The effect of $TiO_2$ and $Fe_2O_3$ on metapelitic assemblages at greenschist and amphibolite facies conditions: mineral equilibria calculations in the system $K_2O$-FeO-MgO-$Al_2O_3$-$SiO_2$-$H_2O$-$TiO_2$-$Fe_2O_3$. Journal of Metamorphic Geology 18, 497–512.

White, S.M., Crisp, J.A., Spera, F.J., 2006. Long-term volumetric eruption rates and magma budgets. Geochemistry, Geophysics, Geosystems 7.

Zegers, T.E., van Keken, P.E., 2001. Middle Archean continent formation by crustal delamination. Geology 29, 1083–1086.

CHAPTER 4

# THE INSTABILITY OF THE EARLIEST LITHOSPHERE, AND ITS THERMAL EFFECTS

## 4.1 Introduction

In all experiments described in Chapter 2, mantle undergoes fast cooling after the removal of the mantle lithosphere and the gravitational unstable portions of the crust. One of the main conclusions of these simulations is that this process limits the upper mantle potential temperature ($T_P$), which could thus not have spontaneously increased to high values, and that high $T_P$ cannot last for geological meaningful time scales. However, although the results are robust and many other independent lines of research yielded similar dynamics (Sizova et al., 2015; Fischer and Gerya, 2016; Lourenço et al., 2018) there are still unsolved questions: Does this chain of events represents a viable cooling mechanism for the entire planet? And how did the occurrence of these events has shaped the early Earth thermal history?

Yet, some of the key results of our simulations, such as the magnitude of mantle cooling, or the point in time that the delamination event is triggered, are not yet fully understood. The goal of this chapter is to systematically analyze these simulations to see if it possible to derive criteria from our simulations with which we can predict many of these parameters without having to perform computationally expansive 2D simulations. In a next step, these results could be integrated upon parametrized cooling models, that are less demanding than normal geodynamic simulations and can provide useful insights at no computational cost. First, I provide a brief theoretical framework of the 1D parameterized cooling history then I describe the stages of the experiments.

**Parametrized cooling histories:** The parametrized Earth cooling histories are relying in a simple principle: the decrease of temperature with time is determined by the balance between volumetric heat production (mainly provided by radiogenic heat) and the heat flux integrated over the surface (Schubert et al., 2001):

$$M \cdot C_p \cdot \frac{D\tilde{T}}{Dt} = M \cdot \frac{H_r}{\rho_{mant}} - S \cdot q_s \tag{4.1}$$

$H_r$ is the amount of radiogenic heat produced per unit of volume, $q_s$ is the surface heat flux, $M$ is the mass of the planet and $S$ its surface, while $C_P$ and $\rho_{mant}$ are the average heat capacity and density (Schubert et al., 2001), and $\tilde{T}$ is the average mantle temperature (which is the mantle $T_p$, if the adiabatic heating is neglected). From geochemical data, radiogenic heat production can be estimated (Urey, 1956, 1955) , while surface heat flux is not known a-priori (Schubert et al., 2001; Solomatov, 1995; Grasset and Parmentier, 1998). $q_s$ can be computed using the relations between Rayleigh number and Nusselt number (Ra-Nu), that connects the convective vigor with the the energy lost by a convecting fluid, where $Ra$[1] describes the vigor of the convection, and $Nu$ measures the efficiency of conductive heat transfer with respect to the convective one:

$$Ra = \frac{\rho_{mant0} \alpha g \Delta T d^3}{\eta \kappa} \tag{4.2}$$

$$Nu = \frac{q_{conv}}{q_{cond}} \tag{4.3}$$

where $d$ is the thickness of the examined layer, $\rho_{mant0}$ is the mantle reference density, $g$ is gravitational acceleration, $\Delta T$ is temperature difference between top and bottom boundaries. $q_{conv}$ and $q_{cond}$ are the heat flux due to convection and conduction respectively. Nusselt-Rayleigh relations usually take the following form:

$$Nu = cRa^{\beta} \tag{4.4}$$

$c$ and $\beta$[2] are experimentally determined constants. However, this relation is further complicated by the mantle rheology. Temperature dependent viscosity promotes the formation of a strong and insulating carapace (lid) at the top of the convective mantle that does not participate to the convection. This convection regime is called Stagnant-Lid (Solomatov, 1995; Moresi and Solomatov, 1995; Grasset and Parmentier, 1998; Sleep, 2000) and it is characterized by a

[1] Ra has many definition as a function of the thermal boundaries condition and radiogenic heat sources. In the following paragraph I refer only to the bottom heated Rayleigh number.

[2] $\beta$ is usually equal to ~ 1/3

comparable less $q_s$ than the iso-viscous case with the same *Ra*. A convective systems may feature different regimes as a function of the internal parameter, for example, if the convective stresses are strong enough to break the lid, the convective regimes evolves towards a plate-tectonic convective style. There are several convection styles, and all of them features their own Nu-Ra relation and thus different heat flux at the surface (e.g. hot stagnant lid, cold stagnant lid, plate-tectonics, magma mush, (Sleep, 2000)). Earth may have been convecting with different regimes during its geological history as function of the $T_P$.

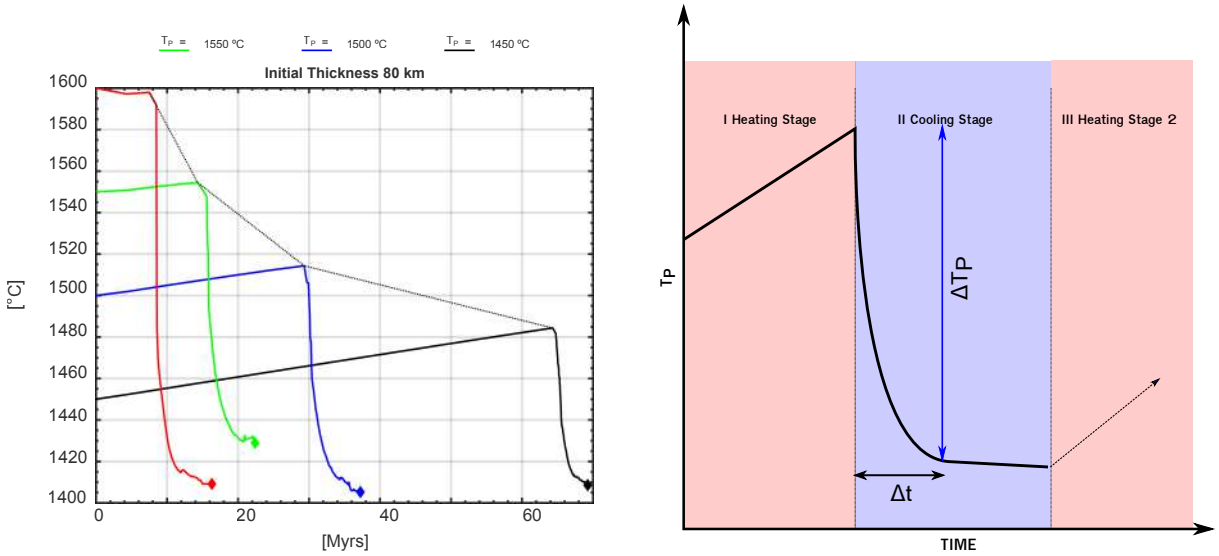


Figure 4.1: All experiments described in Chapter 2 have similar thermal histories: an initial stage of heating, (incubation stage), a cooling stage (dripping stage) and a final stage in which the mantle heats again. The left sub-plot represents the *Time-Cooling* curves of experiments featuring different $T_P$ and with same lithospheric thickness (80 km). The right subplot highlights the key features that will be analysed in this work.

Transient processes are usually neglected in 1D parametrized cooling histories. However, as demonstrated by in the experimental results of the previous chapters, the thermal effect of short lived processes, such as magmatically induced RTIs, are sufficient to reduce the $T_P$ by at least 100 °C. The average mantle temperature has a first order control on the convective regime transitions, thus understanding the relative effect of short-lived processes on long term cooling history, may provide first order insights on the geological evolution of Earth.

**Main evolutionary stage of the experiments:** All numerical experiments described in Chapter 2 have similar cooling-time histories, that can be broadly divided into three main evolutionary stages (see Fig. 4.1 )[3]:

[3]The names of the evolutionary stages are changed to highlight their $T_P$ evolution with time. The *heating stage* is the incubation stage, the *cooling stage* is the dripping stage, while the *heating stage 2* is the steady state stage.

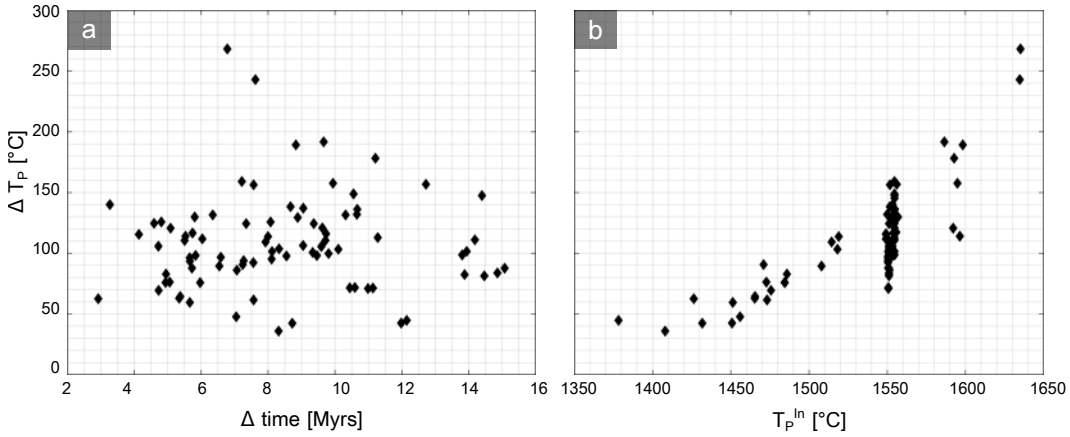


Figure 4.2: **a):** Plot of $T_P$ drop ($\Delta T_P$) vs duration of the dripping stage. Each black dot represents one experiment; **b):** $\Delta T_P$ drop against the initial $T_P^{In}$. The degree of cooling is proportional to initial prescribed mantle potential temperature ($T_P$) of the simulations.

- **Heating stage** in which the $T_P$ increases due to the radiogenic heating, and the initially prescribed crust compositionally evolve as a consequence of the magmatic processes;
- **Cooling stage** in which the unstable portion of the crust is removed through RTIs that cause a continuous production of new mafic melts, and reduces $T_P$;
- **Heating stage 2** in which the mantle is too cold to produce new melts and since the convective vigor is low, it starts to self-heat again, and develop a new conductive lithospheric mantle.

The duration of the heating stage depends on the initially prescribed $T_P$ ($T_P^{In}$) and on the prescribed volumetric radiogenic heating but the duration of the cooling stage does not systematically correlate with the $T_P^{In}$ and other input parameters. In Fig. 4.2a I plot the mantle potential temperature drop ($\Delta T_P$) against the duration of the cooling stage for each experiment, showing that the mantle cooling does not depends on the duration of the cooling stage. The temperature drop, $\Delta T_P$, instead, depends on the $T_P^{in}$ (see Fig. 4.2b), suggesting that the amount of melt that can be produced by the mantle strongly affects the dynamic of experiments. The main questions that needs to be addressed are the following: Why is the mantle heating at the initial stage? Why is the mantle cooling? And what are the conditions that trigger the RTIs and how to parametrize them?

Table 4.1: List of symbols and relative unit of measure

| Symbol | S.I. unit | Definition |
|---|---|---|
| $\frac{D\bar{T}}{Dt}$ | $^{\circ}C/s$ | Average mantle temperature changes with time |
| $\bar{T}^{del}$, $T^{eq}$, $T_P$ | $^{\circ}C$ | Average delaminated crust temperature, equilibrium temperature, potential temperature |
| $\Delta T_P$ | $^{\circ}C$ | Mantle potential temperature drop after dripping stage |
| $\delta_{ul}, \delta_{del}, \delta_{ext}, L, D$ | $km$ | Thickness unstable layer, total delaminated crust thickness, total extracted crust thickness and lithosphere thickness, total numerical box thickness |
| $\delta_{crust}, \delta_{res}$ | $km$ | Crustal thickness, mafic intrusions and dense residuum thickness |
| $\dot{\delta}_{del}, \dot{\delta}_{crust}, \dot{\delta}_{ext}$ | $km/Myrs$ | Delamination rate, crustal thickening rate and magmatic crustal addition rate |
| $\rho_{ul}, \rho_{mant}, \rho_{del}, \rho_{lit}$ | $kg/m^3$ | Average density of unstable layer, average density of mantle, average density of delaminated material and average density of the mantle lithosphere |
| $C_p$ | $J/K/kg$ | Heat capacity |
| $\eta_{ul}, \eta_{mant}, \eta_{lit}$ | $Pa \cdot s$ | Average viscosity of the unstable layer, average viscosity of the mantle and average lithospheric mantle viscosity |
| $\kappa_{ul}$,$\kappa_{mant}$ | $m^2/s$ | Average thermal diffusivity of the unstable layer and average thermal diffusivity of the mantle |
| $K$ | $W/^{\circ}C/m^2$ | Thermal conductivity |
| $q_l, q_s$ | $W/m^2$ | Average heat flux at the base of the lithosphere, average surface heat flux |
| $H_r$ | $\mu W/m^3$ | Volumetric radiogenic heat production |
| $Ra, R_b$ | – | Rayleigh number and compositional Rayleigh number |
| $R_1, R_2$ | $N$ | Resistance force |

## 4.2 Results

During the heating stage, the thickness of the crust ($\delta_{crust}$) increases as a consequence of the continuous mafic melts production (all the symbol are listed in Tab. 4.1) that are converted into new effusive hydrated basalts or dense mafic intrusions. After the heating stage, the crust becomes unstable and gravitational instabilities (RTIs and delamination s.s.) start to occur producing strong and rapid cooling of the mantle. In the following sections I analyse the first two evolutionary stages described above.

### 4.2.1 Mantle Heating

I rearranged the eq. 4.1, assuming a stagnant-lid convection mode, to describe the heating of the numerical experiment showed in Chapter 2[4]:

$$q_l = -(D - L)(\rho_{mant} C_p \frac{DT_P}{Dt} - H_r) \tag{4.5}$$

$q_l$ is the heat flux at the base of the lithosphere, while $D$ and $L$ are respectively the thickness of the entire domain and of the lithosphere. $\frac{DT_P}{Dt}$ is computed using the data of the Chapter 2. $\rho_{mant}$ and $C_p$ are assumed to be constant and equal to 3400 $kg/m^3$ and 1050 $J/kg/K$ respectively. $H_r$ is equal to $0.066 \mu W/m^3$, which is the value employed in all numerical experiment listed in A2.

I start reviewing the Reference Test (the green curve in Fig. 4.2) [5]. During the heating stage (*0-14 Myrs*) mantle heats ( by a total of ~5 $^{\circ}C$). In many parametrized cooling histories, lithosphere is

[4]The numerical box that was employed for all numerical experiments showed in Chapter 2 extends 1000×660 km along $x$ and $z$ direction respectively. I assumed that the length of the $y$ direction is 1 km for rearranging the equation 4.1

[5]Reference Test Lithospheric Thickness 80 km, $T_{Moho}$=800 $^{\circ}C$, $T_P$=1550 $^{\circ}C$, $\lambda_{melt}$=0.01, all the other petrophysical properties are listed in Tab. A1

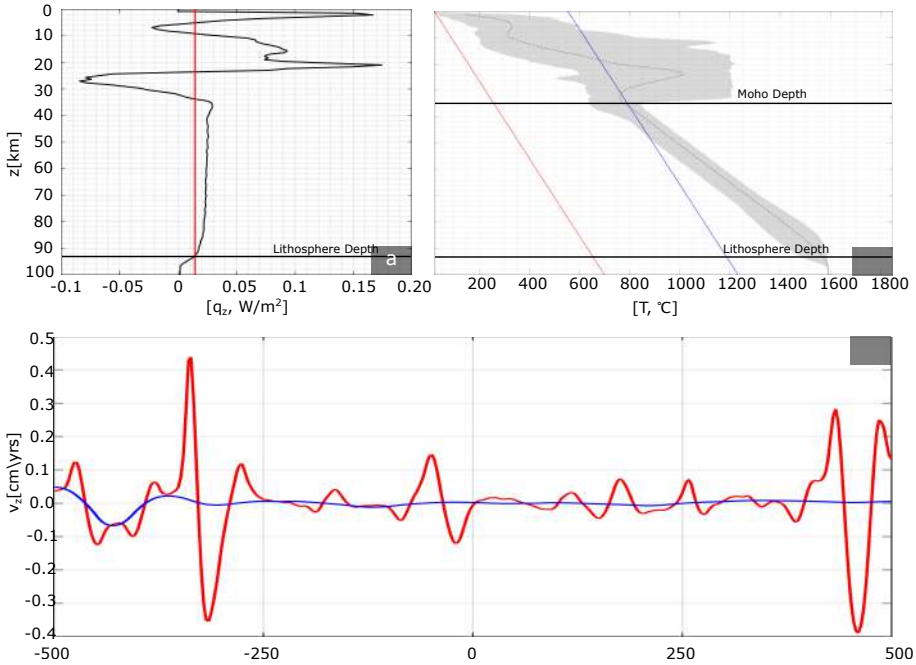


Figure 4.3: All the following picture are taken at 11.818 Myrs from the reference simulation of Chapter 2 (see Fig. 2.2) **a):** Heat flux versus depth, the black thick line is the horizontally averaged heat fluxes along $z$ direction, while the red thick line is the heat flux computed using eq.4.5; **b):** Temperature profiles along $z$ direction, the black shaded area represents the envelope between the maximum and minimum temperature recorded at any depth, while the thick black line represents the horizontally averaged geotherm. The red line is the linear geothermal gradient at the surface, while the blue line is the linear geotherm plotted at the bottom of the crust; **c):** $v_z$ (velocity along $z$ direction) magnitude and direction against $x$. The blue line is the velocity at Moho depth, while the red one is the velocity at the interface between the lithospheric mantle and asthenosphere.

assumed to be in thermal steady-state, which means that the lithospheric geothermal gradient is constant and predictable using eq.4.5. However, in the simulations of Chapter 2, the temperature is not linear with depth and thus not in steady state (see Fig. 4.3b). However, the heat flux at the bottom of the lithosphere is equal to the predictions, suggesting a first order control of the lithosphere on the heating of the asthenosphere (see Fig. 4.3 a). Such effect depends on the fact that a temperature and pressure dependent conductivity is employed ($K$, eq.2.8). The temperature and pressure dependent conductivity is frequently neglected in many geodynamic codes, although it affects the self-heating of the mantle, and the mantle thermal structure (Tosi et al., 2013; van den Berg et al., 2001). In Fig. 4.4 I plot the actual thermal conductivity and diffusivity and the resulting profile features two important minima at the base of the lithosphere and crust (Fig. 4.4a, red circles). The first is controlling the effective thermal exchange between mantle and the lithosphere, while the latter is affecting the stability of the lower crust by reducing the resisting force ($R_1 = \eta \times K(T,P)/(\rho \times C_p)$) of the material with respect to the one computed assuming a constant $K$ value used in Johnson et al. (2013) ($R_2 = \eta \times 3/(\rho \times C_p)$)(Fig.

4.4c-d).

The heating stage is a consequence of the low conductivity at the base of the lithosphere, inhibiting the heat fluxes that are not able to compensate for the radiogenic heat production. However, it is important to highlight that the lithosphere is not in steady-state equilibrium with mantle, due to the continuous thermal perturbation introduced by mafic intrusions, and due to the initial employed geotherm. The other simulations have similar behavior, and the predictions provided by eq.4.5 are robust.

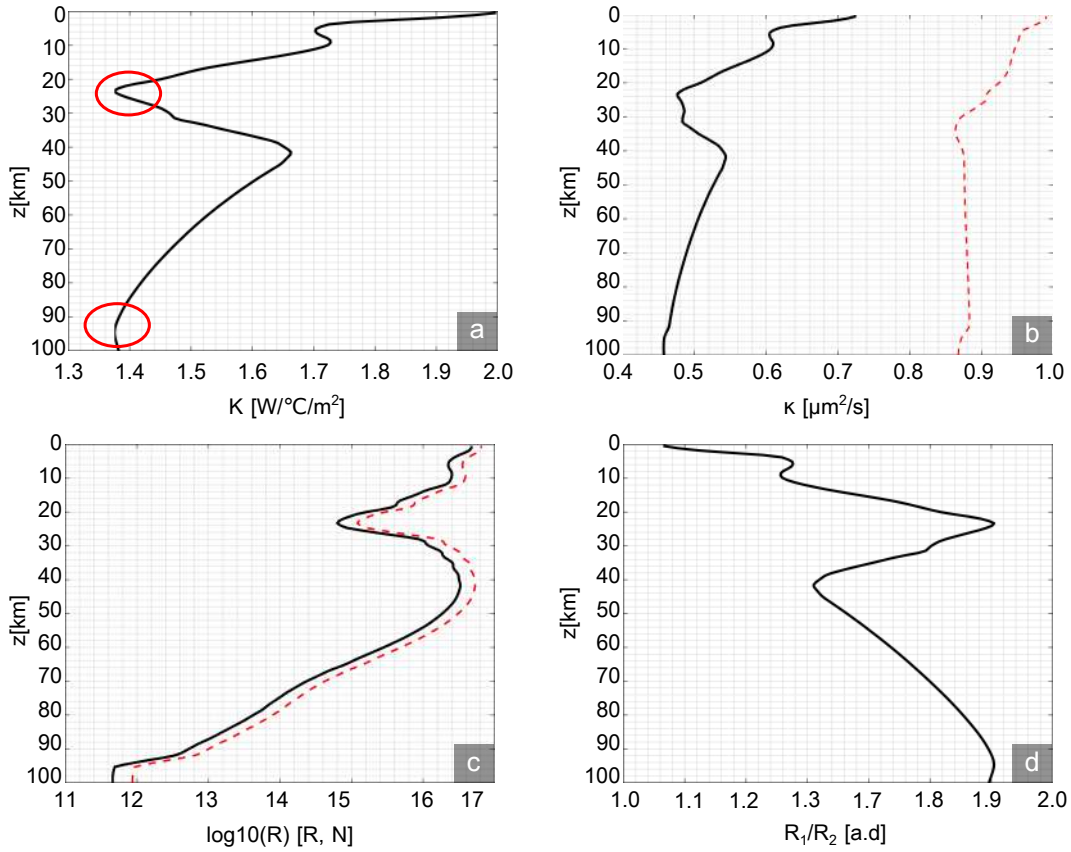


Figure 4.4: All the following picture are taken at 11.818 Myrs **a):** Average conductivity along $z$ direction; **b):** Thermal diffusivity profile along $z$ direction. The black thick line represent the actual average thermal diffusivity computed using the conductivity data plotted in **a)**, assuming a $C_P$ of 1050 $J/K/Kg$. The red dashed line is the thermal diffusivity computed assuming a constant $K$ ($K = 3$, used in Johnson et al. (2013)); **c):** Logarithm of resistance forces along $z$ direction. Black thick lines is the average resisting force computed using the actual data ($R_1$), while the red dashed line represents $R_2$ the resistance force computed using the constant thermal conductivity used in Johnson et al. (2013); **d):** Ratio $R_1/R_2$ along $z$ direction.

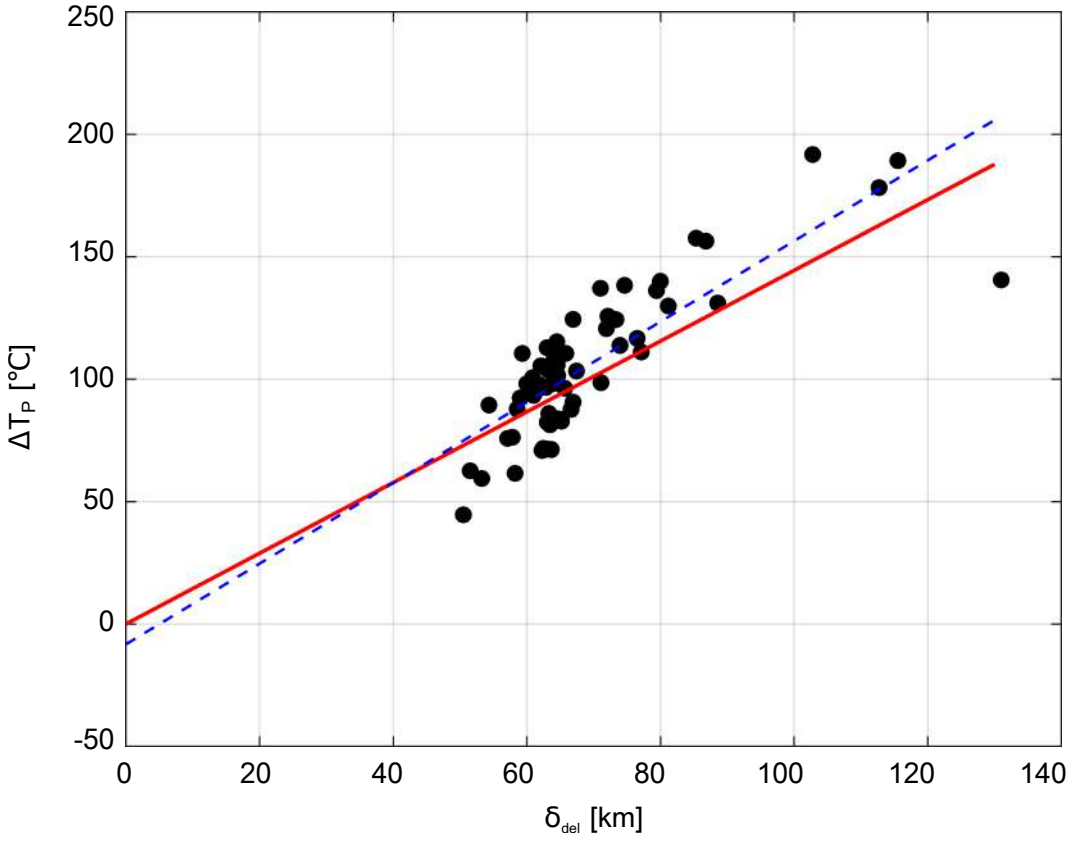


Figure 4.5: The total $\Delta T_P$ of all the experiments are plotted against the total thickness of delaminated crust ($\delta_{del}$). The red line represents a linear fit forced to have the intercept at zero, while the blue dashed line represents the linear regression of all the data. $R^2$ of the linear relation is 0.83. It is worth stressing the differences between linear fitting and regression, because the non zero intercept, although it seems unphysical may indicate a non linear behavior, or simply be an effect of the all the aforementioned cooling/heating mechanisms.

### 4.2.2 Mantle Cooling

Mantle cooling involves heat conduction through the crust, thermal equilibration between delaminated material and asthenospheric mantle, and latent heat of reaction. The most important of those is the one related to mass exchange between crust and mantle. But what is the relation between the $\Delta T_P$ and the total delaminated volume (represented here as an effective delaminated thickness, $\delta_{del}$, see Tab. 4.1)? In the following analysis, I define a simple relationship to predict the cooling as function of the delaminated volume while neglecting the effect of latent heat and heat exchange between crust and mantle[6].

Conservation of mass requires the volume of the crust to remain constant during to tectonic processes, and thus the mass influx can be computed using a volumetric balance equation. I

[6]Heat flux has a timescale higher than the one of the drip growth, so, although it may be important at the end of the cooling stage, it is not a first order effect.

normalized the volumes with the length of the domain to express all the relation in terms of effective thickness:

$$\dot{\delta}_{crust} = \dot{\delta}_{ext} - \dot{\delta}_{del} \tag{4.6}$$

$\dot{\delta}_{crust}$ is the total crustal thickening rate, $\dot{\delta}_{ext}$ is the magmatic crustal addition rate, while $\dot{\delta}_{del}$ is the delamination rate. Since the $\dot{\delta}_{crust}$ and $\dot{\delta}_{ext}$ can be computed from the simulations, it is possible to reconstruct the $\dot{\delta}_{del}$. A plot the total delaminated crust ($\delta_{del}$) versus the $\Delta T_P$ for all the numerical experiments (black dots) shows that they have an approximate linear dependence see Fig. 4.5. From these results it is clear that the first order effects is provided by the delaminated material. The relation between cooling and delaminated thickness is:

$$\Delta T_P = \xi \delta_{del} \tag{4.7}$$

$\delta_{del}$, is the cumulative delaminated crust, $\xi$ is the linear fitting constant (= 1.444 ± 0.010) and its unit of measure is $^{\circ}C/km$. The cooling is most likely due to the thermal equilibration between the delaminated crust and the asthenosphere. In order to test this, I assume that delaminated crust and asthenosphere are in thermal equilibrium. Thermal equilibrium requires that the variation of thermal energy of the mantle and delaminated crust is equal:

$$M^{mant} C_p (T^{eq} - T_P) = M^{del} C_p (T^{eq} - T^{del}) \tag{4.8}$$

where $M^{mant}$ and $M^{del}$ are the mass of the mantle and the mass of delaminated crust respectively. $T^{del}$ is the temperature of the delaminated crust, while $T^{eq}$ is the temperature at the equilibrium of both mantle and delaminated crust (which is the new mantle potential temperature). Mass can be expressed as a function of density and effective thickness of both mantle and delaminated crust :

$$M^{mant}/A = (\rho^{mant}(D - L)) \tag{4.9}$$

$$M^{del}/A = (\rho^{del}\delta^{del}) \tag{4.10}$$

where $\rho^{del}$ and $\rho^{mant}$ are respectively the density of the delaminated crust and the density of the mantle, $\delta^{del}$ is the effective thickness of the delaminated crust, and $A$ is the basal area of the numerical domain. Then it is possible to compute the new mantle potential temperature rearranging eq. 4.8 substituting $M^{mant}$ and $M^{del}$ with eqs.4.9 and 4.10:

$$T^{eq} = \frac{T_P \cdot \rho_{mant} \cdot (D - L - \delta_{del}) \cdot C_p + T^{del} \cdot \rho_{del} \cdot \delta_{del} \cdot C_p}{C_P \cdot (D - L - \delta_{del}) \cdot \rho_{mant} + C_p \cdot \delta_{del} \cdot \rho_{del}} \tag{4.11}$$

I assumed, for simplicity, that the delaminated material compensates for the mantle volume loss due to the melt extraction, and I exclude the mantle lithosphere. As $C_P$ is equal for all phases the equation can be further simplified to :

$$T^{eq} = \frac{T_P \cdot (D - L - \delta_{del}) + T^{del} \cdot \frac{\rho_{del}}{\rho_{mant}} \cdot \delta_{del}}{(D - L - \delta_{del}) + \frac{\rho_{del}}{\rho_{mant}} \cdot \delta_{del}} \tag{4.12}$$

then rearranged to find $\Delta T_P$ as a function of $\delta_{del}$

$$\Delta T_P = \frac{\rho_{del}}{\rho_{mant}} \frac{T^{eq} - T^{del}}{D - L - \delta_{del}} \delta_{del} \tag{4.13}$$

$\xi$, thus, depends on the difference between $T^{eq}$ and the average $T^{del}$ and the actual thickness of the mantle and density contrast between mantle and delaminated material. The density contrast between delaminated crust and mantle is slightly higher than 1 and decreases with depth.

I applied eq. 4.12 to the reference test to verify if the first order feature of the Cooling-Time curve can be replicated. In Fig. 4.6a I plot the temperature drop as a function of the $\dot{\delta}_{del}(t)$. Then I assume that the mantle effective thickness is not changing with time, which is only partially true (see Fig 4.6b) since the total newly crust generated is higher than the actual delaminated thickness. Then, I applied the equation 4.12 using the delamination rate for constructing a Time-Cooling curve to be compared with the actual data. The delamination rate is high at the beginning of the cooling stage (16-17 Myrs) after which it exponentially decays with time (see Fig 4.6c). In order to construct the Time-Cooling curve I assumed a constant $T^{del}$ (600 $^\circ$ C, the average temperature of the crust) and $\rho_{del}/\rho_{mant}$ equal to 1. I took the $T_P$ at the beginning of the cooling stage as starting point, and I compute the new $T^{eq}$ (which is the new mantle potential temperature) using the delamination rate. The results (see Fig.4.6d) is reproducing the first order features of the reference test results.

In this section, I showed that the $\Delta T_P$ is mostly a consequence of the mass exchange between mantle and crust. However, a formulation that can be used in a 1D cooling history model is needed, from which parameters, such as $\delta^{del}$, can be predicted. One strategy is to express the delamination cooling in term of heat fluxes. The effective delamination heat flux must be dependent on the temperature difference between mantle and delaminated crust, which decays with time as function of thermal conductivity and heat capacity. As the efficiency of thermal equilibration must be a function of the specific surface of the drips, the timescale depends on the size of the drip. The size of the drip varies as a function of the rheological properties of the crust, consequently, to better constraint the cooling it is necessary to perform further

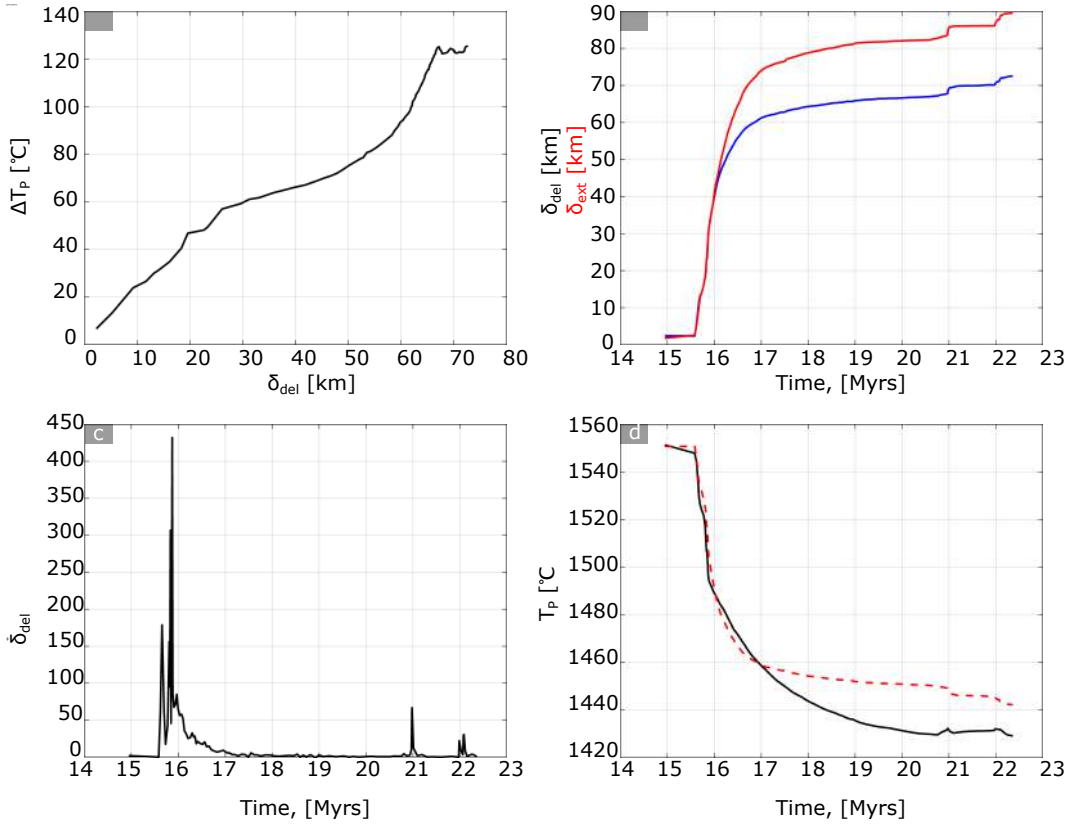


Figure 4.6: **a):** $\Delta T_P$ versus the cumulative $\delta_{del}$. The thick black line represent the evolution of $T_P$ as a function of the total amount of delaminated crust; **b):** The red line represents the cumulative newly generated crust thickness, while the black line represents the total delaminated one with time; **c):** Delamination rate evolution with time; **d):** Temporal evolution of $T_P$. The black thick line represents the temporal evolution of $T_P$ of the reference test, while the red dashed line represents the one produced applying eq. 4.12

experiments and produce a simple scaling law between the aforementioned parameters.

### 4.2.3 Rayleigh-Taylor Instabilities detection criteria

Rayleigh-Taylor Instabilities (RTIs) are generated by the density contrast between mafic dense lithologies (mafic intrusions and mafic residuum) and the underlying lithospheric mantle. The unstable portion of the crust has a finite thickness ($\delta_{ul}$) and, by definition, an average density ($\rho_{ul}$) higher than that of the underlying lithospheric mantle ($\rho_{lit}$). The growth of the RTIs requires the existence of a geometrical-thermal perturbation at the interface between buoyant and unstable layer and the growth of these perturbations depends on two competitive processes: heat diffusion rate and advective velocity. Heat diffusion tends to eliminate thermal anomalies inhibiting the growth, while the advective velocities depends on the rheology (which is temperature dependent) and density contrasts. Thus, the viscosity and thermal diffusivity

of the unstable layer ($\eta_{ul}$ and $\kappa_{ul}$ respectively) play a fundamental role in the evolution of the RTIs (Houseman and Molnar, 1997; Molnar et al., 1998; Johnson et al., 2013). The compositional Rayleigh number ($R_b$) measures the relative efficiency of the two competitive processes:

$$R_b = \frac{C\Delta\rho g \delta_{ul}^3}{\eta_{ul}\kappa_{ul}} \tag{4.14}$$

where $C$ is a constant that depends on the size of the model, the rheological parameter and the density contrast, $g$ is the gravitational acceleration. RTIs nucleate only if $R_b$ is higher than 1. The main goal of this subsection is to verify if $R_b$ can be a suitable parameter to predict the occurrence of RTIs and how dense mafic lithologies are affecting the stability of the crust. If $R_b$ is the right criteria, there must be a transition from sub-critical values (i.e. $R_b \leq 1$) to super-critical values at the beginning of the cooling stage in every experiment performed.

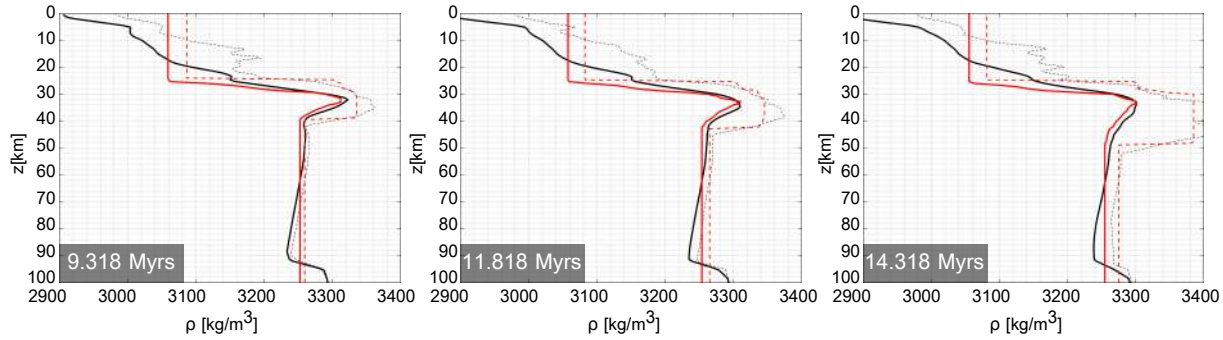


Figure 4.7: Density-Depth profiles. Each figure represents three different instants *reference test* (Chapter 2). The thick black and red lines represents the actual density profile and the simplified one used to compute $R_b$, while the black and red dashed lines represents the maximum density recorded at any depth from the simulation and the simplified one. The right and middle pictures are taken shortly before the onset of the RTI instabilities while the left one is taken during the nucleation of the first RTI.

In order to do this a simple algorithm was developed for detecting the presence of an unstable layer ($ul$) and to compute $R_b$ number for every nodes along $x$ direction and available timestep, assuming $C = 1$. Firstly, I assumed that the density contrast that causes the RTIs is between the lithospheric mantle and the crust. I compute the vertical average density of the lithospheric mantle ($\rho_{lit}(x)$ [7]) for each node in the $x$ direction. Then, I detect the portion of the crust that features higher density than $\rho_{lit}(x)$, computing the thickness of the unstable portion ($\delta_{ul}(x)$) and all the other quantities to compute $R_b(x)$ number ($\Delta\rho(x), \kappa_{ul}(x)$). If no unstable layer is found, locally all variables are set to zero and excluded from post-processing. The viscosity of the unstable layer ($\eta_{ul}(x)$) is computed in a different way because the highest viscosity between the unstable layer and the lithospheric mantle is the one that controls the

[7] (x) is the position along $x$ direction

RTIs process. Therefore the viscosity of the lithosphere and the one of the unstable layer are computed for every node along x-direction and the highest viscosity is used to compute $R_b$. These procedures are repeated for all available timesteps for each numerical simulations. In Fig.4.7 the real horizontally averaged density profiles (black lines) are compared to the simplified ones (red lines), where each of the sub-plots represents timesteps of the reference test shortly before the onset of the cooling stages. The agreement with the post processed data and the real data are good, and show the robustness of the method.

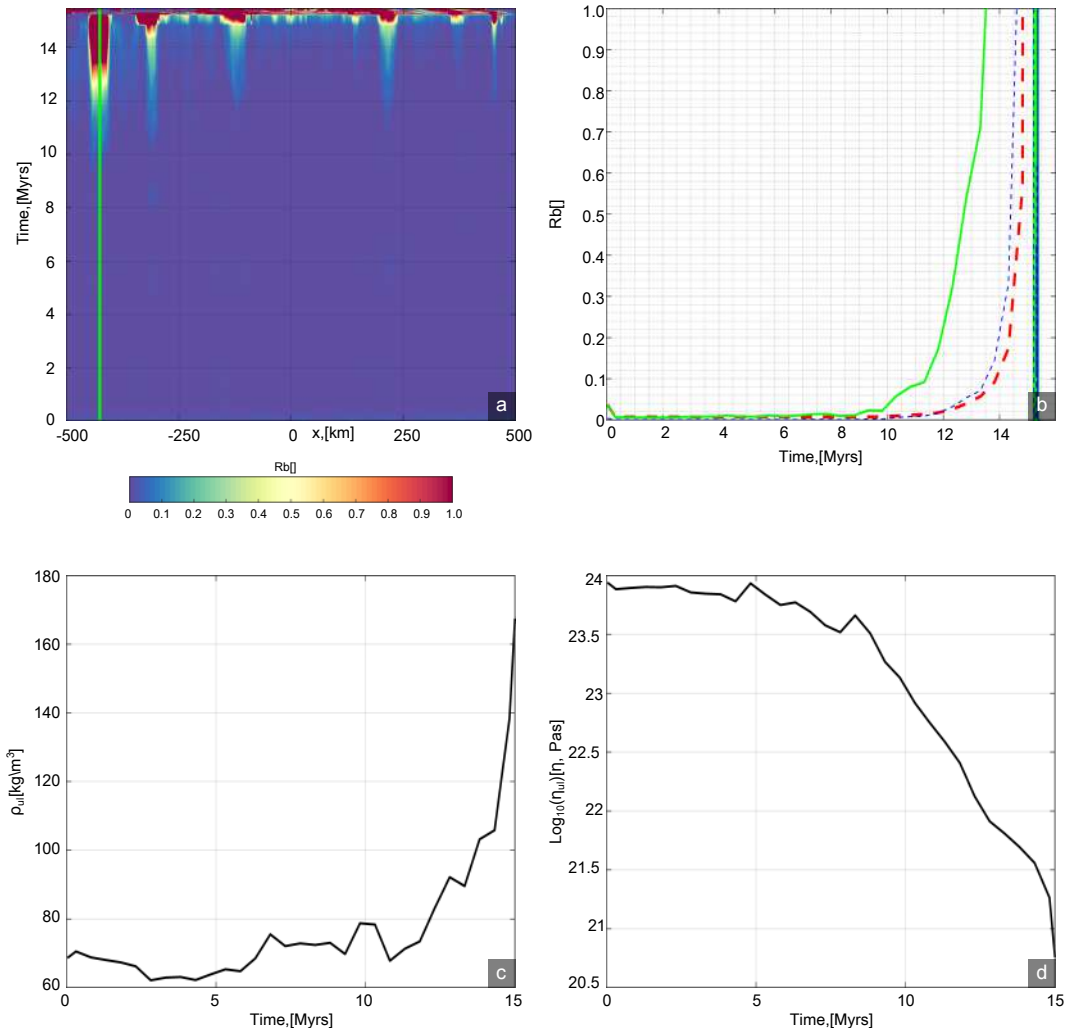


Figure 4.8: **a):** All the $R_b$ profiles along $x$ direction per each timestep of the reference test are merged to visualize the evolution of the gravitational instabilities with time. $R_b(x)$ is computed assuming a $C$ equal to one. The green thick line follows the position of the first RTIs occurring in the simulation; **b):** The temporal evolution of the horizontally averaged $R_b^{av}$ number (red dashed line), and the evolution of the $R_b(x^{st})$ ($x$ = 426 km) (green thick lines) are plotted. The blue dashed line represents the $R_b(x^{st})$ number scaled using a $C$ = 0.1, following Johnson et al. (2013). ; **c):** Temporal evolution of $\Delta\rho(x)$ at the position of the first RTIs; **d):** Evolution of the $\eta_{ul}(x)$ at the position of the first RTIs, with time.

I start reviewing the Reference Test. In Fig 4.8a, I plot the temporal evolution of $R_b$ at each nodal point along $x$ direction, by merging all the $R_b$ monodimensional profiles. During the initial 4-5 Myrs, most of the crust is stable, afterwards $R_b$ starts to increases in some portion of the crust. The increasing of $R_b$ is a consequence of the developing of small convective cells during the heating stage (see Fig 2.2). The growth of these unstable portions is variable with time. The green line in the same sub-plot follows the position of the first drip ($x^{st}$) [8]. The increase of $R_b(x^{st})$ is initially gradual after which it increases rapidly. At 14 Myrs the gravitational instabilities occur, destabilizing the other $R_b$ anomalies and enabling the total removal of lower crust and mantle lithosphere. In Fig 4.8b, the time evolution of the average $Rb^{av}$ and $R_b(x^{st})$ are plotted (red dashed line and green line respectively) , and there is a good agreement with the time of the onsetting of cooling of the reference test (14.818 Myrs). However, $R_b(x^{st})$ computed assuming a $C$ = 1 seems to be higher than the critical values, but, if it is scaled with the value proposed by Johnson et al. (2013), the $R_b(x^{st})$ is higher than one, at the onset of the cooling stage (blue dashed line the 4.8b) . $R_b^{av}$ starts to grow only during the onsetting of the first RTIs, and is thus a good parameter to track the stability of the crust, without need to follow the first drip in each numerical simulation.

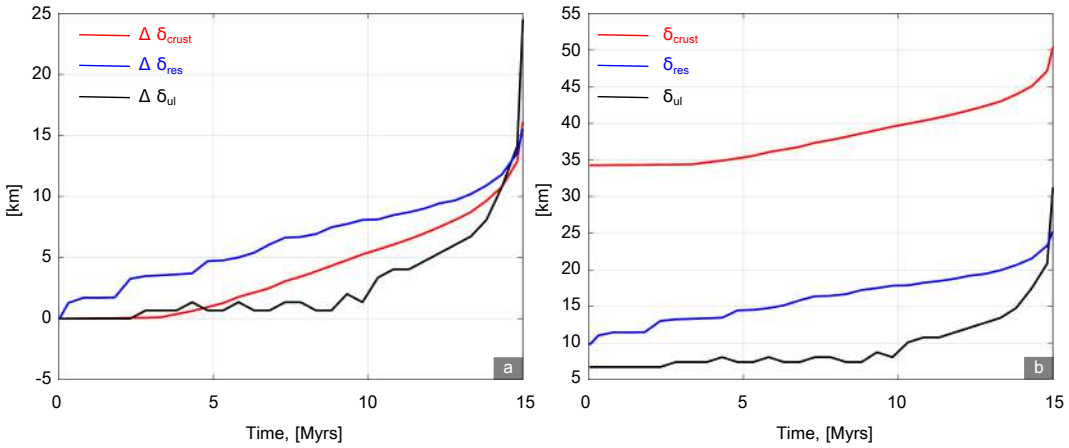


Figure 4.9: **a)**:Time evolution of variation of the total ($\Delta\delta_{crust}(x^{st})$), residuum ($\Delta\delta_{res}(x^{st})$) and unstable layer($\Delta\delta_{ul}(x^{st})$) thickness respect to the initial state; **b):** The effective thickness of the crust, residuum and unstable layer with time, evaluated at the first drip point

The base of the crust becomes gravitationally unstable as a consequence of the continuous extraction of mafic melts from the mantle, that are converted in volcanic and plutonic rocks. The new plutonic rocks emplaced within the lower crust increase the temperatures of the lower crust, which produce a local decreases of the $\eta_{ul}(x^{st})$, see Fig 4.8d. $\Delta\rho(x^{st})$ increases with time

[8] All quantities that feature ($x^{st}$) indicates the position of the first drip in any numerical simulation, while all the quantities that have $av$ as superscript indicate the horizontally averaged value.

because of continuous magmatic thickening and compositional evolution of the crust. In Fig.4.9 I tracked the evolution of the total crustal thickness ($\delta_{crust}(x^{st})$), the thickness of the dense mafic lithologies ($\delta_{res}(x^{st})$) and the unstable layer thickness ($\delta_{ul}(x^{st})$). The sudden and fast growing of $\delta_{ul}$ starts as soon as $\delta_{crust}$ is larger than 40 km, and propagates from bottom to top. This is a consequence of the garnet-in reaction line (see Fig. 2.1), which is progressively shifted toward lower pressures as a consequence of the extraction of felsic melts.

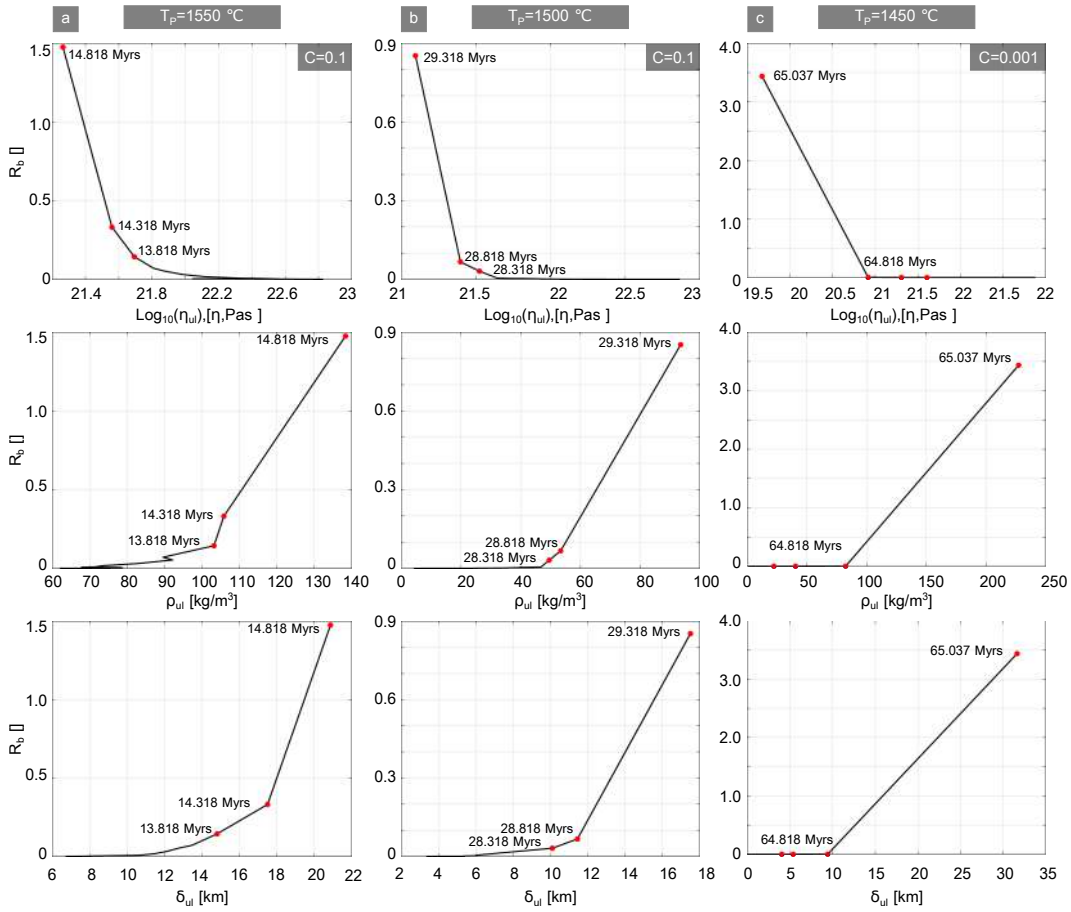


Figure 4.10: All the three column represents three different experiments featuring the same input of the reference test, but different initial $T_P$. The first row is dedicated to the evolution of $R_b(x^{st})$ as function of the $\eta_{ul}(x^{st})$, while the second and last rows are dedicated the evolution of $R_b(x^{st})$ as function of the $\Delta\rho(x^{st})$ and $\delta_{ul}(x^{st})$ respectively. The red dot are indicating the timestep, with the related time. **a):** This column is the Reference test showed in the previous pictures; **b):** Numerical experiments featuring an initial $T_P$ of 1500 $^{\circ}C$; **c):** Numerical experiment featuring $T_P$ of 1450 $^{\circ}C$. The two red dots without the associated timing are from left to right (or right to left for the viscosity plot) representing 63.818 and 64.318 Myrs timesteps. $C$ is lowered to make comparable axis, since $R_b$ increases one hundred time faster in the lowest $T_P$ scenario. All the analysis were carried out assuming the same $C = 0.1$.

The evolution of the $R_b^{av}$ with time is fast, due to the internal feedback between density, thermal conductivity, and upward propagation of the unstable layer thickness. As a consequence,

the transition between stable and unstable state becomes difficult to track in the simulations because it requires high temporal resolution. So three experiments were repeated saving output at high resolution to describe the evolution of the $R_b$, one of them is the reference test (the results are showed on Fig. 4.8 and Fig. 4.9). As for the reference test, I detect the position of the first RTI and track the evolution of $R_b(x^{st})$. To facilitate the analysis I plot the evolution of $R_b(x^{st})$ against $\eta_{ul}(x^{st})$, $\Delta\rho(x^{st})$ and $\delta_{ul}(x^{st})$. $R_b$ is scaled using $C = 0.1$. Low initial mantle potential temperatures prolong the timescales of the incubation stage and make the evolution of $R_b(x^{st})$ discontinuous. In the same plot I indicates three point representing the last three timestep before the onset of the dripping instabilities. These data confirms that even in the most extreme scenarios, the instability starts to grow when the $R_b(x^{st})$ is close to its critical value.

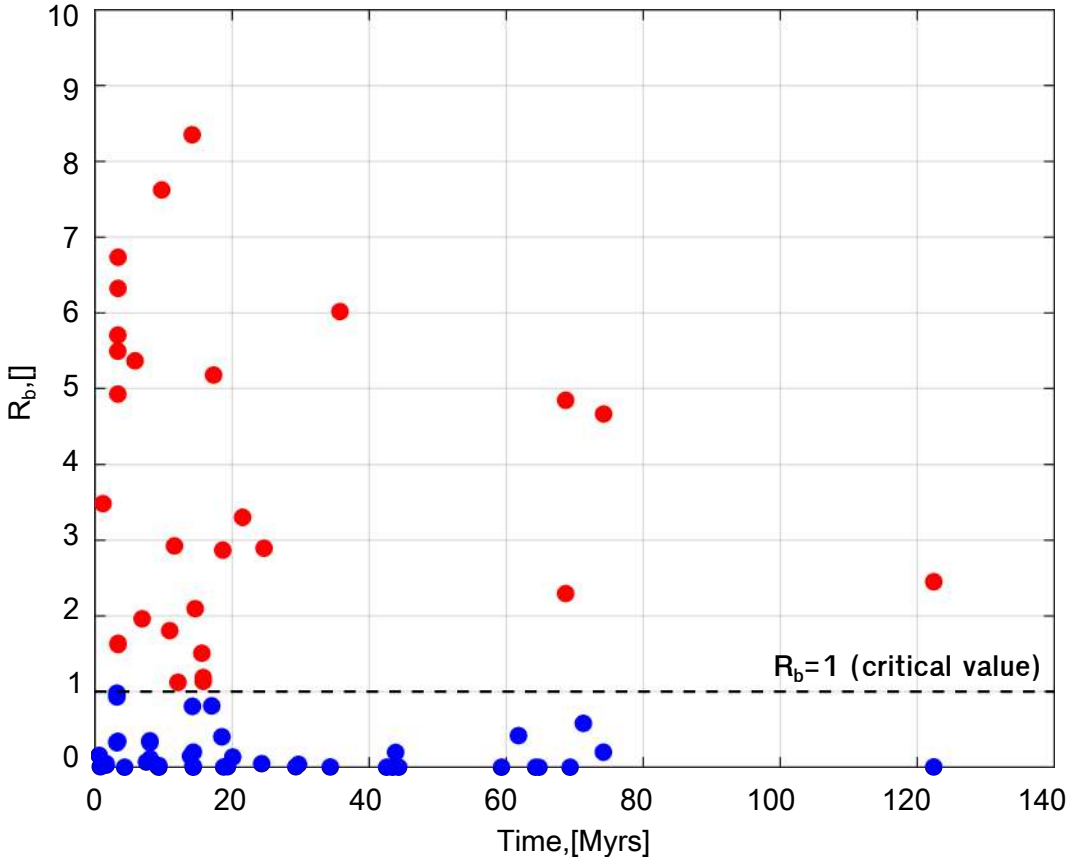


Figure 4.11: Temporal evolution of $R_b^{av}$ versus the time of onsetting of the cooling stage. All the data points have been scaled using a $C = 0.1$. The blue dots represents $Rb^{av}$ before the critical temperature predicted for each experiments, while the red ones represents the timestep at which the maximum $T_P$ is reached.

The last step is to verify if all the experiments follow the same evolution. Therefore, neglecting the non linear effect that occurs near the occurrence of the instability, I plot the $R_b^{av}$ of all the numerical experiments at the timestep in which the maximum $T_P$ is reached (red

dots) and the timestep before (blue dots) see Fig 4.11. The two population of data perfectly cluster above and below the critical $R_b$ number, which demonstrate that $R_b = 1$ is an appropriate criteria that describe the onset of dripping instabilities in the simulations of Chapter 2.

## 4.3 Concluding remarks

In this chapter, it was demonstrated that many effects observed in 2D simulations can be understood physically with either simplified, horizontally averaged, 1D models, or by applying conservation of mass and energy. The main insights are:

1. The mantle radiogenic heating controls the timescales at which the RTIs instabilities occurs and it is a consequence of the low heat flux at the base of the lithosphere.

2. Mantle cooling is mainly caused by the addition of cold material.

3. RTIs instability can be predicted computing the compositional evolution of the crust, and its relative thickness.

The simplest way to integrate the cooling effect of the delaminated crust in a simple 1D parametrized convection code is to compute the heat required to thermally equilibrated the mass.

The onset RTIs can be predicted by computing the compositional evolution of the crust and its relative thickness. Therefore, in 1D parametrized convection codes these key processes have to be integrate in a horizontally averaged manner. This require a 1D melt extraction code, and 1D diffusion code that effectively allows to to predict the crustal geotherm, which are important to predict the crustal viscosity profile, as well as a coupling with crustal and mantle phase diagrams to capture the chemical evolution of the system in a 1D manner.

# REFERENCES

van den Berg, A.P., Yuen, D.A., Steinbach, V., 2001. The effects of variable thermal conductivity on mantle heat-transfer. Geophysical Research Letters 28, 875–878.

Fischer, R., Gerya, T., 2016. Early earth plume-lid tectonics: A high-resolution 3d numerical modelling approach. Journal of Geodynamics 100, 198–214.

Grasset, O., Parmentier, E., 1998. Thermal convection in a volumetrically heated, infinite prandtl number fluid with strongly temperature-dependent viscosity: Implications for planetary thermal evolution. Journal of Geophysical Research: Solid Earth 103, 18171–18181.

Houseman, G.A., Molnar, P., 1997. Gravitational (rayleigh–taylor) instability of a layer with non-linear viscosity and convective thinning of continental lithosphere. Geophysical Journal International 128, 125–150.

Johnson, T.E., Brown, M., Kaus, B.J.P., VanTongeren, J.A., 2013. Delamination and recycling of Archaean crust caused by gravitational instabilities. Nature Geoscience 7, 47–52. URL: http://www.nature.com/doifinder/10.1038/ngeo2019, doi:10.1038/ngeo2019.

Lourenço, D.L., Rozel, A.B., Gerya, T., Tackley, P.J., 2018. Efficient cooling of rocky planets by intrusive magmatism. Nature Geoscience 11, 322.

Molnar, P., Houseman, G.A., Conrad, C.P., 1998. Rayleigh—taylor instability and convective thinning of mechanically thickened lithosphere: effects of non-linear viscosity decreasing exponentially with depth and of horizontal shortening of the layer. Geophysical Journal International 133, 568–584.

Moresi, L.N., Solomatov, V., 1995. Numerical investigation of 2d convection with extremely large viscosity variations. Physics of Fluids 7, 2154–2162.

Schubert, G., Turcotte, D.L., Olson, P., 2001. Mantle convection in the Earth and planets. Cambridge University Press.

Sizova, E., Gerya, T.V., Stüwe, K., Brown, M., 2015. Generation of felsic crust in the Archean: A geodynamic modeling perspective. Precambrian Research 271, 198–224. URL: http://dx.doi.org/10.1016/j.precamres.2015.10.005, doi:10.1016/j.precamres.2015.10.005.

Sleep, N.H., 2000. Evolution of the mode of convection within terrestrial planets. Journal of Geophysical Research: Planets 105, 17563–17578.

Solomatov, V., 1995. Scaling of temperature-and stress-dependent viscosity convection. Physics of Fluids 7, 266–274.

Tosi, N., Yuen, D.A., de Koker, N., Wentzcovitch, R.M., 2013. Mantle dynamics with pressure-and temperature-dependent thermal expansivity and conductivity. Physics of the Earth and Planetary Interiors 217, 48–58.

Urey, H.C., 1955. The cosmic abundances of potassium, uranium, and thorium and the heat balances of the earth, the moon, and mars. Proceedings of the National Academy of Sciences of the United States of America 41, 127.

Urey, H.C., 1956. The cosmic abundances of potassium, uranium, and thorium and the heat balances of the earth, the moon, and mars. Proceedings of the National Academy of Sciences of the United States of America 42, 889.

CHAPTER 5

# CONCLUSIONS

*The Answer to the Great Question... Of Life, the Universe and Everything... Is... Forty-two,' said Deep Thought, with infinite majesty and calm.*

Douglas Adams, The Hitchhiker's Guide to the Galaxy

This thesis explores the implication of felsic crust production on early Earth geodynamic processes. I employed indirect methods to answer this issue: geodynamical and petrological modelling. I performed numerical experiments coupled with state-of-the-art of petrological modelling. The petrological phase diagrams describe the chemical evolution of primitive tholeiitic mafic crust and primitive mantle. The chemical evolution is only a function of melt extraction, which is simulated through a simple parametrization. Phase diagrams provide density and melt fraction information to the numerical codes that I employed during the studies herein presented, and allow a dynamic coupling between chemical composition and geodynamic processes. These realistic phase diagrams allowed to explore the dynamical effects of felsic melts extraction and provide useful insights in Archean geodynamic and continental crust forming processes. In the following section, I briefly summarize the main findings.

## Chapter 2 and Chapter 4

I started experimenting the effect of high upper mantle potential temperature ($T_P \geq 1550\ ^\circ C$). High mantle potential temperatures promote the partial melting of the asthenospheric mantle, generating several small convective cells beneath the lithosphere. The production of high quantities of melt results in the production of new mafic intrusive and effusive crust. Effusive crust promptly equilibrates with the atmosphere, while intrusive crust starts equilibrating with

the pre-existing crust. Therefore, heat is transferred from mantle to crust through advective processes, that are simulated by melt extraction parameterization. Mafic intrusions play an important role, because they heat the crust and create a dense mafic root. The heat flow coming from the mafic intrusions promotes partial melting of the hydrous crust, which results in felsic melts that are extracted to form felsic crust, leaving behind the dense complementary residuum. The temperature increases at lower crustal depth and viscosity and thermal conductivity decrease, favoring the initialization of the Rayleigh-Taylor Instabilities (RTIs). The continuous magmatic thickening increases the density contrast between the lower residual crust and lithospheric mantle, generating an initial unstable layer that propagates upwards as a function of the amount of dense residuum generated. Thus, the compositional evolution favors the occurrence of gravitational instabilities. The RTIs feedback with mantle melting produces new mafic and felsic crust, and forces the mantle to compositionally evolve and ultimately leads to its cooling. The magmatically induced RTIs are an inevitable consequence of the thermal-compositional maturation of the mafic crust. These processes efficiently occur at high $T_P$, while at lower $T_P$ ($\leq$ 1500° C) their occurrence depends on the amount of radiogenic heat element present in the mantle. Mantle self-heating results in an increase of the amount of melt produced per unit time, and sets the stage for the occurrence of magmatically induced RTIs. These results suggest that at Archean-like conditions, magmatically induced RTIs buffer self-heating of the mantle and dissipate the thermal anomalies of the upper mantle efficiently. The gravitational instabilities plays a fundamental role in shaping the composition of both convective mantle and lithosphere, and has an impact that is as important as plate tectonics on the cooling of the planet.

## Chapter 3

Chapter 2 gives insights in the effects of high upper $T_P$ ($\geq$1550 °C) and Archean-like radiogenic heat production rate. The results suggest that high $T_P$ cannot be sustained for geological meaningful timescales and they cannot be spontaneously reached as a consequence of magmatically induce RTIs. Taking these insights as absolutely true, the only possible conclusion is that the inferred high upper mantle $T_P$ might be associated with hot upwelling.

In Chapter 3, the effects of a short-lived mantle plume as a function of the asthenospheric $T_P$, melt extraction efficiency, initial lithospheric thickness and radiogenic heating are tested, using 2D and 3D experiments. All the experiments feature similar behavior: an initial stage featuring tectonic activity is followed by a steady state stage in which the new lithospheric mantle is gradually forming. Most of the magmatic activity is focused in the tectonic active stage, and the production of new mafic and felsic crust is a consequence of the gravitational

instabilities.

Most of the new mafic crust produced is generated by the normal asthenosphere, consequently the background $T_P$ exerts a strong control on the dynamics of the system. The initial lithospheric thickness affects the dynamic of the system as a function of $T_P$. Low lithospheric thickness (<80 km) are always unstable at high $T_P$ (>1500 °C), which implies that all prescribed lithosphere is recycled during the experiments, while at low $T_P$ (≤ 1400 °C) depends on the thermal boundary conditions and mantle radiogenic heat production. If the lithosphere thickness is high (≥ 100 km), then the recycling processes are always efficient regardless the initial conditions.

2D and 3D experiments have many similarities but are different in many important dynamics: the efficiency of gravitational processes are stronger in 3D cases, limiting the crustal thickness, and resulting in different felsic melts extraction P-T conditions. The crustal thickness is an important parameter that controls the pressure at which the felsic melt are produced and extracted. In all experiments, crust is thinned by two mechanisms: gravitational instabilities and intraplate extension caused by the mantle drag forces. If the newly generated mafic crust is not able to compensate for the material that is foundered into the mantle, the crustal thickness decrease with time. The rate at which the mafic dense residuum is recycled depends on the rheology of the crust, the amount of newly generated crust and on the depth at which the mafic intrusion are emplaced. Different than the experiments performed in Chapter 2, the depth of intrusion rather being determined by the rheology contrast within the crust, is an input parameter. This allowed to emplace the intrusions at fixed depth interval, allowing a continous heating of the crust as a function of the newly mafic melt extracted. This allowed to promote the compositional maturation of the crust, and more efficient production of new felsic crust respect the experiment showed in Chapter 2. However the most evident consequence is related with the rate at which the crust is recycled, reducing its possibility to build up thickened plateau. These effects are efficient in 3D, while in 2D cases they are relatively important. The bulk of the observations suggests that in order to sustain thickened crust is necessary a continuous flux of hot mantle. Thus, the observation that 3D experiments are featuring consistent low pressure felsic crust production provide useful insights to understand what is needed to produce high amount of felsic melts at high pressure conditions (>1.0 GPa).

## Concluding remarks

The results presented in my thesis work improve the understanding of the geodynamic processes operating during Archean. This thesis represents a successful attempt to conjugate advanced phase diagrams and chemical evolution model with the state-of-the-art of numerical modeling to investigate the generation of felsic crust during Archean. All numerical experiments show the

importance of magmatic processes on developing lithospheric scale gravitational instabilities and how compositional evolution of the crust exerts a first order control on the geodynamical evolution of the upper mantle.

From the result herein presented, it is clear that the most important processes are related with gravitational instabilities and their feedback with mantle melting. Mantle melting is not a passive feature that mainly depends on plate tectonic, but it is active and depends on the primordial heat and radiogenic heat, and it promotes the structural and compositional evolution of the lithosphere.

The gravitational instabilities are induced by mantle melting production, and once they are triggered, they feedback with mantle melting. Such coupling between these processes allows a continuous production of new felsic crust. Owing to the deformation induced by gravitational instabilities, the felsic melt P-T conditions of extraction are variable and are similar to the ones predicted for the Archean TTGs. Therefore, vertical tectonic induced by mantle melting ultimately produce significant amounts of new felsic crust in short timescales with composition that match the Archean TTGs.

The processes that assisted the generation of the first proto-continents are "energetically" expensive. They require continous mantle melting, which is allowed by the continuous foundering of the residual mafic crust. The consequence of felsic melts extraction and generation of the first proto-continent is to induce a compositional-thermal evolution of the mantle. Therefore, the main consequence of producing the first proto-continents facilitated the mantle cooling during the Archean.

## Outlook

Although this thesis work represents an improvement of our understanding of Archean geodynamics, there are still unsolved question that I have not addressed in my current work:

**When did plate tectonics begin on Earth?** This question is difficult to answer with only lithospheric scale numerical modeling. However, it is still possible to study the lithospheric scale mechanism behind the generation of plates, and their effect on the evolution of the crustal composition. Most of the scientific effort during the last decades was focused on understanding if some sort of subduction was active during the Archean. Subduction is an efficient way to transport water and volatiles into the mantle, and presently it represents the only geodynamic setting in which felsic crust is produced in significant amounts. Therefore, in order to complete the insights that I provided with the current work, it is necessary to study what kind of behaviour a subducting plate during Archean would have, and how the felsic crust is produced in such

scenarios. Studying crustal forming processes in a subduction zone is challenging, as it requires to handle the fluid exchanges between subducting slab and surrounding mantle, and it requires a simplified model to handle both partial melting and fractional crystalization. Therefore, the next step is to integrate all the processes necessary to model Archean subduction and try to compare the production of felsic crust between the setting that have been described in the current work and subduction. Furthermore, it is necessary to explore the effect of the starting compositions in both of the processes and try to integrate a more sophisticated petrological model able to incorporate such complex chemical evolution.

**Did gravitational instabilities assisted the mantle cooling of Earth?** Throughout my thesis, I noticed that magmatically induced RTIs are correlated with a strong mantle cooling. Using this persistent results, I concluded that the upper mantle could not have been so hot without triggering these processes. However, although these results are robust, it is necessary to understand if mantle cooling resulting from these processes affect the long-term cooling history of the planet. However, it is difficult to explore such long timescales in our numerical code, and it would be completely unfeasible to test global-scale numerical simulations with the current petrological implementation, as it they require a high numerical resolution in the crust. To circumvent this limitation, it is possible to use 1D numerical codes that integrate a simplified parametrization of the processes that I described throughout all this thesis to explore the cooling history of Earth. In Chapter 4, I provide a preliminary analysis of the experiment performed, and the next step is to provide simplified relation to describe the cooling, and to integrate with these 1D numerical code. Moreover, it is necessary to provide a better formulation of latent heat in order to track the effect of latent heat of reaction on the thermal state of Earth.

# APPENDIX A

**Introduction** This supplementary contains additional pictures that assist the main manuscript, supporting tables and information concerning the initial setup, experimental designs and the technical information of the hardware used to perform the simulation.

**1. Initial Setup**

We use a regional scale numerical domain (1000 x 660 km along $x$ and $z$ direction). We employ the same number of grid nodes in both direction (331 x 331 nodes, which yields a resolution of 3000 x 2000 meters along $x$ and $z$ direction). We employ LBB stable $Q_2P_{-1}$ elements. The mechanical boundary conditions are free surface at the top (Kaus et al., 2010), and free slip for the right, left and bottom boundary. Temperature has isothermal boundary conditions at the top and bottom (20 $^{\circ}$C at the top, the bottom boundary conditions depends on the initial mantle potential temperature, $T_P$), meanwhile the left and right boundary condition are no flux boundary conditions. The initial compositional field is made of two main layers: lithosphere and asthenosphere mantle. The asthenosphere mantle was modelled as fertile peridotite (MFP) with dry olivine rheology or wet olivine rheology (Hirth and Kohlstedt, 2004) and it extends from the base of lithosphere to the bottom of the numerical model. It represents the source reservoir for the EAT basalts and chemically evolves accordingly the petrological model employed. The initial lithosphere is composed of two layers: lithospheric mantle and the crust. The crust is always 1/3 of the total lithosphere thickness, which is 80 km for the reference test (i.e. 24 km crust thickness). The crust is made of two layers: upper crust (upper 2/3) and lower crust (lower 1/3 of the total thickness (i.e. 8 km, for the reference model). The upper crust is modeled as hydrated enriched basalt (BS1) with a wet quartzite rheological flow law (Ranalli, 1995) meanwhile the lower crust is modelled as intrusive layer with BS4 phase diagrams and with mafic granulite rheology (Ranalli, 1995). Lithospheric mantle is modelled with the MDS1 and it has always dry olivine rheology (which can be modified to simulate stiffening adjusting the

pre-exponential factor value). The initial geotherm is double stage and is fully characterized by the $T_P$ (°C), adiabatic gradient (0.4 °C/Km) and Moho temperature, $T_{Moho}$ (°C). The top boundary is always °C, and the bottom boundary is computed accordingly to the initial mantle potential temperature and adiabatic gradient (e.g. for the reference test is 1814 °C). The Moho temperature varies accordingly the numerical experiments (it ranges from 800 to 1200 °C).

Our systematic analysis tested the role of the differentiation on the geodynamic of the upper mantle. We track several properties: the crust composition, the mantle potential temperature and the relative time-scale of the processes. The crust composition, F, is defined as the relative amount of felsic crust composition respect to the vertical direction:

$$F = \left( \frac{Felsic}{Mafic + Felsic} \right) * 100 \tag{A1}$$

The produced compositional profiles are used to compute the average composition and its standard deviation. As a complementary parameter, we track the conversion factor, which represents the amount of BS1 converted into the other three stages:

$$C = \left( 1 - \frac{BS1}{BS1 + BS2 + BS3 + BS4} \right) * 100 \tag{A2}$$

We tested a wide range of parameters ranging from the Moho temperature, rheology, initial thickness and mantle potential temperature and melt extraction parameters producing several sets of experiments. The duration of the dripping stage is derived using $T_P$ vs Time curves, taking the time before the mantle potential temperature drop and the time associated with the minimum $T_P$. Every $T_P$ vs time curve in the simulations show a slight increase in $T_P$ during the initial stage, a drop of mantle potential temperature and then a slow increase of mantle potential temperature. This approach gives us the opportunity to compare several numerical experiments whose timescale is different, allowing comparison of compositional patterns (F or C) at the beginning or end of the dripping stage.

**2. Experimental Systematic and Hardware informations**

We organize the experiments following different systematics, in which we tested several parameters against each other starting from the reference test. Such approach elucidate the complex interaction between the parameter. S1-S2, which explore the relative effects of the $T_{Moho}$, $\phi_{dry}$, $\lambda_{melt}$ and mantle rheology; S3, which explore the effect of the amount of intrusion respect the extrusion, and the efficiency of melt extraction (represented by M2); S4 exploring the effect of mantle potential temperature and initial thickness (see Table S2, for further details). All the experiments have been performed using *MVEP2*, an open source MATLAB// code (R2016b) (https://bitbucket.org/bkaus/mvep2). The numerical experiments were performed using GAIA

(*4x6276 AMD Interlagos, 16 cores,2.30 GHz,12MB, 12 MB Cache, 512 GB RAM*) and IRIS (*4xE5-4640 Intel Xeon 8 cores CPU, 2.54 GHz,16 MB cache, 512 GB RAM*) at the Institutes of Geosciences, JGU Mainz, Germany. Each simulation takes 4-6 weeks and they were interrupted during the "static stage", when the mantle potential temperature and the low amount of fertile mantle prevents further development.

## 3. Supporting Figures and Tables

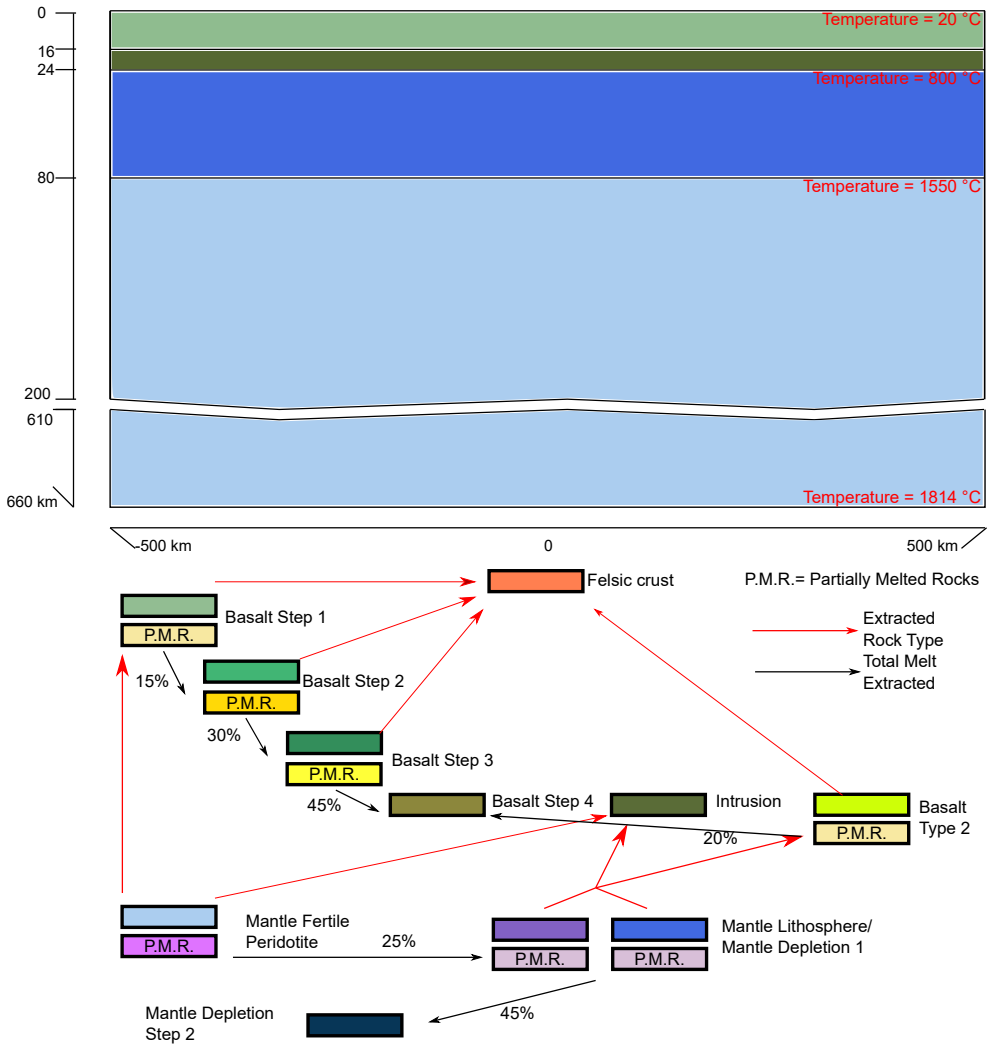


Figure A1: **Initial Setup**: Each extraction events from the mantle produce extrusion and intrusion (Basaltic Step 1 and Intrusion). Red arrows connect the sources with the extracted rock type. Mantle Fertile peridotite produces Basalt Step1 and dry intrusion. Black arrow connects the successive Step of depletion. If a particle associated with Basalt Step 1 reaches 15 % of total melt extracted, its phase diagram and rock type is changed into Basalt Step 2.

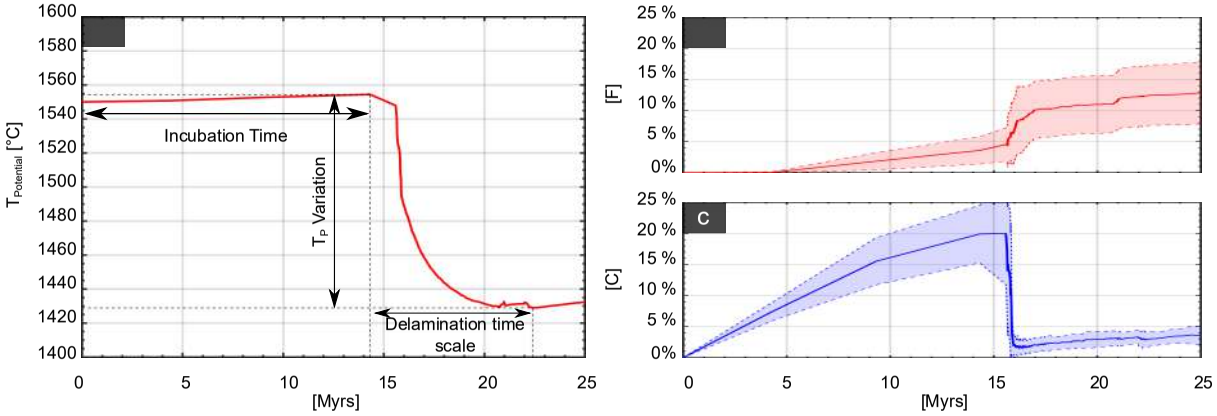


Figure A2: **Complementary Information Figure 1: a):** Temporal evolution of mantle potential temperature; **b):** Average amount of felsic material in the crust (F) (see eq. A1) versus time. The thick line represents the effective average, while the red shaded area between the dashed lines are the standard deviation of the data. Drip formation results in a rapid increase in felsic crust; **c):** Average C against time, where C represents the amount of converted basalt stage 1 (see equation 1.19). When the drip stage starts, C suddenly drops, implying a total foundering of the dense residuum into the mantle, and allowing a steady state consumption of the mafic crust during the static stage. The thick line represents the effective average, while the blue shaded area between the dashed lines are the standard deviation of the data.

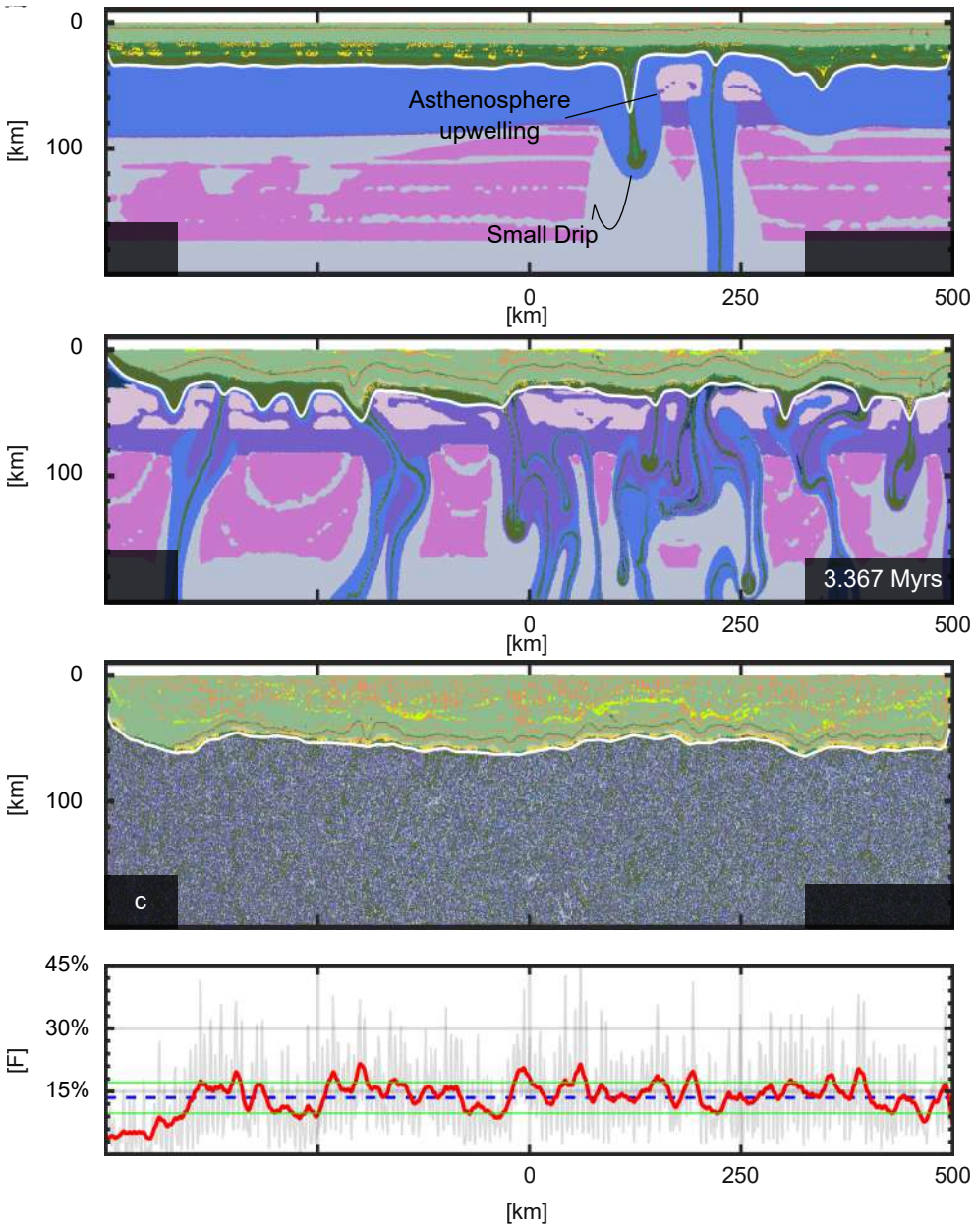


Figure A3: **Effect of high $T_{Moho}$($\lambda_{melt}$ = 0.01, $\phi_{dry}$=30°):** The initial Moho temperature is 1200 °C. **a):** Incubation stage; **b):** Dripping and Magmatic thickening stage; **c):** Static stage and compositional profile along the x direction (see S2 for further details)

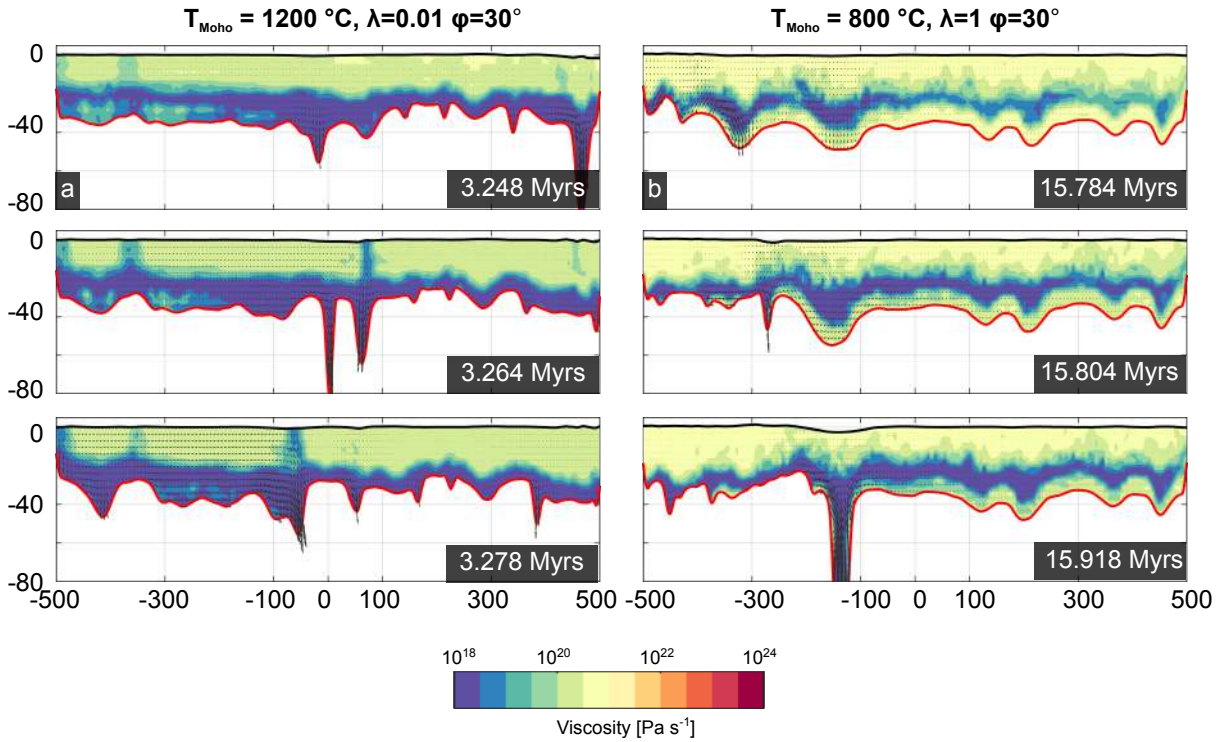


Figure A4: **Effect of high $T_{Moho}$ = 1200 °C and $\lambda_{melt}$=1 on the drips: a):** The initial $T_{Moho}$ is 1200 °C, while the other parameters have been kept the same respect to the reference test. During the onset of the dripping stage, the higher temperature jointly with the production of dense residuum, trigger the RTIs instabilities. Owing to the higher temperature, the dense residuum/intrusion are decoupled from the upper crust. Albeit the upper crust is deformed, is not experiencing significant deformation events; **b):** The melt weakening factor is not active. During the dripping stage the dense material transmit stress, but the crust is strong, and it is not yielding. This entails that the plastic deformation plays a fundamental role in the intraplate deformation stage and controls the ability of the crust to transfer pristine, hydrated/felsic material to the mantle.

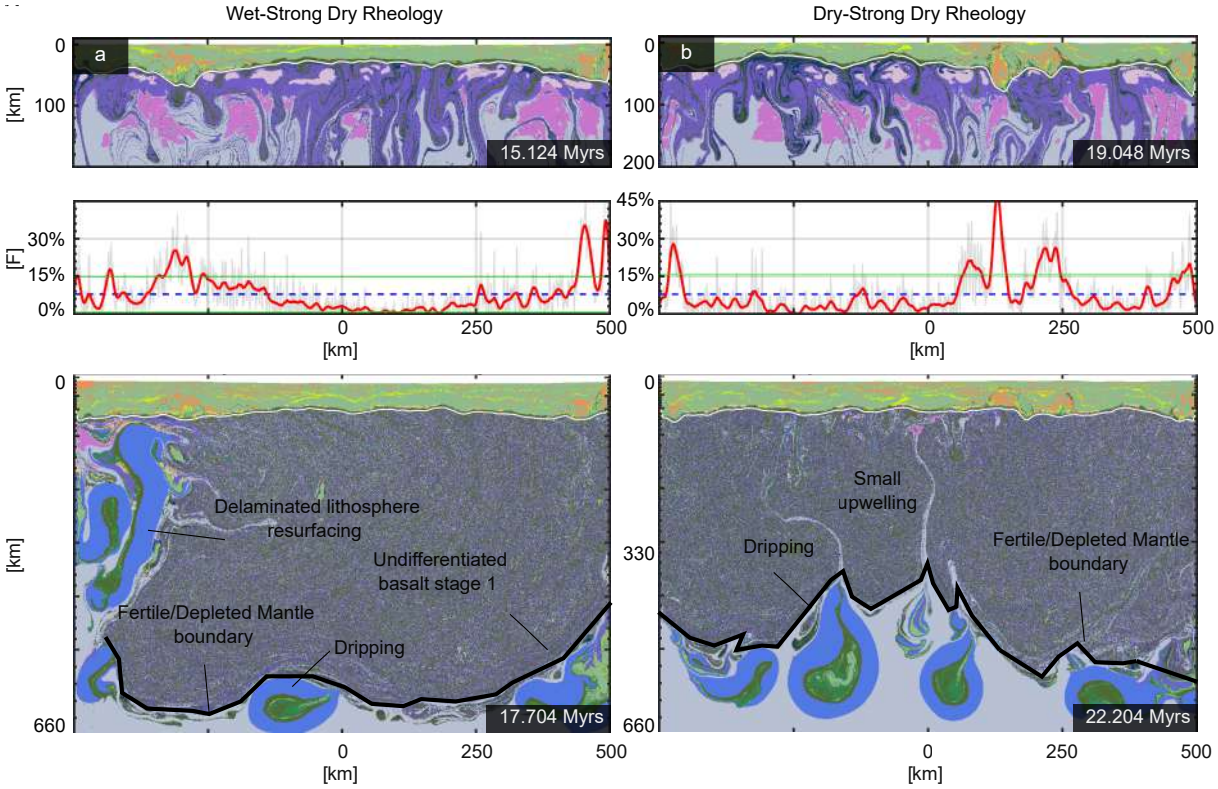


Figure A5: **Effect of the mantle depletion stiffening: a):** Experiment in which the mantle starts from a wet rheology and evolves towards a strong dry olivine rheology. To increase the effective viscous strength of the material, the pre-exponential factor of either the diffusion and dislocation creep has been incremented by one order of magnitude. The first picture in the upper left represents the lithospheric scale view of the tectonic thickening stage together with the compositional plot. The bottom left picture depicts the whole numerical domain during the static stage. The shape of the initial drip spans from tear shape to planar. Most of the mantle has been converted into the second step of depletion, and the mafic and ultramafic residuum are well mixed with the mantle. Only small fraction of primitive mantle has been preserved during the drip stages; **b):** Experiment in which the mantle starts from the dry olivine rheology then it evolves towards the strong dry rheology. The timescales of the processes increase, and most of the initial drip has a tear shape. The amount of converted mantle is less than the left experiments.

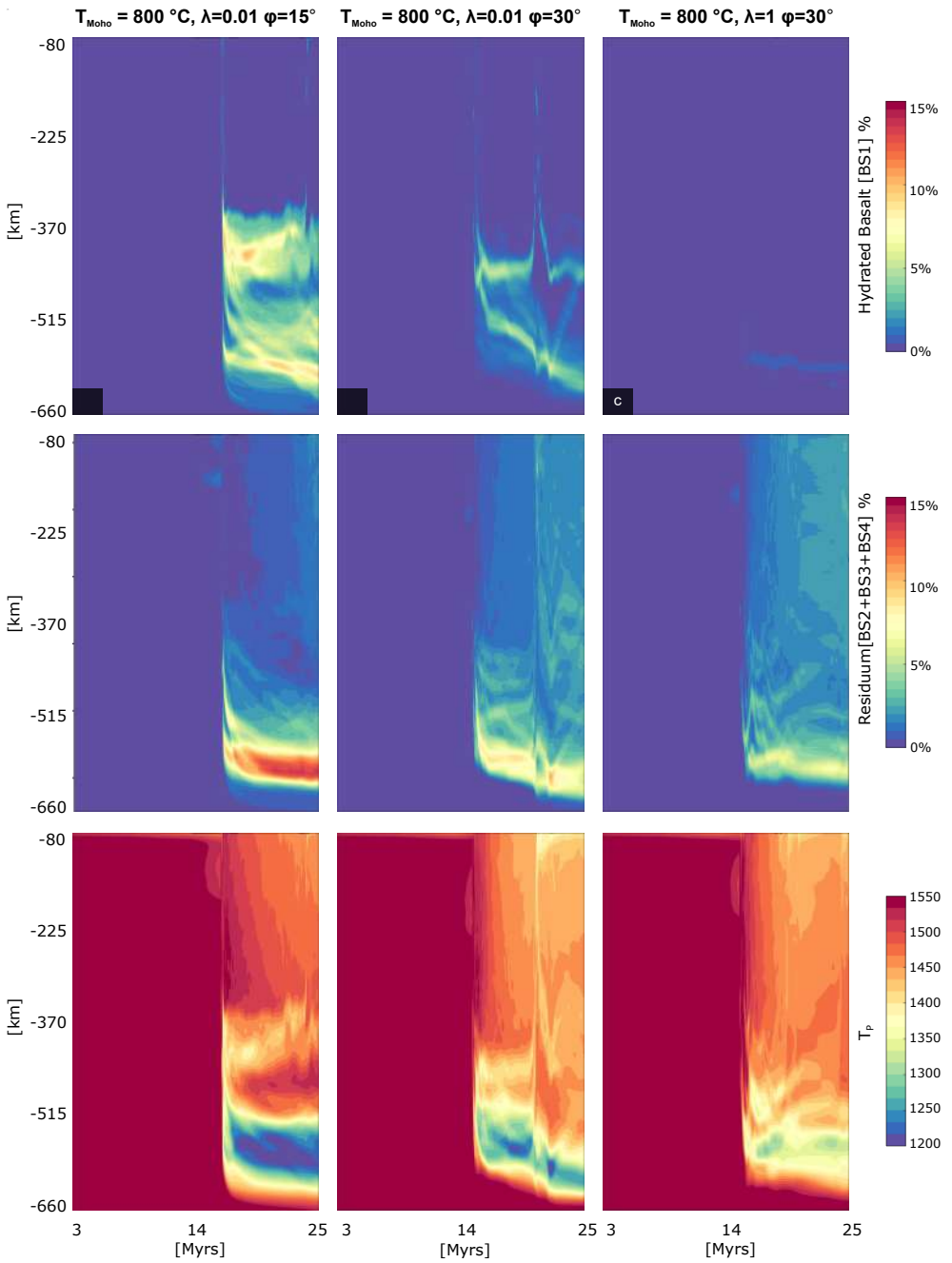


Figure A6: **Mantle thermal-compositional evolution:** Each column represents the data associated with a numerical experiment, while each row represents the different composition profile. The first row is the hydrous basalts that foundered into the mantle, the second row the amount of residuum and the third one the mantle potential temperature. Each plot represents the evolution of the horizontal average composition/temperature against time and depth. The dripping stage mix the mantle, but it may create compositional-thermal heterogeneities. The development of thermal-compositional heterogeneities is function of the mobility of the crust, and its ability to plastically yield.

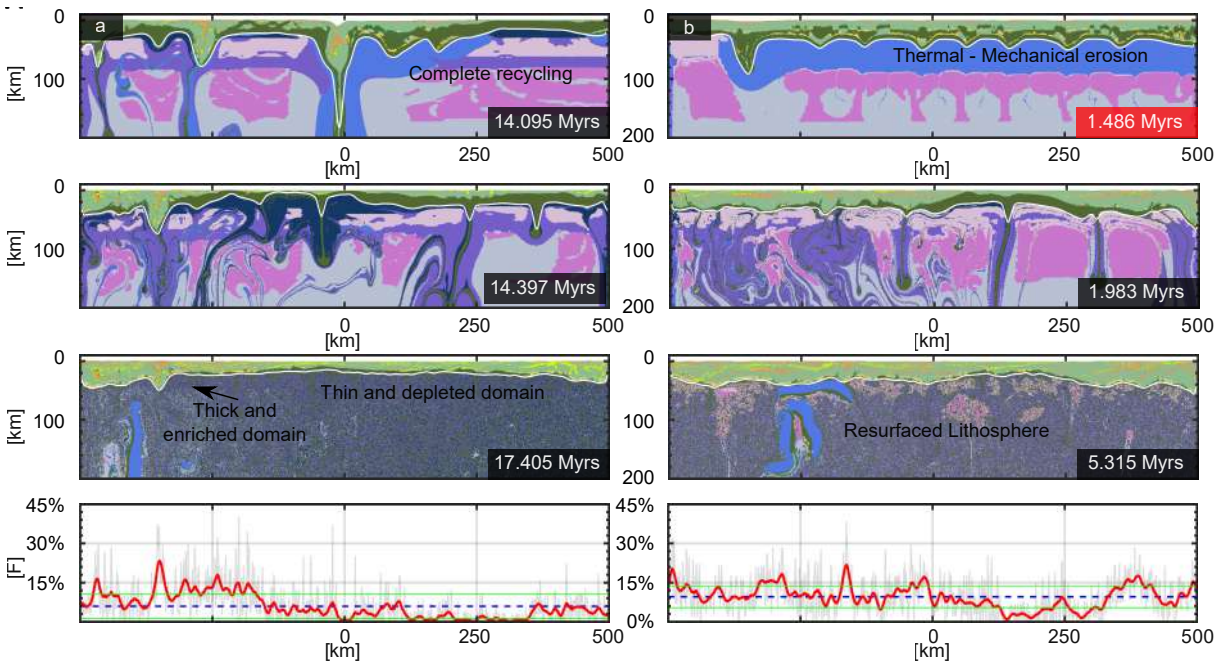


Figure A7: **Effects of the relative amount of intrusion per each extraction event and of the melt left after melt extraction event: a):** Experiment that has higher amount of intrusion per each extraction events. 80% of the total extracted melt from a mantle source (MDF or MDS1 and Lithospheric Mantle) is converted into dense mafic intrusions. The melt that remains on the source is the same of the reference test (0.2%). The first-middle left pictures represent the drip stage in which most of the older crust is recycled into the mantle. The third and the bottom left represent the static stage and the relative compositional profile; **b):** Experiments that has the same data of the left ones. The amount of melt that has to be left in the source is increased (2%). In such condition the drips are promoted since the beginning of the numerical experiments, achieving the static stage in less than 5 Myrs. The final thickness increases and the compositional difference between depleted and enriched domain are less pronounced.

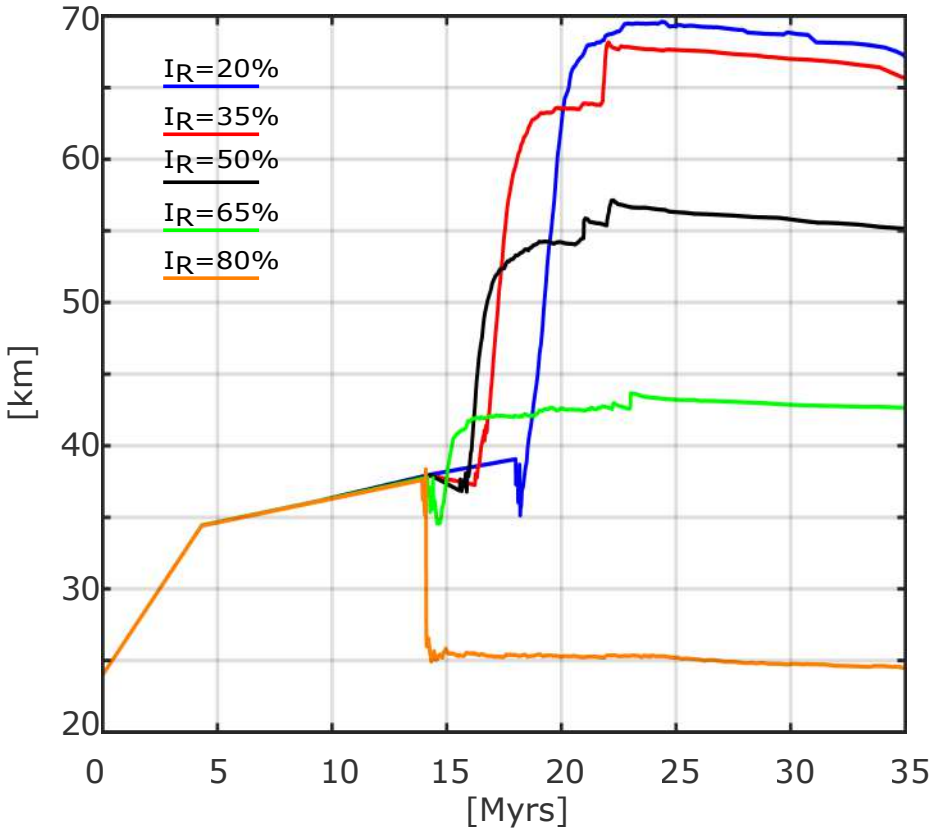


Figure A8: **Average crustal thickness against time for different $I_R$ values;**

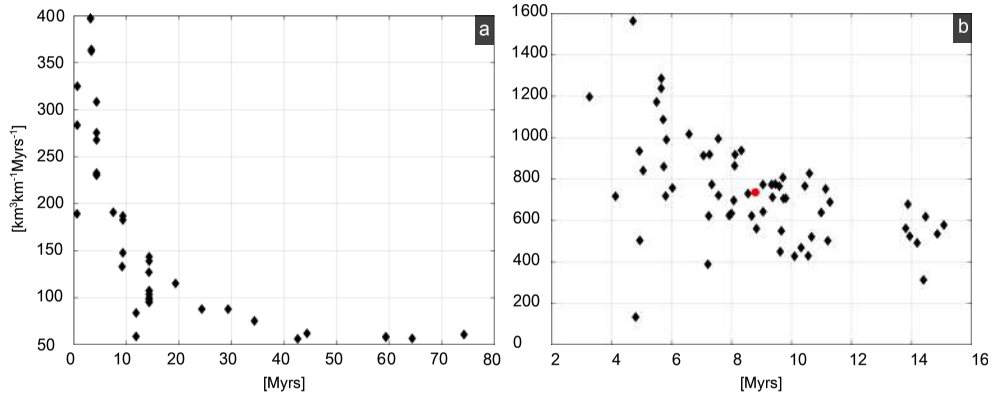


Figure A9: **Crustal production: a):** The continental crust production during the incubation stage vs the duration of this stage; **b):** The continental crust production during the dripping stage vs the duration of the dripping stage. The red dot represents the average crust production of the all experiments.

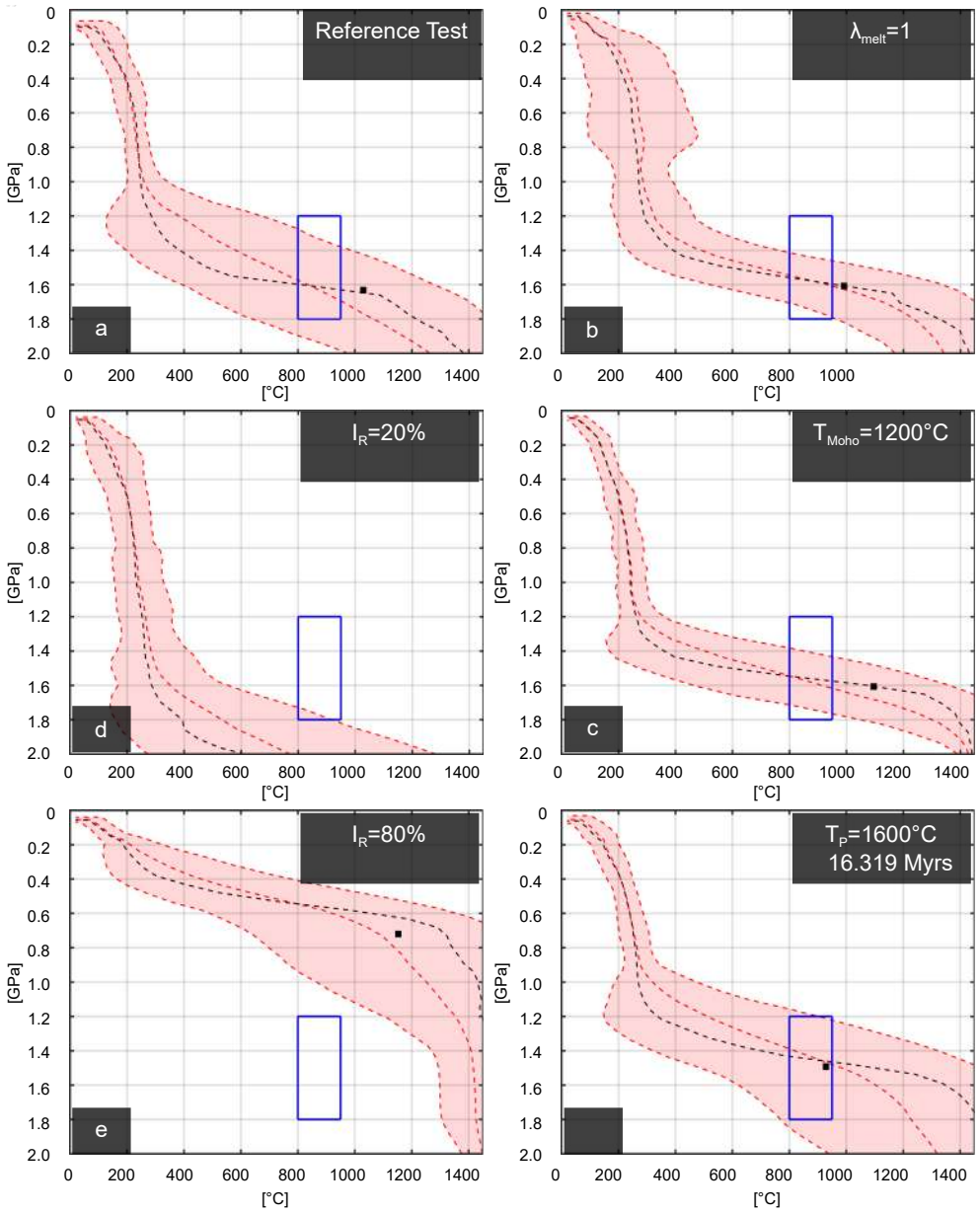


Figure A10: **Geothermal gradient achieved after the drip stage :**Each figure represents the variability and average P–T conditions of the crust. The dashed lines represent the upper and lower standard deviation. The median and average P–T conditions are compute averaging the conditions along x direction. The red dashed line in the middle of the interval represents the average. The black line is the median of the P–T conditions taken. The black square represents the average P–T conditions of the Moho. The blue square box represents the set of optimum conditions to generate TTG trace element signature. All the profiles are taken after the dripping stage when the average velocity at Moho depth reaches the steady state. Each subfigure represents one experiment, in the upper right corner are indicated the parameter that have been chanced respect to the reference test, and the timing at which such profile has been computed.

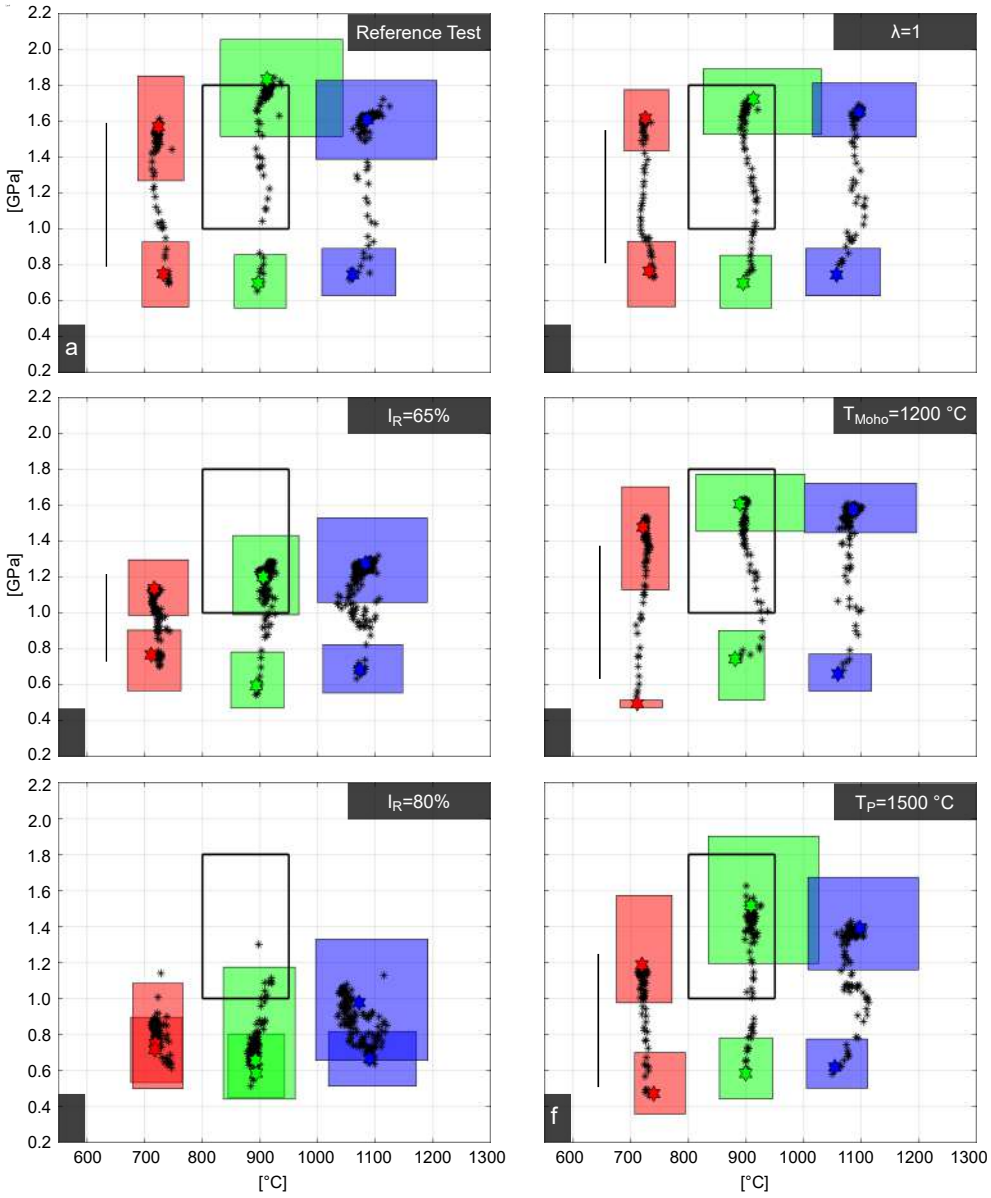


Figure A11: **Melting condition for each basalt step:** The colored boxes represent the average conditions of melting during the incubation stage and at the end of the dripping stage for each Basalt Step (BS1-3). Red is related to BS1, while green and blue are respectively BS2 and BS3. The hexagonal stars are the median condition, while the black asterisk that connect the incubation stage with the end of the dripping stage represent the median melting condition experienced during the whole dripping stage. Each picture represents a different experiment. In the upper right corner are indicated the input parameter that have been changed respect the reference test.

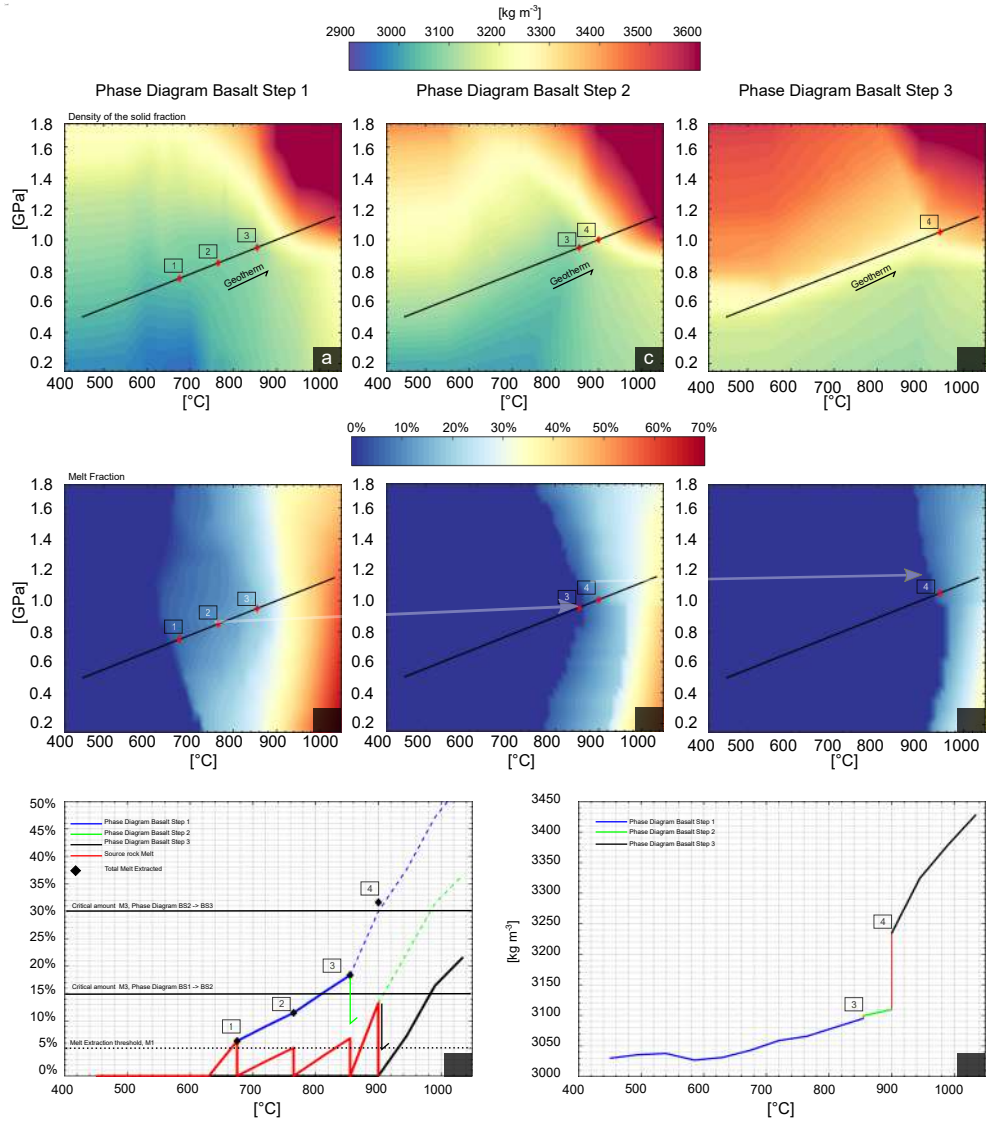


Figure A12: **Melt extraction: a-c-e):** Represents the density field associated with BS1,BS2 and BS3 respectively. The thick black line represents a hypothetical geotherm of 900°C/GPa. The diamond point represents extraction events that have been performed assuming a threshold of 5%; **b-d-f):** Represents the relative volumetric amount of melt. At the top of the field is plotted the geotherm and the relative extractions events; **g):** 1D representation of melt extraction processes. The red thick line represents the effective amount of melt stored in the particles. Melt extraction is allowed if the melt is exceeding 5% (dashed line). Once it exceeds it in the point 1, the melt is taken away from the source, and it remains dry. Then the system starts accumulating again melt. The effective amount of melt is interpolated from the phase diagram BS1 (blue line) then corrected with the total melt extracted within this melting step. The process is repeated other two times, until the total melt extracted (diamonds) exceed 15% threshold. After the third extraction the phase diagrams is changed, and the melt accumulation is ruled by the second phase diagrams (green line). We assume that the increase of temperature is fast, so once it reaches the 4 extraction events the total melt extracted is equal to the final threshold, and then the density and the melt quantity is interpolated from the third phase diagrams; **h):** Represents the density evolution experience by the marker as function of the P-T condition, and as function of the depletion. The last step of melt extraction occurs in the garnet tie line, entailing a significant jump of the density of the system.

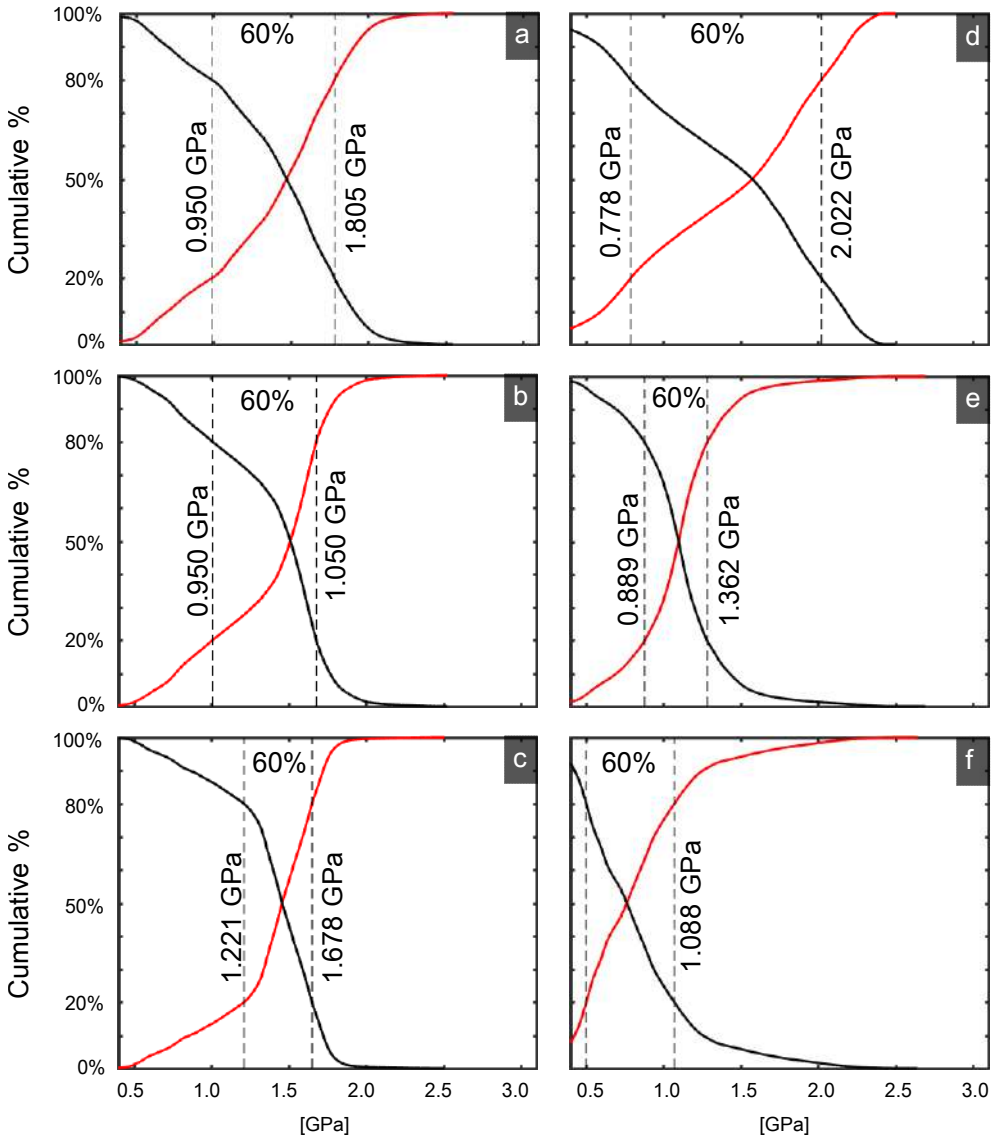


Figure A13: **Distribution of the melting pressures of the all basalt types:** We produce a cumulative distribution of the pressure condition at which any of the basalt types are melting. We plot the cumulative distribution(red thick line) and the reverse cumulative distribution (black thick line). All the experiments have the same condition of the reference test (panel **a)**) except for: **b):** $T_{Moho}$=1000 $^{\circ}C$; **c):** $T_{Moho}$=1200; **d):** $I_R$=20%; **e):** $I_R$=65%; **f):** $I_R$=80%.

Table A1: Reference Test (S1T1a1) input data. All the rock types have the same friction angle $\phi_{dry}$=30°, same cohesion, $C = 20MPa$ and same shear modulus, $G = 5 * 10^{10}$ Pa. The activaction volume for all the rocks types except for the dislocation creep of Dry olivine is $V_{act}$= 5*$10^{-6}$ $m^3mol^{-1}$, meanwhile for the latter is $V_{act}$= 1.5 $m^3mol^{-1}$. Diffusion creep: p=3.0 while d = 10 $m^{-3}$. The thermal expansivity is $\alpha$=3*$10^{-5}$ °$Cm^{-1}$. The compressibility is equal to $\beta$= 0.3 * $10^{-11}$ $Pa^{-1}$ (valid only for the felsic crust density law). $C_p$ =1050 $J/K/Kg$ for all the rock types.Heat conductivity (see (Clauser and Huenges, 1995; Gerya et al., 2008) ). **Rheology flow law** (a):(Hirth and Kohlstedt, 2004);(b):(Ranalli, 1995).**Phase Diagram** (1):(Johnson et al., 2013);(2):(Palin et al., 2016) .**Heat conductivity**:A:$k_1$=0.64,$k_2$=1293, $k_3$=4;B:$k_1$=1.18,$k_2$=474, $k_3$=4;C:$k_1$=0.64,$k_2$=807, $k_3$=4(Clauser and Huenges, 1995; Gerya et al., 2008); **Melt extraction data**: [1] $I_R$ (intrusion/extrusion)=50%;M1=0.5%;M2=0.2%;M3=25%. Mantle dep 2 does not produce any melt;[2]:M1=3%;M2=0.0%;M3=25%,$I_R$=100%; Intrusion and Basaltic stage 4 does not produce any melt.[2*] M3 = 20%. All the changes done are listed in Table S2

| Phase Name | Flow Law | $A_D$ $Pa^{-n}s^{-1}$ | $E_{act}$ $Jmol^{-1}$ | n | $Q_l$ $Jkg^{-1}$ | K $Wm^{-1}K^{-1}$ | $H_r$ $\mu Wm^{-3}$ | Phase Diagram |
|---|---|---|---|---|---|---|---|---|
| Astenophere[1] | Dry Olivile Dsl(a) | 1.1*$10^{-16}$ | 530*$10^3$ | 3.5 | 380*$10^3$ | A | 0.066 | Fertile Mantle(1) |
| Lithospheric M. [1] | | | | | | | 0.044 | Mantle Depleted (1) |
| Mantle D.Step 1[1] | Dry Olivile Diff(a) | 1.1*$10^{-16}$ | 375*$10^3$ | 0 | // | | 0.044 | Mantle Dep.(1) |
| Mantle D.Step 2[1] | | | | | | | 0.022 | Mantle Dep. w.m.(1) |
| Basalt Step 1[2] | W.Quartzite Disl(b) | 5.07*$10^{-18}$ | 154*$10^3$ | 2.3 | 380*$10^3$ | B | 0.88 | EAT B1 (2) |
| Basalt Step 2[2] | | | | | | | 0.69 | EAT B2 (2) |
| Basalt Step 3[2] | | | | | | | 0.5 | EAT B3 (2) |
| Basalt Type 2[2] | | | | | | | 0.88 | EAT B1 (2) |
| Basalt Step 4[2] | Maf. Granulite Disl(a) | 8.83*$10^{-22}$ | 445*$10^3$ | 4.2 | // | B | 0.25 | EAT B3 (2) |
| Intrusions [2] | | | | | | | 0.25 | EAT B3 (2) |
| Felsic | W.Quartzite Disl(b) | 5.07*$10^{-18}$ | 154*$10^3$ | 2.3 | // | C | 1.2 | Density Law |

Table A2: Simulations performed. The relevant input data are listed, all the experiments are based on the reference test, which input data are described in Table.S1. $F_0$ and $F_{fin}$ are respectively the amount of average felsic crust produced before the drip stage and at the end. $C_0$ and $t_0$ are the amount of converted basalts before the drip stage and the timing at which it starts. $\delta$t and $\delta T_P$ are the duration of the drip stage and the mantle potential temperature drop associated with it. $VFel_0$ and $VFel_{fin}$ are the absolute volume of Felsic crust produced before and at the end of the drip stage, and I and R are the relative amount of mafic intrusion and residuum in respect to all the composition field before the drip stage (Ar is the increase of viscosity associated with depletion. Each time the mantle changes composition-e.g. Fertile mantle to mantle depletion stage 1-, the viscosity is increased of a factor 10 or 100; Rh: is the starting rheology, D-D mean dry to dry, W-D wet to dry)

| TestName | $T_{Moho}$ °C | $\phi_{dry}$ | $\lambda_{melt}$ | $F_0$ | $F_{Fin}$ | $C_0$ | $t_0$ Myrs | $\Delta$t Myrs | $\Delta T_p$ °C | $VFel_0$ $km^3 km^{-1}$ | $VFel_{fin}$ $km^3 km^{-1}$ | I | R |
|---|---|---|---|---|---|---|---|---|---|---|---|---|---|
| S1T1a1 | 800 | 30 | 0,01 | 3,6 | 12,4 | 19,7 | 14,3 | 8,1 | 125,5 | 1353,2 | 7055,0 | 35,1 | 11,9 |
| S1T1a2 | 800 | 30 | 0,1 | 3,6 | 12,5 | 19,7 | 14,3 | 7,3 | 124,2 | 1357,6 | 7094,4 | 35,1 | 11,9 |
| S1T1a3 | 800 | 30 | 0,5 | 3,6 | 16,4 | 19,7 | 14,3 | 11,3 | 112,7 | 1358,6 | 9105,4 | 35,1 | 11,9 |
| S1T1a4 | 800 | 30 | 1 | 3,6 | 13,8 | 19,7 | 14,3 | 5,5 | 110,3 | 1358,6 | 7796,3 | 35,1 | 11,9 |
| S1T1b1 | 1000 | 30 | 0,01 | 2,9 | 14,3 | 16,3 | 4,3 | 9,6 | 105,4 | 1004,2 | 8322,8 | 34,6 | 10,1 |
| S1T1b2 | 1000 | 30 | 0,1 | 2,9 | 14,6 | 16,3 | 4,3 | 8,3 | 103,5 | 994,0 | 8829,9 | 34,6 | 10,1 |
| S1T1b3 | 1000 | 30 | 0,5 | 2,9 | 14,3 | 16,3 | 4,3 | 9,3 | 100,5 | 994,0 | 8248,1 | 34,6 | 10,1 |
| S1T1b4 | 1000 | 30 | 1 | 2,9 | 14,6 | 16,3 | 4,3 | 9,7 | 98,0 | 994,0 | 8332,5 | 34,6 | 10,1 |
| S1T1c1 | 1200 | 30 | 0,01 | 3,7 | 14,5 | 29,6 | 3,2 | 7,3 | 93,7 | 1257,0 | 7913,2 | 33,9 | 18,3 |
| S1T1c2 | 1200 | 30 | 0,1 | 3,7 | 16,1 | 29,6 | 3,2 | 7,6 | 92,2 | 1257,7 | 8802,0 | 34,0 | 18,3 |
| S1T1c3 | 1200 | 30 | 0,5 | 3,7 | 14,7 | 29,6 | 3,2 | 5,7 | 93,3 | 1257,7 | 8564,3 | 34,0 | 18,3 |
| S1T1c4 | 1200 | 30 | 1 | 3,7 | 13,7 | 29,6 | 3,2 | 5,7 | 87,7 | 1257,8 | 7530,0 | 34,0 | 18,3 |
| S1T1a115 | 800 | 15 | 0,01 | 4,0 | 12,1 | 20,4 | 14,3 | 9,6 | 120,6 | 1529,6 | 5890,5 | 32,3 | 12,8 |
| S1T1a215 | 800 | 15 | 0,1 | 3,9 | 15,6 | 20,1 | 14,3 | 14,2 | 110,8 | 1475,8 | 8451,9 | 32,3 | 12,7 |
| S1T1a315 | 800 | 15 | 0,5 | 3,9 | 15,2 | 20,1 | 14,3 | 13,9 | 101,3 | 1476,3 | 8748,7 | 32,3 | 12,7 |
| S1T1a415 | 800 | 15 | 1 | 3,9 | 16,1 | 20,1 | 14,3 | 13,8 | 98,4 | 1476,3 | 9256,6 | 32,3 | 12,7 |
| S1T1b115 | 1000 | 15 | 0,01 | 3,9 | 18,2 | 17,9 | 4,3 | 15,1 | 87,5 | 1331,1 | 10048,4 | 31,7 | 11,4 |
| S1T1b215 | 1000 | 15 | 0,1 | 3,9 | 16,4 | 17,9 | 4,3 | 14,9 | 83,6 | 1331,1 | 9308,3 | 31,7 | 11,4 |
| S1T1b315 | 1000 | 15 | 0,5 | 3,9 | 19,1 | 17,9 | 4,3 | 13,9 | 82,3 | 1331,1 | 10745,8 | 31,7 | 11,4 |
| S1T1b415 | 1000 | 15 | 1 | 3,9 | 18,2 | 17,9 | 4,3 | 14,5 | 81,2 | 1331,1 | 10312,6 | 31,7 | 11,4 |
| S1T1c115 | 1200 | 15 | 0,01 | 3,5 | 17,5 | 32,8 | 3,3 | 10,4 | 71,4 | 1206,9 | 9239,8 | 31,2 | 21,2 |
| S1T1c215 | 1200 | 15 | 0,1 | 3,5 | 15,5 | 32,8 | 3,3 | 11,0 | 70,8 | 1207,6 | 8273,6 | 31,2 | 21,3 |
| S1T1c315 | 1200 | 15 | 0,5 | 3,5 | 18,4 | 32,8 | 3,3 | 10,6 | 71,7 | 1212,9 | 10031,8 | 31,2 | 21,3 |
| S1T1c415 | 1200 | 15 | 1 | 3,5 | 17,5 | 32,8 | 3,3 | 11,1 | 71,2 | 1213,2 | 9659,8 | 31,2 | 21,3 |
| S1T1a105 | 800 | 5 | 0,01 | 4,0 | 14,0 | 20,5 | 14,3 | 14,4 | 147,1 | 1533,9 | 6112,4 | 32,2 | 12,9 |
| S1T1a205 | 800 | 5 | 0,1 | 3,7 | 9,9 | 19,4 | 14,3 | 7,2 | 158,8 | 1396,2 | 4246,8 | 35,0 | 11,7 |
| S1T1a305 | 800 | 5 | 0,5 | 3,8 | 12,1 | 19,4 | 14,3 | 10,6 | 148,5 | 1422,3 | 5963,2 | 35,0 | 11,7 |
| S1T1b105 | 1000 | 5 | 0,01 | 2,9 | 13,9 | 16,2 | 4,3 | 9,4 | 124,2 | 995,6 | 7652,2 | 34,7 | 10,1 |
| S1T1b205 | 1000 | 5 | 0,1 | 2,9 | 15,3 | 16,3 | 4,3 | 9,7 | 110,4 | 997,6 | 8860,3 | 34,6 | 10,1 |
| S1T1b305 | 1000 | 5 | 0,5 | 2,9 | 13,4 | 16,3 | 4,3 | 9,0 | 106,2 | 994,9 | 7963,6 | 34,7 | 10,1 |
| S1T1b405 | 1000 | 5 | 1 | 2,9 | 13,6 | 16,3 | 4,3 | 9,8 | 99,6 | 994,9 | 7883,4 | 34,7 | 10,1 |
| S1T1c105 | 1200 | 5 | 0,01 | 3,7 | 15,2 | 29,6 | 3,2 | 8,1 | 101,4 | 1258,6 | 8754,7 | 33,9 | 18,4 |
| S1T1c205 | 1200 | 5 | 0,1 | 3,7 | 13,5 | 29,6 | 3,2 | 8,6 | 97,7 | 1256,6 | 7530,6 | 33,9 | 18,4 |
| S1T1c305 | 1200 | 5 | 0,5 | 3,7 | 14,8 | 29,6 | 3,2 | 8,1 | 95,1 | 1258,7 | 8324,9 | 33,9 | 18,3 |
| S1T1c405 | 1200 | 5 | 1 | 3,7 | 13,8 | 29,6 | 3,2 | 6,6 | 96,6 | 1258,8 | 8003,0 | 33,9 | 18,3 |
| | $A_r$ | Rh | $T_{Moho}$ °C | | | | | | | | | | |
| S2T1A1DD | 10 | DD | 800 | 3,6 | 12,4 | 20,1 | 14,3 | 10,7 | 135,9 | 1366,1 | 7007,7 | 35,2 | 12,1 |
| S2T1A1DDb | 10 | DD | 1000 | 4,7 | 14,9 | 22,5 | 9,3 | 4,7 | 105,7 | 1704,1 | 9049,3 | 35,1 | 13,4 |
| S2T1A1DDc | 10 | DD | 1200 | 3,3 | 13,3 | 30,9 | 4,3 | 5,7 | 96,2 | 1156,2 | 8247,0 | 34,1 | 19,3 |
| S2T1A2DD | 100 | DD | 800 | 5,6 | 11,0 | 25,6 | 19,3 | 5,8 | 129,6 | 2213,9 | 6377,3 | 35,4 | 14,8 |
| S2T1A2DDb | 100 | DD | 1000 | 4,8 | 12,7 | 22,6 | 9,3 | 5,8 | 98,1 | 1741,2 | 7484,0 | 35,0 | 13,5 |
| S2T1A2DDc | 100 | DD | 1200 | 3,4 | 12,4 | 30,8 | 4,3 | 7,1 | 86,0 | 1189,2 | 7601,2 | 34,2 | 19,1 |
| S2T1A0WD | 1 | WD | 800 | 3,5 | 11,9 | 15,1 | 9,3 | 8,7 | 138,0 | 1370,4 | 6796,6 | 34,3 | 9,3 |
| S2T1A1WD | 10 | WD | 800 | 5,1 | 10,6 | 18,1 | 14,3 | 3,3 | 139,7 | 2036,3 | 5991,5 | 34,5 | 10,7 |
| | $I_R$ | M2 | | | | | | | | | | | |
| S3T1M0020 | 20 | 0,2 | | 5,3 | 14,9 | 21,1 | 14,3 | 11,6 | 132,5 | 2024,8 | 10345,0 | 30,3 | 13,4 |
| S3T1M0035 | 35 | 0,2 | | 4,0 | 13,9 | 16,7 | 14,3 | 8,0 | 122,6 | 1504,8 | 9396,0 | 31,9 | 10,6 |
| S3T1M0065 | 65 | 0,2 | | 3,7 | 13,7 | 19,3 | 14,2 | 8,0 | 130,8 | 1398,3 | 5833,0 | 38,7 | 10,9 |
| S3T1M0080 | 80 | 0,2 | | 1,4 | 8,2 | 13,6 | 9,3 | 15,0 | 140,3 | 498,6 | 2081,3 | 42,4 | 7,7 |
| S3T1M1050 | 50 | 2 | | 2,0 | 12,4 | 11,4 | 0,8 | 9,5 | 115,2 | 701,2 | 7000,1 | 32,5 | 7,5 |
| S3T1M1065 | 65 | 2 | | 1,5 | 10,6 | 9,9 | 0,8 | 5,9 | 110,8 | 552,5 | 4776,3 | 36,4 | 6,2 |
| S3T1M1080 | 80 | 2 | | 1,3 | 9,4 | 9,5 | 0,8 | 4,0 | 114,7 | 451,9 | 3209,7 | 40,4 | 5,6 |
| | $T_P$ °C | Thikckness km | M2 | | | | | | | | | | |
| S4T180A | 1450 | 80 | 0,2 | 12,4 | 18,3 | 72,8 | 64,3 | 4,9 | 75,7 | 3655,3 | 8167,2 | 34,8 | 38,3 |
| S4T180B | 1500 | 80 | 0,2 | 7,7 | 15,6 | 38,6 | 29,3 | 7,9 | 109,1 | 2552,6 | 7571,4 | 33,0 | 22,7 |
| S4T180D | 1600 | 80 | 0,2 | 3,2 | 12,5 | 15,8 | 7,5 | 8,8 | 188,9 | 1427,9 | 6387,9 | 34,9 | 9,7 |
| S4T180A$_{m2}$ | 1450 | 80 | 2 | 8,3 | 15,3 | 51,4 | 42,6 | 5,1 | 76,1 | 2384,9 | 6678,5 | 35,1 | 28,9 |
| S4T180B$_{m2}$ | 1500 | 80 | 2 | 5,7 | 16,3 | 28,6 | 18,8 | 6,5 | 89,3 | 1859,4 | 7881,4 | 33,0 | 17,5 |
| S4T180D$_{m2}$ | 1600 | 80 | 2 | 2,4 | 11,2 | 9,0 | 0,6 | 9,9 | 157,2 | 1036,8 | 6721,9 | 33,9 | 5,6 |
| S4T1100A | 1450 | 100 | 0,2 | 14,0 | 15,7 | 82,2 | 74,2 | 4,9 | 82,6 | 4472,7 | 7052,7 | 36,0 | 41,1 |
| S4T1100B | 1500 | 100 | 0,2 | 7,8 | 16,2 | 46,7 | 44,3 | 10,1 | 103,0 | 2737,8 | 7064,5 | 35,5 | 26,4 |
| S4T1100C | 1550 | 100 | 0,2 | 5,3 | 14,6 | 26,5 | 24,3 | 9,1 | 136,7 | 2116,7 | 7946,2 | 33,4 | 16,0 |
| S4T1100D | 1600 | 100 | 0,2 | 2,8 | 12,3 | 14,9 | 9,2 | 11,2 | 178,2 | 1219,2 | 6889,7 | 34,4 | 9,2 |
| S4T1120A | 1450 | 120 | 0,2 | 9,5 | 18,4 | 58,8 | 59,3 | 7,2 | 90,3 | 3468,1 | 8011,1 | 35,8 | 32,1 |
| S4T1120B | 1500 | 120 | 0,2 | 9,1 | 17,5 | 58,0 | 59,3 | 8,0 | 113,3 | 3434,1 | 8453,7 | 36,7 | 31,4 |
| S4T1120C | 1550 | 120 | 0,2 | 6,2 | 14,6 | 40,1 | 34,3 | 7,6 | 155,8 | 2573,6 | 8002,1 | 35,5 | 23,3 |
| S4T1120D | 1600 | 120 | 0,2 | 4,0 | 11,6 | 19,3 | 14,3 | 9,7 | 191,1 | 1812,9 | 7224,7 | 34,7 | 11,7 |

# REFERENCES


Clauser, C., Huenges, E., 1995. Thermal conductivity of rocks and minerals. Rock physics & phase relations 3, 105–126.

Gerya, T.V., Perchuk, L.L., Burg, J.P., 2008. Transient hot channels: Perpetrating and regurgitating ultrahigh-pressure, high-temperature crust–mantle associations in collision belts. Lithos 103, 236–256. doi:10.1016/j.lithos.2007.09.017.

Hirth, G., Kohlstedt, D., 2004. Rheology of the upper mantle and the mantle wedge: A view from the experimentalists. Inside the subduction Factory 138, 83–105.

Johnson, T.E., Brown, M., Kaus, B.J.P., VanTongeren, J.A., 2013. Delamination and recycling of Archaean crust caused by gravitational instabilities. Nature Geoscience 7, 47–52. URL: http://www.nature.com/doifinder/10.1038/ngeo2019, doi:10.1038/ngeo2019.

Kaus, B.J.P., Mühlhaus, H., May, D.A., 2010. A stabilization algorithm for geodynamic numerical simulations with a free surface. Physics of the Earth and Planetary Interiors 181, 12–20. URL: http://linkinghub.elsevier.com/retrieve/pii/S0031920110000877, doi:10.1016/j.pepi.2010.04.007.

Palin, R.M., White, R.W., Green, E.C., 2016. Partial melting of metabasic rocks and the generation of tonalitic–trondhjemitic–granodioritic (ttg) crust in the archaean: Constraints from phase equilibrium modelling. Precambrian Research 287, 73–90.

Ranalli, G., 1995. Rheology of the earth, 413 pp.

# APPENDIX B

## B.1 Post-processing and hardware information

LaMEM is a finite difference staggered-grid code. Melt extraction is performed in the central nodes, which are the one used to compute the continuity equation and where temperature and pressure are defined. The output grid used for visualization and data analysis is defined on the corner nodes of the staggered-grid, and all the variables are interpolated on the visualization grid. This interpolation might affect melt extraction temperatures, as the interpolation slightly smoothen the temperature variation. Furthermore, most of the data are picked each time the output is created. This strategy was necessary to minimize the amount of memory needed to store the numerical experiments. As a consequence, the melt extraction events that we used in our analysis are affected by both interpolation scheme and the number of output steps that are produced. The data concerning TTGs melting condition represents a small population of the total conditions of extractions. 2D experiments are less memory demanding than 3D, and we saved the output every 50 timesteps, while 3D experiments outputs were saved every 200 timesteps. 2D numerical experiments required 10-20 thousands timesteps to be completed (~ 40 Myrs model time, 2-3 weeks per run), while 3D experiments required 30-40 thousands timesteps (~ 10 Myrs model time, 2-3 months per simulations on 512 cores).

### B.1.1 Moho identification and internal free surfaces

We divided the rock-types into three main categories: *1)* Mantle (*Ml*); *2)* Mafic crust (*MC*); *3)* Continental crust (*CC*). At each timestep, the phase proportion of the three categories are computed by summing the phase ratio of mantle, mafic and continental rock-types respectively.

To constraint the Moho depth LaMEM sums the contribution of *CC* and *MC*, after which it loops from bottom to top saving the $z$ coordinates of the nodes featuring $CC + MC < 0.8$ (during this operation the air phases is considered part of the crust as well).
At the beginning of each simulation the free surface is defined and shifted accordingly to the velocity field at the end of each timestep. The topography is corrected if its angle with respect to the horizontal plane is higher than 30°. The topography is measured using as reference the average depth of the free surface. The thickness is computed before solving the system of equations, and it is used to inject particles as a function of melt extraction parameters.
The cumulative melt production is computed by summing the total melt extracted along $z$ direction, at every timestep:

$$V_{cum}^{Tot}(i,j,Ml/MC,t) = \sum_{dts=1}^{ts} V_{ext}^{Tot}(i,j,Ml/MC)(i) \tag{B1}$$

*i,j* are the grid indexes, $V_{cum}^{tot}$ is the total volume cumulated during the whole simulation and computed for $MC$ or $Ml$, $ts$ is the current timestep ($ts$), while $dts$ is the timestep increment. Generation temperatures ($T^{Gen}$) are computed each timestep, averaging the temperature at which the mafic melts are produced along $z$ direction and considering the volumetric contribution of each rock-type.
*F*, the relative amount of felsic crust, is computed by integrating all the *CC* phase ratio along $z$ direction divided by the local thickness (*Tk*) of the crust. The integration is within the local Moho depth and the topography (*Topo*):

$$F = \frac{\sum_{k_{Moho(i,j)}}^{k_{Topo(i,j)}} CC(k)\Delta z(k)}{Tk(i,j)} \tag{B2}$$

### B.1.2 Hardware information and solver option

The simulations were perfomed using the supercomputers offered by Johannes Gutenberg University, MOGON and MOGONII (`hpc.uni-mainz.de`). LaMEM is a PETSc based code (Balay et al., 2018), and the solving of the non linear system of equation were performed thanks to the PETSc infrastructure. 2D experiments were performed using 8 cores and using the direct solver *mumps*, the internal linear solver is *fgmres* with a maximum of 30 linear iteration, and relative tolerance of $10^{-6}$; while the external non linear solver were allowed to iterate maximum 30 times, and the relative tolerance was set to be $10^{-6}$. 3D numerical experiments were performed using 512 processors and using Eisenstadt-Wanker methods, with a tolerance

spanning from $10^{-1}$ to $10^{-4}$; the internal linear solver *fgmres* and the number of iteration allowed spans from 4 to 180.

## B.2 Supplementary table and figures

### B.2.1 Supplementary Tables

Table B1: List of symbols and relative unit of measure

| Symbol | S.I. unit | Definition |
|---|---|---|
| $v_i$ | $ms^{-1}$ | velocity vector component |
| $\dot{S}, \dot{S}$ | $s^{-1}$ | Negative and positive volumetric source terms |
| $\tau_{ij}, \tau_{II}, P$ | $Pa$ | Deviatoric stress component, 2nd invariant of the deviatoric stress tensor,Pressure |
| $\rho$ | $kgm^{-3}$ | Density |
| $g$ | $ms^{-2}$ | Gravity acceleration |
| $\dot{\epsilon}_{ij}, \dot{\epsilon}_{ij}^{el,pl,vis}, \dot{\epsilon}_{II}$ | $s^{-1}$ | Strain rate component, elastic,visco,plastic strain rate component,2nd invariant strain rate tensor |
| $\circ\tau_{ij}$ | $Pas^{-1}$ | Objective deviatoric stress component time derivative |
| $\omega_{ij}$ | $s^{-1}$ | Spin tensor component |
| $G$ | $GPa$ | Shear modulus |
| $\eta$ | $Pas$ | Viscosity |
| $B$ | $MPa^n s^{-1}$ | Pre-exponential factor |
| n | n.d. | Stress exponent |
| $E_a$ | $kJmol^{-1}$ | Activation energy |
| $V_a$ | $JMPa^{-1}mol^{-1}$ | Activation volume |
| $\phi, \phi_0, \phi_1$ | // | friction angle, initial friction angle, final friction angle |
| $C, C_0, C_1$ | $MPa$ | cohesion, initial cohesion, final cohesion |
| $T$ | $K, ^\circ C$ | Temperature |
| $k$ | $WK^{-1}$ | Heat conductivity |
| $A$ | $\mu Wkg^{-1}$ | Radiogenic heating per unit of mass |
| $H_a, H_s, H_r$ | $Wm^{-3}$ | Adiabatic, Shear and Radiogenic heating per unit of volume |
| $ph_{Rat}$ | n.d. | Phase proportion |
| $M_{ext}$ | n.d. | Melt fraction extracted |
| $V_{ext}$ | $m^3$ | Extracted volume |
| $V_{ext}^{tot}$ | $m^3$ | Total volume extracted along $z$ |
| $V_{eff}, V_{int}$ | $m^3$ | Effusion and intrusion volume |
| $Vol_{cor}$ | n.d. | Volumetric correction |
| $v_{int}$ | $m^3 m^{-1}$ | Volume of intrusion per unit of length |
| $D_{min}, D_{max}$ | $m$ | Extreme of depth interval of intrusion |
| $D, D_{int}$ | n.d. | Relative distance from Moho, and relative half interval of intrusion |
| $Tk, Tkl$ | $km$ | Crust and lithosphere thickness |

Table B2: List of the petrophysical properties and phase diagrams. The symbol and relative unit of measures are listed Tab. B1. All rock types share the same: shear modulus, ($G$ = $40GPa$); initial and final friction angle ($\phi_0$ = $30^\circ$ and $\phi_1$ = $9^\circ$); initial and final cohesion ($C_0$ = $10MPa$ and $C_1$=3 MPa); heat capacity ($C_p$ = 1200 $J/K/Kg$); thermal conductivity ($k$ = 3). (a)(Hirth and Kohlstedt, 2004); (b) (Ranalli, 1995). Mantle phase diagrams are produced for the current work, while the mafic crust phase diagrams are taken from Piccolo et al. (2019).

| | **Rock Type** | **Phase Diagram** | **Viscous Rheology** | **B** | **n** | **A** | **$E_a$** | **$V_a$** |
|---|---|---|---|---|---|---|---|---|
| Mantle(*MI*) | MD0% | MD0% | Dry Olivile Dsl(a) | 1.1 $10^5$ | 3.5 | $2 \times 10^{-5}$ | 530 | 15 |
| | MD10% | MD10% | | | | $1.6 \times 10^{-5}$ | | |
| | MD20% | MD20% | | | | $1.3 \times 10^{-5}$ | | |
| | MD30% | MD30% | | | | $1.0 \times 10^{-5}$ | | |
| | MD40% | MD40% | | | | $0.67 \times 10^{-5}$ | | |
| | MD50% | MD50% | | | | $0.33 \times 10^{-5}$ | | |
| Mafic Crust(*MC*) | BS0% | BS0% | Wet Quarzite(b) | 3.20 $10^{-4}$ | 2.3 | $2.93 \times 10^{-4}$ | 156 | 0 |
| | BS15% | BS15% | | | | $2.2 \times 10^{-4}$ | | |
| | BS30% | BS30% | | | | $1.467 \times 10^{-4}$ | | |
| | BS45% | BS45% | Mafic Granulite (b) | 1.4 $10^4$ | 4.2 | $0.7 \times 10^{-4}$ | 445 | 0 |
| | Intrusions | BS45% | | | | | | |
| | Continental Crust | 2700 | Wet Quarzite(b) | 3.20 $10^{-4}$ | 2.3 | $2 \times 10^{-3}$ | 156 | 0 |

Table B3: Test names and list of parameters. $D$, $D_{int}$ , $dM$ and $M^{trs}$ are the melt extraction parameter of mantle phases. The mafic crust extraction parameter are equal for most of experiments($dM$ = 0.01, $M^{trs}$ = 0.08, $D$ = 0.7 and $D_{int}$ = 0.2).(1) $A$ of all mantle phases is $0.33 \times 10^{-5}$ $\mu W/kg$ and the lower thermal boundary condition is 1600 °C. (2) Mafic crust melt extraction parameters $dM$ and $M^{trs}$ are 0.08 and 0.15 respectively.

| **Test Name** | | | | | | | |
|---|---|---|---|---|---|---|---|
| **2D** | **Mtrs** | **dM** | **T**$_P[^\circ C]$ | **D** | $D_{int}$ | **TkL**$[km]$ | **R**$[km]$ |
| Test1L | 0.001 | 0.001 | 1500 | 0.3 | 0.3 | 100 | 200 |
| Test2L | 0.001 | 0.01 | 1500 | 0.3 | 0.3 | 100 | 200 |
| Test3L | 0.001 | 0.05 | 1500 | 0.3 | 0.3 | 100 | 200 |
| Test4L | 0.01 | 0.001 | 1500 | 0.3 | 0.3 | 100 | 200 |
| Test5L | 0.01 | 0.01 | 1500 | 0.3 | 0.3 | 100 | 200 |
| Test6L | 0.01 | 0.05 | 1500 | 0.3 | 0.3 | 100 | 200 |
| Test7L | 0.05 | 0.001 | 1500 | 0.3 | 0.3 | 100 | 200 |
| Test8L | 0.05 | 0.01 | 1500 | 0.3 | 0.3 | 100 | 200 |
| Test9L | 0.05 | 0.05 | 1500 | 0.3 | 0.3 | 100 | 200 |
| Test3L$_{D0102}$ | 0.001 | 0.05 | 1500 | 0.1 | 0.2 | 100 | 200 |
| Test3L$_{D0202}$ | 0.001 | 0.05 | 1500 | 0.2 | 0.2 | 100 | 200 |
| Test3L$_{1400}$D0202 | 0.001 | 0.05 | 1400 | 0.2 | 0.2 | 100 | 200 |
| Test3L$_{1550}$ | 0.001 | 0.05 | 1550 | 0.3 | 0.3 | 100 | 200 |
| Test3L$_{1450}$ | 0.001 | 0.05 | 1450 | 0.3 | 0.3 | 100 | 200 |
| Test3L$_{1450}$LT | 0.001 | 0.05 | 1400 | 0.3 | 0.3 | 80 | 200 |
| Test3L$_{1400}$ | 0.001 | 0.05 | 1400 | 0.3 | 0.3 | 100 | 200 |
| Test3L$_{1400}$LT | 0.001 | 0.05 | 1400 | 0.3 | 0.3 | 75 | 200 |
| Test3L$_{1400}$LR-LT(1) | 0.001 | 0.05 | 1400 | 0.3 | 0.3 | 75 | 200 |
| Test3L$_{1350}$LR-LT(1) | 0.001 | 0.05 | 1350 | 0.3 | 0.3 | 65 | 200 |
| **3D** | | | | | | | |
| TestD1$^{r150}$ | 0.001 | 0.001 | 1500 | 0.3 | 0.3 | 100 | 150 |
| TestD3$^{r150}$ | 0.001 | 0.05 | 1500 | 0.3 | 0.3 | 100 | 150 |
| TestD3$^{r200}$ | 0.001 | 0.05 | 1500 | 0.3 | 0.3 | 100 | 200 |
| TestD3$^{r200}_{D0202}$ | 0.001 | 0.05 | 1500 | 0.2 | 0.2 | 100 | 200 |
| TestD3$^{r200}_{HFEL}$(2) | 0.001 | 0.05 | 1500 | 0.3 | 0.3 | 100 | 200 |
| TestD3$^{r200}_{1550}$ | 0.001 | 0.05 | 1550 | 0.3 | 0.3 | 100 | 200 |
| TestD3$^{r200}_{1450}$ | 0.001 | 0.05 | 1450 | 0.3 | 0.3 | 100 | 200 |
| TestD3$^{r200}_{1400}$ | 0.001 | 0.05 | 1400 | 0.3 | 0.3 | 100 | 200 |
| TestD3$^{r200}_{1350}$LLT | 0.001 | 0.05 | 1350 | 0.3 | 0.3 | 65 | 200 |
| TestD3$^{r200}_{1400}$LT | 0.001 | 0.05 | 1400 | 0.3 | 0.3 | 80 | 200 |

## B.2.2 Supplementary Figures

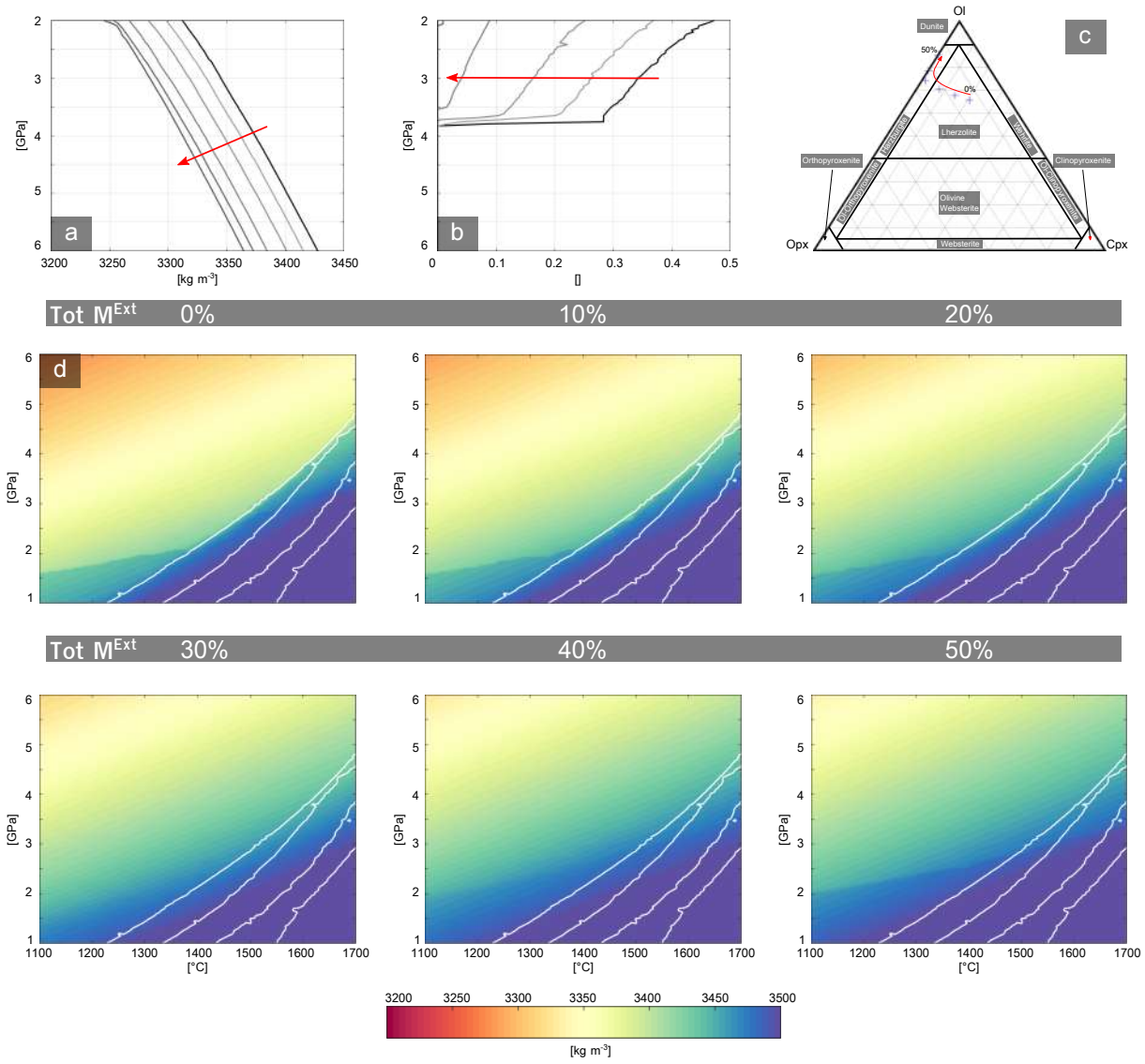


Figure B1: **a):** Density as a function of pressure at constant $T_P$ (1200 °C), red arrow indicate increase depletion; **b):** Melt quantity as a function of pressure at constant $T_P$ (1550 °C), red arrow indicates the increase depletion; **c):** Mode amount of clinopyroxene, orthopyroxene and olivine; **d):** Density of each depletion step.

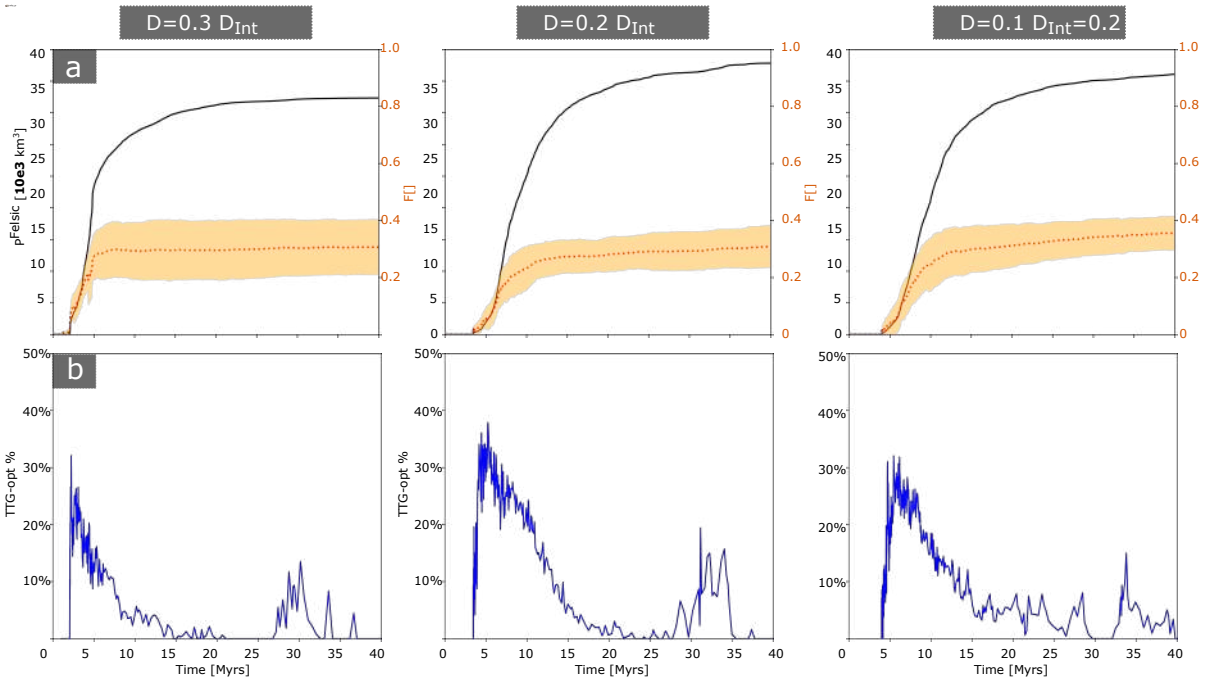


Figure B2: Every figure refers to different 2D experiments. The black boxes list the key parameters of each simulation (e.g. $D$, the depth of intrusions and $D_{Int}$ the depth interval of intrusion). All experiments were performed using $dM = 0.05$ and $M^{trs} = 0.001$. **a):** The orange dashed line represents the average amount of felsic components stored in the crust, while the colored area represents 1 STD of F. The black line represents the total amount of felsic crust produced versus time; **b):** The amount of felsic melts extracted within the TTG optimum field versus time.

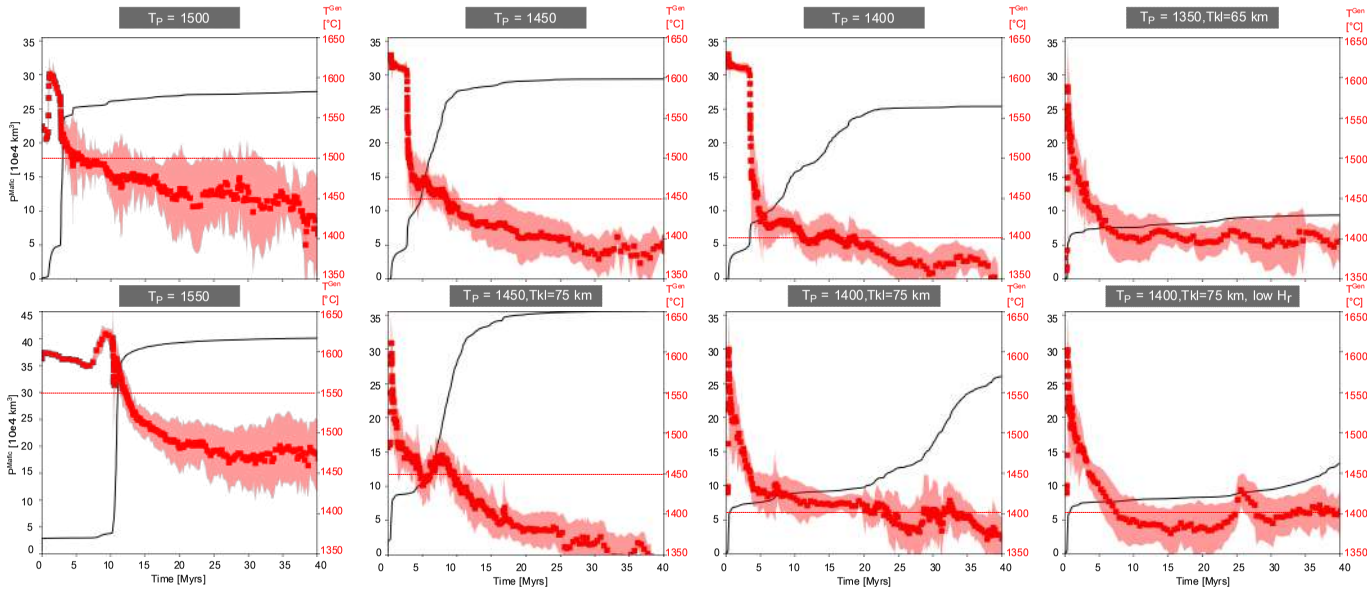


Figure B3: The evolution of the cumulative amount of mafic melts produced (black line). The black boxes list the key parameters of each simulation (e.g. Tkl, thickness of lithosphere, initial $T_P$). All the experiments were performed using $dM$ = 0.05 and $M^{trs}$ = 0.001. The red dashed line represents the initial $T_P$. The colored area represents 1 STD of $T^{Gen}$. The red square represents the average $T^{Gen}$.

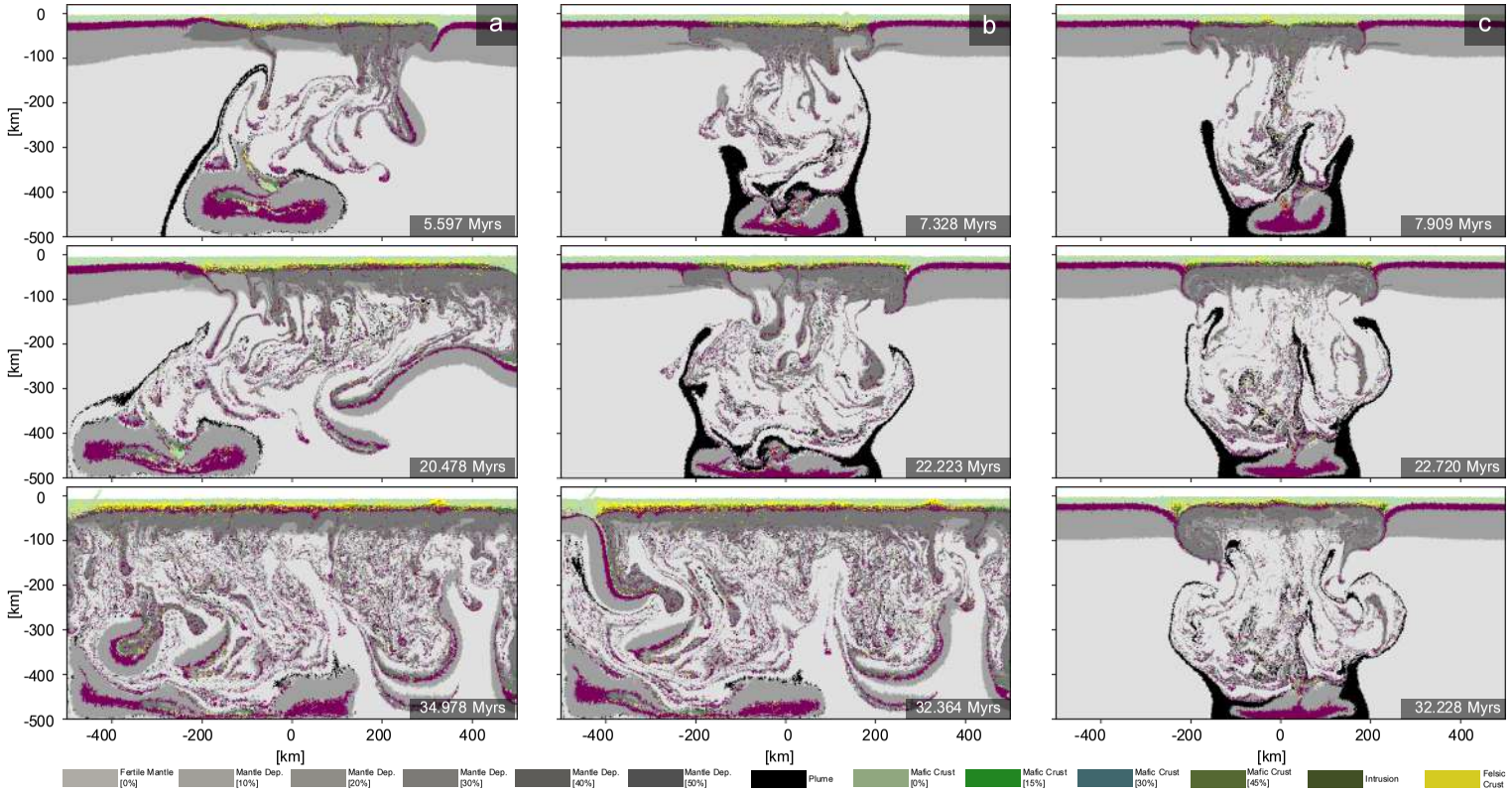


Figure B4: All experiments features the same $dM$ (0.05) and $M^{trs}$ (0.001). **a):** Initial $T_P$ = 1400 °C, lithospheric thickness, $Tkl$ = 100km ($Test3L_{1400}$ in Tab. B3); **b):** Same as *a* except for the lithospheric thickness, $Tkl$ = 75km ($Test3L_{1400}LT$ in Tab. B3); **c):** Same as *b)*, but lower radiogenic heating and with a bottom lower thermal boundary equal to 1600°C ($Test3L_{1400}LR\text{-}LT$ in Tab. B3).

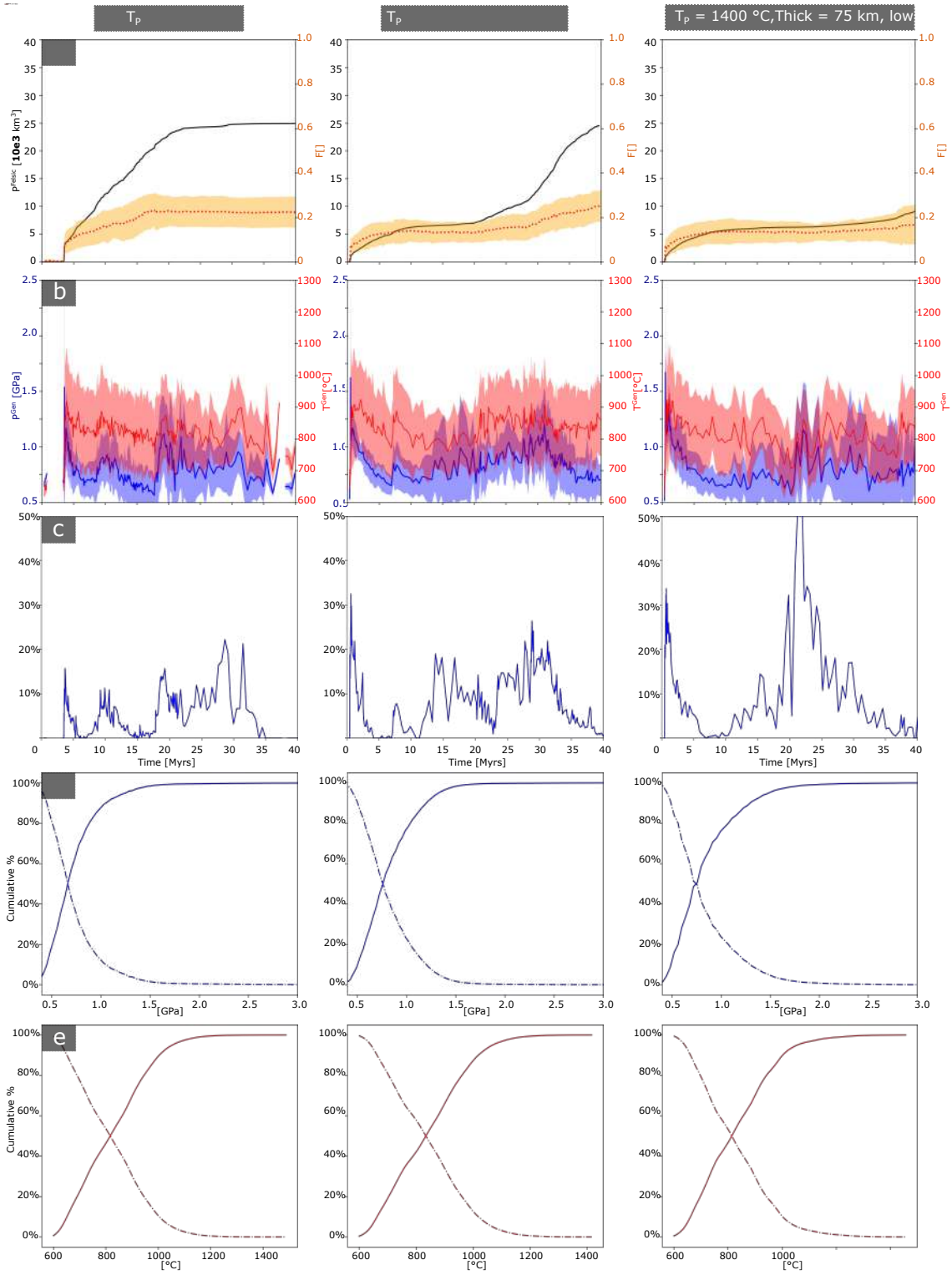


Figure B5: All the experiments are shown in B4 the list of input parameter are listed in B3. **a):** $P^{Felsic}$ vs time. **b):** The left axis is the $P^{Gen}$, pressure at which the felsic melts have been extracted, the blue thick line represents the average pressure of extraction vs time, and the shaded blue area represents the standard deviation. The right axis represent the $T^{Gen}$, the temperature at which the felsic melt are extracted. The red thick line represent the average temperature of extraction, while the red shaded area represents the standard deviation of the temperature of extraction;**c):** Relative amount of TTGs vs time, where the TTG-opt % is the volume of the melt extracted in the optimum field predicted by Palin et al. (2016). **d-e):** Cumulative frequency of the pressure and temperature of extraction evaluated for the all numerical experiment. The dashed lines represent the reverse cumulative distribution.

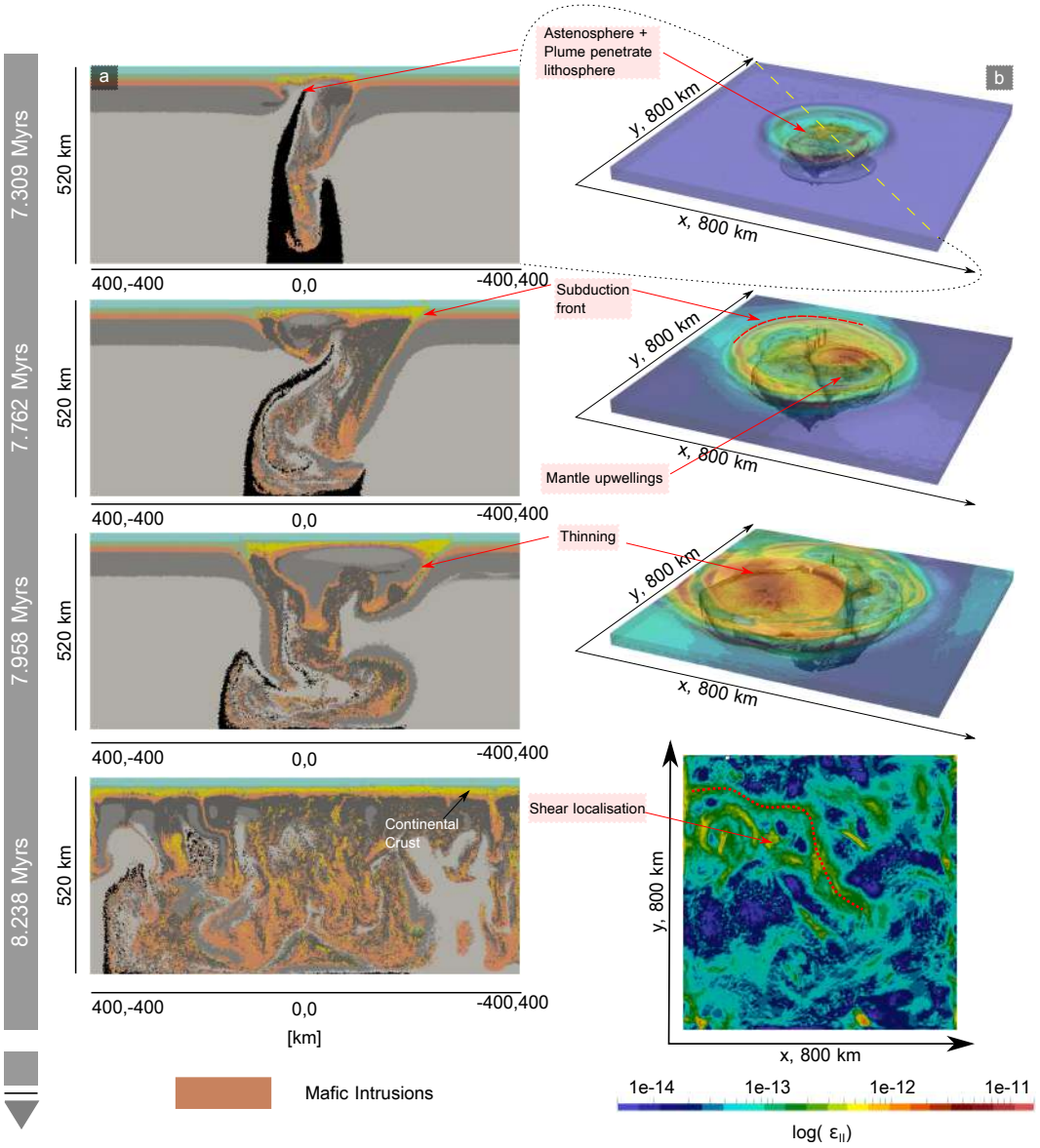


Figure B6: **Inefficient melt extraction, plume radius:150 km, dM=0.001** All the picture are ordered chronologically from top to bottom. **a):** Compositional profile taken along a1-a2 *[400 x,-400 y][-400 x,400 y]*; **b):** The transparent plot represents the strain rate state of the crust, while the gray underlying volumes is the contour of the volume of depleted mantle (the total melt extracted is ≥ 30%); **c):** Planar view of the strain rate invariant.

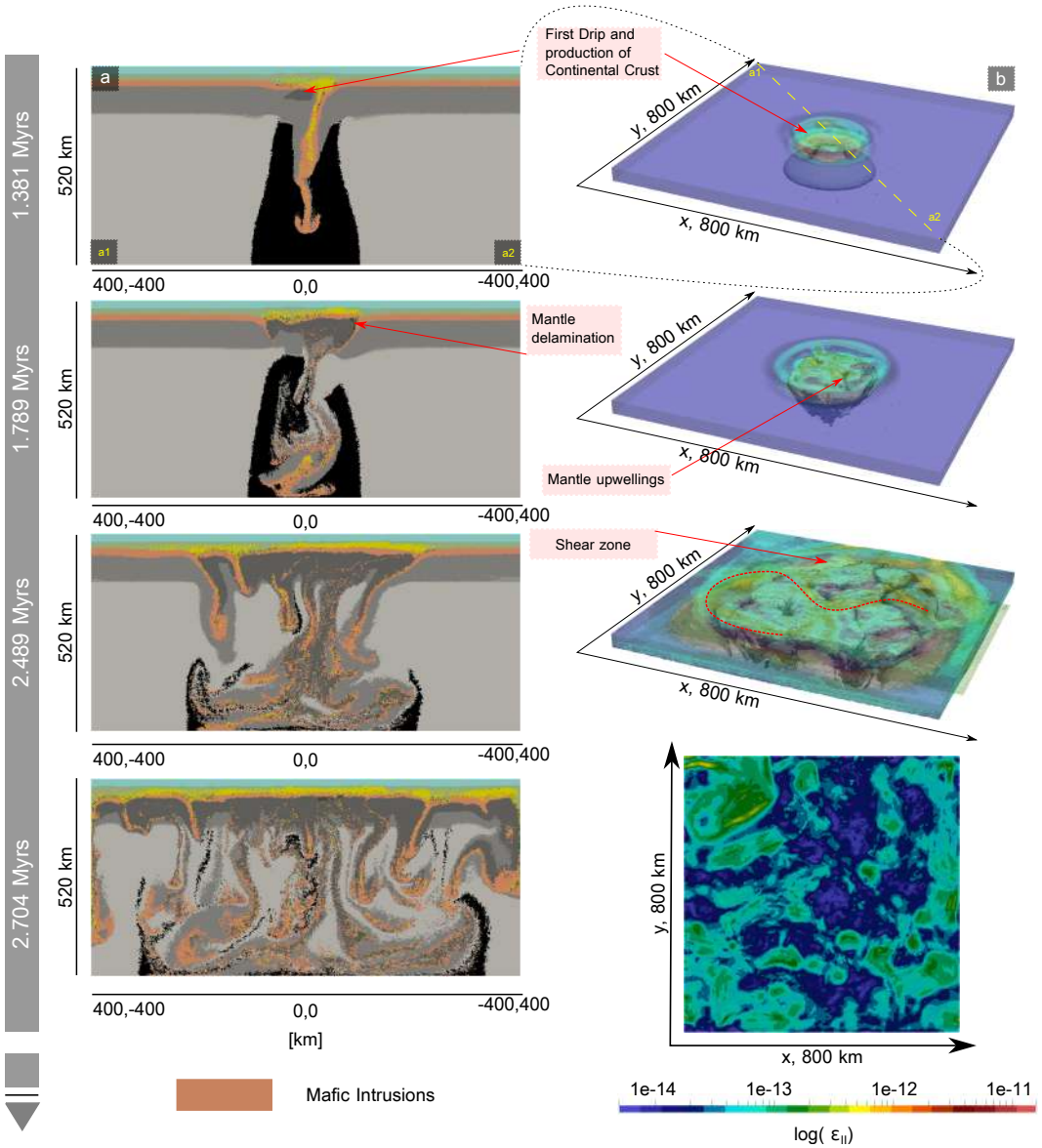


Figure B7: **Efficient melt extraction, plume radius:200 km, dM=0.001** All pictures are ordered chronologically from top to bottom. **a):** Compositional profile taken along a1-a2 *[400 x,-400 y][-400 x,400 y]*; **b):**The transparent plot represents the strain rate state of the crust, while the gray underlying volumes is the contour of the volume of depleted mantle (the total melt extracted is ≥ 30%); **c):** Planar view of the strain rate invariant.

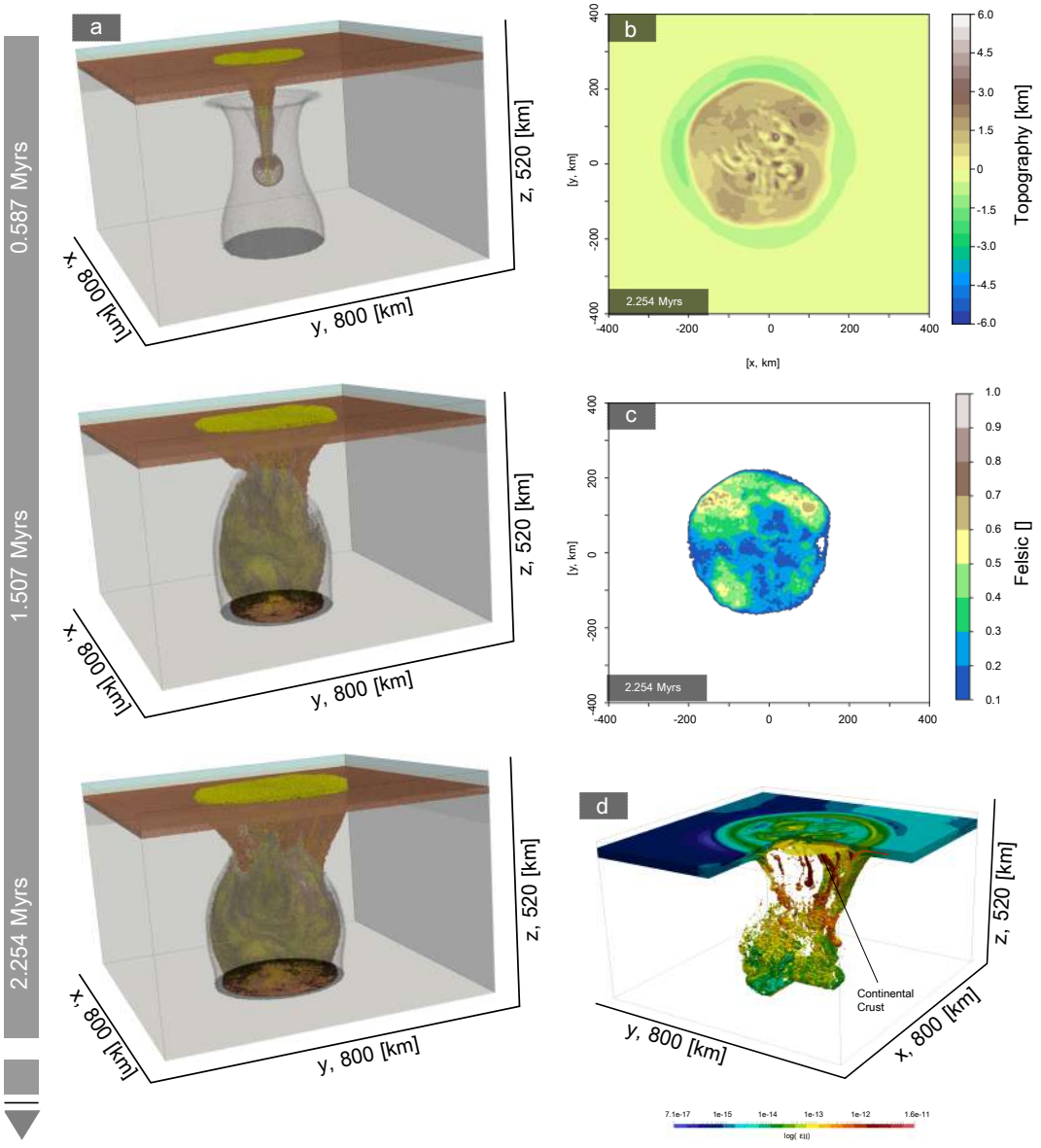


Figure B8: $\mathbf{T}_P$ **= 1400 °C, r=200 km, Tkl = 100 km, dM=0.05** All pictures are ordered chronologically from top to bottom. **a):** Compositional field; **b):** Topography; **c):** Felsic crust relative amount; **d):** Crustal strain rate field.

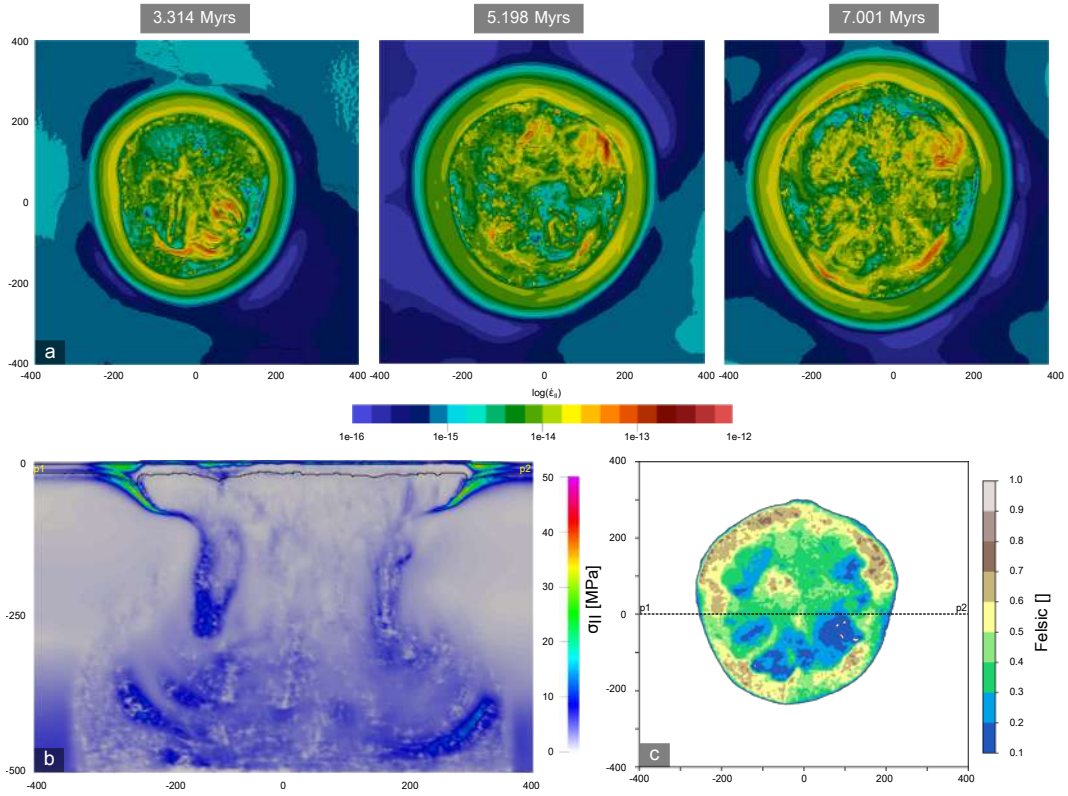


Figure B9: **Low $T_P$, $T_P$ = 1400 °C,r=200 km, Tkl = 75 km, dM=0.05 a):** Surface strain rate pattern; **b):** Slice taken at y=0 of the deviatoric stress tensor second invariant; **c):** Relative amount of felsic crust.

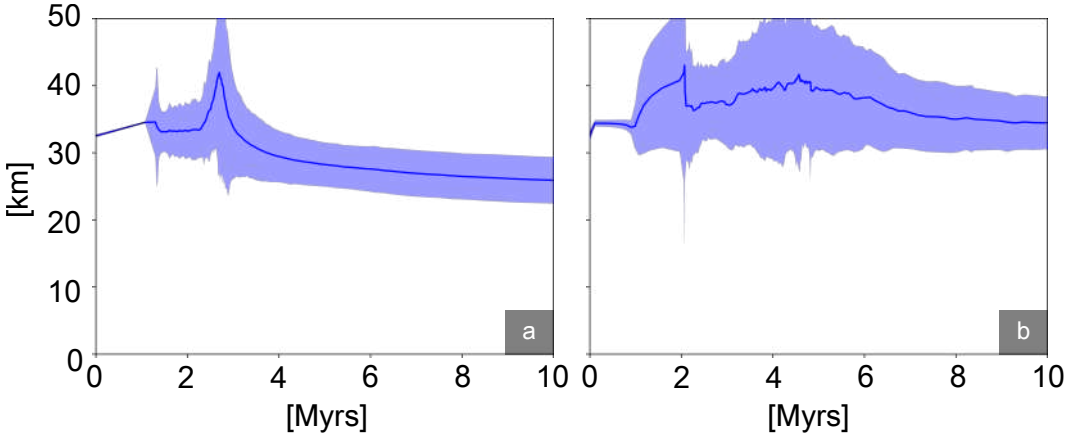


Figure B10: Comparison of crustal thickness evolution of 3D (**a)**) and 2D experiments (**b)**). Both the experiments feature the same dM (0.05), $T_P$ (1500 °C) and plume radius (200 km).

# REFERENCES


Balay, S., Abhyankar, S., Adams, M.F., Brown, J., Brune, P., Buschelman, K., Dalcin, L., Dener, A., Eijkhout, V., Gropp, W.D., Kaushik, D., Knepley, M.G., May, D.A., McInnes, L.C., Mills, R.T., Munson, T., Rupp, K., Sanan, P., Smith, B.F., Zampini, S., Zhang, H., Zhang, H., 2018. PETSc Users Manual. Technical Report ANL-95/11 - Revision 3.10. Argonne National Laboratory. URL: `http://www.mcs.anl.gov/petsc`.

Hirth, G., Kohlstedt, D., 2004. Rheology of the upper mantle and the mantle wedge: A view from the experimentalists. Inside the subduction Factory 138, 83–105.

Palin, R.M., White, R.W., Green, E.C., 2016. Partial melting of metabasic rocks and the generation of tonalitic–trondhjemitic–granodioritic (ttg) crust in the archaean: Constraints from phase equilibrium modelling. Precambrian Research 287, 73–90.

Piccolo, A., Palin, R.M., Kaus, B.J., White, R.W., 2019. Generation of earth's early continents from a relatively cool archean mantle. Geochemistry, Geophysics, Geosystems 0.

Ranalli, G., 1995. Rheology of the earth, 413 pp.

# ACKNOWLEDGEMENTS

## Declaration

I hereby declare that the contents of this dissertation are original and have not been submitted for any other degree or qualifications. This dissertation is the result of my own work, except where specifically indicated in the text.

## Erklärung

Ich versichere hiermit gemä≎ §10 Abs. 3d der Promotionsordnung des Fachbereichs 09 (Chemie, Pharmazie und Geowissenschaften) der Johannes Gutenberg-Universität Mainz vom 24.07.2007, die als Dissertation vorgelegte Arbeit selbständig und nur unter Verwendung der in der Arbeit angegebenen Hilfsmittel verfasst zu haben. Ich habe oder hatte die hier als Dissertation vorgelegte Arbeit nicht als Prüfungsarbeit für eine staatliche oder andere wissenschaftliche Prüfung eingereicht. Ich hatte weder die jetzt als Dissertation vorgelegte Arbeit noch Teile davon bei einer anderen Fakultät bzw. einem anderen Fachbereich als Dissertation eingereicht.

——————————

(Andrea Piccolo)

Mainz, Friday 7th June, 2019